



DISSERTATION

Simulating Transient Effects of Pulsed Beams on Beam Intercepting Devices

ausgeführt zum Zwecke der Erlangung des akademischen Grades eines
Doktors der technischen Naturwissenschaften

unter der Leitung
von

Em.Univ.Prof. O.Univ.Prof. Dipl.-Ing. Dr.techn. Hannes AINGER
E141
Atominstitut

eingereicht an der
Technischen Universität Wien
Fakultät für Physik

von
Dipl.-Ing. Herta Richter
0025492
Hormayrgasse 23
1170 Vienna
Austria
herta.richter@cern.ch

Wien, am 12. Oktober 2011



DISSERTATION

Simulating Transient Effects of Pulsed Beams on Beam Intercepting Devices

submitted to attain the academic degree of a
Doctor of Technical Sciences

carried out
under the guidance of

Em.Univ.Prof. O.Univ.Prof. Dipl.-Ing. Dr.techn. Hannes Aigner
and under the survey of
Dr. Etam Noah Messomo
within the framework of the
CERN Austrian Doctoral Student Program

presented at the
Vienna University of Technology
Faculty of Physics
Vienna, Austria

by
Dipl.-Ing. Herta Richter
0025492
Hormayrgasse 23
1170 Vienna
Austria
herta.richter@cern.ch

Vienna, 12th of October 2011

Contents

Zusammenfassung	iii
Summary	v
Acknowledgments	vii
1 Introduction	1
2 Development of High Power Targets	3
2.1 Spallation Targets	6
2.2 RIB Targets	7
2.3 Neutrino Facilities	8
2.4 Design Issues Common to all High Power Targets	9
2.4.1 Liquid Targets	10
2.4.2 Solid Targets	11
2.4.3 Target Selection Criteria	12
3 Load and Transient Effects of Beams Interacting with Matter	13
3.1 Interaction of Particles with Matter	13
3.1.1 Interaction of Charged Particles with Matter	13
3.1.2 Interaction of Photons with Matter	16
3.2 Transient Effect on Beam Intercepting Devices	18
3.2.1 Static and Quasi-static Behavior of Materials	18
3.2.1.1 Definitions and Terminology	18
3.2.1.2 Elastic Deformation	19
3.2.1.3 Plastic Deformation	20
3.2.1.4 Fracture	22
3.2.2 Dynamic Behavior of Materials	25
3.2.2.1 Elastic Waves	26
3.2.2.2 Plastic Waves	29
3.2.2.3 Shock Waves	30
3.2.2.4 Crossing the Phase Space	50
4 Experimental Investigation	67
4.1 Surface Velocity Measurements of Collimator Jaw Exposed to Proton Beams	67
4.1.1 Motivation	67
4.1.2 Experimental Background	68

4.1.2.1	Collimator Setup	68
4.1.2.2	Laser Doppler Vibrometer Setup	68
4.1.2.3	Proton Beam Parameters and Energy Deposition	71
4.1.3	Measurement Results	73
4.1.3.1	Data Handling	73
4.1.3.2	Reproducibility Test	79
4.1.3.3	Collimator Response	92
4.1.4	Summary	105
4.2	Irradiation of Metallic Targets with Uranium Ion Beam	107
5	Simulating Dynamic Target Response upon Impact of Uranium Ion Beams	109
5.1	Energy Deposition Simulation	109
5.1.1	Energy Deposition Simulation for Copper	110
5.2	Simulating Dynamic Response	113
5.2.1	Material Description	113
5.2.1.1	Copper	114
5.2.2	Interfacing ANSYS AUTODYN® with FLUKA	115
5.3	Results	116
5.3.1	Copper	117
5.3.1.1	Simulation of Sample 26	117
5.3.1.2	Simulation of Sample 28	126
5.3.1.3	Comparison Results of Metallurgical Examination of Samples 26 and 28	126
5.3.2	Simulation of Other Metallic Targets	130
5.3.2.1	Lead	130
5.3.2.2	Tantalum	132
5.3.2.3	Tungsten	132
6	Summary and Outlook	135
A	FLUKA Parameters	139
B	Beam Parameters	141
List of Figures		143
List of Tables		157
References		161

Zusammenfassung

Der Trend in der Physikgemeinschaft in Richtung höherer Strahlbrillianz durch höhere Strahlintensitäten und -leistungen durch die Möglichkeiten der Teilchenstrahlbeschleuniger hat zu Herausforderungen für die EntwicklerInnen von strahlabfangenden Elementen (beam intercepting devices = BIDs) geführt. Für die Gestaltung der BIDs müssen die zunehmende Wärmebelastung auf diesen Bauteilen aufgrund von energetischen und fokussierten Strahlen sowie – für viele Fälle – auch ihre hohe gepulste Natur berücksichtigt werden. Die BIDs werden in unterschiedlichen Einsatzgebieten verwendet: Einerseits gibt es Bauteile, die nur einem Teil der gesamten Partikelstrahlhüllkurve ausgesetzt sind, und die eventuell entwickelt wurden, der vollen Belastung durch den Strahl nur sporadisch Stand zu halten oder auch nur für ein Unfallszenario (z. B. Kollimatoren). Andererseits scheinen BIDs auch als Targets auf, die gezielt in den Strahl eingebracht werden, um von der reichhaltigen Produktion von sekundären (oder auch tertiären) Teilchen zu profitieren (z. B. Targets für die Produktion von Neutronen).

Die Ansprüche seitens der Physik – vor allem für die Targets, die absichtlich in den Strahl eingebracht werden – stehen manchmal im Gegensatz zum aktuellen Stand der Technik und bedürfen gründlicher Studien. Physikziele für Targets müssen gegebenenfalls angepasst werden, um alle konkurrierenden Aspekte zu vereinen. Darüber hinaus erhöhen zusätzliche Kriterien, wie Auswirkungen auf die Umwelt, Kosteneffizienz und Sicherheit, die technischen Anforderungen für den Gestaltungsprozess.

Als eine Möglichkeit von vielen, die verschiedenen Aspekte dieser anspruchsvollen Anforderungen miteinander zu verknüpfen, wurden in dieser Dissertation zwei hoch entwickelte Computerprogramme, nämlich FLUKA und ANSYS AUTODYN[®], kombiniert. Das Erste ist ein weit entwickelter Monte-Carlo-Code, der auf die Wechselwirkung von Teilchen mit statischer Materie spezialisiert ist, während Letzteres ein vielseitiger expliziter Code für die Simulation hochdynamischer Vorgänge, wie etwa Hochgeschwindigkeitsaufschläge, ist. Beide Computerprogramme wurden intensiv über viele Jahre entwickelt und werden kontinuierlich überarbeitet, damit ihr bestmögliches Potenzial erreicht werden kann. Als Folge ihrer getrennten Entwicklungsgeschichte erfordert eine Kombination beider Programme einen großen Arbeitsaufwand — sowohl an den Grenzen ihres physikalischen Anwendungsbereiches, als auch bei Anpassungen im Bereich der Informationstechnologie. Diese aktuelle Arbeit kann nicht und hat auch nicht alle notwendigen Integrationspunkte berührt, aber ist ein Versuch, einen ersten Schritt der Koppelung innerhalb eines praktikablen Zeitrahmens zu erreichen.

Zur Einleitung dieser Arbeit werden zwei wesentliche Aspekte des erforderlichen Verständnisses auf dem Weg zu Hochleistungstargets eingeführt: Erstens werden die physikalischen Anforderungen und technologischen Herausforderungen für Hochleistungstargets an

Hand von Beispielen von Produktionseinheiten für Neutronen, radioaktive Isotope und Neutrinos vorgestellt, die die High-End-Anforderungen von BIDs demonstrieren. Zweitens enthält diese Dissertation eine kurze Einführung der Physikmodelle von Teilchenwechselwirkungen mit statischer Materie sowie die Darstellung mechanischer Aspekte von Materie, die dynamischen Lasten unterworfen ist. Diese dienen als Einstieg in ein sehr komplexes und weitreichendes Feld, das zwar schon lange erforscht wird, aber immer noch hochaktuell ist. Die experimentellen Beiträge zu dieser Arbeit bestehen einerseits aus der Präsentation der gesammelten Messergebnisse eines Laser-Doppler-Vibrometers (LDV) von der wiederholten Belastung eines Kollimators durch einen Bruchteil des Strahles bei Injektionsenergien des Large Hadron Collider (LHC) am CERN und andererseits aus den Hintergrundinformationen eines Bestrahlungsexperimentes von Metallen mit energetischen Uranionen. Letztere dienen als Basis für die in dieser Arbeit durchgeführten Simulationen. Beide Simulationswerkzeuge sowie die für deren Kopplung benötigten programmietechnischen Abänderungen sind beschrieben. Für die Targets wurden verschiedene Materialmodelle miteinander verknüpft und ein Parameter, der die Schädigung des Materials beschreibt, wurde variiert. Im Fall von zwei Kupfer-Targets führte dieses Verfahren erfolgreich zu einer qualitativen Übereinstimmung der Simulationen mit den experimentellen Ergebnissen. Zuletzt werden die Einschränkungen der verwendeten Codes alleine sowie deren Kombination im Detail dargestellt, wobei mögliche zukünftige Entwicklungen umrissen werden.

Summary

The trend inside the physics community towards higher beam brilliance, through both higher beam intensities and beam powers, due to the possibilities of particle beam accelerators has lead to challenges for the developers of beam intercepting devices (BIDs). For the design of BIDs, the increasing heat load onto these devices due to energetic and focused beams as well as – in many cases – their highly pulsed nature have to be taken into account. The beam intercepting devices are used within different settings: On one end of the spectrum, there are devices that are only exposed to part of the beam particle envelope and might be designed to withstand the full load only sporadically, or maybe even only in an accident scenario (e.g. collimators). On the other end of the spectrum of BIDs are targets purposefully introduced into the beam in order to benefit from the copious production of secondary (or even tertiary) particles (e.g. targets for the production of neutrons).

The desired criteria from the physics side – especially those for the targets which are introduced into the beam – are sometimes diametrically opposed to the current available technology and are in need of thorough studies. Physics goals of targets might have to be adjusted in order to optimize the balance between the rival aspects. In addition, other issues such the impact on environment, cost efficiency and safety compound the constraints on the design process.

With the many possibilities to marry different aspects of these challenging requirements, this thesis was conceived as one exercise of many in which two highly developed software frame-works, namely FLUKA ([1],[2]) and ANSYS AUTODYN® [3] are joined. The first is a richly developed Monte-Carlo code that specializes in particle interaction with static matter, while the latter is a versatile explicit piece of software capable of simulating highly dynamic processes such as high velocity impacts. Both these computer programs were developed intensively over many years and are still works in progress, yet to achieve their highest possible potential. As a consequence of their separate development histories, a fusion of the two frame-works requires a large amount of work — both on the frontiers of their applicable physics domains, and simple adjustments from the point of view of information technology. This current thesis cannot and has not touched on all of the needed integration points, but attempts to achieve a first step of interconnection within a feasible time-frame.

As an introduction to this thesis, two main aspects of understanding needed for the road to high power targets are introduced: firstly, the physics needs and technological challenges for high power targets are presented with the help of examples of production units for neutrons, radioactive isotopes and neutrinos to demonstrate the high end performance needs of BIDs. Secondly, this thesis contains brief introductions of physics models behind particles interacting with static matter as well as the mechanical aspects of matter

subjected to loads. These serve as an entry point to a very complex and rich field of an already substantial but still ongoing body of research.

The experimental contributions to this work are, on one hand, the presentation of the collected measurement results obtained with a Laser Doppler Vibrometer (LDV) for the repeated impact of the fraction of the beam load of the Large Hadron Collider (LHC) at CERN at injection energies onto a collimation device and, on the other hand, the experimental background information of the irradiation of metallic targets with energetic uranium ions serving as the basis for the simulation work of this thesis. Both simulation tools are described, as well as the computational requirements needed for their connection. The simulation results are compared with the samples examined after irradiation while the main emphasis lies on copper targets. For the targets, different material models were joined and one parameter which describes the damage of the material was varied. In the case of two copper targets, this procedure successfully led to a qualitative agreement of simulations and experimental results. Finally, the limitations of the used codes and those of their combination are discussed in detail while possible future developments are also outlined.

Acknowledgments

Numerous people have contributed in just as many ways to the success of this thesis. The order in which they are mentioned should not be understood as ranking their input in order of importance. Each and every contribution is greatly appreciated.

I would like to express thanks to my thesis supervisors Professor Hannes Aigner and Dr. Etam Noah. To Professor Aigner, I am grateful for giving me the opportunity to work at CERN and his guidance throughout the PhD. I am greatly indebted to Dr. Noah for carrying over the thesis supervision from Dr. Jacques Lettry and Dr. Roman Wilfinger after their responsibilities changed, which allowed me to continue working on an already started subject. Dr. Noah not only guaranteed continuity but also provided new inputs and ideas based on the parts in place. Moreover, after having started a different position at CERN himself, he committed himself to the continuous guidance of my PhD. I profited not only from this stability itself but also from his eagerness to share the expertise and insights from target development for the high power target for the European Spallation Source (ESS).

Dr. Karin Poljanc's invaluable advice on matters both related to the concept of the thesis and on organizational manners is greatly appreciated. The dedication of my two former supervisors during the first part of my thesis at CERN, Dr. Lettry and Dr. Wilfinger, as well as sharing the results of the GSI experiment wherever available are very much appreciated. I want to express my gratitude to both thesis reviewers, Professor Aigner and Associate Professor Benedikt, for the careful reading and comments.

Thanks are given to the Austrian government for the financial support of the Austrian Doctoral Student Program at CERN through the Austrian Federal Ministry for Education, the Arts and Culture. The coordinators of this program at CERN, Dr. Benedikt and Dr. Werner Riegler, as well as the – former – head of the CERN Doctoral Student Program, Dr. Erik Heijne, and Ingrid Schmid, as contact within human resources, are all thanked for their monitoring efforts. The staff of the physics deanery of the Vienna University of Technology demonstrated high flexibility regarding all matters complicating the administration for a PhD student working abroad.

From my time at ISOLDE, I would like to thank Richard Catherall in his function as section leader for ongoing support especially during the time of transition of supervisors. Luca Bruno, who was my first office colleague at ISOLDE, shared his vast professional expertise and practical knowledge on how CERN works, allowing me a quick start in many different aspects. I received my first and well structured introduction to FLUKA by my ISOLDE colleague and fellow PhD student Dr. Elian Bouquerel. Later, Dr. Francesco Cerutti from the FLUKA development and teaching team willingly shared his knowledge with me. All fellow ISOLDE PhD students in the target and physics sections, namely

Dr. Sandrina Fernandes da Visitaço, Dr. Tania de Melo Mendonça, Gry Tveten, Martin Eller, Dr. Martin Breitenfeldt, and Dr. Liviu Penescu, as well as fellow Austrian PhD student Katharina Kaska here at CERN are thanked for their professional advice and friendship. The group of technical engineers, namely Ermanno Barbero, Daniel Carminati, Bernard Crepieux and Stefano Marzari, and Martin Eller delivered good and precise preparatory work for the Laser Doppler Vibrometer measurements of the Large Hadron Collider collimator jaw as well for the GSI experiment. In addition I would also like to thank Dr. Tim Giles, Paweł Kasprówicz, Michael Owen and Dr. Thierry Stora for the cooperative atmosphere within the ISOLDE target group.

My sincere thanks to the collaborators of the GSI experiment for providing the experimental setup and know-how, cooperative partnership and sharing experimental results: Dr. Boris Achenbach, Dr. Karl-Heinz Behr, Dr. Adolf Brünle, Dr. Hans Geissel, Dr. Victor Gryaznov, Dr. Dieter H. H. Hoffmann, Dr. Alexander Hug, Dr. Christos Karagiannis, Dr. Aleksandra Kelić, Dr. Birgit Kindler, Dr. Klaus Knie, Dr. Markus Krause, Dr. Misha Kulish, Dr. Bettina Lommel, Dr. Jurij Menzel, Dr. Victor Mintsev, Dr. Nina Müller, Dr. Klaus Sümmerer, Dr. Naeem Ahmad Tahir, Dr. Anna Tauschwitz, Dr. Andreas Tauschwitz, Dr. Marilena Tomut, Dr. Christina Trautmann, Dr. Šerban Udrea, Dr. Dmitry Varentsov, Dr. Helmut Weick, Dr. Martin Winkler and Dr. Yongtao Zhao.

For the summary of the work on the LHC collimator impact test, I wish to thank the contributions of Dr. Oliver Aberle, Dr. Alessandro Bertarelli, Dr. Chiara Bracco, Dr. Markus Brugger, Dr. Alessandro Dalocchio, Dr. Verena Kain, Dr. Michael Lazzaroni, Dr. Helmut Vincke and the ATB-EA and collimation teams.

To the non-CERN experts in their fields I contacted, a warm thanks for their willingness to share their knowledge: Dr. Scott Crockett, the Los Alamos SESAME database manager, Dr. Stefan Hiermaier, from the Fraunhofer Institute for High-Speed Dynamics, Ernst-Mach-Institut (EMI in Freiburg, Efringen-Kirchen and Kandern), Dr. Peter Sievers, who retired from CERN and now works for the ESS project, Dr. Roger Bennett, from the Science and Technology Facilities Council in the United Kingdom.

I enjoyed the quick technical support, suggestions from and discussions with the team of ANSYS AUTODYN® – including when they were still AUTODYN®. For matters regarding the Laser Doppler Vibrometer, the technical support team of Polytec is thanked.

During the time on working on my thesis I had the pleasure to – sometimes briefly – work with people whose collaborative efforts have not become part of this thesis. However, those works contributed to my scientific advancements and therefore I would like to extend my gratitude to Dr. Edda Gschwendtner, Dr. Jan Borburgh, Dr. Adrian Fabich, Dr. Friedrich Lackner, Dr. Thierry Masson, Dr. Volker Mertens, and Dr. Friedrich Szoncso.

Most sincere thanks go to my current section within radiation protection (DGS-RP-AS): Dr. Stefan Roesler, Dr. Thomas Otto – who changed position – and Dr. Joachim Vollaire, who made the finalization of my thesis possible through all conceivable efforts from their side. I would also like to thank the publishers for their prompt answers regarding my requests for permission to use pictures and text within my thesis.¹ Many thanks go to Helen Lambert for her fast and meticulous proofreading.

¹ I have made an effort to locate all owners of copyrighted material in order to receive their endorsement for the usage of this material for this thesis. In case of any infringement of copyright emerging I would like to ask for immediate notification.

ACKNOWLEDGMENTS

Last, but certainly not least, I want to thank my family in Austria and my friends from all around the world for their encouraging support.

Many others who have not been mentioned explicitly and who contributed in one way or another shall be thanked: the CERN library team, the human resources team at CERN and any other CERN supporting service. I might have forgotten to mention certain aspects of support I received or people themselves. If this is the case it is entirely unintentional. I hope, however, that I showed my gratitude immediately upon receiving any help and kindness.

Chapter 1

Introduction

The demand of the physics community towards higher beam brilliance together with the development towards higher beam intensities and beam powers within the possibilities of accelerating structures has lead to challenges for the developers of beam intercepting devices (BIDs): two realms of pure design aspects have to be taken into consideration. Firstly the increasing heat load onto these devices due to energetic and focused beams and secondly – in many cases – their highly pulsed nature. There are different kinds of BIDs. On one end of the spectrum, there are devices that are only exposed to part of the beam particle envelope, and might be designed to withstand the full load only sporadically or maybe even only in an accident scenario (e.g. collimators). On the other end of the spectrum of BIDs are targets purposefully introduced into the beam in order to benefit from the copious production of secondary (or even tertiary) particles (e.g. targets for the production of neutrons).

From a design point of view, the ideal physics requirements, especially for the latter, are sometimes incompatible with the current available technology and therefore require deep studies during which the physics needs might have to be adjusted in order to optimize the balance between these rivaling aspects. From the point of views of management and of the impact on environment, cost efficiency and safety add extra constraints to the design process. Marrying these different fields of expertise is still a challenging work in progress.

This thesis was laid out as one of many possible exercises to bridge this gap by joining two highly developed software frame-works:

- FLUKA ([1],[2]), a richly developed Monte-Carlo code that specializes in particle interaction with static matter,
- ANSYS AUTODYN[®] [3], a versatile explicit piece of software capable of simulating highly dynamic processes such as high velocity impacts.

Both these computer programs have emerged from many years of development and are still being developed to their highest possible potential. However, their separate development histories make it clear that their fusion was not foreseen and therefore requires substantial advancements — not only on the frontiers of their applicable physics domains, but also simple adjustments from the point of view of information technology. This work has not touched on all of the needed integration points, but attempted to achieve a first step of interconnection within a feasible time-frame.

This thesis is structured in the following way: Chapter 2 presents the physics needs and technological challenges for high power targets, with the help of examples of production units for neutrons, radioactive isotopes and neutrinos to demonstrate the high end performance needs of BIDs. Chapter 3 concentrates on the physics models behind particles interacting with static matter (section 3.1) in addition to the mechanical aspects of matter subjected to loads (section 3.2). The reader should however be aware of the following limitations: the introductory chapters of this thesis (both chapter 2 and even more so chapter 3) do not – and in fact, cannot – describe all underlying physical and mechanical principles in detail, but only serve as an entry point to a very complex and rich field of an already substantial but still ongoing body of research.

Chapter 4 comprises the experimental aspect of this thesis: for experimental investigations in section 4.1, the repeated deposition of the fraction of the beam load of the Large Hadron Collider (LHC) at CERN at injection energies onto a collimation device was recorded with a Laser Doppler Vibrometer (LDV). The experimental results of this investigation served as direct input to the collimation team. In section 4.2 the experimental background information of the irradiation of metallic targets with energetic uranium ions is briefly summarized in relation to the simulation parameters in the following chapter. Chapter 5 is dedicated to the main concept of this thesis, the connection of FLUKA and ANSYS AUTODYN®. Both the simulation tools and their combination are described in sections 5.1 and 5.2, while the results are presented in section 5.3, concentrating on two specific copper samples. Finally, chapter 6 summarizes the knowledge gained and points out needed future developments.

Chapter 2

Development of High Power Targets

The acronyms and abbreviations throughout chapter 2 are summarized in tab. 2.1. The increasing beam powers of existing and future accelerators allow increasing yields for different fixed target facilities. However, this opportunity for more advanced physics research, comes with high demands for these beam-intercepting targets. This chapter summarizes the main physics needs and engineering suggestions to provide targets with sufficiently long-lasting performance for spallation and radioactive ion beam (RIB) targets, as well as targets for the generation of neutrino beams. Other targets for the production of, for instance, muons and kaons, face similar technical challenges. In tab. 2.2 starting on p. 4 one can see a selection of current (high power) targets.

Table 2.1: Names, acronyms and abbreviations in chapter 2 (including those used in tab. 2.2 starting on p. 4).

BB	B eta- b eam
BNL	B rookhaven N ational L aboratory, USA
CSNS	C hina S pallation N eutron S ource
CW	C ontinuous W ave
ESS	E uropean S pallation S ource
EURISOL	E uropean I sotope S eparation O n- L ine R adioactive I on Beam Facility
FRIB	F acility for R are I sotope Beams, USA
IFMIF	I nternational FMIrradiation F
ISAC	I sotope Separator and Accelerator at T, Canada
ISIS	I pulsed nmuon source at R, UK
ISOL	I sotope Separator O
ISOLDE	I sotope Separator O at CERN
JSNS	J - P ARC S NS, Japan
J-PARC	J apan P roton A ccelerator Research Complex
LANSCE	L os A lamos NScience Center, USA
LINAC	L inear A ccelerator
LPSNS	L ong P ulsed S pallation NS ource
NSB	NSuperbeam
ORNL	O ak RNL
RAL	RA ppleton L

table continued on next page

Table 2.1: Names, acronyms and abbreviations in chapter 2 (including those used in tab. 2.2 starting on p. 4).

RIB	Radioactive Ion Beam
RIBS	RIB Source
SINQ	Swiss Spallation Neutron Source
SNS	Spallation Neutron Source
SPES	Selective Production of Exotic Species, Italy
SPIRAL	Séperateur et Postaccélérateur d’Ions Radioactifs produits en Ligne (Separator and postaccelerator of radioactive ions produced online), France
SPSNS	Short Pulsed Spallation Neutron Source
TEM	Transmission Electron Microscopy
TRIUMF	Canada’s National Laboratory for Particle and Nuclear Physics
TS	Target Station

 Table 2.2: Example of target facilities around the world (inspired by slide 3 of [4]). Abbreviations and Symbols: stat. (status); mat. (material), t_{pulse} (beam pulse duration), f_{pulse} (pulse repetition rate), E_{kin} (kinetic beam energy), $\langle P_{beam} \rangle$ (time averaged beam power), \dagger (per nucleon); bl (blanket), $(Xx)^{cl}$ (cladding/tubes with material Xx), C-C (carbon-carbon composite), δ (with regards to direct target), Xx^f (foil of material Xx), $^\lambda$ (liquid), η (with regards to neutron-converter), ZA (Zirkaloy); driver beam types: $^{(p)}$ (proton), $^{(3)He}$ (3 He), $^{(d)}$ (deuterium), $^{(Ar)}$ (argon), $^{(U)}$ (uranium); for beta-beam: 6He for production of 6 He and 18Ne for production of 18 Ne; abbreviations for status of facilities: E (existing), DF (design study finalized), UC (under construction), US (under study).

target name (type)	stat.	target mat.	t_{pulse} [μ s]	f_{pulse} [Hz]	E_{kin} [GeV]	$\langle P_{beam} \rangle$ [MW]
BNL NSB [5]	US	C-C	2.58	2.5	$28^{(p)}$	1
CERN-Fréjus NSB [6]	US	C, Ti	400	50	$4.5^{(p)}$	4
CSNS-I / CSNS-II (SPSNS) [7], [8]	UC	W (Ta) cl	<0.5	25	$1.6^{(p)}$	0.1 / 0.2
ESS (LPSNS) [9], [10]	US	W	2860	14	$2.5^{(p)}$	5
EURISOL (CW-RIBS) [11]	DF	Hg $^\eta$; Ta $^{f,\delta}$, C/SiC $^\delta$, Nb/Al ₂ O ₃ $^\delta$, Pb $^{\lambda,\delta}$	CW	–	$1^{(H^-)}$	4^η ; 0.1^δ
EURISOL (BB) [11]	DF	η BeO 6He , MgO 18Ne	+	CW	$2^{(p)}, 6^{He}$, 0.0148 $(^3He), 18^{Ne}$	0.2^{6He} , 2^{18Ne}
FRI B (CW-RIBS) [12], [13], [14]	US	C	CW	–	$0.6^{(p)}$ – $0.2^{(U)}$ \dagger	0.4

table continued on next page

Table 2.2: (continued) Example of target facilities around the world (inspired by slide 3 of [4]). Abbreviations and Symbols: stat. (status); mat. (material), t_{pulse} (beam pulse duration), f_{pulse} (pulse repetition rate), E_{kin} (kinetic beam energy), $\langle P_{beam} \rangle$ (time averaged beam power), \dagger (per nucleon); bl (blanket), $(Xx)^{cl}$ (cladding/tubes with material Xx), C-C (carbon-carbon composite), δ (with regards to direct target), Xx^f (foil of material Xx), $^{\lambda}$ (liquid), η (with regards to neutron-converter), ZA (Zirkaloy); driver beam types: $^{(p)}$ (proton), $^{(3He)}$ (3 He), $^{(d)}$ (deuterium), $^{(Ar)}$ (argon), $^{(U)}$ (uranium); for beta-beam: 6He for production of 6 He and 18Ne for production of 18 Ne; abbreviations for status of facilities: E (existing), DF (design study finalized), UC (under construction), US (under study).

target name (type)	stat.	target mat.	t_{pulse} [μ s]	f_{pulse} [Hz]	E_{kin} [GeV]	$\langle P_{beam} \rangle$ [MW]
ISAC (CW-RIBS) [15], [16], [17]	E	... ¹	CW	—	0.5 ^(p)	0.05
ISIS-TS1 / ISIS-TS2 (LPSNS) [18], [19]	E	W (Ta) ^{cl}	2×0.1	40 / 10	0.8 ^(p)	0.145–0.16 / 0.048
ISOLDE (pulsed RIBS) [20], [21], [22]	E	... ²	2.4	0.83– 0.42	1.4 ^(p)	$2\text{--}5 \cdot 10^{-3}$
JSNS (SPSNS) [23]	E	Hg	1	25	3 ^(p)	1 (0.3 [24])
LANSCE: Lujan area (SPSNS) [25], [26], [27]	E	W	0.29	20	0.8 ^(p)	0.08 – 0.1
Neutrino Factory [28]	US	Hg ³	$1\text{--}3 \cdot 10^{-3}$	50	5–15 ^(p)	4
ORNL SNS (SPSNS) [29]	E	Hg	0.695	60	1 ^(p)	1.4
SINQ ⁴ (CW-SNS) [30], [31], [32]	E	Pb (ZA) ^{cl} , Pb ^{bl}	CW	—	0.59 ^(p)	0.8
SPES (CW-RIBS) [33]	UC	UC _x	CW	—	0.04 ^(p)	$8 \cdot 10^{-3}$
SPIRAL-I [34], [35], [36] / SPIRAL-II [37], [38] (CW-RIBS)	E / UC	C	CW	—	0.060– 0.095 [†] / 0.04 ^(d) , e.g.: 0.0145 ^(Ar) †	$0.6\text{--}3.2 \cdot 10^{-3}$ / $6 \cdot 10^{-3}$ – 0.2 ^(d) , e.g.: 0.1305 ^(Ar)

¹SiC, TiC, ZrC, Ta, Nb, Nb₅Si₃, Al₂O₃, TaC, UO₂, ...

²molten: Ge, Sn, La, Pb, Bi, La-Th, Au, TeO₂, KCl, LiCl, Sn/graphite, Pt/graphite, ...; solid: Ti, Nb, Ta, W, C, Al₄C₃, SiC, VC, LaC₂, ThC₂, UC₂, MgO, Al₂O₃, CaO, TiO₂, SrO, ZrO₂, BaO, La₂O₃, CeO₂, ThO₂, CaB₆, ...

³with alternatives: PbBi, low-Z-bed (Be), W-powder-jet, W.

⁴Target 7 since 2009.

2.1 Spallation Targets⁵

Neutrons are used as probes of the structure and dynamics of condensed matter at the atomic scale and neutron scattering is used in a number of fields (condensed matter physics, materials science, chemistry, polymer science, biology, engineering, geology, etc.) due to the characteristics of neutrons which complement other experimental means, e.g. X-rays and TEM. As neutrons are uncharged, they only interact weakly with matter and can penetrate deeper into the material under investigation. The wavelengths of neutrons are in the order of inter-atomic distances in condensed matter, and the magnetic moment of the neutron leads to varying cross-sections for different target materials.

Spallation is the process of a (heavy) nuclei breaking up following an impact of an energetic incident particle which also leads to the generation of unbound neutrons. The higher the incident particle energy, the higher the probability for the inelastic nuclear reaction triggering the spallation process. Heavy ions are less suitable as projectiles in the driver beam and even though deuterium has a slightly higher yield than protons, the cost of producing a deuterium beam is the single reason why protons are given the preference as projectiles, with typical proton energies in the order of GeV (see tab. 2.2 starting on p. 4). Spallation is an endothermic process – and therefore cannot be used for energy generation – with thresholds in the energy range of around 25 MeV⁶. This is a lower threshold than for fission (190 MeV) or photon-neutron production by $(e, \gamma n)$ reactions (2000 MeV) induced by an electron accelerator; but higher than for fusion (13 MeV). Other advantages over fissile materials for neutron generation are the larger choice of different materials as well as a smaller heat release per released neutron. Spallation targets are either used directly for their neutron yield or together with a moderator-reflector structure, which lowers the neutron energy towards the thermal or cold end of the spectrum.

There are three types of beam driven spallation sources differentiated by the proton time structure through which they are generated: continuous, long, and short pulse neutron sources. The continuous beam driven spallation sources are run with either an accelerator with no macro-time structure (e.g. cyclotron) or a CW-LINAC, and their design goal is therefore a high (and reliable) time average neutron flux. Continuous neutron sources can also provide pulsed beams to time-of-flight experiments by using choppers, thus reducing the total flux. The limiting parameter for neutron scattering experiments is high intensity. In the past, high intensity neutron beams were harvested from so-called high flux reactors, but their output was already in the saturation regime in the early 1970s. Pulsed neutron sources cater specifically to an increasing interest, with their design optimized such that the neutron scattering experiments make more efficient use of the neutron stream as well as their specific time-structure. The main driving idea behind pulsed beams is to deliver higher pulse-peak fluxes (about one to two orders of magnitude higher) than high-flux reactors and even have the time-averaged flux at pulsed neutron spallation sources approaching a comparable level.

The long pulse sources deliver neutrons in the order of one millisecond, and the pulse length of the LINAC that feeds the source is higher than the slowing down time of the neutrons in the surrounding moderator material. Their technical implementation is

⁵ based on [39], [40], [41] and [42].

⁶ Ranges from as low as 12 MeV (lower production rates) up to 120 MeV (considerable production rates).

usually closer to a continuous source. Fluxes at long pulsed sources can also be trimmed to provide shorter pulse lengths than the short pulsed neutron sources (in the order of microseconds), providing a flat (trapezoidal) time pulse structure (in comparison to the exponential decay structure of short pulsed neutron sources) – a method that is used for thermal/cold neutrons (100 *meV*). The short pulses of the driver beam are achieved by either a synchrotron or by collecting protons in a proton ring (so-called compressor ring) which is steered onto the spallation target in single pulses. The neutron pulse shape (both in beam cross section as well as in the time domain) can then be further modified according to the design of the target-moderator-reflector system.

Any high density heavy material serves as a good source for spallation neutrons. The higher the atomic number Z of the target nuclei, the higher the number of neutrons available as secondaries. Hence, heavier nuclei of dense materials are preferred. The yield Y of neutrons per incident proton onto a non-actinide target can be estimated by equ. 2.1 [42] (see also [40]):

$$Y = (E_{GeV} - 0.12) \cdot (A + 20) \cdot 0.1 \quad (2.1)$$

where E_{GeV} is the kinetic energy of the impinging proton in GeV and A the atomic mass number (atomic nucleon number). For uranium, the neutron production is further increased due to fission which creates additional radiological problems with target handling – apart from the metallurgical issues that occur with uranium. The neutron yield for actinide targets can be approximated by multiplication of approximately two in equ. 2.1. So when it comes to choice of target material, one has to weigh neutron yield with any other related design issues.

Higher neutron yield can be simply achieved by increasing the driver beam intensity. If none of the technical challenges existed, the ideal (pulsed) neutron source would be determined by the maximum available driver beam power density technically feasible from the accelerator side – together with an optimized moderator-reflector system. Therefore the wishes from the scientific community for neutron beams push the limits of mechanical design, but must also adapt to the boundaries of the current design possibilities.

The IFMIF project [43] is an example of another neutron target type which is a neutron source not based on spallation: this project concentrates on providing a high flux neutron spectrum close to that of a fusion reactor in order to test materials for use in these reactors. IFMIF has foreseen creating neutrons by stripping an accelerated deuterium beam of its protons by passing through a flowing lithium target.

2.2 RIB Targets⁷

The scientific community is interested in more and more intense RIBs with isotope species of shorter and shorter half lives. Direct targets as well as spallation targets serving as so-called neutron converters can be used for ISOL-type RIBs. Hundreds of unstable isotopes for roughly three quarters of all elements have been produced in RIB facilities. As it is done for the European RIB project EURISOL one can use both spallation neutrons to provoke fission in a secondary actinide target, as well as direct targets producing RIBs

⁷ based on [44] and [45].

through fragmentation and spallation reactions induced by a driver beam. The intensity of the RIB target I_{RIB} depends on different parameters as seen in equ. 2.2.

$$I_{RIB} = \sigma \cdot \Phi \cdot N \cdot \epsilon_{RT} \cdot \epsilon_S \cdot \epsilon_D \quad (2.2)$$

with σ as the formation cross-section for the nuclear reactions of interest, Φ as the beam intensity of the driver beam, N as the usable target thickness, ϵ_{RT} as the product release and transfer efficiency, ϵ_S as the ion source efficiency and ϵ_D as the transfer efficiency due to radioactive decay losses. If the temperature induced by the interaction of the driver beam in the direct target is too low, the production target must be heated to higher temperatures to increase the release of RIB particles. From a given power threshold, the new direct high power targets require active cooling to maintain target temperatures at acceptable levels.

2.3 Neutrino Facilities⁸

Incident particles at energies higher than about some hundreds of MeV not only create the already introduced spallation neutrons and protons, but also generate large portions of pions (π^+ , π^- , π^0). Therefore the choices for target materials in neutrino facilities which utilize the production of pions to generate neutrino beams are strongly based on those used for spallation and RIB neutron converters. On the other hand, one should keep in mind that high-Z materials also have higher absorption cross sections than low-Z materials.

Superbeam facilities and neutrino factories use neutrino beams that are generated when the pions from the target decay into muons, which in turn decay into neutrinos. As a consequence, the target system contains a focusing system and a sufficiently long decay tunnel. The focusing system can be comprised either of a very strong – therefore usually superconducting – magnet, or of a magnetic horn. Also, it has been thought of using the – in this case liquid mercury-jet – as focusing element by feeding high currents through the liquid metal itself. A different method to produce a neutrino beam is performed in beta beam facilities, where neutrinos are obtained from the decay of short-lived beta emitting nuclei generated in RIB targets (e.g. BeO target for ^6He , MgO target for ^{18}Ne). Therefore the choices for target materials in neutrino facilities which utilize the the production of pions to generate neutrino beams are strongly based on those used for spallation and RIB neutron converters.

The pulse structure in neutrino facilities needs to be such that the background in the distant experiment or detector can be sufficiently rejected against the signal. A duty factor for the proton driver beam for superbeam experiments lower than $5 \cdot 10^{-3}$ has to be provided. When muon storage rings are involved, the pion precursor beam has to be generated with proton bunches in the order of nanoseconds.

The neutrino flux is directly proportional to the beam power – as this is the case for the spallation and the RIB targets. The optimal driver beam energy for the highest pion production yield depends on the material.

For soft pion production, the optimum beam energy seems to be 5 and 10 GeV for graphite and mercury respectively, with mercury yields consistently higher for any given beam energy. The targets for beta beams have to guarantee a high yield of ideal beta

⁸ based on [42], [46], [47], [48], [45] and [49].

emitters. Therefore the material of choice should produce one of the four proposed (anti-)electron-neutrino sources (ν_e : ^{18}Ne , ^8B ; $\bar{\nu}_e$: ^6He , ^8Li). One possibility is a target made of MgO (but also NaF is considered [50]), or BeO respectively, positioned next to a spallation source (serving as a neutron converter) which generates ^{18}Ne , or ^6He respectively.

2.4 Design Issues Common to all High Power Targets⁹

As for the technical implications, continuous sources – this is true for any high power targets – are less challenging than pulsed sources. The physics requirements – see tab. 2.3 – have to be balanced with designs feasible with current technology. The main concerns for pulsed sources are firstly to minimize target fatigue by keeping the temperature at a constant level, as well as reducing the thermal stresses to the limits given for irradiated material; and secondly, to avoid shock or cavitation phenomena as well as uncontrolled phase-changes. As a first order approximation of the reached stress or pressure differences these equations are used for liquid and solid targets (as stated in e.g. [47]):

$$\Delta P_{liquid}(r) = \frac{\alpha_V \Delta T(r)}{\kappa} \quad (2.3)$$

$$\Delta \sigma_{solid}(r) = \frac{E \alpha_L \Delta T(r)}{1 - 2\nu} \quad (2.4)$$

where ΔP_{liquid} is the pressure difference caused by the impinging beam into the liquid target at the position r , $\Delta \sigma_{solid}$ the stress difference for the case of a solid target, α_V and α_L the volumetric and linear expansion coefficients, ΔT the temperature increase, κ the compressibility of the liquid material, E the modulus of elasticity and ν the Poisson ratio of the solid material – while it is assumed that α_V or α_L , κ or E and ν and the specific heat at constant volume (in order to calculate ΔT) are constants.

For any target either liquid or solid, the material of choice should ideally combine good thermal properties at temperature of operation with the lowest possible activation – this is also true for neighboring elements e.g. a focusing horn or magnet – and afterheat production in case of emergency intervention, as well as for shutdown cooling and also in order to reduce radioactive waste.

Table 2.3: Physics driven requirements (+ ... required, ++ ... emphasized) for high power targets (based on [39], [40], [42], [44], [45], [48], [51], [52] and [46]).

<i>Requirement</i>	Spallation sources	Direct RIBS	Neutrino factory, Superbeam
Pulsed beam	+ (μs and ms range)		+ (ns range)
Operation temperature		++	
Target compactness	+	++	+

There are different advantages, technical challenges and restrictions for liquid and solid targets, and each of these effects are more relevant the higher the beam power. While spallation sources can in principle reduce the load on the target by allowing the irradiation

⁹ based on [39], [40], [42], [45], [48], [51], [52], [46], [41], [47], [49], .

of a larger volume, the targets for neutrino beam and RIB facilities need to be kept compact in order to allow the efficient release of the secondaries that need to be captured and utilized farther. For neutrino beam targets, the additional effects of magnetic fields must be taken into account, especially systems where the capture solenoid field interacts with the target levitation and drive fields (eddy currents) [53].

2.4.1 Liquid Targets

For liquid targets, minimization of pressure bumps and cavitation are important issues with pulsed beams. Highly concentrated energy deposition leads to local evaporation of the liquid which creates temporary voids, called cavitation bubbles. When these bubbles collapse, micro-jets are created. If these cavitation bubbles form near the container wall and the jets hit the wall, the material is locally hardened and becomes brittle. After a certain time material leaves the wall – a process referred to as cavitation erosion. The first problem is the thinning of the wall as the walls are usually already thin so that heat removal is facilitated and thermal stresses are kept small. The second problem is that cracks are also initiated through the cavitation jets, which reduces the life-time significantly. As one countermeasure, surface hardening of the container walls has been introduced but only results in a small gain in time until cavitation erosion occurs. Lastly, the injection of gas counteracts cavitation erosion – either as a curtain next to the wall¹⁰ or as micro-bubbles inside the whole liquid metal volume. The additionally introduced bubbles have two functions: firstly, rapidly attenuate the pressure waves and secondly, the bubbles allow the pressure to expand into their volume and therefore reduce the buildup of pressure in the liquid. Another issue that needs to be considered is that the proton beam bunch-to-bunch spacing has to be chosen so that the generated pressure waves cannot result in constructive interference which would otherwise lead to higher stresses on the target container.

For a given target material, the liquid phase offers the most compact arrangement and hence the highest yield, and also does not exhibit any radiation damage compared to the solid phase. The structural material for the liquid metal container can be chosen according to its mechanical resilience under high irradiation. However, the design of the beam window needs to be optimized as it is now the one life-time limiting target component, and its cooling becomes a crucial point in the design of liquid metal target stations. With this in mind, window-less target stations have been taken into consideration, rendering all issues related to the beam window irrelevant and therefore also allowing the reduction of the beam size of the driver beam, leading to a higher beam power density, generating more intense neutron beams. Omitting any cooling circuit reduces the needed material in the interaction region as well. In addition, any afterheat removal system can be installed farther away from the interaction point. One needs to keep in mind that the choices available for liquid metal targets are rather limited (Hg, Pb, Pb-Bi alloy). Alloys based on lead are chosen both for when operating temperatures can be high (the material needs to be liquefied) and when the absorption of thermal neutrons should be low. Keeping the alloy liquid so to avoid freezing out (expansion of the solidified alloy) complicates the design of the heat removal system. A candidate alloy is an eutectic mixture of 45% lead and 55%

¹⁰ This solution has to be implemented such that the thermal connectivity with the wall is still established.

bismuth (with a melting temperature $T_m = 125 \text{ }^{\circ}\text{C}$). Mercury is chosen when the operating temperatures of the target should be low and for SPSNSs, as its thermal neutron absorption cross-sections lead to sharper time-distributions of cold neutrons out of the moderators. For these reasons, the latest MW spallation targets commissioned in 2006 and 2008 were mercury targets. Another advantage to mercury lies in the fact that no radioactive ^{210}Po is produced, while this occurs for both lead and bismuth. Mercury can – in principal – also be distilled in order to remove many of the radioactive nuclides generated by the impinging proton driver beam. It should be noted however that the process of solidification of mercury for final disposal is not demonstrated, so it remains unacceptable for many waste disposal repositories. In Europe is in unclear whether mercury would be licensable [10]. Further properties of the liquid metal target are relevant when it comes to the final choice of the material: wetting behavior towards the solid materials of the containers and solubility of species other than the target material, which are both relevant for heat transfer properties between liquid metal target and container walls (cooling efficiency of beam window if one exists, dimensioning of heat removal system), radiochemistry and final disposal, and destructive interaction such as liquid metal corrosion and liquid metal embrittlement.

2.4.2 Solid Targets

For solid targets, the material should offer a small thermal expansion in order to avoid thermal stresses (fatigue stresses in particular); good elastic properties and sufficient ductility even after irradiation; resistance to corrosion (especially under irradiation); in addition to good mechanical properties for machining (manufacturability and joinability to other materials through welding, hipping, etc.) [41]. If a target coolant which also reduces the average density of the target is required, radiolysis and generation of radioactive residual nuclei (such as ^{7}Be in water) has to be suppressed or minimized in the coolant. Fins which increase thermal radiation can be installed on the outer surface of the target container. Another idea to reduce the heat load on the target is to install it as a rotating target. One solution considered for a neutrino factory is a magnetically levitating and driven ring shaped material of high atomic number [53]. Tungsten and tantalum both have high densities and high melting points. Tungsten has a higher neutron yield than tantalum but it is brittle, it can only be shaped by powder metallurgy and is severely corroded by water – serving as a coolant – under irradiation. The last point is also true for tungsten alloys. The ductile tungsten-rhenium alloys embrittle rapidly under irradiation. While tantalum stays ductile under irradiation and is easy to machine, it has a higher neutron absorption cross section and therefore stays more activated and retains more afterheat. After using tantalum targets, Ta-cladded tungsten targets have been designed, such as the ISIS target [18]. A tantalum container with densely packed solid spheres of tungsten with diameters in the millimeter range cooled with either water or helium was proposed in order to minimize the thermal shock effect inside a stationary target, as each granule sees a smaller fraction of the beam power and is heated almost uniformly. In the form of closely packed spheres, the mechanical coupling is smaller than for bulk material [46]. Helium-cooled solid tungsten spheres are seen as attractive solutions for LPSNS since the lack of corrosion means cladding is no longer required.

2.4.3 Target Selection Criteria

The final decision on which target design to pursue is not made solely by balancing physics requirements and technical challenges. The issues which need to be taken into account include safety, environmental impact, personnel and machine protection, cost, physics performance as well as availability/maintainability.

Chapter 3

Load and Transient Effects of Beams Interacting with Matter

3.1 Interaction of Particles with Matter¹

3.1.1 Interaction of Charged Particles with Matter

Particles interact with matter through various different mechanisms such as excitation and ionization of target electrons, projectile excitation and ionization, electron capture, recoil loss (nuclear stopping) and electromagnetic radiation in addition to nuclear and chemical reactions.

The equation describing the energy loss for charged particles (excluding electrons² and positrons³) by ionization and excitation is called the Bethe-block equation after their inventors and gives the average energy loss dE per unit length dx :⁴

$$-\frac{dE}{dx} = 4\pi N_A r_e^2 m_e c^2 z^2 \frac{Z}{A} \frac{1}{\beta^2} \left(\ln \frac{2m_e c^2 \gamma^2 \beta^2}{I} - \beta^2 - \frac{\delta}{2} \right) \quad (3.1)$$

with N_A as the Avogadro number⁵, r_e as the classical electron radius⁶, m_e as the electron mass, c as the velocity of light, z as the charge of the incoming particle in units of elementary charge, Z and A as atomic number and atomic weight of the target material, $\beta = \frac{v}{c}$ (with

¹ based on [54], [55], chapt. 27., [56] and [57]. [56] summarizes the theoretical approaches specific to ions interacting with matter. [55], chapt. 27 provides a more condensed overview of charged particles interacting with matter, while [57] summarizes the "basic aspects of particle interactions and showers in the energy range from a few tens of MeV up to several hundreds GeV", mainly concentrating on the implementation as it is done in FLUKA but also providing references for more details.

² Electrons experience a slightly different treatment: firstly, electrons in MeV range already experience losses through bremsstrahlung. Secondly, projectile and target are both electrons and therefore have the same mass. Thirdly, one cannot distinguish between primary and secondary electrons.

³ For positrons one needs to take into account the annihilation process upon slowing down.

⁴ The energy loss $-\frac{dE}{dx}$ can be displayed in $\frac{\text{MeV}}{\text{g/cm}^2}$. Instead of dx in cm , one writes equ. (3.1) with the energy loss per area density: With the density ρ in g/cm^3 and the length ds in cm one redefines dx with $dx = \rho \cdot ds$ (unit: g/cm^2).

⁵ $N_A = 6.022 \cdot 10^{23}$

⁶ $r_e = \frac{1}{4\pi\epsilon_0} \cdot \frac{e^2}{m_e c^2}$, where ϵ_0 is the permittivity of free space.

v as the velocity of the incoming particle), γ the Lorentz factor⁷, I as the mean excitation energy⁸, and δ as a parameter describing the screening effect of the charge density of the atomic electrons towards the incoming (relativistic) particle⁹.

Strictly speaking, equ. (3.1) on p. 13 is an approximation for the average energy loss by excitation and ionization which is valid up until some hundreds of GeV and for velocities larger than those in the order of atomic electrons.¹⁰ For even larger energies, radiation losses have to be taken into account. The mechanism for energy loss is different for ions since they collect electrons from the target when slowing down, reducing their effective charge. One also needs to know that equ. (3.1) is only valid for thick absorbers as the energy loss distribution for thin absorbers is asymmetric, with the average energy loss $\langle \Delta E \rangle \ll E_{max}$, where E_{max} is the maximum energy loss.¹¹

The energy transferred to ionization electrons can be large enough to ionize further electrons. These knock-on electrons are also called δ rays and their energy spectrum for $I \ll E_{kin} \leq E_{kin}^{max}$, (where I is the mean excitation energy, E_{kin}^{max} is the maximum transferable energy) is

$$-\frac{dN}{dE_{kin}} = \zeta \cdot \frac{F}{E_{kin}^2} \quad (3.2)$$

with N as the number of knock-on electrons, E_{kin} as the kinetic energy, ζ as a proportionality factor, and F a spin-dependent factor¹².

The direction of the impinging particle onto crystals matters significantly. Energy loss along channeling directions has to be treated in the framework of coherent scattering along regular rows or planes of absorber atoms.

Another important process which impinging particles experience in an absorber is multiple scattering. Multiple scattering occurs through the Coulomb potentials of nuclei and electrons within the target.¹³ The amount of scattering processes is usually large with little deviation from the original direction. Molière's theory describes the distribution of scattering angles due to multiple scattering:

$$\Theta_{rms}^{proj.} = \sqrt{\langle \Theta^2 \rangle} = \frac{13.6 MeV}{\beta c p} z \sqrt{\frac{x}{X_0}} \left[1 + 0.038 \ln \frac{x}{X_0} \right] \quad (3.3)$$

with Θ as the scattering angle, βc as the particle velocity, p as the particle momentum, and $\frac{x}{X_0}$ as the thickness of the scattering medium measured in units of radiation length X_0

⁷ $\gamma = \frac{1}{\sqrt{1-\beta^2}}$

⁸ The mean excitation energy can be approximated by $I = 16Z^{0.9}$ eV for $Z > 1$, but also depends on the state of aggregation of the target material (gaseous, liquid or solid) and the molecular state (mono-atomic, diatomic, ...).

⁹ This parameter is more important for dense materials and relativistic velocities while it is negligible for gases under normal pressure with low energy impinging particles.

¹⁰ The energy loss of the slow particles following the inequality $\alpha z \gg \beta \geq 10^{-3}$ – with α as the fine-structure constant ($\alpha = \frac{e^2}{4\pi\epsilon_0\hbar c}$) – is proportional to β . For the energy range $\beta\gamma \lesssim 0.1$ strategies for energy loss calculations are discussed in [55], sec. 27.2.3.

¹¹ The energy distribution for thin absorbers is parameterized with a Landau distribution, e.g. [54], equ. (1.19) ff.

¹² F is usually close to unity and starts to play an important role at the end of the spectrum where the energy approaches E_{kin}^{max} , the maximum transferable energy

¹³ Strong interactions also contribute to the multiple scattering for hadronic particles – [55], sec. 27.3.

$(X_0 = \frac{A}{4\alpha N_A Z^2 r_e^2 \ln(183Z^{-1/3})})$. The interaction of the lighter particles with the electrons of the traversed medium is small in comparison to the much stronger effect (heavy) ions exert for the same material. In addition, the more electrons an ion carries, the more pronounced the interaction with the target's free and bound electrons.

On the other hand, incoming particles can also be decelerated within the Coulomb fields of the constituents of the target body and can emit part of their kinetic energy via bremsstrahlung photons. For high energy particles, the energy loss due to bremsstrahlung is:

$$-\frac{dE}{dx} \approx 4\alpha N_A \frac{Z}{A} z^2 \left(\frac{1}{4\pi\epsilon} \frac{e^2}{mc^2} \right)^2 E \ln \frac{183}{Z^{1/3}} \quad (3.4)$$

with Z and A as atomic number and atomic weight of the absorber medium and z , m , E as the charge number, the mass and the energy of the impinging particle respectively.

At high particle energies, virtual photons in the Coulomb field of the target nuclei can facilitate the generation of electron-positrons pairs. In inelastic nuclear interaction, charged incoming particles can exchange virtual photons with the nuclei of the target material, which causes them to lose energy. This mechanism – also called photonuclear interaction – is more prevalent for leptons than for hadrons, for which direct nuclear interactions are more important.

The total energy is the sum of all appearing processes during the interaction of the incoming charged particle with the absorber material:¹⁴

$$-\frac{dE}{dx} \bigg|_{total} = -\frac{dE}{dx} \bigg|_{ionization} - \frac{dE}{dx} \bigg|_{bremsstrahlung} - \frac{dE}{dx} \bigg|_{pairproduction} - \frac{dE}{dx} \bigg|_{photonuclear} \quad (3.5)$$

$$= a(Z, A, E) + b(Z, A, E) \cdot E \quad (3.6)$$

with $a(Z, A, E)$ as the term representing equ. (3.1) from p. 13 and $b(Z, A, E)$ as the sum over energy losses due to bremsstrahlung, direct electron-positron pair production and photonuclear interactions.

If a charged particle travels into an absorber with a velocity $v \geq \frac{c}{n}$ (c as the velocity of light and n as the refractive index of the absorber), the atoms along the track of the particles are polarized. Because of the speed of the incoming particle, there is not enough time for the symmetrical arrangement of the created dipoles which would lead to a zero dipole field outside of the interaction region. Instead, a field with a non-zero dipole moment is created, which causes the emission of electromagnetic waves called Cherenkov radiation. However, the contribution to the total energy loss is in the order of a few percent of the energy loss by ionization and excitation.¹⁵ Another negligible contribution to the energy loss of a traveling charged particle can occur when the particle crosses from one medium into another medium with differing dielectric properties.¹⁶

¹⁴ In fact, it is easier to describe an average energy loss for ionization and excitation. Phenomena such as bremsstrahlung, electron-positron pair production and photonuclear interactions show larger fluctuations around their average values.

¹⁵ This percentage is even very low in the part of the Bethe-Block equation (equ. (3.1)) on p. 13 where the energy loss is minimal – in this energy range the charged particles are called minimum-ionizing particles. [54] quotes 1% as the energy loss by Cherenkov radiation in comparison to energy loss due to ionization and excitation for gases with $Z \geq 7$ and 5% for helium and hydrogen gases.

¹⁶ This mechanism is exploited in transition-radiation detectors (TRDs).

Inelastic reactions become more dominant when an impinging hadron has an energy of higher than some tens of MeV. As already mentioned in section 2.1 p. 6 ff, secondary particles such as neutrons and protons can be generated. These secondaries can – if the energy of the incident particle is high enough – themselves generate more and more hadronic particles. This chain reaction is called "hadronic cascade". Pion production starts around 290 MeV – see also section 2.1. Mesons such as π^0 decay into positrons, electrons and γ rays, creating similar chain reactions of those secondaries – called "electromagnetic cascade".

The dominant energy loss mechanism for electrons and positrons with a few hundreds of MeV is bremsstrahlung while for photons with the energy of some MeV pair production dominates (see section 3.1.2). Therefore electrons and positrons will be generated until the energy of the charged particles becomes so low that they lose their energy through ionization.

The behavior of the electromagnetic cascade is completely described by quantum electrodynamics (QED) while for the hadronic cascade, no complete frame-work has been developed yet and different models must be employed to gain insight into the physics processes (see [57]).

The higher the energy of the incident particle, the more pronounced the pion production, also causing the rise in generation of heavier particles (kaons, hyperons). At the onset of pion production, intranuclear cascade models are used to describe the interaction of hadrons with nuclei, while below that threshold nucleon interaction can be simply described through elastic scattering. Pions themselves reacting inelastically with nucleons have an even lower threshold (170 MeV) than nucleon-nucleon interactions. The nonelastic interactions can be described well, up until 2 – 3 GeV, with simple two-body models. However, when one has to consider the formation and decay of not one but several resonance channels – some of which are not even known – this approach becomes unfeasible. At this stage, the momentum or energy distribution of the constituents of the involved hadrons must be described and one has to define a useful model for the formation of hadrons out of quarks and gluons (known as "hadronization"). According to [57] there are different models and one of them is the so-called "Dual Parton Model" (DPM).

On the low energy end of the hadronic interaction, nuclei are left in excited states. This excitation energy can either be consumed, by evaporating nucleons or light fragments (α , d, 3H , 3He) with energies of a few MeV, or by deforming the nuclei, leading to fission. Light nuclei ($A \leq 16$) break up into two or more fragments. The left-over fragments remain in an excited state which can de-excite through the emission of γ rays.¹⁷

3.1.2 Interaction of Photons with Matter

Photons are either completely absorbed by matter (photoelectric effect, pair production) or scattered with a large angle (Compton effect). These are the statistical mechanisms leading to exponential attenuation equation:

$$I = I_0 \exp -\mu x \tag{3.7}$$

¹⁷ The emission of γ rays also happens during all other processes though with a much lower probability.

with I_0 as the intensity before entering the medium, x as the area density (usually in g/cm^2),¹⁸ and μ as the mass attenuation coefficient (in $(g/cm^2)^{-1}$):

$$\mu = \frac{N_A}{Z} \sum_i \sigma_i \quad (3.8)$$

with σ_i as the atomic cross section for a process i , N_A as the Avogadro number, and A the atomic weight of the material.

The above mentioned interaction mechanisms are dominant in different energy ranges E_γ :

- Low energies ($100\text{keV} \geq E_\gamma \geq$ ionization energy I): photoelectric effect¹⁹
- Middle energies ($E_\gamma \approx 1\text{ MeV}$): Compton effect
- High energies ($E_\gamma \gg 1\text{ MeV}$): pair production

The photoelectric effect describes the complete absorption of an incoming photon: the photon ionizes an absorber atom and gives all its energy to the atomic electron. The absorption efficiency is higher for the inner electron shells due to the fact that the proximity of the nucleus acting as the third collision particle, picking up the recoil momentum. The gap in an inner shell can be replaced with an electron of a higher shell. The difference in energy can be balanced out, either by the emission of an X ray photon (characteristic wavelength of a material) or by emitting another atomic electron, if the binding energy can be overcome. If the photons are scattered on the quasi-free electrons of the absorber, this is called the Compton effect (as mentioned above). The energy lost by the incoming photon is transferred to the hit electron as kinetic energy. Complete absorption of the incoming photon due to the production of an electron-positron pair only occurs for photons of energies higher than the rest masses of the electron and positron and the recoil energy transferred to the nucleus (which is usually negligible²⁰). For $m_{nucleus} \gg m_e$ this term is small in comparison to the rest masses of electron and positron ($2m_e c^2$)). In addition to these three mechanisms, there are also other processes photons are subjected to, such as photonuclear interactions and photon-photon scattering, but their cross sections are much lower than for the three main energy loss processes.

At even higher energies, incident photons²¹ cause a chain-reaction of electrons and photons of lower energy – the electromagnetic cascade mentioned in section 3.1.1 (p. 13 ff). The deeper into the material the greater the energy deposited through photons.

¹⁸ If x was in units of lengths (e.g. cm) the mass attenuation coefficient μ would be divided by the density ρ of the material.

¹⁹ Rayleigh scattering (= coherent, elastic scattering) occurs in the same energy domain as the photoelectric effect, but plays a secondary role for energy loss. ([55], sec. 27.4.4.)

²⁰ The recoil energy is $2\frac{m_e^2}{m_{nucleus}}c^2$

²¹ The same is also true for electrons – as described in section 3.1.1.

3.2 Transient Effect on Beam Intercepting Devices

"One can easily waste a lot of time going through abstracts, and still not be sure that some important article has not been missed."

(S. G. Brush in [58], p. 16)

Both static and dynamic mechanics are large fields by themselves. The section on static material response serves as recapitulation of the terminology in use as well as an introduction to dynamic reactions. It is impossible to account for all observed phenomena or available theoretical material, but one can familiarize oneself with the different concepts in an abbreviated manner.

3.2.1 Static and Quasi-static Behavior of Materials²²

3.2.1.1 Definitions and Terminology

Static or quasi-static load tests are performed on test materials under tension, compression, and/or shear to obtain test-curves which are characteristic for each material. In a tension test in particular, the (mostly cylindrical) specimen is subjected to a slowly increasing tensile uniaxial load along its symmetry axis. The test curves are displayed as stress-strain curves and mainly generated at room temperature. In simple terms, stress is caused by externally applied load, while strain describes the resulting deformation.

In continuum mechanics, both stress and strain can be expressed as tensors²³ describing the stress and deformation state for each point: in order to describe the stress state, one assumes a certain generic volume within the body under consideration. Stress is defined as force ($\Delta \vec{F}$) divided by the small part of this volume's surface on which it is acting (ΔS). One obtains the stress state for a given direction of the surface in form of a stress vector (\vec{T}) by calculating the limit ($\Delta S \rightarrow 0$) of the ratio $\Delta \vec{F}/\Delta S$:

$$\vec{T}_n = \frac{d\vec{F}}{dS} \quad (3.9)$$

where n denotes the surface normal vector and \vec{F} is a function of the area and orientation of the surface. For the notation of the stress tensor in Cartesian coordinates, one depicts a small cubic volume²⁴ whose surfaces are parallel to the coordinate axes x , y and z . Combining the stress vectors of the surfaces – whose normal vectors point in the positive direction of the coordinate axes – (\vec{T}_k , $k = x, y, z$) results in the stress tensor \tilde{T} :

$$\tilde{T} = \begin{pmatrix} \vec{T}_x^\dagger \\ \vec{T}_y^\dagger \\ \vec{T}_z^\dagger \end{pmatrix} = \begin{pmatrix} \tau_{xx} & \tau_{xy} & \tau_{xz} \\ \tau_{yx} & \tau_{yy} & \tau_{yz} \\ \tau_{zx} & \tau_{zy} & \tau_{zz} \end{pmatrix} \quad (3.10)$$

²² The herein mentioned definitions, terminology, and material can be found in introductions or specialized editions on material science and engineering (e.g. [59]), solid mechanics (e.g. [60]), or fracture mechanics (e.g. [61], [62], [63]).

²³ see e.g. chapt. 3 and 4 of [60] or chapt. 1.1 and 1.2 of [63].

²⁴ For the notation of the stress tensor in general coordinates, see [60] chapt. 3.12 ff.

where $\vec{T}_k^\dagger = (\tau_{kx}, \tau_{ky}, \tau_{kz})$, $k = x, y, z$. The tensor elements τ_{kk} ($k = x, y, z$) are the normal stresses, sometimes also denoted as σ_k , while the remaining components τ_{km} ($k \neq m$) are the shearing stresses. For a body in an equilibrium state²⁵ the stress tensor is symmetric ($\tau_{km} = \tau_{mk}$, $k \neq m$), reducing the number of nine tensor elements to six. By calculating the invariant principal stresses one can again reduce the number of tensor components down to three.²⁶ However, here one-dimensional (therefore scalar) expressions are used for simplicity.

There exist two definitions each for both stress and strain; firstly, the engineering stress and engineering strain and secondly, the true stress and true strain. The engineering stress σ_{eng} for the case of tensile load is defined as

$$\sigma_{eng} = \frac{F}{A_0} \quad (3.11)$$

where F is the applied tensile force which acts perpendicular to the initial specimen cross section A_0 . The equivalent shear stress τ is defined as $\tau = \frac{F}{A_0}$ where – for a cubed specimen – F is the load imposed parallel to the upper and lower faces with both faces of an area of A_0 . With l_0 being the initial length of the specimen and l_f its final length, the corresponding engineering strain ϵ_{eng} can be calculated from

$$\epsilon_{eng} = \frac{l_f - l_0}{l_0} = \frac{\Delta l}{l_0} \quad (3.12)$$

However, if one takes into account that the cross section of the specimen can change upon (plastic) deformation²⁷, one arrives at the definitions for the true stress σ_{true} and true strain ϵ_{true} :

$$\sigma_{true} = \frac{F}{A_i} \quad (3.13)$$

$$\epsilon_{true} = \ln \frac{l_f}{l_0} \quad (3.14)$$

with A_i as the instantaneous cross section of the specimen, l_f and l_0 as the final and initial specimen length. Up until a possible necking²⁸ the engineering variables can be related to the true variables as follows:

$$\sigma_{true} = \sigma_{eng} \cdot (1 + \epsilon_{eng}) \quad (3.15)$$

$$\epsilon_{true} = \ln (1 + \epsilon_{eng}) \quad (3.16)$$

3.2.1.2 Elastic Deformation

A material behaves elastically when the change of shape under load is reversible. Metals – among other materials – exhibit a strain proportional to the applied stress. In the notation for one-dimensional and tensile or compressive considerations (equ. (3.17) on p. 20) this

²⁵ For a short discussion of non-equilibrium states see [60] chapt. 3.4, p. 76 ff.

²⁶ See e.g. [60] chapt. 3.7, p. 82 ff.

²⁷ assuming a constant volume of the specimen.

²⁸ preceding the failure of ductile metals – see sect. 3.2.1.3 starting on p. 20.

constant of proportionality E is called the modulus of elasticity or Young's modulus (see slope marked with 'E' in fig. 3.1 on p. 21).

$$\sigma = E \cdot \epsilon \quad (3.17)$$

The shear stress τ and shear strain γ are equally proportional and linked through the shear modulus G : $\tau = G \cdot \gamma$.²⁹ When the applied stress is plotted against the resulting elastic deformation, known as the stress-strain curve, one obtains a straight line (see fig. 3.1 on p. 21). The slopes for different materials can be compared with each other, where a material with a larger gradient is stiffer than a material with a shallower one, resulting in a bigger elastic deformation of the latter (in fig. 3.1 the brittle material is stiffer than the ductile one). The modulus of elasticity (slowly) decreases with the rise in temperature as the material's stiffness depends on the resistance of interatomic bonds to separation.

3.2.1.3 Plastic Deformation

As soon as a material loses the ability to revert to its previous shape, plastic (= irreversible) deformation occurs. Then, the strain is no longer proportional to the applied stress, which is called yielding. From a microscopic point of view, plasticity is caused by the breaking and reforming bonds of adjacent atoms. In the stress-strain curve, one can observe a parabolic curvature after the onset of plastic deformation. The point of onset of plastic deformation is called the elastic limit, proportional limit³⁰ P or yield point. However, for most metals the change from elastic to plastic is gradual. Therefore an alternative definition of the onset is given: a straight line parallel to the slope of the elastic part of the stress-strain curve starting from a specified strain offset (usually 0.002 or 0.2% strain) intersects with the stress-strain curve. The value for the stress at the intersection point of these two curves is the (0.2% offset) yield strength σ_Y (see fig. 3.1 on p. 21).

Depending on whether a material is ductile or brittle, the stress-strain curve will exhibit a different behavior. For a ductile metal in the plastic regime, the tensile stress needed to further deform the specimen will reach a maximum (see M in fig. 3.1), the (ultimate) tensile strength σ_{TS} .³¹ Until this point, the applied stress is acting on the whole cross section of the specimen. From then onwards, a constriction of the specimen starts to develop.³² In the stress-strain curve this necking manifests as a decrease in applied stress (= engineering stress). However if one compares the applied stress with the increasingly shrinking cross section of the target, the (true) stress increases (see schematic true ductile

²⁹ However in the three-dimensional case, where stress and strain are represented by tensors themselves – see sect. 3.2.1.1 (p. 18 ff), the fourth rank elasticity tensor (also called elastic modulus tensor) is needed to describe their relation (see for example [61] chapt. 1.2.1.1, equ. (1-12), [60], chapt. 6.1, equ. (1) or [63], chapt. 1.3.1.1, equ. (1.35a)).

³⁰ To be more precise, the elastic limit is the value for the applied stress below which deformation caused by the applied load result in completely reversible deformations. The proportional limit is the stress level below which stress and strain are proportional. For the majority of metals these two values are equal. One should be aware that metals exist which show non-linear stress-strain curves, but are nevertheless fully elastic.

³¹ The following concentrates on specimens under tensile load. For metals, the compression part of the stress-strain curve is roughly symmetric to the tensile part, meaning the values for the compressive yield strength and the tensile yield strength are about equal.

³² For compression, there is no necking, but barreling occurs.

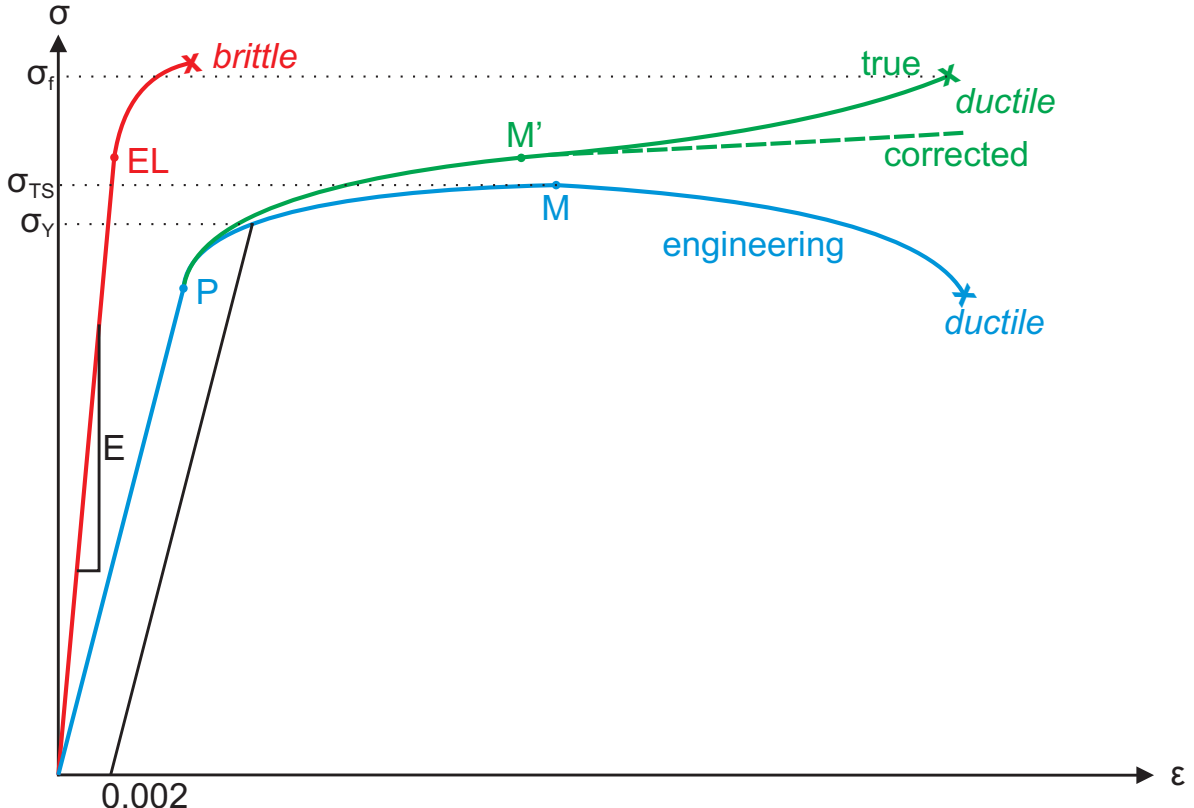


Figure 3.1: Schematic stress-strain curves for ductile and brittle materials.

The elastic region for the brittle curve is marked with the elastic limit EL after which plastic deformation occurs. The slope of the stress-strain curve in the elastic regions is equal to the elastic modulus E (here marked only for the brittle material). The transition from elastic to plastic behavior for ductile materials is gradual. The proportional limit P is reached before the ductile material shows a fully plastic response. Due to the difficulties of setting a specific value for this transition, the yield strength σ_Y is defined by the following convention: the stress value at the intersection of the engineering stress-strain curve with a parallel line to the proportional elastic part of its stress-strain curve. Generally, the parallel line is offset by 0.2% along the strain axis. M marks the maximum load reached during a tensile test, indicating the necking of the material. The hereby reached stress is called tensile strength σ_{TS} . While the engineering stress decreases, the true stress increases. In the true stress-strain curve, M' marks the onset of necking. The corrected true stress-strain curve accounts for the non-uniaxial stress state in the necked region.

Ductile fracture occurs at strains far greater than that of brittle fracture. The true fracture stress is noted as σ_f for ductile failure. By definition, brittle materials fracture after little plastic deformation, without necking.

curve in fig. 3.1). As a matter of fact, this true stress also needs to be corrected (see schematic corrected curve in fig. 3.1)³³ for the appearance of non-axial stress components in the necked cross section. For brittle materials necking does not occur, therefore true and engineering stress are virtually the same.

Ductility of a material is a function of material temperature, stress state of the specimen and strain rate: e.g. a rise in temperature not only decreases the stiffness of the material but also reduces the yield and tensile strength.

3.2.1.4 Fracture

Ductility measures the degree of plastic deformation until fracture. Brittle materials are those that only show very little or no plastic deformation at fracture while ductile materials show the behavior as described in sect. 3.2.1.3 (p. 20 ff) until the necked region fractures. The load at fracture divided by the final cross section of the specimen³⁴ is then termed true fracture stress σ_f (see fig. 3.1 on p. 21).

Brittle materials under compression will manifest in a shattering type of fracture. However, it is difficult to describe a final fracture state of ductile materials under uniaxial compressive load. The specimen will simply barrel³⁵, so that one needs to define a value of distortion that is considered as the complete failure of the material.

The theoretical strength of materials (assuming a defect free single crystal) is a factor two to three higher than the strength obtained on real polycrystalline materials which is a direct result of both the inhomogeneity of materials and their imperfections. Fracture of a material is the result of crack formation (due to stress concentrations at these imperfections – therefore known as stress raisers) in the material and crack propagation is a reaction to an imposed stress.

In ductile materials under tension, the crack propagation advances slowly due to extensive plastic deformation around the initial cracks: after initial necking, small cavities form at second-phase particles, grain boundaries, and other obstacles to the motion of dislocations or even from cracking of brittle inclusions. These microvoids slowly coalesce into the initial crack. Then the crack increases growing rapidly and finally parts the specimen through shear deformation in the outer necked region at an angle of 45°. This leads to the so-called cup-and-cone fracture pattern. However, very soft ductile metals like pure gold or lead neck down to an almost point-like fracture.

For brittle fractures under tension the crack propagation is very fast and perpendicular to the applied stress. The initial characteristic length of the cracks is determined by the microstructure of the material, e.g. grain size. Beyond a critical load (also termed the critical stress for crack propagation σ_c ³⁶) the initial cracks start to expand and the quantity of cracks increases. Fracture does not occur yet, only the macroscopic stiffness of the material decreases nonlinearly while the undamaged areas still behave elastically. The material becomes unstable as soon as a single dominating crack occurs that starts growing. For compressive stresses the initial cracks start to form parallel to the maximum

³³ see e.g. [61], equ. (1-24) & fig. 1.8.

³⁴ which should be including corrections for any non-uniaxial stress components during necking.

³⁵ or "squash".

³⁶ For brittle materials the critical stress for crack propagation is $\sigma_c = \sqrt{\frac{2E\gamma_S}{\pi a}}$, where E is Young's modulus, γ_S the specific surface energy of the crack surface and a half of the internal crack length.

stress component – unlike the material under tension.. For most of the brittle fractures of crystalline materials cleavage occurs: the crack propagates through grains of material by breaking atomic bonds and is therefore called "transgranular" or "transcrystalline". Intergranular fracture occurs along grain boundaries of some brittle alloys due to weakening processes.

Both a rise in temperature and hydrostatic pressure can alter the fracture pattern of the specimen. In fact, materials can behave in either a brittle or ductile way under certain conditions (for general trends see tab. 3.1 on p. 24). Since fracture is strongly linked to imperfections within the material, one should keep in mind that in a real material there are, on one hand, imperfections introduced through the manufacturing process (e.g. porosity, shrinkage cavities, quench cracks, grinding and stamping marks, seams and weld-related cracks), and on the other, those due to inclusions of microconstituents (e.g. inclusions, brittle second-phase particles, grain boundary films). Also (as already pointed out in tab. 3.1) the shape of the specimen alters its fracture response. In addition to the mechanism mentioned above, environment assisted cracking can lead to a reduced resistance of the material under load, e.g. stress corrosion cracking, hydrogen embrittlement and liquid-metal embrittlement, where not just temperature or pressure, but humidity also come into play.

In order to describe the failure of a material in relation to the stress state, mathematically simple fracture and failure hypotheses – called strength hypotheses – were developed. For these simple classical models, failure does not depend on the deformation history and it is also assumed that the material can be described as a continuum without macroscopic defects. With these assumptions the material can be described by either its momentary stress or strain state (σ_{ij} or ϵ_{ij} in the tensor notation). Such stress states can simply be noted down as

$$F(\sigma_{ij}) = 0 \text{ or } G(\epsilon_{ij}) = 0 \quad (3.18)$$

Then the failure conditions as stated in equ. (3.18) can be interpreted as a failure surface in the six-dimensional stress or strain space or three-dimensional principal stress or strain space.³⁷ The two simplest and most intuitive models are the principal stress hypothesis and the principal strain hypothesis.³⁸

- The former defines failure as the principal stresses exceeding either of the two characteristic strengths, namely the tensile strength σ_t or the compressive strength σ_p . The failure surface for this hypothesis is represented by a cube in the three-dimensional principal stress space. Due to its simplicity it is applicable for brittle materials assuming that the separation into two parts is dominated by the largest principal stress while the influence of the other two principal stresses is ignored.
- Within the principal strain hypothesis it is assumed that failure occurs when the principal strain rises above a critical value ϵ_t . For elastic behavior up to failure the failure surface in the principal stress space is a three-sided pyramid centered around

³⁷ See sect. 3.2.1.1 on p. 18: Six different components for the stress tensor and three for the case of principal directions.

³⁸ see e.g. [63] chapt. 2.2 - also for a short summary of other classical failure hypotheses, such as the strain energy hypothesis, the Coulomb-Mohr hypothesis or the Drucker-Prager hypothesis.

	<i>Ductile behavior</i>	<i>Brittle behavior</i>	
<i>Temperature</i> (*)	Higher	Lower	
<i>Rate of loading</i>	Lower	Higher	
<i>Geometry</i> (**)	No stress concentration	Stress concentration	
<i>Size</i> (***)	Smaller or thinner	Larger or thicker	
<i>Type of loading</i> (****)	Torsion	Tension or compression	
<i>(Hydrostatic) Pressure</i> (*****)	Higher	Lower	
<i>Strength of metal</i>	Lower	Higher	
<i>Electron bond</i>	Metallic	Ionic	Covalent
<i>Crystal structure</i>	Close-packed crystals	Low-symmetry crystals	
<i>Degree of order</i>	Random solid solution	Short-range order	Long-range order

Table 3.1: General trends of ductile-brittle relationship (compiled from [62] p. 25 ff. and [61] tab. 10.1)

(*) The ductile-to-brittle transition temperature is observed for low-strength steels that have a body centered cubic crystal structure. No transition temperature is found for ductile low-strength face centered cubic and most hexagonal close packed metals, or for brittle high-strength metals.

(**) The lack of notches or stress concentrations allows shear deformation to occur so that high stresses can spread within the specimen, which is needed for ductile behavior of the material.

(***) The larger (or thicker) the specimen, the more likely the occurrence of discontinuities (serving as stress concentrations) and triaxial tensile stresses, which both serve as a basis for brittle fracture.

(****) A more pronounced effect for metals with high strength levels.

(*****) Brittle materials fracture in a ductile manner when exposed to high hydrodynamic pressures.

the so-called hydrostatic axis with the apex at $\sigma_1 = \sigma_2 = \sigma_3 = \sigma_t / (1 - 2\nu)$ where σ_t is the critical tensile stress corresponding to the maximum principal strain ϵ_t and ν is Poisson's ratio relating to Young's modulus E and shear modulus G : $\nu = \frac{E}{2G} - 1$. However, with this model the failure under uniaxial compressions (at $\sigma_p = \sigma_t/\nu$) is not in agreement with the behavior of most materials.

From fracture mechanics, a relation between the crack length a^{39} and the critical stress for crack propagation σ_c can be established through the the crack-tip field, describing stresses and strains controlling the processes around the crack tip.⁴⁰ The parameter describing the ability of the material to resist fracture when flaws are pre-existing is called fracture toughness K_c . For the case of brittle fracture K_c can be stated as

$$K_c = Y\sigma_c\sqrt{\pi a} \quad (3.19)$$

where Y is a dimensionless parameter or function depending on crack and specimen sizes and geometries.⁴¹ The fracture toughness is usually obtained from specimens with pre-existing cracks through monitoring the crack displacement under load – usually for plane strain conditions (no strain component perpendicular to crack faces) – and can be corrected for different specimen or crack geometries.⁴²

The fracture toughness for ductile materials is higher than for brittle ones and in addition is reduced by a decrease in temperature or an increase in strain rate. An inverse relationship exists between fracture toughness of a material and its strength: generally speaking, if the material is strengthened by metallurgical strengthening procedures⁴³ this is usually at the cost of a reduced resistance to fracture. In order to enhance both properties at the same time, there are different metallurgical procedures available:⁴⁴ firstly, one can obtain a greater material toughness by impeding crack propagation through mechanical means. Cracks can be deflected at grain boundaries, flow lines or inclusions. Preferred directions of crack development can be introduced through production processes which deform originally equiaxed grains of a polycrystalline material, such as rolling, drawing, or even forging. Secondly, unwanted tramp elements which serve as crack nucleation sites can be reduced by complex melting techniques. Thirdly, on the other hand, one can add desired elements in order to improve toughness. Lastly, a reduction of grain size within a material increases the probability of the crack being stopped at the grain boundary or at least being slowed down due to the energy needed for re-initiation of the crack.

3.2.2 Dynamic Behavior of Materials⁴⁵

If the rate of the application of an external force is low, the movement can be seen as a sequence of consecutive equilibrium events. However, one should be aware of the fact that

³⁹ a is defined as either half the length of an interior crack or the whole length for an edge crack.

⁴⁰ see e.g. [63] chapt. 4 ff for an introduction to Fracture Mechanics.

⁴¹ see [63] tab. 4.1 for examples of different flaw distributions and varying specimen geometries.

⁴² For more information see the measurement standard [64].

⁴³ See [59] chapt. 7.8 ff and [61] chapt. 4 for an overview of strengthening mechanisms.

⁴⁴ [61] chapt. 10.1 ff for a comprehensive overview on the following processes.

⁴⁵ Equations and statements within sections 3.2.2.1 starting on p. 26, 3.2.2.2 starting on p. 29 and 3.2.2.3 starting on p. 30 are mainly based on [65]. Other references in these sections are explicitly referenced. For references of section 3.2.2.4 (p. 50 ff) see footnote 109 on p. 50.

the internal stresses are propagated within the body under load at a specific velocity. These wave equations are usually derived for a continuum body while a more correct description would involve the representation of atoms and their governing interatomic forces. A small discrete portion of this oscillating continuum – misleadingly denoted as a "particle" – moves with the particle velocity U_p . The wave itself propagates with the wave velocity U and does not have to follow the same direction as the "particle".

In fig. 3.2 on p. 27, one can see the interconnectedness between strain-rate, time scale, obtained stress levels and thermodynamic conditions for different methods of mechanical testing including quasi-static as well as highly dynamic phenomena. In principle, an additional energy or temperature dimension would add an even more global overview to this representation. It is obvious that any dynamic behavior of materials has to be understood in the domain it is observed, while a change from one domain to another can occur later in time or farther in distance from the dynamic location.

3.2.2.1 Elastic Waves

Elastic waves are waves whose amplitude is below the plastic limit of the material. According to the direction of movement and the boundary conditions, one distinguishes the following elastic wave types: ⁴⁶

1. longitudinal waves⁴⁷: for which $U_p \parallel U$ – for infinite and semi-infinite waves they are usually called "dilatational" waves
2. distortional waves⁴⁸: for which $U_p \perp U$; no resulting change of density (unlike longitudinal waves)
3. surface waves⁴⁹: for which the particle follows an elliptical trajectory while the movement of the particles is restricted to the surface (while the amplitude decreases exponentially away from the surface)
4. interfacial waves⁵⁰: where two semi-infinite media with different properties are in contact with each other
5. waves in layered media⁵¹: horizontal component of displacement > its vertical one (the opposite of surface waves)
6. bending waves⁵²

In order to derive the equations of propagation of elastic waves in a continuum, one looks at a small cubed volume of the body – as in sect. 3.2.1.1 (p. 18 ff). As the volume under consideration is not in a static equilibrium, the stresses of the opposite faces are not equal.⁵³

⁴⁶ The following classification can - to some extent - also apply for plastic waves.

⁴⁷ irrotational waves; in seismology: push waves, or primary waves, or P waves.

⁴⁸ shear waves, or transverse waves, or equivolumal waves; in seismology: secondary waves, shake waves, or SH and SV waves.

⁴⁹ called Rayleigh waves in solids.

⁵⁰ Stoneley waves.

⁵¹ Love waves – which play a very significant role in seismology due to their destructive nature.

⁵² flexural waves.

⁵³ For an illustrative step-by-step procedure on what follows see e.g. [65], chapter 2.4.

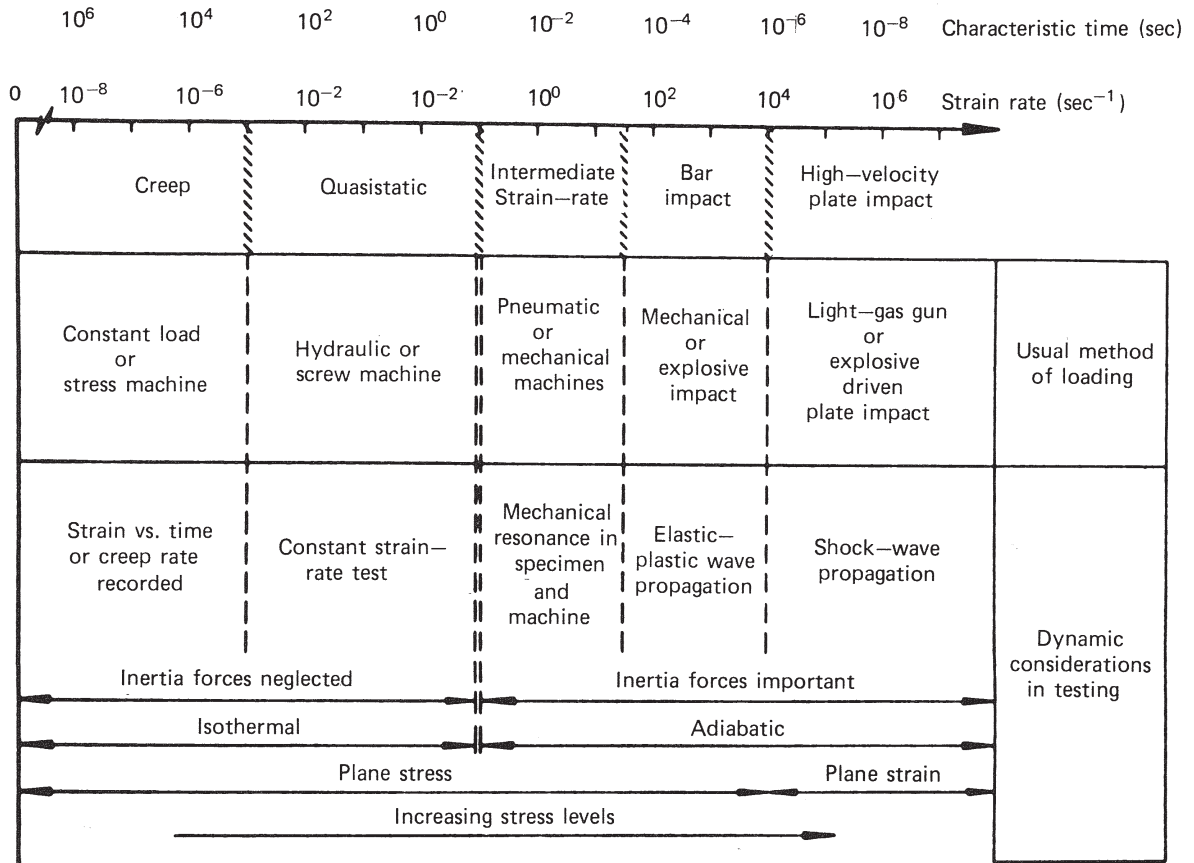


Figure 3.2: Ranges in dynamic mechanical testing:

The characteristic time scale is given as the time required to produce 1% strain at the corresponding strain rate. The creep behavior is usually investigated at high temperature for metals. Although the quasistatic stress-strain curve is often treated as an inherent property of a material, it is a valid description of the material only at the strain rate at which the test was conducted. Constant strain-rate tests can be performed with specialized testing apparatus to a certain strain rate limit. At the high rates and the associated very short time scale involved in shock waves, thermodynamic considerations become important. At these high rates, the nominal transition between isothermal and adiabatic conditions happens. The internal heat generated during the inelastic deformation process does not have time to dissipate, and therefore the mean temperature of the specimen is increased. Fig. 1 (p. 201) from [66], modified original figure caption of fig. 1 (p. 280) in [67] and with text mostly taken from section 8.1.1 of [67] and chapter 4 in [66]. Used with kind permission of Wiley & Sons.

By solving the equations of momentum conservation for the stresses on the faces of the cube – without considerations of body forces such as gravitation and moments – one obtains the following system of differential equations:

$$\frac{\partial \sigma_{ij}}{\partial x_j} = \rho \frac{\partial^2 u_i}{\partial t^2} \quad (3.20)$$

with $i, j = x, y, z$ and where the σ_{ij} are the surface stresses, $\frac{\partial}{\partial x_j}$ the partial derivatives along the coordinate axes, ρ the density of the cube, the u_i are the displacements in the direction of the i -axes and therefore $\frac{\partial^2 u_i}{\partial t^2}$ are the accelerations of the surfaces of the cube in the direction of the coordinate axes. An isotropic material is assumed for simplicity. The stresses σ_{ij} are replaced by expressions using the strains ϵ_{ij} (employing the Lamé constants⁵⁴ λ and μ). In turn the strains are substituted by their original definitions⁵⁵. After applying mathematical simplifications, one obtains the longitudinal wave equation for an unbound medium:

$$\frac{\partial^2 \Delta}{\partial t^2} = \frac{\lambda + 2\mu}{\rho} \nabla^2 \Delta \quad (3.21)$$

where Δ is the dilatation ($\Delta = \epsilon_{xx} + \epsilon_{yy} + \epsilon_{zz}$), the operator nabla squared ∇^2 is $\frac{\partial^2}{\partial x^2} + \frac{\partial^2}{\partial y^2} + \frac{\partial^2}{\partial z^2}$ and λ and μ are the Lamé constants. From the second-order partial differential equation (3.21) one obtains the bulk sound speed:

$$V_{long} \equiv C_l = \sqrt{\frac{\lambda + 2\mu}{\rho}} \quad (3.22)$$

In order to obtain the distortional wave velocity for unbound media, one re-writes the wave equations such that they include rigid body rotations⁵⁶ ω_{ij} , $i, j = x, y, z$ and obtains the shear velocity

$$V_s \equiv C_s = \sqrt{\frac{\mu}{\rho}} \quad (3.23)$$

Compressive waves – for which the particle and wave velocity have the same direction and sense – reaching a free surface are reflected as tensile waves – for which particle and wave velocity have opposite senses – and vice versa. If compressive (or tensile) waves are reflected from a rigid boundary (into which they cannot penetrate), they maintain their nature as compressive (or tensile) waves. For real applications such as the Hopkinson bar experiments, where a striker cylinder hits a specimen with a constant velocity – a cylindrical bar – such that longitudinal stress waves propagate through the bar, the wave velocity can be calculated under the assumption of uniaxial stress:

$$C_0 = \sqrt{\frac{E}{\rho}} \quad (3.24)$$

⁵⁴ with $\mu = E/[2(1 + \nu)]$, $\lambda = \nu E/[(1 + \nu)(1 - 2\nu)]$ where E is the elastic modulus and ν is Poisson's ratio – e.g. [63], tab. 1.1, page 16.

⁵⁵ $\epsilon_{kl} = \frac{1}{2} \left(\frac{\partial u_k}{\partial x_l} + \frac{\partial u_l}{\partial x_k} \right)$, $k, l = x, y, z$.

⁵⁶ see e.g. [65], chapter 2.5.

where E is the elastic modulus and ρ the material density. With this simplistic approach one would expect a rectangular wave traveling through the whole length of the specimen. In reality, however, effects of dispersion will be superimposed onto the ideal wave. The compression of the material will also cause radial waves interacting with the free surfaces of the cylinder.

Wave equation (3.21) on p. 28 is a second-order partial differential equation. For obtaining a general solution of this equation for traveling waves, one employs the method of characteristics.⁵⁷ In this approach, the wave equation is split into first-order partial differential equations which are then transformed into ordinary differential equations⁵⁸. As the intermediate solutions, one obtains $x = x_0 \pm Ct$, where x is spatial position in one dimension, C is the wave velocity, t is time and x_0 depends on the initial conditions (at $t = 0$). For each initial condition, there is a straight line in a $x - t$ -graph and therefore all the solutions for each signs are parallel. The general solution for the linear wave equation in one dimension of the displacement u is $u(x, t) = F(x - Ct) + G(x + Ct)$, with x as the position, t as time, F & G as some arbitrary functions and C as the wave velocity. This represents two waves – which keep their shape in time – traveling in opposite directions. Characteristics can also be obtained for equations where C depends on other factors such as stress or pressure. For these cases the characteristics are not parallel anymore: for dispersions they display a fan, while they intersect for shock waves.⁵⁹

3.2.2.2 Plastic Waves⁶⁰

Plastic waves occur when the amplitude of a transmitted wave is larger than the elastic limit of the material in which it is transported. In the simplest case – when the stress is strain-rate independent and one assumes uniaxial stress conditions – the wave splits into two, namely into the elastic and plastic part.⁶¹ the velocity of propagation for both elastic and plastic waves is proportional to the square root of the slope of the stress-strain curve ($\frac{d\sigma}{d\epsilon}$):⁶²

$$V_p = \sqrt{\frac{\frac{d\sigma}{d\epsilon}}{\rho_0}} \quad (3.25)$$

The shape of the wave can be retrieved by applying the boundary conditions respecting the law of momentum conservation. For uniaxial stress, the slope of the plastic region is lower than the elastic one (this can be seen demonstratively in fig. 3.1 on p. 21). Therefore, the plastic wave will propagate slower than the elastic wave, leading to the dispersion of the wave.⁶³

⁵⁷ For standing waves one prefers to use the the separation of variables.

⁵⁸ see [65], chapt. 2.12 for an insight in the methodology.

⁵⁹ Examples can be seen in [68], chapter 2.2.

⁶⁰ Another overview on plastic waves (apart from [65], chapter 3) is [69], chapter 3 – covering plastic wave theory (section 2), waves of one-dimensional stress (section 3), of one-dimensional strain (section 4) and combined stress (section 5).

⁶¹ This also applies for more complex stress dependencies.

⁶² One can derive equation (3.25) simply by applying Newton's second law and rewriting the equation. A generalized approach can be found in [70].

⁶³ For the case of uniaxial strain the slope of the stress-strain slope increases with plastic strain and the wave front steepens during its propagation and a shock front is created. Shock waves are described later

In real materials, its strength can depend on strain ϵ , strain rate $\dot{\epsilon}$, temperature T and even the strain rate history. The simplest dependencies are that of strain (see equ. (3.26)) only, as well as both strain and strain rate (see equ. (3.27)):

$$\sigma = \sigma_0 + k\epsilon^n \quad (3.26)$$

$$\sigma = \sigma_0 + k\epsilon^n \dot{\epsilon}^m \quad (3.27)$$

where σ_0 is the strain and strain rate independent stress and the exponents n and m govern strain and strain rate ($n < 1$ and m ranging from one to zero for metals). The calculation of plastic waves for more complex constitutive equations can be studied in [69]. More complicated constitutive models are discussed in chapter 3.2.2.3 on page 47.

3.2.2.3 Shock Waves⁶⁴

Ideal and Real Shock Waves

One talks about shock waves firstly, when the amplitude of the stress waves generated in a medium is far greater than the dynamic yield strength (also called dynamic flow strength), by several factors, and secondly, the created disturbance front can steepen up to a traveling discontinuity. A shock wave can only be generated for media whose shock wave velocity U_s increases with pressure P ($\frac{\partial^2 P}{\partial^2 U} > 0$ for $P \uparrow, U \uparrow$).⁶⁵ If shear stresses of the shocked material are negligible in comparison to the hydrostatic stress component⁶⁶, the shock problems can be treated as hydrodynamic problems. Apart from the negligence of shear stresses, several other criteria have to be met within the framework of the simplified shock theory:

- no lateral material flow is allowed
- the shock disturbance front is assumed to be a traveling discontinuity with zero thickness
- body forces and heat conduction in the disturbance front are not included in the formalism
- no elastic or plastic behavior
- no phase transformations

In order to describe the shock wave mathematically, a simple model of a piston pushing into a compressible medium is used: the piston is initially at rest and pushing into the material. Writing down the equations for conservation of mass, momentum, and energy of the uncompressed and compressed regions leads to the so-called Rankine-Hugoniot

in section 3.2.2.3 on p. 30 ff.

⁶⁴ A few introductory words on the history of shock wave physics can be found in [71], section I. Apart from [65] chapter 4 ff, also [72] serves as a quick introduction to shock physics while one finds an extensive review of the field in [73].

⁶⁵ The steepening of the shock waves happens due to the faster traveling of the higher amplitude components of the disturbance front in comparison to the lower amplitude ones.

⁶⁶ $\sigma_{hydrostatic} = -\frac{1}{3}(\sigma_1 + \sigma_2 + \sigma_3)$, where $\sigma_i, i = 1, 2, 3$ are the principal stresses .

equations:

$$\rho_0 U_s = \rho(U_s - U_p) \quad (3.28)$$

$$P - P_0 = \rho_0 U_s U_p \quad (3.29)$$

$$E - E_0 = \frac{1}{2}(P + P_0)(V_0 - V) \quad (3.30)$$

with ρ_0 and ρ as the densities of the uncompressed and compressed region (with their specific volumes $V_{(0)} = 1/\rho_{(0)}$), U_s as the velocity of the shock wave (while $\rho_0 U_s$ is called shock impedance), and U_p as the velocity of the particles after the front – being driven by the piston – has passed, P as the pressure after the shock wave and P_0 the pressure of the undisturbed medium as well as the internal energies of the undisturbed medium (E_0) and behind the shock front (E).

In order to be able to express any of the variables (P , U_p , U_s , E , V or ρ) as functions of each other, a fourth equation needs to be introduced, known as the shock equation of state (shock EOS). The shock EOS is an experimentally derived equation connecting shock velocities with particle velocities for non-porous materials that did not undergo any phase transformation:

$$U_s = C_0 + S_1 U_p + S_2 U_p^2 + \dots \quad (3.31)$$

where the parameters C_0 , S_1 and S_2 are experimentally determined⁶⁷; in fact, $S_2 = 0$ for most metals.

With the Rankine Hugoniot equations (equ. (3.28) until (3.31)) – also called "shock equations" – one can plot either P - U_p - or the more common P - V -graphs. The latter curve is called the Hugoniot – as seen schematically in fig. 3.3 on p. 32 – with the following underlying relation⁶⁸:

$$P - P_0|_{P_0=0} = P = \frac{C_0^2 (V_0 - V)}{[V_0 - S_1 (V_0 - V)]^2} \quad (3.32)$$

The Hugoniot is the summary of all possible states that can be reached by shocking a material (not including phase changes). Whenever a material is shocked to a certain state (P_1 , V_1) it does not follow the Hugoniot but reaches its new state discontinuously. Hence a number of shock experiments have to be conducted to establish a Hugoniot. The slope of the straight line – called Rayleigh line – is then proportional to the square of the shock wave velocity, or to be more precise, to the square the shock impedance $\rho_0 U_s$:

$$\frac{P - P_0}{V - V_0} = -\rho_0^2 U_s^2 \quad (3.33)$$

The ideal shock wave pressure profile consists of a discontinuous rise in pressure of the shock front, with a constant plateau as long as the duration of shock, with constant force (e.g. as is the case for a plate impact) followed by the pressure returning to zero during

⁶⁷ The experimental data is collected in large compendia, e.g. [74], [75] or [76] or even in databases available online [77] – the latter contains shock wave parameters as a subset.

⁶⁸ see [78], equ. (16).

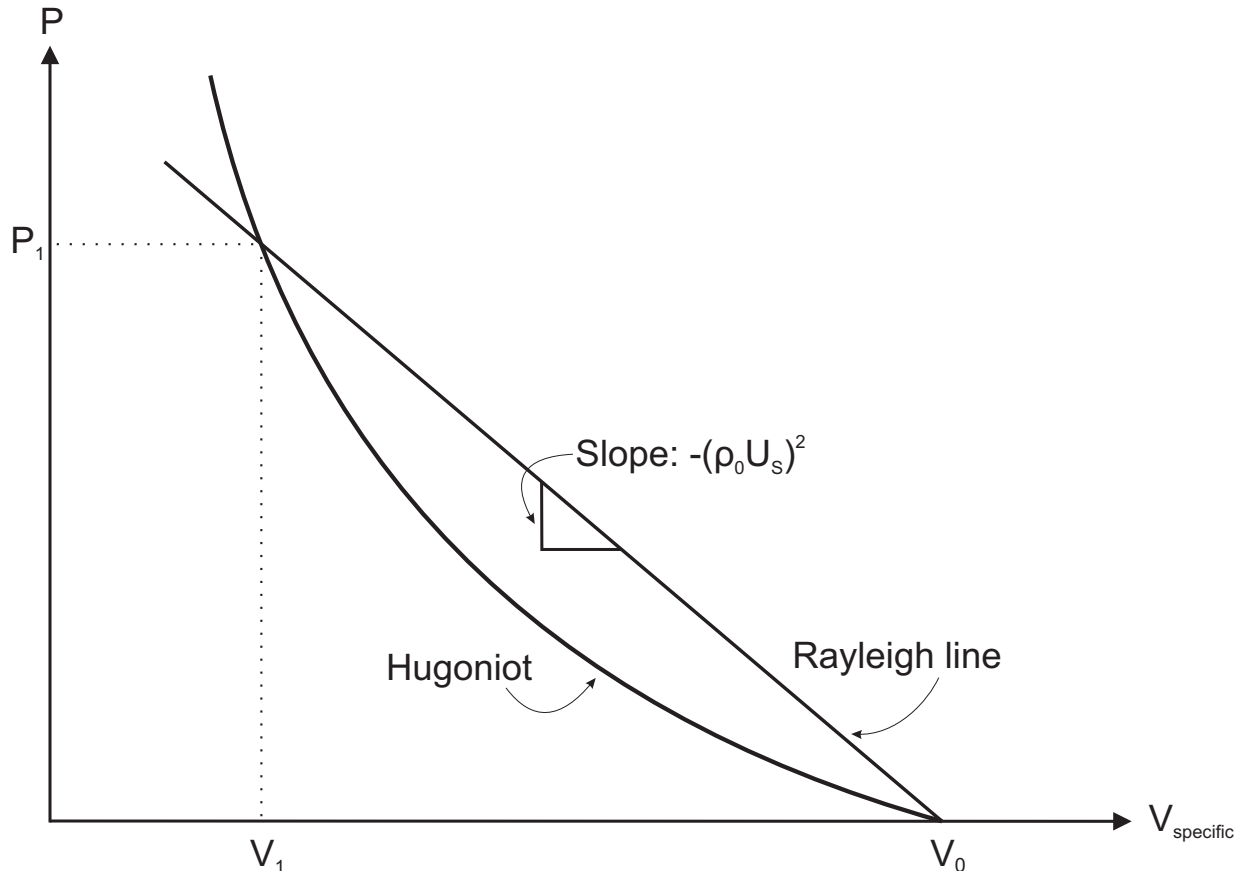


Figure 3.3: Schematic pressure-specific volume curve for shocked material – the Hugoniot (see e.g. [65], fig. 4.5). The Hugoniot is the sum of all possible states that can be reached by shocking a material. However, the transition from unshocked to shocked material is not along the Hugoniot, but a discontinuous jump from the undisturbed to the shocked state. The Rayleigh line is a straight connection between the unshocked and the shocked material – here drawn between the initial state (P_0, V_0 with the approximation of $P_0 = 0$) and the final state (P_1, V_1). Its slope is proportional to the square of the shock impedance $\rho_0 U_s$.

release (see fig. 3.4 (a) on p. 34).⁶⁹ In reality however, the pressure profile⁷⁰ displays a different behavior (see fig. 3.4 (b))⁷¹:

- Real materials do not behave entirely hydrodynamically, thus the pressure-volume curve is not the simple Hugoniot, but includes – at low pressures – a straight line until the so-called Hugoniot elastic limit (HEL)⁷² (see fig. 3.5 on p. 35). If the reached shock pressure is high enough that the velocity of the shock U_s is as big as or bigger than the velocity of elastic wave propagation, the plastic and elastic loading waves coincide, and no separation into a two-wave loading structure occurs. If however the shock velocity U_s is smaller than the elastic wave propagation, the elastic part of the loading wave will – after impact – separate from the plastic one, traveling ahead of the plastic part (see fig. 3.6 (c) on p. 36 for the development of a shock wave with time in a perfectly elastic-plastic material). In a real velocity-time profile taken from the rear of a target (see fig. 3.4 (b)), the pressure first rises steeply until the HEL is reached, and only afterwards rises to a plateau described by the Hugoniot state. The shape of the plastic part of the loading wave and its pressure rate is subject to the constitutive behavior of the material. In addition, the transition between elastic and plastic regions is also visible in the release part of the shock wave (see – again – fig. 3.6 (c)). First the material behaves elastically, then plastically.⁷³
- Real material can undergo phase transitions which leave a typical signal in the shock wave profile (see fig. 3.4 (b)).
- As the shock wave is reflected at the end of the specimen, the tensions created in the target material can lead to spalling of the target (see page 49).
- The shock rises steeper the higher the pressure (see fig. 3.7 on p. 37). It was found empirically that the maximum strain rate is proportional to σ_{peak}^4 [83] – which is valid above the yield stress σ_Y .⁷⁴

Despite the fact that the real shock wave profile exhibits differences to the ideal one, one can obtain a good insight in propagation and interaction of the present waves within the target (and the projectile - if present) when depicting the simplified situation in a distance-time plot (also called $x - t$ -plot). In a $x - t$ -plot, the movement of the

⁶⁹ This shock wave profile is expected for a sudden constant pulse of constant pressure over a given time period, e. g. a plane plate impact.

⁷⁰ See [79] as an introduction – and historical review until 1978 – to the devices and methods used to obtain pressure profiles in shock experiments. Another well documented review (from 1987) is [80]. For a more recent summary see chapter 3.1 in [68].

⁷¹ A short overview of the shock wave profiles of geomaterials, ceramics and metals can be found in [81].

⁷² The HEL is the stress at which materials deform plastically. HELs for metals are usually smaller than for ceramics (even though the actual meaning of a HEL for ceramics is debatable) and are therefore less important for metals.

⁷³ Chapters 2.1 – 2.5 in [82] are dedicated to an overview of the effects of the HEL and its effect on the free surface velocity profile, while chapter 2.8 covers observed unloading phenomena.

⁷⁴ According to [84], a possible upper limit might be the bulk modulus K (which for most solids is in the order of 100 GPa or higher), but so far no evidence of the break down of the fourth-power law was found within the limits of today's experimental strain rate measurement instrumentation. [84] also offers a brief history and summary of the fourth-power law.

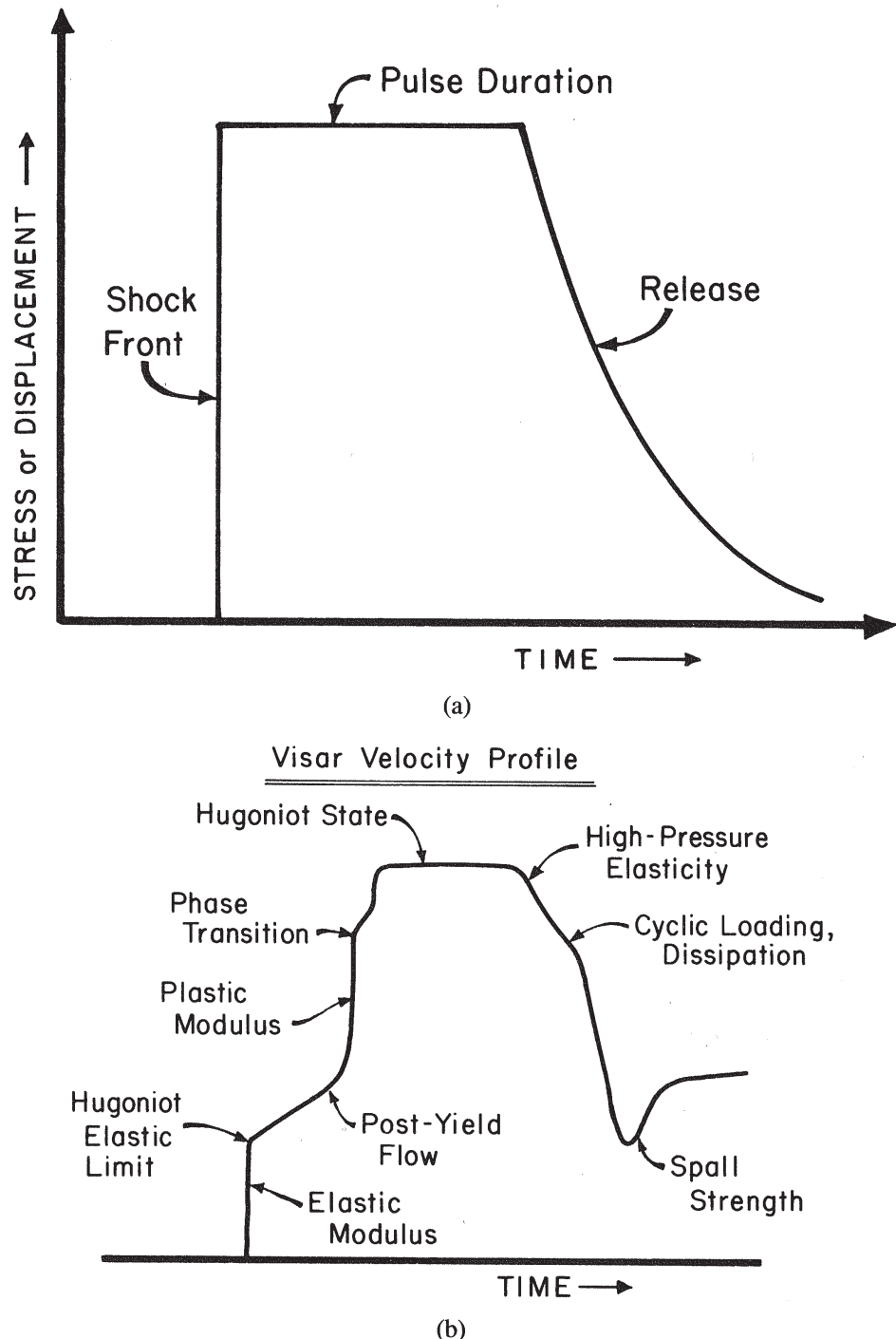


Figure 3.4: Shock wave profile of flyer plate impact: (a) idealized and (b) "generic" realistic shock wave profile.

Fig. 2 (p. 36) from [85] with modified figure caption of fig. 4.8 (p. 118) from [65]. Used with kind permission of Sandia National Laboratory and Wiley & Sons.

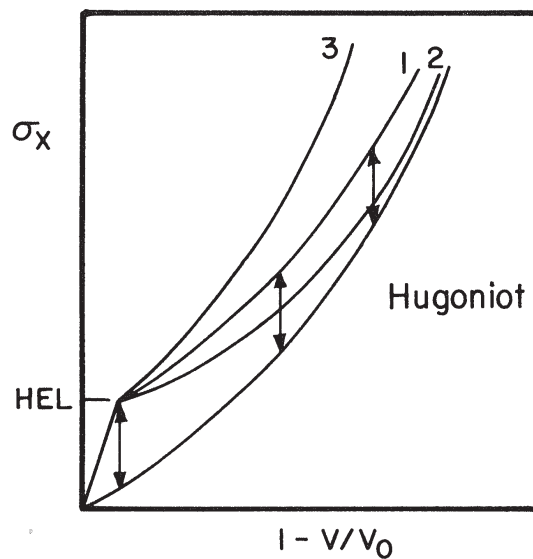


Figure 3.5: Schematic representation of Hugoniot modified by the Hugoniot elastic limit ("HEL"). Three different types of behavior of the deviatoric stress components are compared with the Hugoniot for the hydrostatic case ("Hugoniot"): (1) deviatoric component is independent of pressure (2) deviatoric component decreases with pressure – softening (3) deviatoric component increases with pressure – hardening.

Fig. 4.9 (p. 119) from [65] with modified original figure caption with text adapted from section 4.5 (p. 118) in [65]. Used with kind permission of Wiley & Sons.

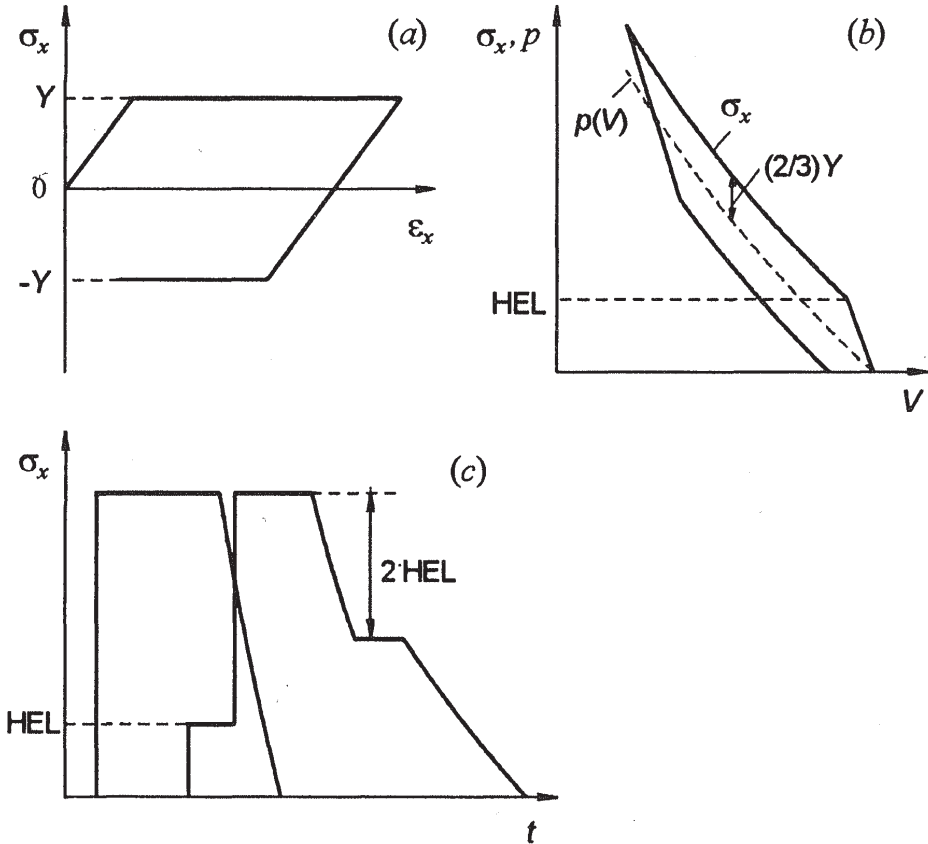


Figure 3.6: (a) Stress-strain diagram of a perfectly elastic-plastic body under uniaxial stress. Until the yield strength Y is reached, the material responds elastically to the load so that $\sigma_x = E\epsilon_x$. In the plastic region $\sigma_x = Y$.

(b) Stress-volume curve for passing shock and release wave (uniaxial strain state). Above the yield point, the state of an elastic-plastic material deviates from the corresponding hydrostatic curve $P(V, T)$ by as much as $\frac{2}{3}Y$.

(c) Evolution of an initially square compression pulse in an ideal elastic-plastic material: The elastic precursor propagates both in compression and release waves with the velocity of longitudinal elastic waves:

$$C_l = \sqrt{\frac{1}{\rho} \left(K + \frac{4}{3}G \right)}$$

(K ... bulk modulus $K = -\frac{dp}{dV}$, G ... shear modulus)

The velocity of wave propagation in the plastic part is the bulk sound velocity:

$$C_b = \sqrt{\frac{K}{\rho}}.$$

Fig. 2.1 (p. 32) from [82], modified original figure caption with text adapted from [82] section 2.1. (p. 31 ff). Used with kind permission of Springer Science+Business Media.

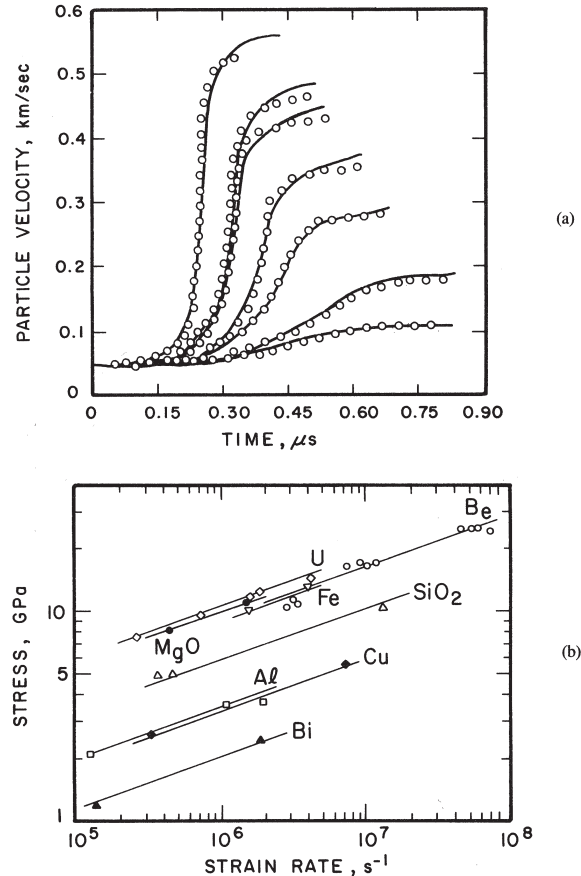


Figure 3.7: Steepening of the shock rise time with peak pressure:

(a) comparison of experimental (open dots) and calculated (solid lines) shock profiles for uranium at stress levels of 3.3, 5.7, 8.7, 11.2, 13.2, 14.4, and 16.7 GPa. The shock front is steeper for higher pressures. Strain rate dependent constitutive models were needed to obtain the same profiles as observed experimentally.

(b) relationship between stress and strain rate for a number of materials.

Fig. 3 and 1, p. 356 and 354 from [86], modified original figure caption of fig. 4.11 (p. 121) in [65] with text adapted from [65] section 4.5 (p. 119 ff). Used with kind permission of Springer Science+Business Media and Wiley & Sons.

contributing constituents (target and projectile) and the following occurring waves are depicted as straight lines with the inverse of their velocity as their slopes.

- Elastic precursor: the amplitude is equal to the elastic limit of the material (HEL) and exists in the loading part only if the shock velocity U_s is smaller than the elastic wave propagation velocity.
- Shock wave front.
- Release wave: this is the part of the wave where the pressure reduces to zero. The term "rarefaction" is used synonymously. A constant rate of release is assumed; however in reality this is not the case: The rate of release is not constant – it depends on materials for target/projectile and the traveled pulse distance – but decreases, hence the slope becomes less steep with time.

From the $x - t$ -plots, one can deduce the development of the shape of the shock wave over time, also taking into account the reflection of waves (see fig. 3.8 on p. 39). In general, the immediate shock wave profile generated through plate impact will show a plateau following the shock wave front, while that caused by explosives or laser pulses⁷⁵ is triangular. Taking the HEL into account and assuming that the shock wave passes through the material under uniaxial stress condition, the Hugoniot curve is displaced by $\frac{3}{4}\tau_{max}$, where τ_{max} is the maximum dynamic shear stress. The Rankine-Hugoniot curve then displays the hysteresis effect leading to a residual strain. In addition, the release wave attenuates faster than without the HEL.

The release wave following the peak pressure travels with a velocity $U_p + C$, where U_p is the particle velocity and C is the pressure dependent sound velocity. As a consequence, the release wave overtakes the shock front ($U_p + C > U_s$), leading to a decrease of the plateau time (if the shock profile was rectangular), followed by a decrease in the peak pressure. The release rate \dot{P}_R is itself very sensitive to the maximum peak pressure. Finally, the reduction in peak pressure leads to a slow-down of the shock front due to reduction of the shock velocity with decreasing pressure. In addition to the release effect, the peak pressure is reduced by traveling through the material and dissipating energy in the target e.g. as heat or through generation of defects. With this simplified assumption of a purely hydrodynamic response of the material, one can calculate the distance traveled at which the peak pressure of the shock wave is preserved.⁷⁶ For further decay of the peak pressure numerical tools are needed.⁷⁷ Comparison with experiments had shown that not only is the attenuation rate substantially larger than what expected from the hydrodynamic assumptions⁷⁸, but also the pressure inside the target is lower than predicted.⁷⁹

⁷⁵ For strong laser induced shocks, the shock wave is caused by the hot plasma generated at the target surface rather than by the momentum of the laser photon themselves. The heated material is quickly ablated from the surface. The pressure at the surface drops and therefore the shock wave can be approximated by a triangular shape.

⁷⁶ see [65], chapter 7.2., equ. (7.5): $S = \frac{U_s^2 t_p}{U_p + C - U_s}$, where S is the traveled distance at which the peak pressure is preserved, U_s is the shock velocity, t_p is the shock plateau time, U_p is the particle velocity, C is sound velocity at the particular peak pressure and $U_p + C$ is the velocity with which the release wave travels.

⁷⁷ see [65], chapter 7.2.

⁷⁸ For details on the dissipative mechanisms taking place, consult [65], chapter 13.

⁷⁹ for the first observations of these facts see the exemplary references in [65], chapter 7.2, p. 186 ff.

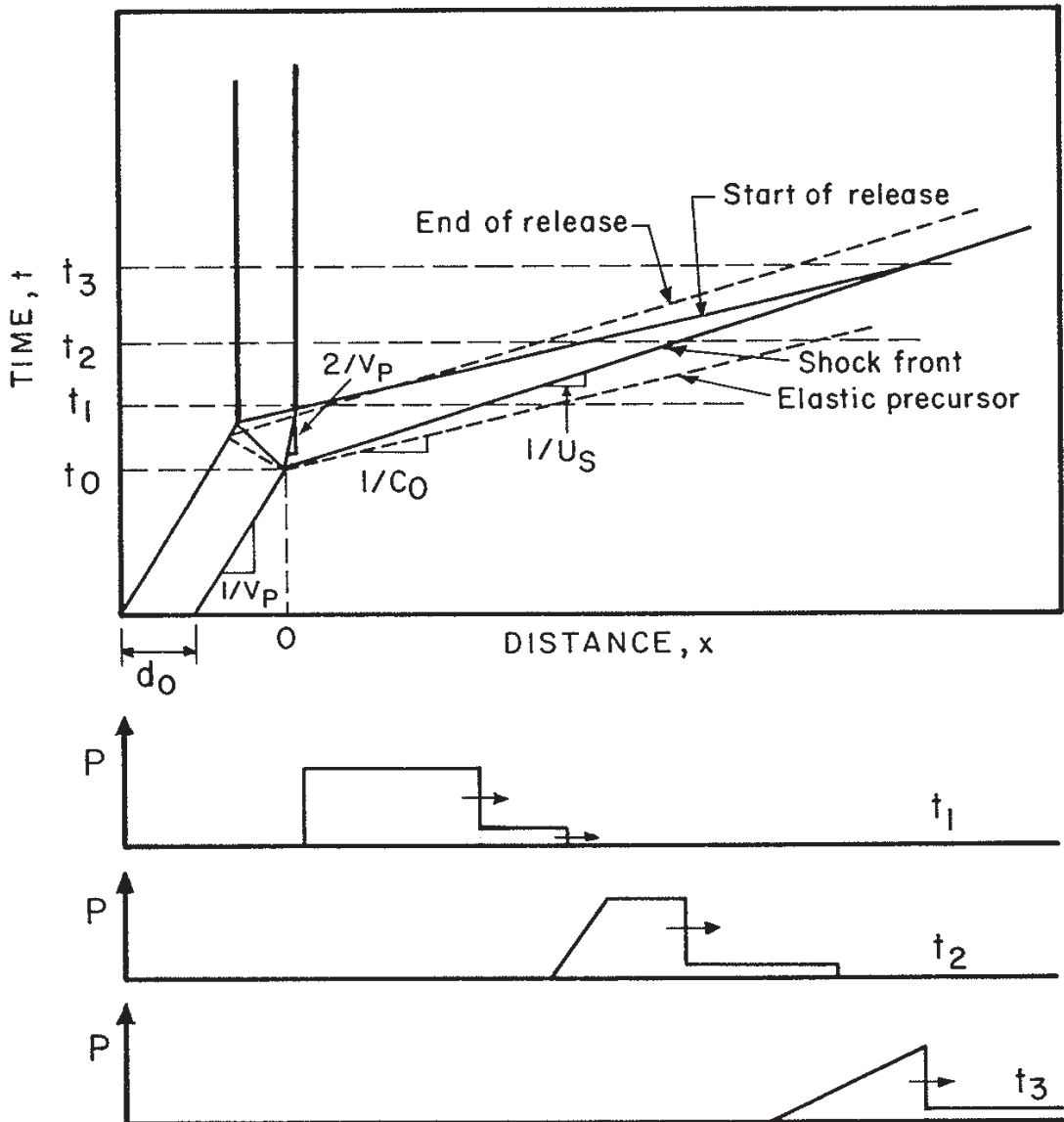


Figure 3.8: Flyer plate impacting on semi-infinite target of same material.

Top: the $x - t$ -plot allows visualization of the sequence of events: in this figure the elastic waves propagate with velocities higher than the shock waves. The flyer plate of thickness d_0 propagates at a velocity V_P prior to impact and hits the target at time t_0 from the left. Its velocity is reduced to $\frac{V_P}{2}$. Elastic waves with velocity C_0 and shock waves with velocity U_S are emitted into the target as well as into the projectile. The slopes of the elastic wave are smaller than those of the plastic waves. All waves are reflected at the back surface of the projectile and return into the target as release waves.

Bottom: pressure-distance profiles at three times t_1, t_2 and t_3 : it is the relative position of the various waves at different times that establishes the shape of the stress pulse. In this simplified figure, the shock part of the reflected wave is used to mark the start of the release wave while the elastic part is used to approximate the end of it. At t_2 , the plateau period is already reduced through the release wave. At the time t_3 the release part of the wave has overtaken the plateau. This leads to the reduction of peak pressure. Fig. 7.2 (p. 181) from [65], modified original figure caption with text adapted from section 7.1 (p. 179 f) of [65]. Used with kind permission of Wiley & Sons.

It is a strongly simplified assumption that a shock wave does not alter the material through which it travels. In reality, the shock wave triggers transformation due to the change in pressure and temperature – such as melting⁸⁰, vaporization⁸¹, sublimation, polymorphic phase transformation (transition between different types of crystal structures), chemical processes (synthesis, decomposition, polymerization) and generation of defects (point and line defects, twinning, etc.). With the assumption of the shock state as a sequence of equilibrium states, one obtains the Clausius-Clapeyron equation (equ. (3.34)) linking pressure P to the transformation temperature T (sometimes also called "saturation", "coexistence" or "equilibrium" temperature) between two phases (Entropy of phase change ΔS , change of specific volume ΔV , enthalpy of phase change ΔH):

$$\frac{dP}{dT} = \frac{\Delta S}{\Delta V} \text{ or } \frac{dP}{dT} = \frac{\Delta H}{T\Delta V} \quad (3.34)$$

In the Hugoniot curve, phase transformations are represented as cusps and the consequence of these phase transformations can be the splitting of the shock wave front in multiple shock fronts. In order to understand the influence of phase transformations on the propagation of shock waves and their stability, one has to first look at the isothermal processes. Isothermal processes are equilibrium processes whose compression curves can be used to build up Mie-Grüneisen EOS (see e.g. [87], chapt. 10 and later on page 55 ff in section 3.2.2.4). This Mie-Grüneisen EOS is an EOS that correlates a point defined in pressure-internal energy-space different from a state on the Hugoniot with the state on the Hugoniot at the same volume. Hence any reference curve – including an isothermal compression curve – can, in principle, be used to establish a Hugoniot. Phase changes such as melting and solidification are known as first order transitions as they are characterized by a volume change at constant temperature.⁸² For $\Delta V < 0$ an isotherm in pressure-volume space will look like fig. 3.9 on p. 41. In the case of decreasing volume the Clausius-Clapeyron equation (equ. (3.34)) can be evaluated with either $\Delta S < 0$ to $\frac{dP}{dT} > 0$ or $\Delta S > 0$ to $\frac{dP}{dT} < 0$. The first will lead to an increase in pressure with temperature during the phase change – which is the more common case – while the second will lead to a decrease of temperature.

If one displays the isotherms for different temperatures for the former, one obtains fig. 3.10 on p. 42. From these isotherms one can obtain the Hugoniot, since the Hugoniot lies close to the isentrope which in turn can be calculated via the Mie-Grüneisen EOS. The Hugoniot in fig. 3.10 reaches from the state O with $(P = 0, T_1)$ through the two phase region $Q'H$ to the state J and is represented in the usual pressure-volume plot in fig. 3.11 on p. 43, in which one can see the cusp in the Hugoniot marking the onset of phase transformation. The equivalent representation of fig. 3.10 and 3.11 for the second case ($\Delta V < 0, \Delta S > 0$ hence $\frac{dP}{dT} < 0$) are in fig. 3.12 on p. 44:

The shape of the Hugoniot has implications on the stability and shape of the shock wave (see the schematic drawing in fig. 3.13 on p. 45). For the effect on the first case see fig. 3.13: In the pictured two-wave structure (fig. 3.13 (a)) the first wave travels with the velocity U_{s1} while the particle velocity is U_{p1} . The second shock wave S_2 has a shock velocity U_{s2} within its own reference system, but travels through material which itself has

⁸⁰ See [82] chapter 6.6 for a quick review on melting during decompression.

⁸¹ See [82] chapter 6.7 for an overview of vaporization of shock-compressed polymers.

⁸² Via the definition of Gibbs free energy G one arrives at $(\frac{\partial G}{\partial P})_T = V$ and $(\frac{\partial G}{\partial T})_P = -S$ with P as pressure, T as temperature, V as volume and S as entropy.

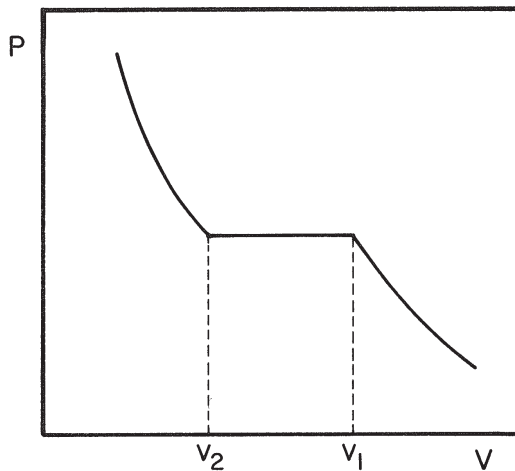


Figure 3.9: Pressure-volume isotherm for a first-order phase transformation with $\Delta V < 0$. In the interval $V_1 - V_2$ the two phases coexist.

Fig. 8.2 (p. 207) from [65], modified original figure caption with text adapted from section 8.3 (p. 206 ff). Used with kind permission of Wiley & Sons.

a particle velocity U_{p1} . Therefore the shock front S_2 travels with the velocity $U_{s2} - U_{p1}$ with respect to the material. If the second shock wave S_2 continuously falls behind the first wave S_1 , the two-wave structure will persist which is the condition for the two-wave stability: $(U_{s2} - U_{p1}) < (U_{s1} - U_{p1})$ or equally $U_{s2} < U_{s1}$. On the other hand if $U_{s2} > U_{s1}$, the second wave will coincide with the first wave. Re-writing the stability criterion with the help of the Rayleigh slopes (see equ. (3.33) on p. 31) and the mass conservation equations (equ. (3.28) on p. 31) for the two-wave profile as seen in fig. 3.13 (a) on p. 45 leads to the two-wave stability criteria for the Rayleigh slopes of the Hugoniot:

$$\frac{P_2 - P_1}{V_2 - V_1} > \frac{P_1 - P_0}{V_1 - V_0} \quad (3.35)$$

where the indices 1 and 2 are for the shock wave fronts S_1 and S_2 , respectively. In fig. 3.13 (b), one can see that the two-wave structure is stable for peak pressures below P_3 . At peak pressures P_3 and higher, single shock waves will form.⁸³

For most materials, the melting point increases with pressure, which is not the case for water/ice, plutonium and silicon, as their volume decreases upon melting. Nevertheless, shock-induced melting of Hugoniot beyond the mixed phases region can be achieved at high temperatures (see fig. 3.14 on p. 46). For low temperatures, no phase transformation will occur (see Hugoniot EI in fig. 3.14). For higher temperatures, the shock adiabat passes through the mixed phase – as can be seen in the exemplary Hugoniot $ABCD$ in fig. 3.14.

In addition to the cusps in the Hugoniot curve due to phase changes upon loading, release isentropes can also exhibit discontinuous changes in their slopes. Therefore shock waves can be generated in the release part of the wave.⁸⁴

⁸³ An in-depth understanding of phase transitions in shock waves can be acquired from [78].

⁸⁴ for more information see [88], vol. 2, chapt. XI, sect. 3, paragraph 20 "Rarefaction shock waves in medium undergoing phase transition".

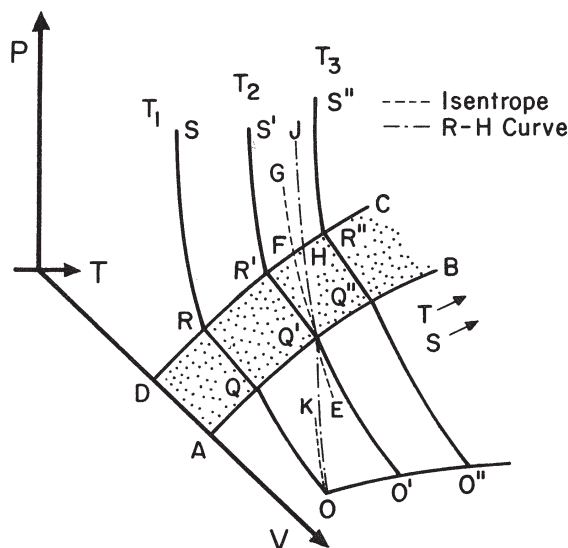


Figure 3.10: Pressure-volume-temperature surface for a first order phase transformation with $\Delta S < 0$, $\Delta V < 0$, $\frac{dP}{dT} > 0$. $OQRS$, $O'Q'R'S'$, and $O''Q''R''S''$ are isotherms at temperatures $T_1 < T_2 < T_3$, respectively. OK and $EQ'FG$ are isentropes, while $OQ'HJ$ is the Hugoniot for states starting from point O . $ABCD$ is the mixed phase region. The isentrope $EQ'FG$ experiences a break in slope at the boundaries of the mixed phase region. The Hugoniot $OQ'HJ$ touches the isentrope OK at O , intersects the phase boundary at Q' , therefore creating its discontinuity cusp by touching $EQ'F$ at Q' , going through the coexistence region and continuing through the second phase boundary at H into the second phase.

Fig. 9, p. 529 from [78], modified original figure caption from fig. 8.3 (p. 207) in [65] with text adapted from section 8.3 (p. 206 ff) of [65] and [78], section II.D, p. 529. Used with kind permission of American Physical Society and Wiley & Sons.

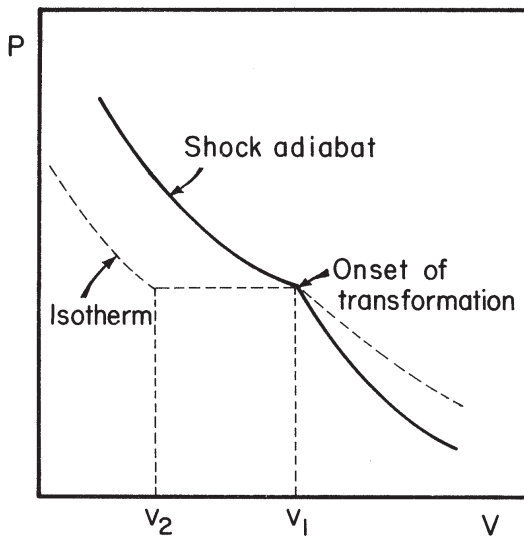


Figure 3.11: Pressure-volume cut of fig. 3.10 on p. 42 with Hugoniot ("shock adiabat"). Fig. 8.4 (p. 208) from [65], modified original figure caption. Used with kind permission of Wiley & Sons.

The passage of a shock wave – even without crossing phase boundaries – introduces a high density of defects in the material which – in general – leads to a hardening of the material.⁸⁵ The defect generation depends on pressure (e.g. generation of dislocation) and on pulse duration (e.g. occurrence of twinning). The generation of defects increases with pressure, then saturates and decreases at levels of pressure which induce a temperature rise high enough to lead to recrystallization. Hydrostatic stress and deviatoric stresses⁸⁶ play different roles in generation and movement of defects, e.g. the generation and motion of dislocations are dominated by deviatoric stresses while hydrostatic stress impacts on the stacking-fault energy.⁸⁷

Generation of Shock Waves

Shock waves can be generated in a multitude of ways in order for them to interact with material in whose equation of state one is interested. However the determination of the observables in the experiments can be rather challenging: the initial conditions of the driver – the shock generation procedure – can only be known with limited precision and the outcome of the experiment is afflicted with measurement errors. For experimental procedures certain assumptions on the interaction of the tested material with the "impactor" (and their equations of state) have to be made. Most of the drivers themselves are used both directly onto the target specimen as well as indirectly by accelerating another driver (multi-stage

⁸⁵ As a matter of fact, due to the comparatively small strain in comparison to other hardening methods – such as rolling, forging and extrusion – shock hardening is a broadly commercially applied hardening method.

⁸⁶ The deviatoric stress tensor is defined as $s_{ij} = \sigma_{ij} - \sigma_{hydrostatic} \cdot \delta_{ij}$, where the indices i, j are referring to the principal stress directions and $\sigma_{hydrostatic}$ is the hydrostatic stress component - see footnote 66 on p. 30.

⁸⁷ See [65], chapter 14, p. 382 ff for an overview on strengthening mechanisms, dislocation mechanisms and models, point-defect generation and deformation twinning including these phenomena.

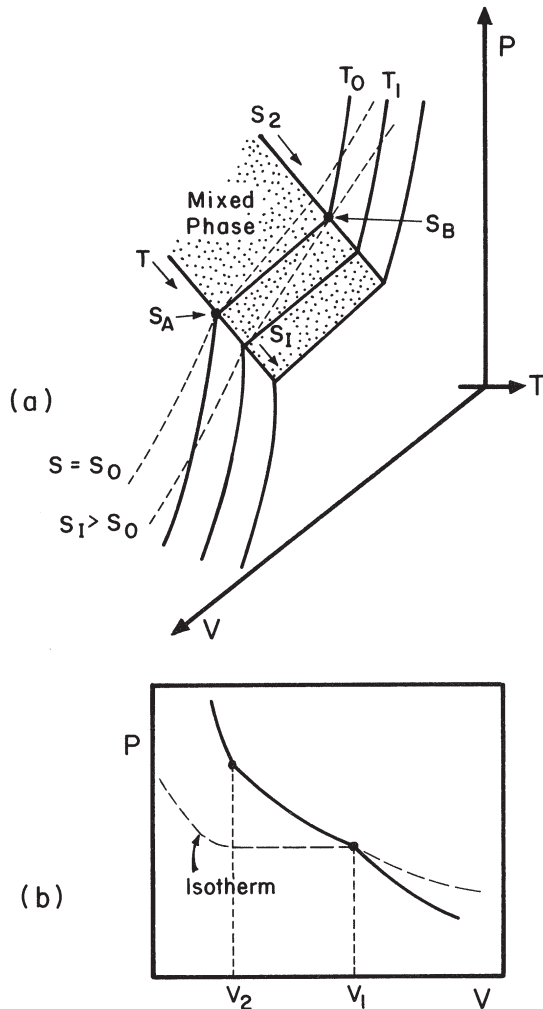


Figure 3.12: First order phase transformation of type $\Delta V < 0$, $\Delta S > 0$, and $\frac{dP}{dT} < 0$.
 (a) Pressure-volume-temperature surface: the dashed lines show the isentropic ($S = S_0$) and adiabatic compressions ($S_1 > S_0$).
 (b) Hugoniot in pressure-volume cut from (a).
 Fig. 11, p. 529 from [78], modified original figure caption of fig. 8.5 (p. 209) in [65] and with text adapted from section 8.3 (p. 206 ff) of [65]. Used with kind permission of American Physical Society and Wiley & Sons.

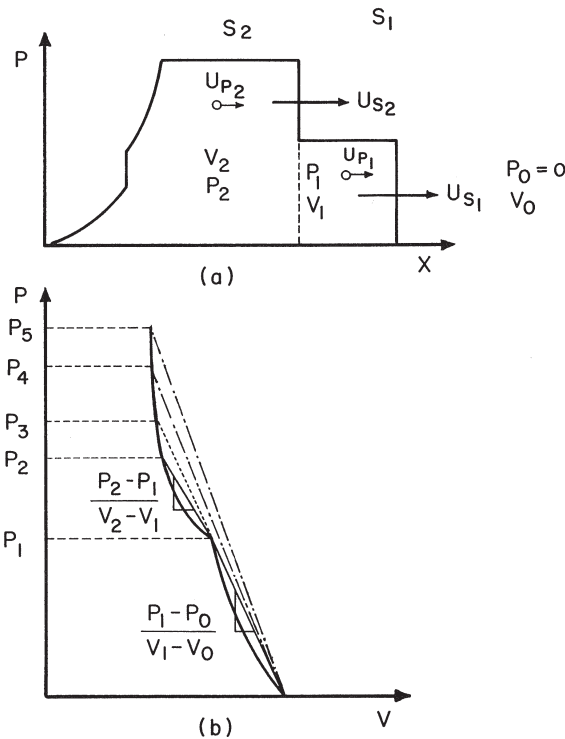


Figure 3.13: Propagation of shock waves in materials undergoing phase transformations of the type $\Delta V < 0$, $\Delta S < 0$, $\frac{dP}{dT} > 0$.

(a) Stable two-shock wave structure.

(b) Hugoniot curve with discontinuity in slope with their Rayleigh slopes for each phase: a shock with a peak pressure P_2 is an example of a stable two-shock wave structure, while the peak pressure P_3 serves as a limit case between two-wave and single-wave structure and a shock with peak pressure P_4 is another example showing a stable single-shock wave structure above the phase transition. Shock waves with peak pressures below P_1 will result in no phase transformation, hence the shock wave will also display a single shock.

Fig. 8.6 (p. 210) from [65], modified original figure caption with text adapted from section 8.3 (p. 206 ff) of [65]. Used with kind permission of Wiley & Sons.

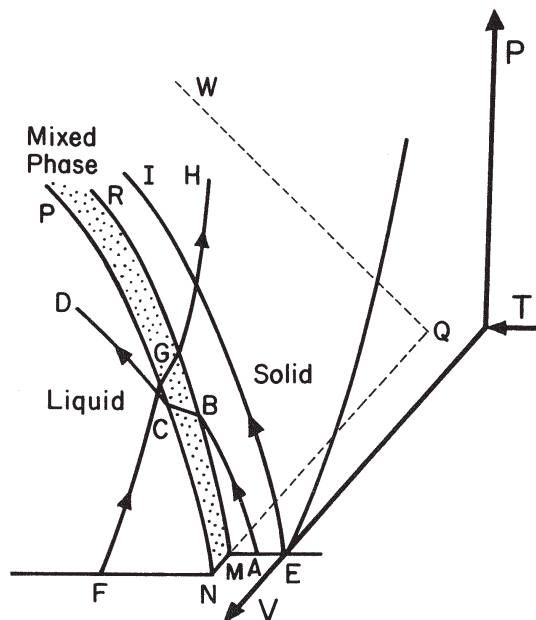


Figure 3.14: Pressure-volume-temperature surface for a material with solid to liquid transition of the type $\Delta V > 0$, $\Delta S > 0$, $\frac{dP}{dT} > 0$. The melting pressure increases with temperature. The mixed phase region is shown by the dotted strip within the area $NMRP$. The dashed line QW is the projection of the mixed phase region on the pressure-temperature plane. FGH is an isotherm originating in the liquid.

Fig. 14, p. 534 from [78], modified original figure caption of fig. 8.11 (p. 218) from [65] with text adapted from section 8.3 (p. 206 ff) in [65] and section VI, p. 557 in [78]. Used with kind permission of American Physical Society and Wiley & Sons.

approach). The following is a selection of shock wave generation processes. Developed procedures overlap with studies of equations of state (see section 3.2.2.4 p. 50 ff):⁸⁸

- explosive in contact with sample material (see e.g. [65], chapt. 5.1): the explosive material is arranged such that the detonating material creates a plane wave (this configuration is called "explosive lens").
- impact of plate or combination of sabot and projectile onto target sample (see e.g. [65], chapt. 5.1): the plate/sabot is accelerated with explosives or compressed air; electrodynamic guns – also called "railgun accelerators" – as well as magnetodynamic guns (as mentioned e.g. in [91], sect. 4)
- pulsed relativistic electron beam: the electron beam hits the material under investigation directly (see e.g. [92] and [93]⁸⁹) or indirectly (see e.g. [94]) – using the electron beam as the driving force of an impact plate.
- nuclear (underground) tests: using generated x-rays (as mentioned in [95]) or – as done in [96] – neutrons generated in a nuclear explosion used to create heating induced by fission in a enriched uranium slab, which in turn would produce a high pressure shock wave in the material under investigation⁹⁰.
- proton beams (see e.g. [97]): high power proton beams lead to vaporization or ablation of material. This effect can be used to directly heat a small volume of a target, generating a shock wave in the residual part of the target, or in an indirect way by ablating material layers of a flyer which hits the material under investigation with high velocities.
- heavy ion beams (see e.g. [98]) – which are used to probe high energy density matter (HED)
- soft X-ray radiation interacting both directly and indirectly with the material under investigation (e.g. [91], sect. 4).⁹¹
- highly focused high power laser beams (e.g. [91], sect. 4)

High Strain Rate Deformations

For high-strain rate deformations a constitutive equation of the type (3.26) or (3.27 on p. 30) was observed to be too simplistic, and more suitable constitutive equations were developed. These include dependencies on strain ϵ , strain rate $\dot{\epsilon}$ and – in some cases – temperature T , as well as the deformation history. For simplicity the tensorial terms are transformed into scalar effective stresses and strains (σ_{eff} and ϵ_{eff}). It was observed

⁸⁸ In addition to the references mentioned, the review paper [89] contains the state of the art methods for dynamic high pressure experiments in 1983. The publication [90] – following the bestowal of the Percy William Bridgman Award to Vladimir E. Fortov – reviews the driver methods to generate strongly nonideal plasmas.

⁸⁹ In these two early papers, electron beams had been used to study thermoelastic effects.

⁹⁰ In fact, a moderator foil had to be used to avoid direct heating through neutrons of the material under investigation (Molybdenum in this experiment).

⁹¹ In fact, in [91] the soft X-ray radiation itself is produced by the impact of a current accelerated by a plasma xenon liner.

that the yield stress σ_Y increases with increasing strain rate, while it decreases with rising temperature. A very widely applied empirical constitutive equation is the so-called Johnson-Cook constitutive equation([99]):⁹²

$$\sigma = (\sigma_0 + B\epsilon^n) \left(1 + C \ln \frac{\dot{\epsilon}}{\dot{\epsilon}_0} \right) \left(1 - \left(\frac{T - T_r}{T_m - T_r} \right)^m \right) \quad (3.36)$$

where σ_0 , B , C , n and m are experimentally determined material constants, $\dot{\epsilon}_0$ is the reference strain rate (usually $1s^{-1}$), T_r the reference temperature and T_m the melting temperature. Other models for plastic deformation take dislocation dynamics⁹³ into account – including thermally activated dislocation motion – and are of the form:

$$\sigma = \sigma_G (\text{structure}) + \sigma^* (T, \dot{\epsilon}, \text{structure}) \quad (3.37)$$

where σ_G represents the athermal (long range) barriers solely depending on the crystal structure while σ^* represents the (short range) barriers that can be overcome by thermal energy.

Microstructural effects play an important role in the response of the target. Ideally, dislocation movement, mechanical twinning, lattice rotation, phase transformations and strain hardening should be included in physically based constitutive equations. One of the more advanced models is the Zerilli-Armstrong model⁹⁴, developed for face-centered cubic (FCC) and body-centered cubic (BCC) metals where even grain size is considered:

$$\sigma_{FCC} = \sigma_G + C_2 \epsilon^{1/2} \exp(-C_3 T + C_4 T \ln \dot{\epsilon}) + k d^{-1/2} \quad (3.38)$$

$$\sigma_{BCC} = \sigma_G + C_1 \exp(-C_3 T + C_4 T \ln \dot{\epsilon}) + C_5 \epsilon^n + k d^{-1/2} \quad (3.39)$$

where σ_G represents – again – the athermal component of stress associated with initial dislocation density and – in addition – effects of solutes, C_2 and C_1 are parameters including the dependence on dislocation energy barrier (note that for the BCC metals the plastic strain is uncoupled from the strain rate and temperature), C_3 and C_4 are strain and strain rate dependent constants, d is the average grain diameter and the term $k d^{-1/2}$ is accounting for the decrease in yield stress with increasing grain size. Even though some parameters show a weak temperature and strain-rate dependence (particularly σ_G and k), they are – within this model – assumed to be constant for the given material. High strain rate phenomena can usually be assumed to be adiabatic processes and for most metals only a tenth of the generated energy is consumed by material defect generation. The remaining 90% is converted into heat⁹⁵ (assuming a constitutive equation of the form of equ. (3.36)):

$$\int_{T_0^*}^{T_f^*} \frac{dT^*}{1 - (T^*)^m} = \frac{0.9(1 + C \ln(\dot{\epsilon}/\dot{\epsilon}_0))}{\rho C_P} \int_0^{\epsilon_f} (\sigma + B\epsilon^n) d\epsilon \quad (3.40)$$

⁹² see [65], chapter 13.2, p. 325 ff or [100], chapter 3.2, p. 186 as an introduction to the multitude of available constitutive equations.

⁹³ see [65], chapter 13.3, p. 330 ff.

⁹⁴ see their work summarized in [101] (copper and iron), [102] (tantalum), and [103] (copper, iron, and tantalum).

⁹⁵ $\Delta T = \frac{\beta}{\rho C_P} \int_0^{\epsilon_f} \sigma d\epsilon$, where β is the fraction converted into heat. In this case $\beta = 0.9$.

where T^* is the homologous temperature⁹⁶, the parameters B , C , n and m are the same experimentally determined material constants as in equ. (3.36) on p. 48, ρ is the density and C_P the specific heat at constant pressure (which is assumed to be a constant), the fraction 0.9 accounts for the 10% loss of energy via dislocation generation, the strain rate $\dot{\epsilon}$ is assumed to be constant and ϵ_f is the final strain. If $m \neq 1$ the integral on the left hand-side has to be evaluated numerically, while for $m = 1$:

$$T^* = 1 - \exp \left[-\frac{0.9(1+C \ln(\dot{\epsilon}/\dot{\epsilon}_0))}{\rho C_P (T_m - T_r)} \left(\sigma_0 \epsilon + \frac{B \epsilon_f^{n+1}}{n+1} \right) \right].$$

Dynamic Fracture

For the dynamic fracture of a material, it is important to notice that stress waves exist which can both originate from the appearing crack tip or be caused by an external load. Hence, dynamic fracture models deal with rapidly propagating cracks and their interactions with each other, in order to represent fracture phenomena such as spalling and fragmentation. The propagation of a material fracture is then influenced by the stress field present around the crack tip and the crack front. The stress field is then correlated with the crack speed which relates in turn to the local stress field.

The first apparent difference between dynamic and (quasi-)static fracture is that dynamic fracture is initiated independently at different void and crack sites, while in static cases fracture originates from a single site. In addition, the limiting velocity for the propagation of cracks is the Rayleigh wave velocity.⁹⁷ Dynamic fracture can lead to fragmentation via a single crack branching out into multiple branches - called "bifurcation".⁹⁸ Finally, the fracture toughness frequently depends on the rate of crack propagation.⁹⁹

For the fracture toughness K_{IC} of materials, there is no simple relation - such as increase or decrease - for high strain rates $\dot{\epsilon}$. The situation is complicated through the complex interaction between dynamically applied load, and stationary and traveling cracks. Preexisting cracks can present a different response than an already traveling crack. It has also been observed that the fracture toughness is independent above a pulse duration of the externally applied load typical of the investigated material, but increases below this specific value with decreasing time duration. For ductile failure, the fracture toughness increases with increasing strain rate, while it decreases in case of brittle failure. Also, the ductile-to-brittle transition temperature for dynamic situations is significantly higher than for static events. The dynamic fracture toughness has to be measured directly in experiments since there is no simple relation between applied stress and fracture toughness - in contrast to the situation in static setups.¹⁰⁰

When (compressive) shock waves are reflected from free surfaces, they return as (tensile) release waves which can lead to spalling¹⁰¹ – sometimes also called chipping or

⁹⁶ $T^* = \frac{T-T_r}{T_m-T_r}$, where T_r is the reference temperature (usually room temperature) and T_m the melting temperature.

⁹⁷ see [65], chapter 16.3 for elementary examples and for recommended introductory references.

⁹⁸ whose problematics is briefly touched on in [65], chapter 16.4.

⁹⁹ [65], chapter 16.5.

¹⁰⁰ see [65], chapter 16.7 for an introduction to the intricacies of the experimentally determined dynamic fracture toughness.

¹⁰¹ The extensive review paper [104] – from 1983 – covers the mechanics of the spalling process including the computational treatment with the models then available, as well as metallurgical observations. With [68] an entire book is dedicated to the understanding of spall phenomena. It is a reference book for

scabbing – if the created tension is higher than a material specific spalling strength (σ_c or σ_{spall}).¹⁰² For tensions significantly larger than the spalling strength, multiple spalling can occur. Not surprisingly, the investigations of spall accompanied the development of failure models.¹⁰³ However, one should keep in mind that failure is defined more broadly than spall, and can comprise complete material separation or just simple loss of stiffness. Dynamic failure can occur in tension, in compression, and in shear:¹⁰⁴ ductile metals fail in tension by the nucleation, growth, and coalescence of voids, while tensile failure of brittle material is caused by nucleation, growth, and coalescence of cracks. Adiabatic shear bands are the precursors for dynamic shear failure since they facilitate crack propagation. Compressive failure occurs in brittle materials through existing flaws in the material's microstructure. A constitutive model would need to include the following processes: the void nucleation stage, its growth, the coalescence, the fragmentation and final stress relaxation.¹⁰⁵ In what follows, the concentration lies on the research conducted on spall fracture: the ability to spall depends on material characteristics such as grain size, phase and possible phase transformations, stress amplitude, crystallinity (mono- or polycrystalline materials) and purity: impurities reduce the spall strength of the material, while for spall experiments conducted at high temperatures close to melting temperature it was discovered¹⁰⁶ that the spall strength for single crystals is maintained above the expected melting point, while the spall strength decreases for melting polycrystalline metals. On the other hand, the experimental setup for spalling experiments also influences obtained results with their specific peculiarities such as peak pressure, strain rate, initial temperature, load duration and load direction.¹⁰⁷ It has even been observed, that the micrographical appearance of a spall fractured material can change from a brittle spall pattern (associated with a network of isolated and intersecting cracks) to a ductile spall pattern (identified through coalescence of isolated holes) with increased loading rate.¹⁰⁸

3.2.2.4 Crossing the Phase Space¹⁰⁹

In principle one should be able to work out the equation of state (EOS) of a material covering the whole of the temperature-pressure-volume phase space (see the schematic drawing of the equilibrium surface in fig. 3.15) on p. 51 purely by applying theoretical considerations. In practice, this is only partially possible. However, shock wave experiments can be used to help establish EOS' in very large fraction of this phase space (e.g. [108]¹¹⁰) – see one example Hugoniot crossing the phase boundary upon unloading in the schematic

the different investigating sides involved: experimental techniques, constitutive spall models and their implementation into computational codes.

¹⁰² For an introduction to quantitative models developed for spalling see [65], chapter 16.8.2.

¹⁰³ For a comprehensive overview on failure models for metals and brittle materials as well as ductile failure through shear banding see [100], chapter 3.3, p. 219 ff.

¹⁰⁴ A good review paper on mechanical modeling and metallurgical perspective on these three failure types is [105].

¹⁰⁵ see e.g. [67], section 9.2 "Constitutive modeling of fracture", p. 340 ff.

¹⁰⁶ [82], chapter 3.1, p. 91, fig. 3.10 and 3.11.

¹⁰⁷ Compare with [68], chapter 5.

¹⁰⁸ [106] section 5, p. 366 ff.

¹⁰⁹ References for this section are [88], vol. 2, chapt. XI, [65], chapter 5 and [107].

¹¹⁰ Young defines – on page 8 – static high pressure, shock compression and isobaric heating (at low pressure) experiments as the three pillars in order to build pressure-temperature phase diagrams.

drawing of fig. 3.16 on p. 52.

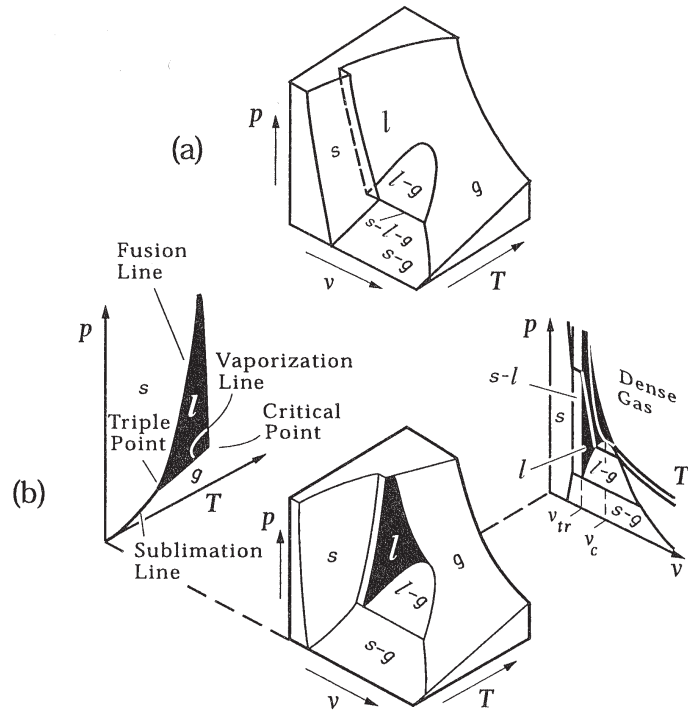


Figure 3.15: Schematic pressure-volume-temperature plots summarize possible equilibrium phases and phase changes. Non-equilibrium states take place in the remainder of the pressure-volume-temperature space. The slope $\frac{\partial p}{\partial T}$ of all phase-equilibrium lines obey the equation (3.34) on p. 40. A line separating a single-phase region from a two-phase region summarizes the saturation states. (a) Phase diagram for a pure substance that contracts upon melting and (b) for a substance that expands upon melting (also shown are the projections in pressure-temperature and pressure-volume space). s ... solid phase, l ... liquid phase, and g ... gaseous phase. Fig. 1.4 (p. 27) from [109], modified original figure caption and with text mostly taken from section 1.5.1 in [109]. Used with kind permission of Springer Science+Business Media.

Pressure P and (specific) internal energy E of a cold solid consist of an elastic part (P_c , E_c) – which is connected to the force of interaction between the atoms of the material – and a thermal component (P_{th} , E_{th}). At absolute zero only the elastic parts are contributing to the pressure and internal energy, which is why they are also called "cold" pressure and "cold" energy. The volume of a solid at absolute zero (V_{0c}) is only slightly smaller¹¹¹ than the volume at standard condition¹¹² (V_0). Atoms create a potential around themselves with an area of attraction and strong repulsion where their electronic shells interact. From such a potential (e.g. the Condon-Morse potential in fig. 3.17 (a) on p. 53) one can obtain a pressure-volume plot (fig. 3.17 (c)) – in this case an isothermal 0 Kelvin (or 0K) compressibility curve. If the material is subjected to tension ($V > V_{0c}$ in fig. 3.17 (a)), the binding energy (usually denoted as U) has to be overcome in order to separate the

¹¹¹ 1 – 2% – [88], vol. 2, chapt. XI, sect. 1, paragraph 2.

¹¹² at $T_0 = 300K$ and $P = 0$ or $P = 1$ atm (1 atm = 101 325 Pa).

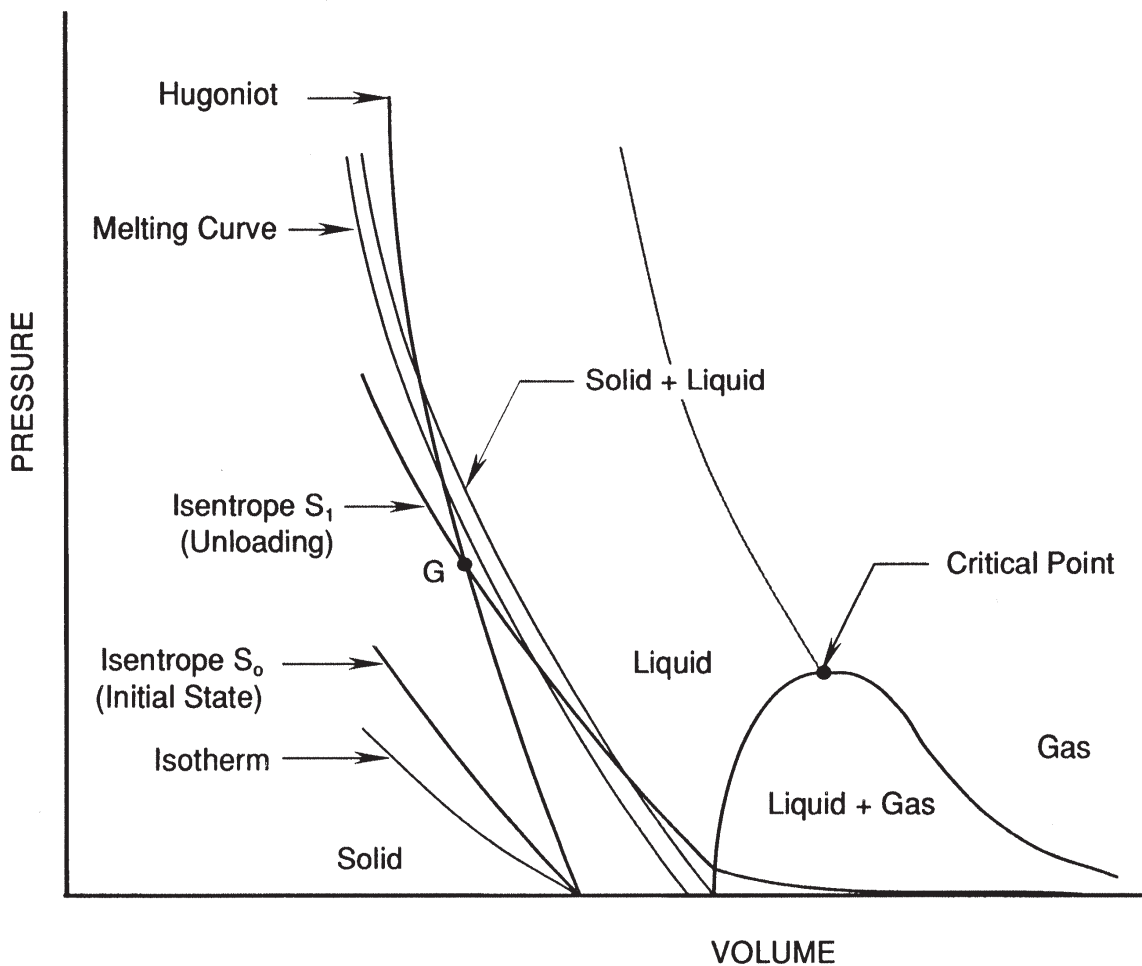


Figure 3.16: Schematic phase diagram of matter in pressure-volume space. The diagram shows the relative position of the Hugoniot, isotherm, isentrope, and melting curve. The **Hugoniot** is the summary of all possible states that can be reached through shock wave transitions. In this case the Hugoniot is for a material at zero stress and it is assumed that the hydrodynamic elastic limit (HEL) is insignificantly small. The **isentrope** is the loci of all possible states with constant entropy, which includes reversible processes where there is no exchange of heat with the surrounding and no dissipation. For weak shocks, loading paths of Hugoniots can be approximated by isentropes. For high stress shock compression this is not possible, due an increase in entropy and irreversible heating of the shocked material. There are two isentropes: S_0 corresponds to the initial (or reference) state, while S_1 represents a possible unloading path of the material if it was shocked to the state G . It should be noted that the material may melt or even reach the mixed liquid-vapor state upon unloading. If the material was shock loaded to a higher stress state, the isentrope could lie above the critical point leading to evaporation of the material during unloading. The **isotherm** is the series of states connected to each other through processes during which the temperature does not change. Quasi-static loading conditions follow isotherms. In this figure the isotherm is drawn for the initial (or reference) state. Fig. 2.6 (p. 45) from [68], modified original figure caption and with text mostly taken from section 2.3.1 in [68]. Used with kind permission of Springer Science+Business Media.

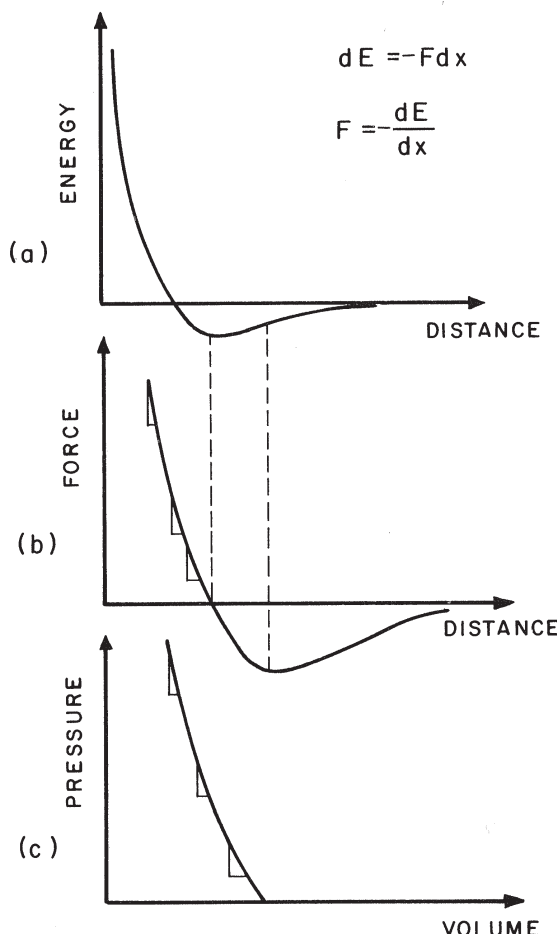


Figure 3.17: Condon-Morse curve. (a) Energy E vs. atomic distance x .
 (b) Force $F = -\frac{dE}{dx}$ vs. atomic distance x .
 (c) Pressure P vs. volume V . The shape of this isothermal 0 Kelvin compressibility curve is the reason for the steepening of the shock wave front.
 Fig. 5.3 (p. 127) from [65], modified original figure caption. Used with kind permission of Wiley & Sons.

atoms from each other.¹¹³ Under compression, the repulsive forces grow strongly. Once can obtain the elastic pressure from the potential energy via

$$P_c = -\frac{dE_c}{dV} \quad (3.41)$$

This follows from the general thermodynamic expression $TdS = dE + PdV$ with $T = 0$. For $T = 0$, the isotherm is also the isentrope due to the application of the Nernst's theorem.¹¹⁴ The elastic pressure is zero at V_{0c} and is formally negative in expansion (not shown in fig. 3.17 (c), but in fig. 3.17 (b) on p. 53) – indicating that a tensile force needs to be applied until the atoms are not bound in the solid. Experimentally, the heat of vaporization can be used to estimate negative pressure since it is not possible to expand a solid isotropically with a mechanical process.¹¹⁵ Theoretical models of cold compression curves – $P_c(V)$ or $E_c(V)$ – are based on quantum-mechanical formulation of the interatomic interaction. For strong compressions (high pressures and densities), the solid can be described by Thomas-Fermi (see e.g. [87], chapt. 9) or Thomas-Fermi-Dirac models (see e.g. [87], chapt. 9.3) and $P_c \sim \rho^{5/3} \sim V^{-5/3}$.

The total energy and pressure of a solid need to take into account the elastic contributions ($P_c(V)$ or $E_c(V)$) as well as the thermal contributions of both nuclei ($P_T(V)$ or $E_T(V)$) and electrons ($P_e(V)$ or $E_e(V)$) – although the electronic components only play a significant role for temperatures higher than tens of thousands degrees:

$$P = P_c + P_T + P_e \quad (3.42)$$

$$E = E_c + E_T + E_e \quad (3.43)$$

At low temperatures, the thermal motion of nuclei within a material¹¹⁶ is an oscillation around their equilibrium positions, which are harmonic for vibrational energies well below the potential barrier preventing them – in a solid – from leaving their (lattice) positions into interstitial or vacant locations. At high temperatures, nuclei move randomly like a gas succumbing to strong interactions with neighboring nuclei. Under compression, the repulsive forces become stronger – the potential barrier becomes larger. Therefore, thermal motion up to about 20 000 to 30 000 K can still be assumed as oscillatory motions around their equilibrium position. The thermal contribution to the specific energy can be written as

$$E_T = C_V(T - T_0) + E_0 \quad (3.44)$$

where C_V is the specific heat at constant volume with $C_V = 3Nk$ (Boltzmann constant k , number of nuclei N) in cases where quantum effects are negligible and E_0 is the thermal energy at room temperature¹¹⁷. For high temperatures the terms with T_0 and E_0 in equ. (3.44) can be neglected in comparison with $C_V T$. As soon as the oscillatory movement is no longer a valid assumption for the behavior of the nuclei¹¹⁸, the contribution for each

¹¹³ This binding energy is equal to the heat of vaporization at absolute zero.

¹¹⁴ "The entropy of any equilibrium system at absolute zero can always be taken [as] equal to zero."
[110].

¹¹⁵ $\int_{V_{0c}}^{\infty} P_c(V)dV = -U$

¹¹⁶ solid or liquid materials; the thermal motion of a liquid is not significantly different than in a solid.

¹¹⁷ for which the value of $E_0 = \int_0^{T_0} C_V(T)dT$ can be found in tables.

¹¹⁸ The vibrational movement gradually transforms into a translational motion.

nuclei is $\frac{3}{2}k$ – the contribution of a monatomic gas – plus the binding energy ΔU . The pressure for high temperatures (when the nuclei behave like a gas) is

$$p_T = nkT = \frac{NkT}{V} = \frac{2}{3} \frac{E_T}{V} \quad (3.45)$$

where n is the number of nuclei per volume ($\frac{N}{V}$).

For nuclei vibrating around their equilibrium position – with the additional assumption that the electronic contribution can be neglected, the pressure and internal temperature can be written as:

$$P = P_c(V) + P_T(V, T) \quad (3.46)$$

$$E = E_c(V) + 3NkT \quad (3.47)$$

The specific heat does not depend on the (specific) volume, hence the thermal pressure is proportional to the temperature and one can choose to write P_T in equ. (3.46) in the following form:¹¹⁹

$$P_T = \Gamma(V) \frac{C_V T}{V} = \Gamma(V) \frac{E_T}{V} \quad (3.48)$$

$\Gamma(V)$ is the Grüneisen coefficient and describes the ratio of the thermal pressure component to the thermal (lattice) energy.¹²⁰ The Grüneisen coefficient at standard condition (Grüneisen constant Γ_0) can be expressed as:¹²¹

$$\Gamma_0 = \Gamma(V_0) = \frac{V_0 \alpha}{C_V K_0} = \frac{\alpha}{\rho_0 C_V K_0} \quad (3.49)$$

where α is the coefficient of thermal expansion at constant pressure, C_V is the specific heat at constant volume, K_0 is the isothermal compressibility (also called bulk modulus) at standard condition and ρ_0 is the standard density. Grüneisen constants for metals have values around 2, but one should be aware that in the limiting case of $T \rightarrow \infty$ is $\Gamma \rightarrow \frac{2}{3}$ (which is the Γ of a monatomic gas). It was shown experimentally that the Grüneisen coefficient decreases slightly for compression. $\Gamma = \Gamma_0 = \text{constant}$ usually holds for states not too far from standard condition. The entropy can be expressed as¹²²

$$S = C_V \ln \frac{T}{T_0} \left(\frac{V}{V_0} \right)^{\Gamma_0} + S_0 \quad (3.50)$$

¹¹⁹ Inserting $E_T = 3NkT$ into the thermodynamic identity $(\frac{\partial E}{\partial V})_T = T (\frac{\partial P}{\partial T})_V - P$ results in a thermal pressure equal $P_T = \varphi(V)T$, where $\varphi(V)T$ is a function depending only on the volume.

¹²⁰ In statistical mechanics, Γ is used as an abbreviation for $-\frac{\partial \ln \bar{\nu}}{\partial \ln V}$, where $\bar{\nu}$ is the average vibrational frequency related to the Debye temperature θ by $h\bar{\nu} = k\theta e^{1/3} = 0.715k\theta$ – with h as Planck's constant and k as the Boltzmann constant.

¹²¹ Using the thermodynamic relation $(\frac{\partial P}{\partial T})_V (\frac{\partial T}{\partial V})_P (\frac{\partial V}{\partial P})_T = -1$ and both the definitions of the isothermal compressibility at standard condition ($K_0 = -\frac{1}{V_0} (\frac{\partial V}{\partial P})_T$) and the coefficient of thermal expansion at constant pressure ($\alpha = \frac{1}{V_0} (\frac{\partial V}{\partial T})_P$).

¹²² Following from $dS = \frac{dE + PdV}{T} = \frac{dE_T + P_T dV}{T} = C_V \frac{dT}{T} + \Gamma_0 C_V \frac{dV}{V}$.

where S_0 is the entropy at standard condition ($S_0 = S(V_0, T_0)$)¹²³. Using the isentropic relation between temperature and volume ($T/T_0 = (V/V_0)^{\Gamma_0}$) one arrives at the isentropic relation between pressure and volume:

$$\frac{P - P_c(V)}{P_{T_0}} = \left(\frac{V_0}{V}\right)^{\Gamma_0+1} \quad (3.51)$$

with P_{T_0} as the thermal component of the pressure at standard condition ($P_{T_0} = \Gamma_0 C_V T_0 / V_0$).¹²⁴

The simplest model taking into account the electronic contribution is that of freely moving outer valence electrons inside the metal which behave like a free electron gas governed by Fermi-Dirac quantum statistics (see e.g. [87], chapt. 6). At absolute zero the electrons possess energies up to the Fermi energy E_0 (the gas is completely degenerate):

$$E_0 = \frac{h^2}{8\pi^2 m_e} (3\pi^2 n_e)^{\frac{2}{3}} \quad (3.52)$$

h is Planck's constant, m_e is the electron mass and n_e is the number density of free electrons. The energy of the electrons at absolute zero does not contribute to the thermal energy (nor pressure) and is part of the elastic component of the energy. The electrostatic interaction between valence electrons and ions also contributes to the elastic component of the energy. For temperatures below the Fermi temperature T_F ($T_F = E_0/k$ with E_0 from equ. (3.52)) – the Fermi temperature is sometimes also called the degeneracy temperature T^* – the thermal component of the electrons totals to

$$E_e = \frac{1}{2} \beta T^2 \quad (3.53)$$

$$\beta = \beta_0 \left(\frac{V}{V_0}\right)^{\frac{2}{3}} \quad (3.54)$$

$$\beta_0 = \frac{4\pi^4}{(3\pi^2)^{2/3}} \frac{k^2 m_e}{h^2} N_e^{\frac{1}{3}} V_0^{\frac{2}{3}} \quad (3.55)$$

where β is a parameter depending on the material's density, N_e is the number of free electrons per unit mass and V_0 is the standard specific volume. The electronic specific heat at constant volume C_{V_e} is βT . β_0 is determined experimentally at low temperatures where the electronic specific heat exceeds the contributions of the lattice.¹²⁵ The above equations are only true for $T < T_F$. If $T \gg T_F$ – the free electron gas is not degenerate any more and one expects the classical value $C_{V_e} = \frac{3}{2} N_e k$. However, as soon as the temperature rises, more electrons become part of the free electron pool and the electronic specific heat cannot be described by simple equations. Because T_F increases in compression ($T_F \sim V^{-2/3}$), equ. (3.53) on p. 56 and $C_{V_e} \sim T$ are valid at even higher temperature ranges rather than

¹²³ Values of S_0 are usually tabulated.

¹²⁴ Equivalently, the isotherm is $\frac{P - P_c(V)}{P_{T_0}} = \frac{V_0}{V}$.

¹²⁵ The lattice specific heat C_V at low temperatures is proportional to T^3 . At standard condition, the electronic specific heat $C_{V_e} < C_V$ where $C_V = 3Nk$. C_{V_e} can be a factor of tens or even a hundred smaller than C_V .

only at standard condition. The given equation of state results in the electron pressure – for both degenerate and non-degenerate electron gas – as

$$P_e = \frac{2}{3} \frac{E_e}{V} = \frac{1}{3} \beta \frac{T^2}{V} \sim V^{\frac{1}{3}} T^2 \text{ or } P_e = \Gamma_e \frac{E_e}{V} \quad (3.56)$$

with the definition of an electronic Grüneisen coefficient Γ_e . However, $\Gamma_e = \frac{2}{3}$ only holds for high temperatures and high densities and Γ_e was found to be 0.5 - 0.6 in shock experiments so that $\Gamma_e = \frac{1}{2}$ is usually a valid assumption. Because of this experimental result, equ. (3.54) from p. 56 and (3.56) need to be changed to equ. (3.57) and (3.58) while equ. (3.53) from p. 56 stays formally the same.

$$\beta = \beta_0 \left(\frac{V}{V_0} \right)^{\frac{1}{2}} \quad (3.57)$$

$$P_e = \frac{1}{2} \frac{E_e}{V} \quad (3.58)$$

The energy ($E = E_c(V) + E_T + E_e$) and pressure ($P = P_c(V) + P_T + P_e$) of a metal subjected to temperatures below about ten thousand degrees (for small compressions) can therefore be stated as:

$$E = \underbrace{\int_V^{V_{0c}} P_c(V) dV}_{E_c(V)} + \underbrace{3Nk(T - T_0) + E_0}_{E_T} + \underbrace{\frac{1}{2} \beta_0 \left(\frac{V}{V_0} \right)^{\frac{1}{2}} T^2}_{E_e} \quad (3.59)$$

$$P = P_c(V) + \underbrace{\Gamma(V) \frac{E_T}{V}}_{P_T} + \underbrace{\frac{1}{2} \frac{E_e}{V}}_{P_e} \quad (3.60)$$

where T_0 is room temperature, E_0 is the thermal energy of the atomic lattice at room temperature (whose values are tabulated), β_0 can be obtained from low temperature measurements and the Grüneisen coefficient $\Gamma(V)$ can be obtained from $P_c(V)$ via $\Gamma(V) = -\frac{\partial \ln \bar{\nu}}{\partial \ln V} = -\frac{2}{3} - \frac{V}{2} \frac{(d^2 P_c / dV^2)}{(dP_c / dV)}$.¹²⁶ It is now obvious that under the given restrictions only $P_c(V)$ needs to be obtained from experiments.

Isothermal compressibility curves can be obtained by static high pressure experiments up to a certain pressure. For higher pressures, shock experiments allow the determination of shock Hugoniots which allow the construction of the already mentioned Mie-Grüneisen EOS: using statistical mechanics with the assumptions of that firstly, the atoms are quantized harmonic oscillators and secondly, the same increase in oscillation frequency of all these oscillators with decreasing volume, one obtains the form of the Mie-Grüneisen EOS

¹²⁶ This relation follows from the following considerations: the average frequency of the spectrum of elastic vibrations of the lattice $\bar{\nu}$ is close to the maximum frequency. The maximum frequency itself is the ratio of the speed of propagation of elastic compression waves (C_0) to the minimum wave length (in the order of the interatomic distance r_0): $\bar{\nu} \sim C_0 / r_0$. With $C_0 = (-V^2 dP_c / dV)^{1/2}$ and $r_0 \sim V^{1/3}$ one obtains $\bar{\nu} \sim V^{2/3} (-\frac{dP_c}{dV})^{1/2}$. Taking the logarithmic derivative of the latter expression yields the relation stated above.

as seen in equ. (3.61):¹²⁷

$$P - P_c = \frac{\Gamma_0}{V} (E - E_c) \quad (3.61)$$

where P (E) is the pressure (energy) of the thermodynamical state of interest. If the shock Hugoniot is known, the Hugoniot pressure P_H and energy E_H at the same volume can be used instead of P_c and E_c as the reference state. In addition, one assumes that $\frac{\Gamma}{V} = \frac{\Gamma_0}{V_0} = \text{constant}$, where the index 0 refers again to the state of zero pressure.

The Mie-Grüneisen model also allows for the calculation of the temperature rise due to a passing shock wave not causing a phase transformation (see fig. 3.18 on p. 59): the passing shock brings the material to the state (P_1, V_1) and with the assumption of a purely adiabatic process and applying thermodynamical transformations along with the Rankine-Hugoniot equations, one obtains the temperature T_1 from:

$$T_1 = T_0 e^{\left[\frac{\Gamma_0}{V_0} (V_0 - V) \right]} + \frac{V_0 - V}{2C_V} P + \frac{e^{\left[-\frac{\Gamma_0}{V_0} V \right]}}{2C_V} \int_{V_0}^V P e^{\left[\frac{\Gamma_0}{V_0} V \right]} \left[2 - \frac{\Gamma_0}{V_0} (V_0 - V) \right] dV \quad (3.62)$$

where the integral has to be numerically calculated. Once T_1 is known, the residual temperature T_2 after the pressure has returned to zero can be calculated via the isentropic path from 1 to 2 and using $\frac{\Gamma}{V} = \frac{\Gamma_0}{V_0} = \text{constant}$:

$$T_2 = T_1 e^{\left[\frac{\Gamma_0}{V_0} (V_1 - V_2) \right]} \quad (3.63)$$

As already mentioned in the beginning of section 3.2.2.4 on page 51, phase changes can also occur during unloading of a shocked material (see in fig. 3.16 on p. 52). This can be easily understood if one assumes shock waves strong enough to generate an internal energy of the shocked material much higher than the binding energy U . Upon unloading into a comparatively low pressure environment ($P \sim 0$) the material will be entirely vaporized. If one assumes that the latent heat used for melting is nonexistent in comparison to the heat of vaporization and that the volume change from solid to liquid phase is also negligible, one can describe vaporization upon unloading in a simplified manner.¹²⁸ The unloading isentropes can cross the phase space at different regions – depending on the pressure applied through the shock (see fig. 3.19 on p. 60): as the limiting case for low pressures one can examine isentrope S_1 . At point B_1 the solid (or liquid) is expected to boil. In reality, the formation of vapor bubbles is suppressed due to a very low formation rate caused by a rather large activation energy. Therefore the material will continue to cool down to zero pressure along this "superheated liquid" isentrope (dashed line from point B_1 to volume at zero pressure V_2).¹²⁹ On the high pressure end (isentrope S_4), the material will cross into

¹²⁷ An alternative approach to reach equ. (3.61): one assumes that the pressure wave is not too strong so the electronic components of pressure and energy can be omitted, and that $\Gamma = \Gamma_0$, but the shock wave is still strong enough so that the thermal energy of the thermal lattice E_0 is insignificant. In addition, one does not distinguish between standard volume V_0 and zero Kelvin volume V_{0c} . Setting $P_0 = 0$ in equ. (3.30) from p. 31 and equating $E = E_c + E_T$ as well as expressing the thermal energy distribution E_T in terms of pressure by means of $P = P_c(V) + \Gamma_0 \frac{C_V T}{V}$, one arrives at $P - P_c = P_T = \Gamma_0 \frac{E_T}{V}$ and equ. (3.61).

¹²⁸ In fact, for the following one also needs to assume that the solid was initially at 0 Kelvin in vacuum ($P = 0$) with the volume V_{0c} .

¹²⁹ The fraction of the vaporized material is in the order of $\frac{C_V T_{B_1}}{U}$, where U is the binding energy and for metals at temperatures T_{B_1} of hundreds of degrees $\frac{U}{C_V} \sim 10^4 K$.

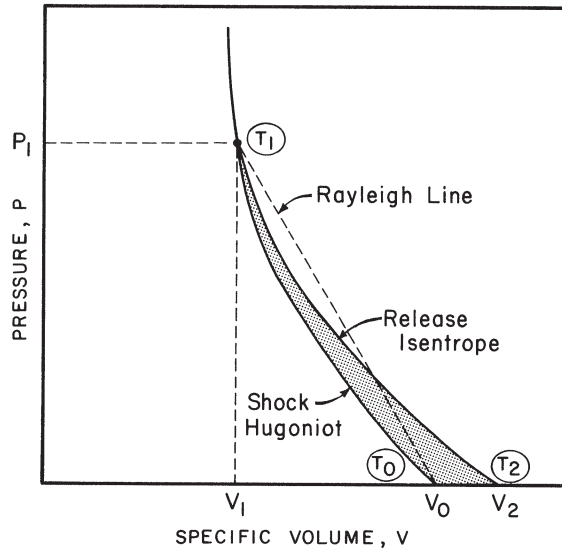


Figure 3.18: Shock Hugoniot and release isentrope leading to calculation of temperatures T_1 and T_2 : in solid materials the shock Hugoniot and release isentrope are fairly close. The point P_1 , V_1 is on the shock Hugoniot. When the pressure is released, unloading follows the release isentrope to point 2. It can be seen that V_2 is different from V_0 , because T_2 is higher than T_0 . This irreversibility of the process produces lost energy (shown by the hatched area). Indicated are the three temperatures T_0 , T_1 and T_2 .

Fig. 5.10 (p. 147) from [65], modified original figure caption with text taken from section 5.5 of [65]. Used with kind permission of Wiley & Sons.

the gaseous region above the critical point K . Since the unloading isentrope will cross the saturated vapor curve at point B_4 condensation is expected to happen. Also in this case, the condensation is hindered from taking place due to greatly reduced interaction time between the gas particles. The material continues along the "supercooled vapor" isentrope (dashed curve from point B_4 onwards).

The Tillotson EOS ([111]) is an example of an analytical equation of state which was developed for cases where the energy of hypervelocity impacts was sufficiently high to cause melting or vaporization. It is based on the combination of both theory (Thomas-Fermi statistical theory for the atom) in the high pressure region (1 – 100 TPa) and data (from shock experiments) for the low pressure region (up to 1 TPa)¹³⁰, not specifically treating material under tension. In the Tillotson EOS, the phase space is subdivided into different regions in which different analytical EOS' are established.

The validity of equations of state models in phase space covering several orders of magnitude is limited and upon certain thresholds, new equations of state have to be adopted in order to allow for a general purpose equation of state. One demonstrative classification can be seen in fig. 3.20 on p. 61, which allows for a good qualitative overview – even though this illustration dates from the 1960s:¹³¹

¹³⁰ The Tillotson equation of state was derived 1962, while in 1983 already 10 TPa were reached dynamically([89]).

¹³¹ A more modern version of this diagram, covering a larger temperature and density range can be found in fig. 1.1 in [87]. Also in [87], fig. 1.3 covers the pressure-temperature space. Theoretical calculations can

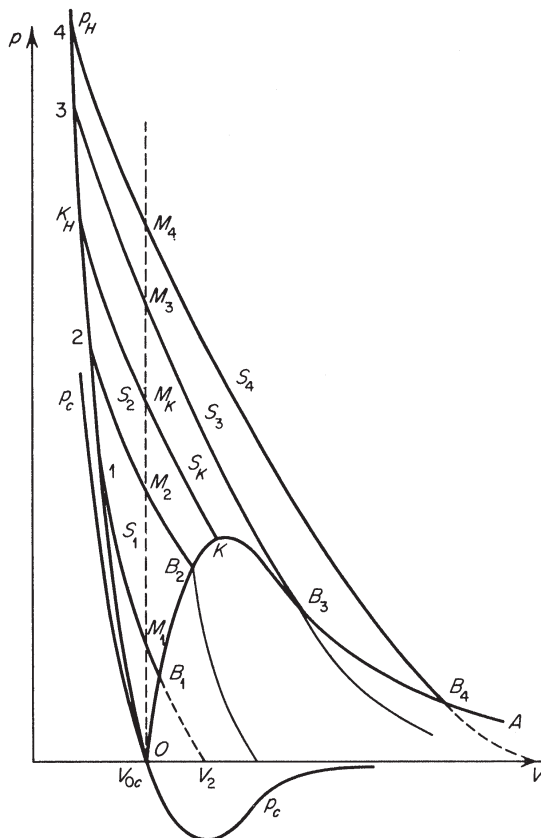


Figure 3.19: Unloading isentropes on a P-V-diagram: the unloading isentropes (S_1 to S_4) will pass through a base boundary according to the strength of the shock wave - from low pressures (e.g. isentrope S_1 at p_1) to high pressures (e.g. isentrope S_4 at p_4). p_c represents the cold curve (elastic pressure curve) – even extending into the negative pressures – while p_H stands for the Hugoniot. The curve OKA separates single- and two-phase regions where the point K represents the critical point. The first branch OK is the boiling curve (beginning of vaporization) and the second branch KA is the saturated vaporization curve (beginning of condensation).

Fig. 11.58 (p. 765) from [88], modified original figure caption with text taken from section §21 of [88]. Used with kind permission of Elsevier.

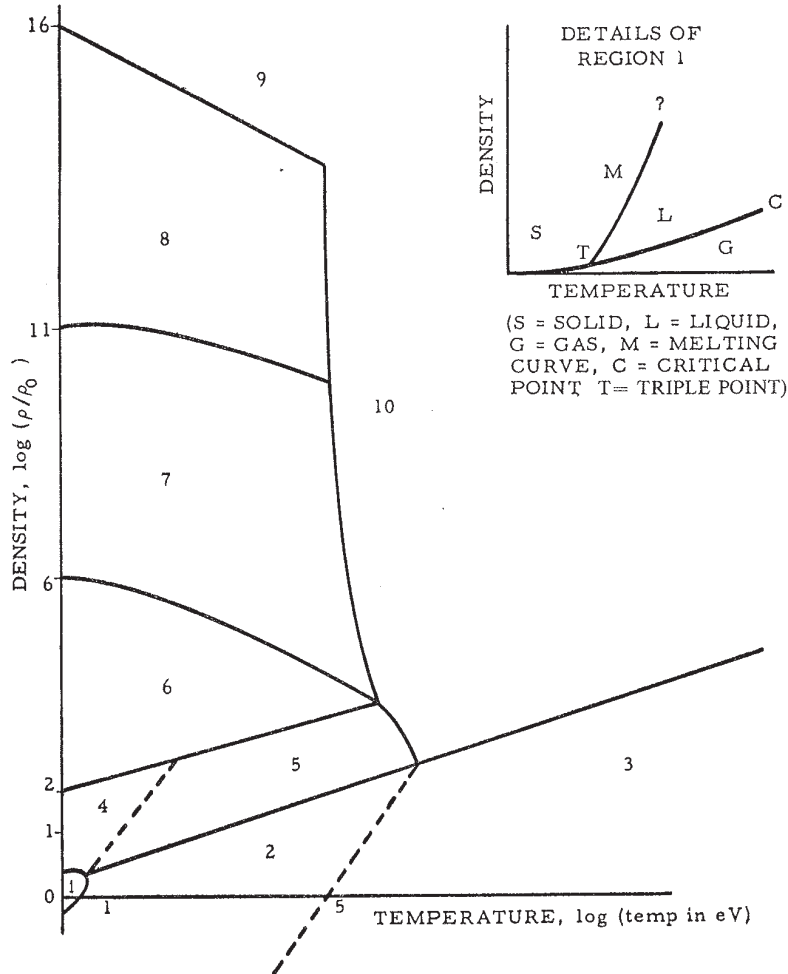


Figure 3.20: Dominating effects of states of matter: the numerical values are only approximate and correspond to a material with normal density $\rho_0 = 1 \text{ g/cm}^3$. Modifications according to the atomic number Z will have to be considered as various effects scale differently with Z . $1 \text{ eV} = 1/k_B \text{ Kelvin}$, where k_B is the Boltzmann constant. $1 \text{ eV} \approx 11604.5 \text{ Kelvin}$.

Region 1 corresponds to material around room temperature in which the chemical properties (determined by the structure of the outer electron shells of the atom) are important. The inset on the right shows details of this region (solid (S), liquid (L) and gaseous (G) phase, melting (M), critical point (C) and triple point (T)).

Fig. 1 (p. 5) from [107], modified original figure caption with text taken from section 1(a) in [107]. Used with kind permission of Elsevier.

The density-temperature space is divided into several regions (region 1 to region 10). In region 1, properties like compressibility, thermal expansion, melting and boilings points are approximately periodic functions of the atomic number Z . When increasing the density at constant temperature, the very same properties show a power law dependence on Z . Region 2 represents the gaseous mixture of atoms, molecules, ions, and electrons with an EOS of the form $PV \approx \bar{N}RT + \delta$, where \bar{N} is the number of independent particles per nucleus ($\bar{N} = \bar{N}(V, T)$) and δ is the correction term dealing with the effects of interatomic forces and includes the atomic and molecular partition functions. Region 3 covers the density-temperature space in which the gaseous material is completely ionized and also includes areas where the pressure from the radiation field needs to be taken into account. At even higher temperatures, the creation of particle-anti-particle pairs¹³² have to be included.

Region 4 is primarily interesting for geophysics (low temperatures, higher densities). In both regions 4 and 5, the electron is described by a partially degenerate Fermi-Dirac gas of electrons, in which the non-degenerate nuclei move: the nuclear contribution to pressure originates from either the oscillations of the nuclei around their fixed equilibrium positions in the solid (region 4), or traveling of the nuclei in the electron gas as is the case for liquids and gases. Regions 4 and 5 are separated by the melting region which is a continuation of the melting curve of region 1.¹³³ In regions 4 and 5, the electron pressure is best described with the Thomas-Fermi theory including Dirac exchange effects¹³⁴, quantum or inhomogeneity corrections, and electron-electron correlation effects. In region 6 the electron gas is completely degenerate and corrections applied for the material models of regions 4 and 5 are insignificant. The electron gas can however become relativistic for higher densities or temperatures.¹³⁵

In region 7, nuclear reactions start to play an important role and the material is not in a state of equilibrium any more.¹³⁶ Region 8 already consists of matter whose nuclei have disintegrated to neutrons to a large extent.¹³⁷ Region 9 contains neutron gas that is more compressed than in region 7 leading to a relativistic behavior and causing particle-anti-particle production due to the high energies. Region 10 represents the high temperature region in which equilibrium of all the different elementary particles have to be considered.

The SESAME database – developed and maintained at Los Alamos National Laboratory¹³⁸ – is one of the grand examples of developing theoretical models covering a large phase space. The SESAME EOS is obtained in tabular form¹³⁹. The SESAME database

be found in [107] – starting from section 3 – as well as in [87].

¹³² starting with electron-positron-pairs.

¹³³ A simple melting curve is a simplification since the transitions between the regions is not a sharp one.

¹³⁴ This is an approximation for the exchange interaction based on the homogeneous electron gas.

¹³⁵ In the non-relativistic case the pressure is proportional to $(\rho/\rho_0)^{5/3}$, while it is $(\rho/\rho_0)^{4/3}$ for the extreme relativistic region.

¹³⁶ The lower limits for an equilibrium are very high: for densities they are in the order of $10^{10} g/cm^3$ and temperatures in the orders of $1 MeV$ (approx. $1.16045048 \cdot 10^{10} K$).

¹³⁷ For temperatures around $0.1 MeV$, the probability increases that electrons are captured by the nucleus converting protons into neutrons, which leads to the break-up of the nucleus. The pressure will be proportional to $(\rho/\rho_0)^{5/3}$ – as for the degenerate electron gas in region 6 – but also inversely proportional to $m^{8/3}$, where m is the mass of the particle.

¹³⁸ homepage of the Theoretical Division: <http://t1web.lanl.gov/>

¹³⁹ As opposed to analytical equations which are generally easier to handle in computation. When equations of states are complicated, the calculation of phase boundaries can consume much of the computing

not only includes EOS', but also other material properties. In the 1970's, the collection – which was previously only used at the Los Alamos National Laboratory – was made available to the scientific community [113] and cooperation for the advancement of the database was fostered (e.g. [114]). In 1984, the data was summarized for the first time in a bulk manual [115]. SESAME contains not only simple materials, but also compounds, minerals, polymers and mixtures and is updated with new material models and better version of already existing models, including data on opacity and conductivity (mean ion charge, electrical and thermal conductivity, thermoelectric coefficient and electron conductive opacity) and even tables of vaporization, melt and shear for some materials [116]. The global EOS for a given entry is a combination of theoretical models¹⁴⁰ with – usually thermodynamically consistent – interpolations between the various regions of validity: "The aim of the SESAME Library is to have thermodynamically self-consistent EOS's that are made with the best possible physics and the best possible agreement with available experimental data-given realistic time constraints. [...] Other features of various EOS's in the SESAME Library include treatments of shock data, incorporation of various phase transitions (including Maxwell constructions or van der Waals' loops for first-order phase transitions), modeling of foams or porous materials, and calculation of dilute gas mixtures." [116]. Experimental methods were developed at Los Alamos hand in hand with the theoretical work (see e.g. [117]).

Another wide-range equation of state has been developed around Aleksey V. Bushman, Vladimir E. Fortov, Igor' V. Lomonosov¹⁴¹ et al. Their work is based on a semiempirical approach defining the success of the models firstly by comparison with how well these models fit the different types of experimental data, secondly by covering the largest possible range in phase space and thirdly, whether the models allow for extrapolation calculations [118]: in regions in which neither theories have been developed nor experiments have been performed, hypotheses can be developed. These hypothetical models can lead to unexpected new phase states or other material properties which call for new experimental studies and vice versa. The developments by and around A. V. Bushman, V. E. Fortov, I. V. Lomonosov are manifold, covering a wide range of materials and enhancements for different regions of their models throughout the years (see fig. 3.21 on p. 65 for a recent example of a copper EOS). The following publications serve as a glimpse at the efforts undertaken: in [119] a semiempirical quasiharmonical equation of state for 27 metals – covering a phase space with normalized densities (ρ/ρ_0) from 0.03 to 100 and temperatures

time. Therefore, tabulated EOS' are preferred (see e.g. [112]).

¹⁴⁰ [116] lists the following examples: Thomas-Fermi-Dirac theory for thermal electronic contributions to the EOS; INFERNO model for an atom embedded in an electron gas at finite temperature, electron-band structure models, including augmented plane-wave, LMTO, KKR, and Gaussian orbital approaches; Saha model for ionization equilibrium (see e.g. [87], chapt. 7); Einstein, Debye, Cowan, Chart-D and generalized Chart-D models for lattice vibrations in solids; hard-sphere perturbation approaches for fluids; and rigid-rotator and harmonic-oscillator methods for molecular rotational and vibrational terms; molecular-dynamics (MD) computer simulations of metals, of rigid diatomic and triatomic molecules, and of nonrigid diatomic molecules, including pseudo-potentials and melting in metals, glasses and as well as solid-solid transitions;

as more empirical models are stated: virial expansions; analytic fits of data to various intermolecular potentials, including Lennard Jones (6,12), Buckingham (exp-6), and modified Morse potentials; multi-parameter functional fits of data; Mie-Mie-Grüneisen equation of state.

¹⁴¹ In alphabetical order.

from 0 to 10^6 Kelvin – has been presented in comparison to static and dynamic experiments. [120] shows the development strategy of an EOS for copper including a wide range of measurements.¹⁴² In [122] the emphasis lies on high pressure melting and evaporating, including direct temperature measurements to establish pressure-temperature phase diagrams as well as indirect information on phase transitions gathered from shock wave experiments. In [77], an online database is presented for data including shock wave and isobaric expansion experiments as well as measurements of sound velocities that can be compared with equation-of-state calculations. [123] concentrates on the simulations along the development of the EOS and already includes some modeling of yield and strength effects as well as failure modeling. In two more recent papers new experimental data, which is irregularly distributed in the phase space, was used to develop multi-phase EOS' for aluminum ([124]) and iron ([91]). The existing simulation package called "BIG2"¹⁴³ has also been used to calculate the dynamic response of solid material blocks in studies concerning the accelerator complex at CERN by Naeem Tahir et al., for example the $450 \text{ GeV}/c$ protons of the Super Proton Synchrotron (SPS) impinging on copper and tungsten targets [126] as well as the nominal $7 \text{ TeV}/c$ proton beam of the Large Hadron Collider (LHC) impacting on copper [127] and graphite [128].

¹⁴² The report [121] summarizes how tabular data can be generated from the analytical wide-range EOS.

¹⁴³ "BIG2" is a two-dimensional hydrocode ([125]) that includes the equation of state database generated by A. V. Bushman, V. E. Fortov, I. V. Lomonosov et al.

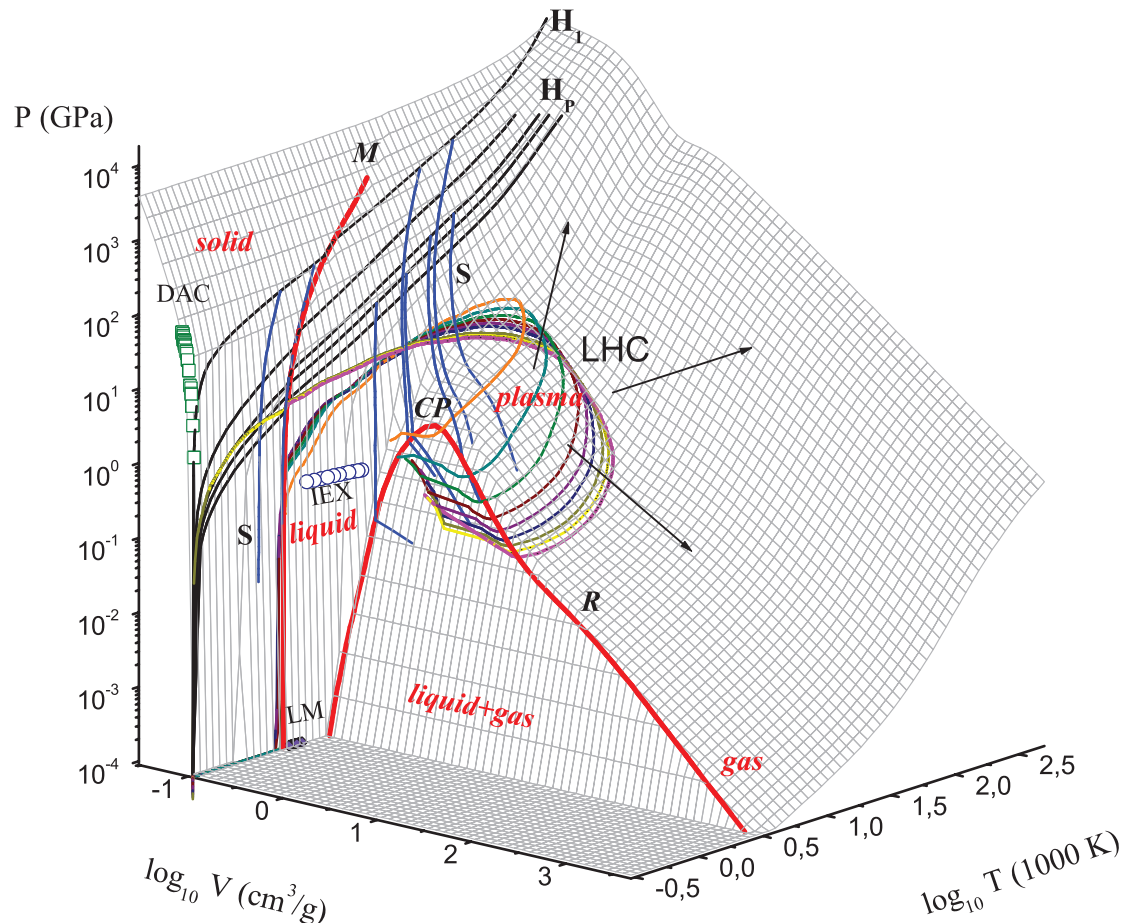


Figure 3.21: Three-dimensional pressure-volume-temperature surface for copper:
 M ... melting region; R ... evaporating region with the critical point(CP); physical states: *solid*, *liquid*, *gas*, *liquid + gas*, and *plasma* (arrows indicate the decrease in plasma non-ideality parameter); H_1 , H_p ... principal and porous Hugoniots; S ... release isentropes of shock-compressed metal; *IEX* ... isobaric expansion ("exploding wires") data; *DAC* ... static compression in diamond anvil cells; *LM* ... density of liquid metal at room pressure; states generated in copper by the LHC beam covering strongly coupled plasma region: *LHC*. Fig. 12 from [127], with slightly modified original figure caption. Used with kind permission of N. Tahir and American Physical Society.

Chapter 4

Experimental Investigation

4.1 Surface Velocity Measurements of Collimator Jaw Exposed to Proton Beams¹

4.1.1 Motivation

As described in [130], the Large Hadron Collider (LHC) secondary collimator (TCS) is designed to withstand a worst-case injection failure scenario: a full Super Proton Synchrotron (SPS) batch dumped on a collimator consisting of 288 bunches (with a nominal bunch intensity at top energy larger than $1.15 \cdot 10^{11}$ protons [131]) at 450 GeV (which corresponds to a total kinetic energy of approximately 2.4 MJ). A collimator test was carried out in 2004 in TT40 to verify the robustness of the jaw design, where the LHC high intensity beam ($3.2 \cdot 10^{13}$ protons) was extracted onto a collimator prototype installed in TT40 nearby the TT40 external beam absorber for injection (TED). The copper support of the C-C jaw exhibited a permanent deformation of approximately $300\text{ }\mu\text{m}$ (required surface flatness is $40\text{ }\mu\text{m}$) ([132], [133]). A stronger Cu alloy material (Glidcop[®]) was selected and a collimator robustness test was repeated in November 2006. The priorities of this test were ([134]):

1. Repetition of 2004 robustness jaw tests at high intensity for the worst-case injection failure scenario case in order to validate the new jaw design where the support is made of Glidcop[®] instead of copper.
2. Determination of the maximum temporary transverse displacement of the jaw during and after the beam impact.
3. Investigation of the utilization of accelerometers and microphones for impact detection in the LHC.

The injection error at 450 GeV on LHC secondary collimator was simulated via Finite Element Method ([133]): the energy deposition due to beam impact was calculated with FLUKA and the energy distribution was used as input for the thermo-structural analysis. Both temperature distribution and structural response to this beam load have

¹ Based on [129] – Draft in discussion.

been calculated and simulation results are in good agreement with LDV experimental measurements ([135] and [136]). The principle of using microphones and accelerometers for the localization of high energy beam impacts on the LHC collimators was demonstrated ([137]). The acronyms and abbreviations throughout section 4.1 are summarized in tab. 4.1. This section concentrates on the outcome of the measurement of the transverse surface velocity measurements with a Laser Doppler Vibrometer (LDV).

Table 4.1: Acronyms and abbreviations of section 4.1

Acronym or abbreviation	Full name
FFT	Fast Fourier Transform
FWHM	Full Width at Half Maximum
LDV	Laser Doppler Vibrometer
LHC	Large Hadron Collider
SPS	Super Proton Synchrotron
TCS	LHC secondary collimator
TED	Beam Absorber for Injection, External
TT40	Transfer Tunnel between SPS and CNGS

4.1.2 Experimental Background

This section contains both the relevant information on the experimental setup related to the measurement with the LDV, and the simulated energy deposition.

4.1.2.1 Collimator Setup

The collimator had to be changed to meet the requirements of the LDV measurement device. Only one of the two jaws was used to allow the recording of the transversal (out-of-plane) surface velocities of the jaw. As a consequence the collimator tank had to be equipped with four windows (see fig. 4.1 on p. 69). In addition a retro-reflecting tape was applied to the surface in order to enhance the signal quality of the reflected laser beam due to the long measurement distance (see section 4.1.2.2). These pieces of tape were placed off the proton beam axis to avoid direct interaction with the incident proton beam (see tab. 4.2 on p. 69 and fig. 4.2 on p. 70). One of these measurement points (namely window #2) was omitted and newly defined outside the collimator tank at a strap connected to the collimator jaw [138] (see tab. 4.3 on p. 69 and fig. 4.3 on p. 71) to be compared with the accelerometers. Priority was given to measurement points #1 and #3, as #1 and #3 would be representative for a small and large jaw displacement, respectively (simulation from [139]).

4.1.2.2 Laser Doppler Vibrometer Setup

The LDV sensor head was placed 18 m upstream from the collimator position behind a shielding of iron and concrete blocks to protect the device from radiation damage (see fig. 4.4 on p. 72). The probing laser beam had to be deflected via two surface coated mirrors

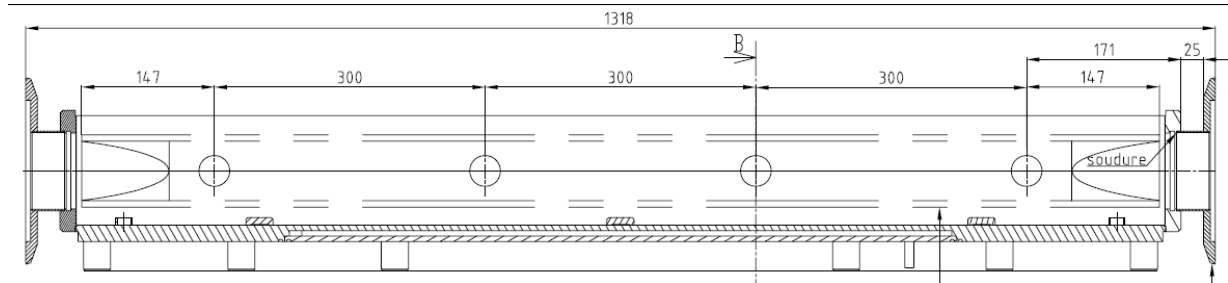


Figure 4.1: Vertical cut in proton beam direction through the collimator tank used for the tests in TT40 in November 2006. The proton beam from the SPS arrives from the right. Windows are numbered downstream from the upstream face, starting at 147 mm (counted from the upstream face of the collimator jaw itself). The collimator tank installed for the TT40 test was turned upside down (figure from [140]).

Table 4.2: Positions of the retro-reflecting tape on the collimator jaw for every window in the collimator tank. The distances are counted from the side facing upstream to the beam. Priority was given to the measurement points behind window 1 and 3.

Window number	Distance of center of tape along proton beam axis [mm]	Vertical distance of lower edge of tape from central axis of collimator jaw [mm]
1	147	2
2	447	10
3	747	2
4	1047	10

Table 4.3: Positions of measurement points on the collimator as assigned during the TT40 test.

Measurement point	Location
#1	through window #1
#2	outside collimator tank – connected to jaw
#3	through window #3
#4	through window #4

**Laser spot on c-c jaw through quartz window
(view in beam direction)**

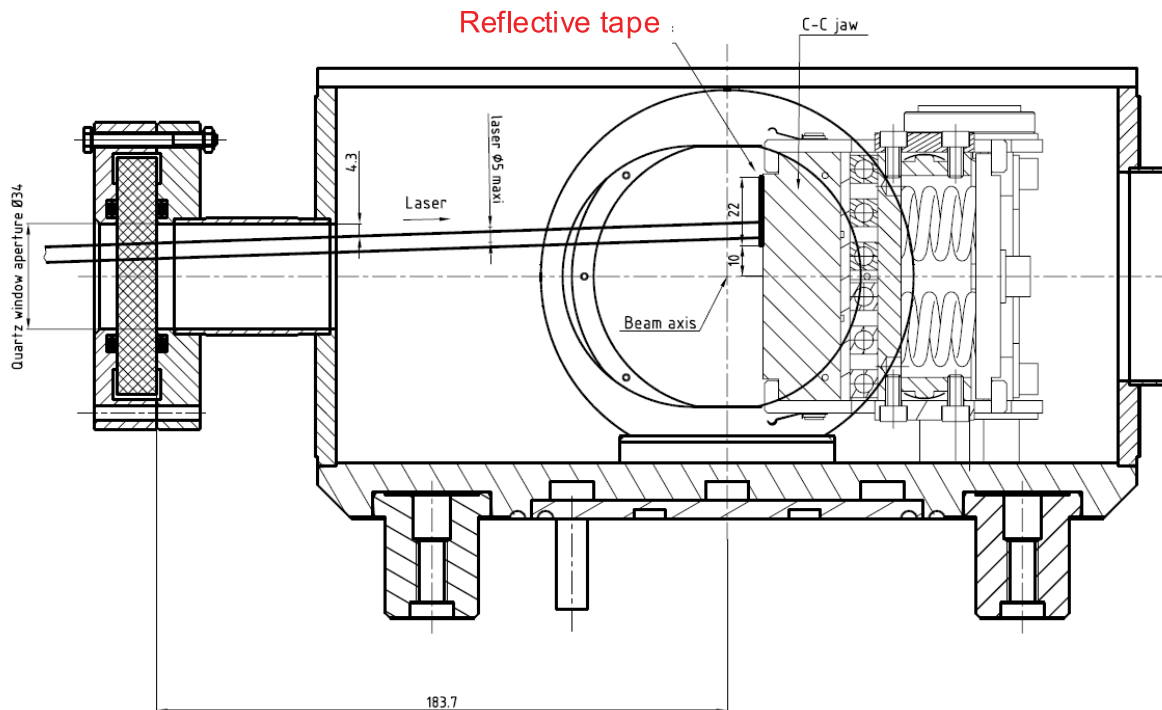


Figure 4.2: Vertical cut orthogonal to proton beam direction through the collimator tank used for the tests in TT40 in November 2006 (modified figure from [141]). The retro-reflective tapes (in this figure called "reflective tape") were placed behind the quartz windows on the jaw surface either 2 or 10 mm (in this figure 10 mm) above the central axis of the collimator jaw. The collimator tank installed for the TT40 test was turned upside down. The positioning of the C-C collimator jaw is controlled by stepper motors. For this picture the beam axis center is assumed to lie outside the collimator jaw (corresponding to a negative beam impact parameter).

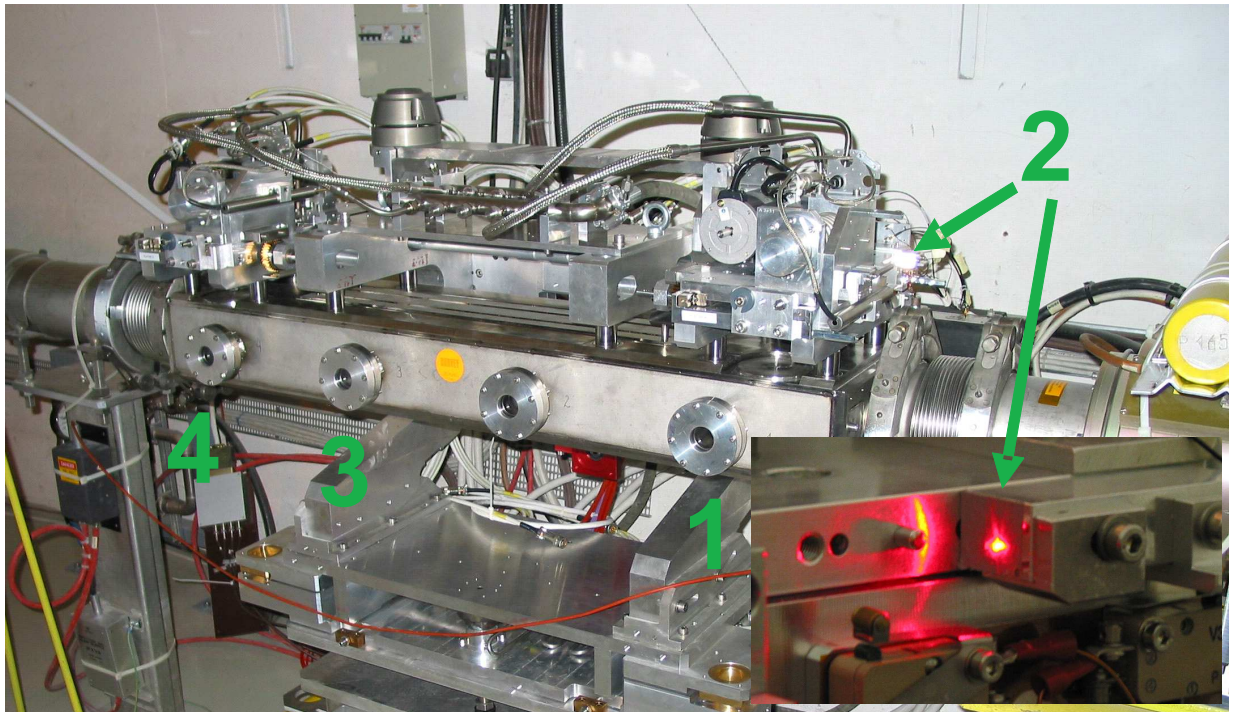


Figure 4.3: Installed collimator tank for the TT40 test in November 2007 with marked measurement point positions. The proton beam comes from the right. (Pictures courtesy Roman Wilfinger [142])

through the window of the collimator tank onto the measurement point. The LDV sensor head was built on a vertically movable platform with a step motor. The first mirror (0) could be rotated around its vertical axis with a step motor and was positioned in front of the shielding hut. For every measurement point a fixed mirror (1, 2, 3, 4) was placed in front, onto which the rotating mirror could divert the laser beam (see fig. 4.5 on p. 72). The error on the displacement measurement with the LDV lies in the order of picometers ([143], [144]). A detailed description of the LDV measurement principle and LDV sensor head can be found at [143].

4.1.2.3 Proton Beam Parameters and Energy Deposition

The 450 GeV proton beam from the SPS was steered onto the collimator with (see also tab. 4.4 on p. 74):

- Different proton beam intensities:
 - $4.8 \cdot 10^{12}$ (1 batch)
 - $9.6 \cdot 10^{12}$ (2 batches)
 - $19.2 \cdot 10^{12}$ (4 batches)
 - $28.8 \cdot 10^{12}$ (6 batches)
- Different proton beam impact parameters (distance of the beam center with respect to collimator jaw surface; defined as positive for the case of the beam center lying inside the collimator jaw):

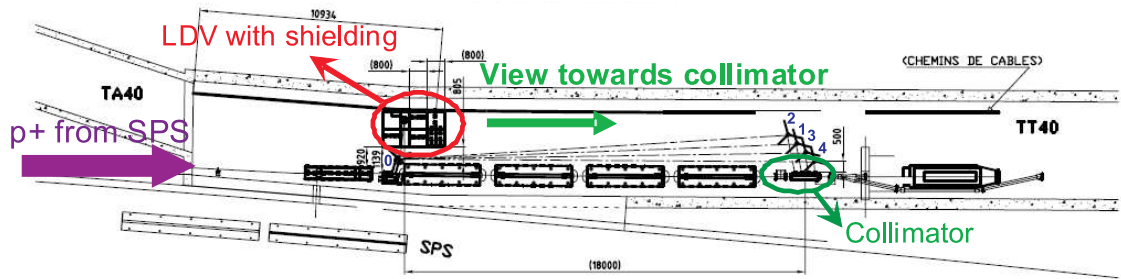


Figure 4.4: Layout of the experimental setup for the experiment in November 2006: The LDV sensor head is positioned in a shielding hut 18 m upstream of the collimator while the laser beam itself is steered towards the jaw surface via a rotating mirror (number 0) – in front of the shielding hut – towards the fixed mounted mirrors (one for every measurement point: number 1 – 4) in front of the collimator (modified figure from [145]).



Figure 4.5: Picture of the fixed mirrors in front of the collimator (on the right side). In the back the paper wall for aiming the laser beam with the help of webcams onto the correct measurement point can be seen. One can see that the mirror for the measurement point #2 was not in line with those for measurements #1, #3 and #4. Wilfinger (Picture courtesy Roman Wilfinger [142])

- +5 mm
- +4 mm
- +3 mm
- +2 mm
- +1 mm
- 0 mm
- -1 mm
- -2 mm

During the collimator test in November 2006 the total batch length was about $8 \mu s$ and one batch consisted of 48 bunches with roughly $1 \cdot 10^{11}$ protons each [147]. The batches were separated by 200 ($= 8 \cdot 25$) ns. The bunch spacing was 25 ns [148]. The transverse horizontal and vertical FWHM beam sizes were measured to be 1 mm [149]. The energy deposition in the collimator jaw was calculated by means of the Monte-Carlo code FLUKA ([1], [2]). In figures 4.6 on p. 75, 4.7 on p. 76 and 4.8 on p. 77 the energy deposition for the beam impact at +5 mm is shown. The maximum values for the energy deposition are summarized in tab. 4.5 on p. 75. One GeV is $1.602 \cdot 10^{-10} J$, therefore 1 GeV/cm^3 is $7.121 \cdot 10^{-11} \text{ J/g}$ assuming a density of graphite of 2.25 g/cm^3 ([150]). In fig. 4.9 (left) on p. 78 one can see that for these values the maximum reached temperature in the collimator jaw was expected to be about $300^\circ C$.

4.1.3 Measurement Results

4.1.3.1 Data Handling

In this section the measured surface velocities of the collimator jaw along with the numerically calculated displacements (algorithm template provided by [154]) are presented. In [143] (chapter 7, p. 176) the choice of the numerical integration method is explained:

"Different integration formulas (Gauss trapezium algorithm, Kepler formula, Simpson algorithm of different orders) are possible. The Kepler formula, which is implemented in the many commercial mathematic software-packages was used to calculate the displacement signal. This algorithm is also recommended by the producer of the LDV and the error between the measured and calculated signal is less than 10 pm."

The displacement signal in [154] is calculated as

$$d_i = \frac{t_{i+1} - t_{i-1}}{6} \frac{v_{i-1} + 4v_i + v_{i+1}}{2} + d_{i-1} \quad (4.1)$$

with d as the displacement, v as the recorded velocity, t as the time stamp, i as the index of the current calculation step, and $i-1$ and $i+1$ as the indices of the previous and following calculation step.

Two different issues had to be addressed in the course of this analysis:

1. Some calibration factors of the velocity range were not logged automatically.

Table 4.4: Extract of the two logbooks by the collimator team [146] and the LDV team. The LDV was recording the surface velocities with different sample frequencies. The total number of samples was limited to 32 768 ($= 2^{15}$), hence an increase of the LDV sample frequency results in a shorter LDV recording time. Abbreviations (see section 4.1.3.1 starting on p. 73 for more details): (a) = arbitrarily chosen (could not be reobtained), (l) = logged, (r) = reobtained, (r,a) = only partly reobtained (see section 4.1.3.2.4 starting on p. 86).

Extraction No. CCC	Measurement No. LDV	Total number of protons [$\cdot 10^{12}$]	Number of batches	Proton beam impact parameter [mm]	Measurement point number	Calibration factor [mm/s/V]	LDV sample frequency [MHz]	LDV recording time [ms]
2	14	4.8	1	5	3	1000 (l)	1.024	32
4	15	9.6	2	5	3	1000 (l)	0.256	128
5	16	19.2	4	5	3	1000 (l)	5.12	6.4
7	18	28.8	6	5	3	1000 (l)	5.12	6.4
8	19	28.8	6	4	3	1000 (l)	5.12	6.4
9	20	28.8	6	3	3	1000 (l)	51.2	0.64
10	21	28.8	6	2	3	1000 (l)	25.6	1.28
11	22	28.8	6	1	3	1000 (l)	25.6	1.28
12	23	28.8	6	0	3	1000 (l)	25.6	1.28
13	24	28.8	6	-1	3	1000 (l)	25.6	1.28
14	25	28.8	6	-2	3	– (a)	25.6	1.28
17	27	4.8	1	4	3	125 (l)	25.6	1.28
18	28	4.8	1	4	3	1000 (l)	0.1024	320
19	29	4.8	1	4	3	125 (l)	2.56	12.8
20	30	4.8	1	4	3	125 (l)	5.12	6.4
21	31	4.8	1	4	4	125 (l)	5.12	6.4
22	32	4.8	1	4	4	1000 (l)	5.12	6.4
23	33	4.8	1	4	4	1000 (r)	25.6	1.28
24	34	4.8	1	4	4	125 (r)	25.6	1.28
25	35	4.8	1	4	1	1000 (a)	25.6	1.28
26	36	4.8	1	4	1	1000 (a)	5.12	6.4
27	37	4.8	1	4	1	1000 (a)	1.024	32
28	38	4.8	1	4	1	1000 (a)	0.256	128
29	39	4.8	1	4	2	125 (r,a)	0.256	128
31	40	4.8	1	4	2	125 (r,a)	25.6	1.28
33	41	4.8	1	4	2	125 (r,a)	10.24	3.2
34	42	4.8	1	4	2	25 (r,a)	5.12	6.4

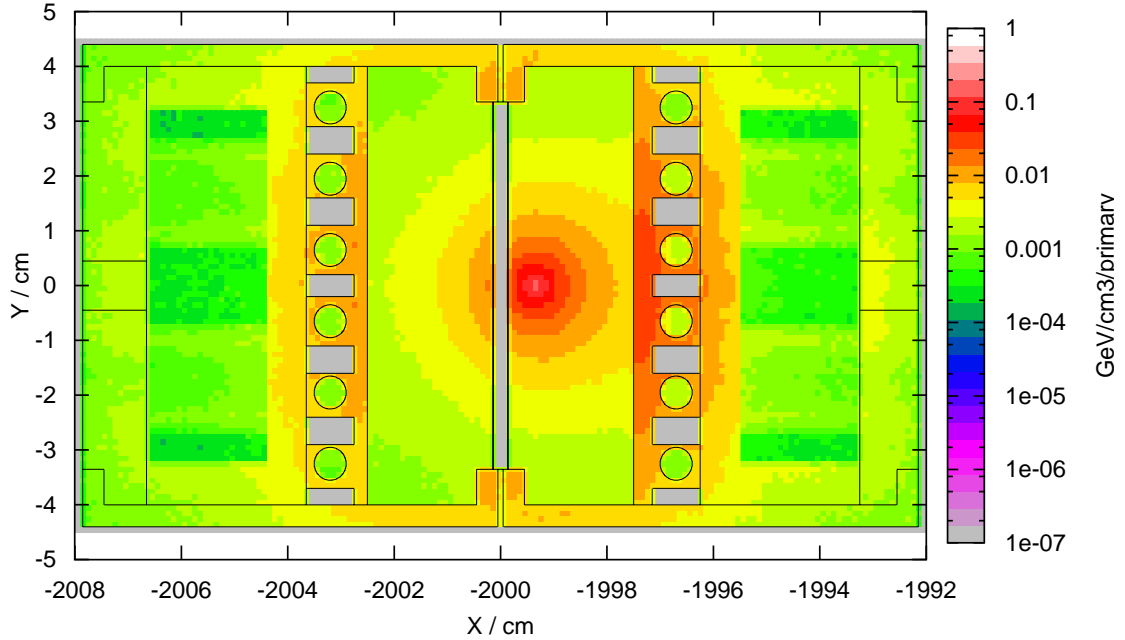


Figure 4.6: Calculated energy deposition of collimator jaw in $\frac{GeV}{cm^3}$ per incident primary proton for proton beam impact parameter $+5\text{ mm}$. Incident proton beam axis is z -direction. Provided by [151]). The mesh size was 1 mm for both x - and y -direction and 10 mm for z . Cross section in the x - y -plane at 85 cm with averaged values between 80 and 90 cm downstream from frontal face. Center of the collimator geometry: $x = -2000\text{ cm}$, $y = 0\text{ cm}$.

Table 4.5: Maximum values of simulated energy deposition for the collimator jaw C-C composite and copper (Glidcop[®]) support plate by FLUKA (provided by [151]). The coordinates of the maxima given are the same as in figures 4.6, 4.7 on p. 76 and 4.8 on p. 77. The mesh size was 1 mm for both x - and y -direction and 10 mm for z .

Component	$\frac{dE}{dx}_{max}$ [$\frac{GeV}{cm^3}$] per primary	Absolute statistical error [$-$]	Coordinates [cm]		
			x	y	z
Carbon	0.128	0.0214	-1999.35	0.05	4073.5
Copper	0.057	0.086	-1997.45	-0.15	4110.5

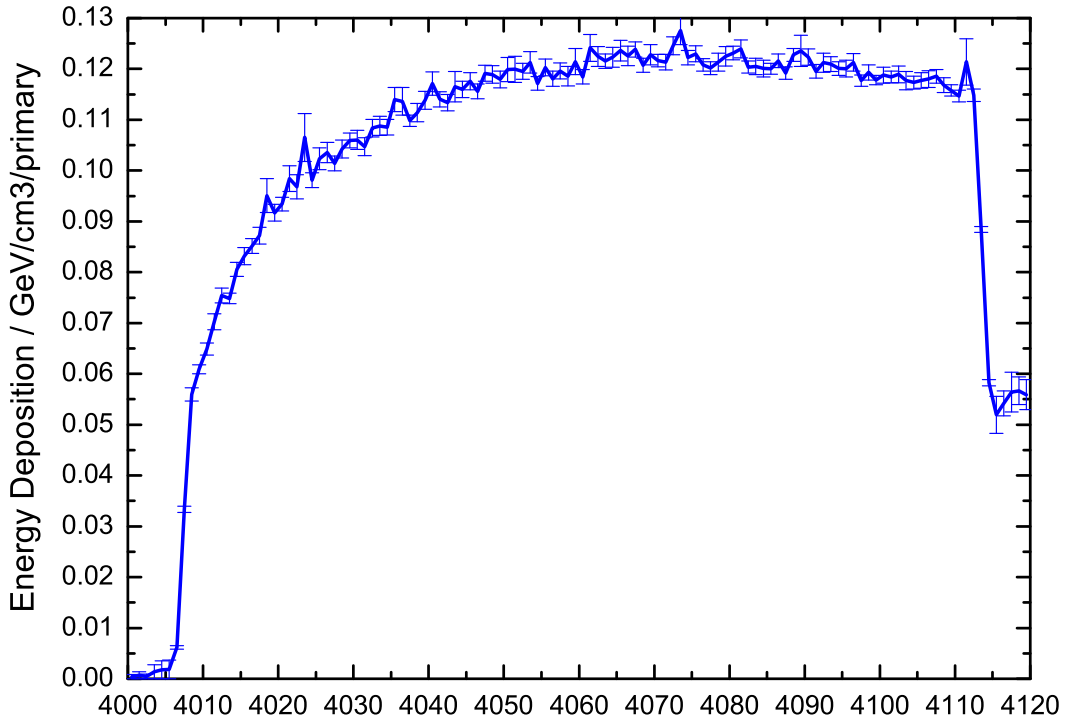


Figure 4.7: Calculated energy deposition of collimator jaw in $\frac{GeV}{cm^3}$ per incident primary proton for proton beam impact parameter $+5\text{ mm}$. Incident proton beam axis is z -direction. Provided by [151]). The mesh size was 1 mm for both x - and y -direction and 10 mm for z . Along z -axis (collimator front face starts at 4000 cm) representing the maximum energy deposition values within the jaw ($x = 5\text{ mm}$ and $y = 0\text{ mm}$). The drop in energy deposition at 4110 cm at the end of the collimator is due to its tapering.

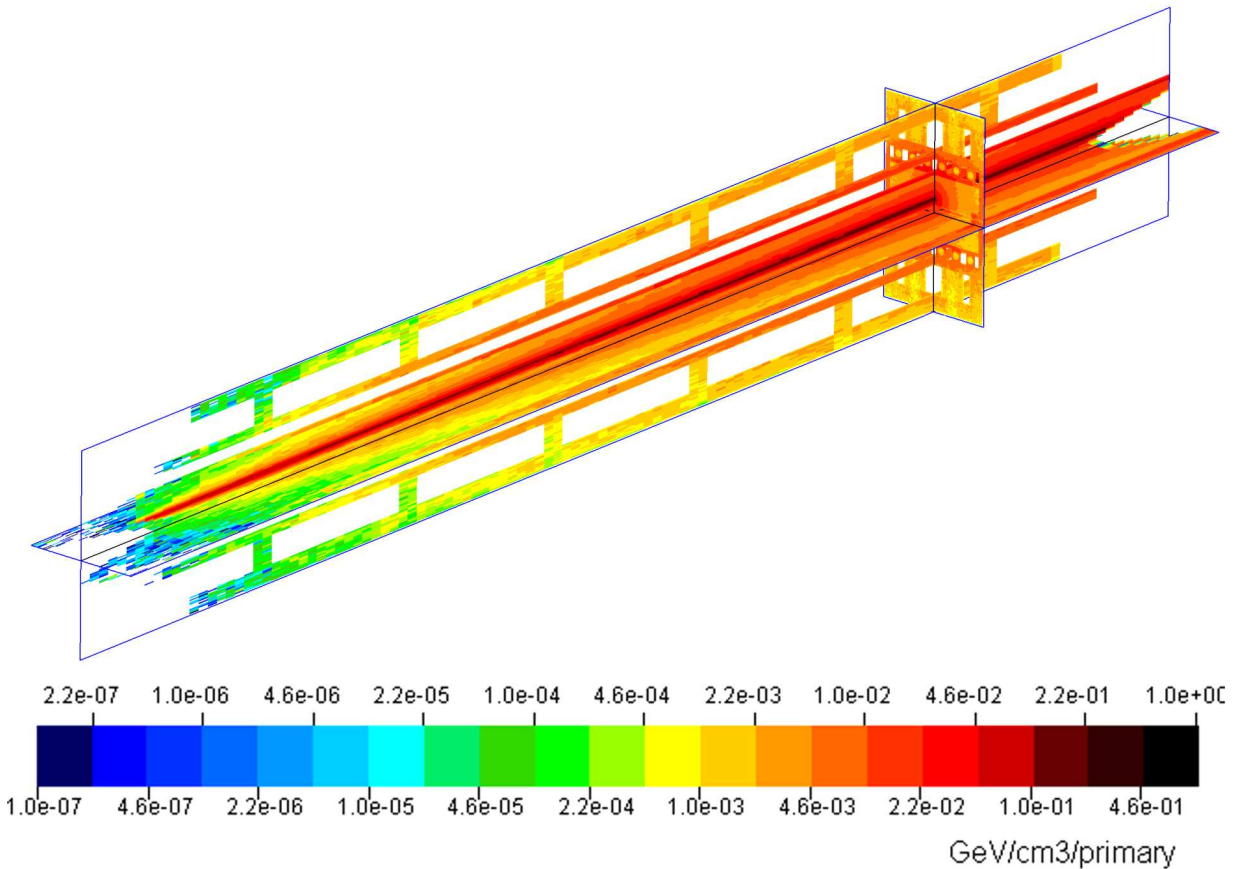


Figure 4.8: Calculated energy deposition of collimator jaw in $\frac{GeV}{cm^3}$ per incident primary proton for proton beam impact parameter +5 mm. Incident proton beam axis is z -direction. Two intersecting planes along z -axis ($z = 0$ mm) for $x = 0$ mm and $y = 0$ mm. The intersecting plane in x - y -plane at $z = 85$ cm is the same as in fig. 4.6 on p. 75 (provided by [151], using "SimpleGeo" [152]). The plot is rotated around the z -axis by 90° in order to show the region of maximum energy deposition in the x - z -plane undistorted. The mesh size was 1 mm for both x - and y -direction and 10 mm for z .

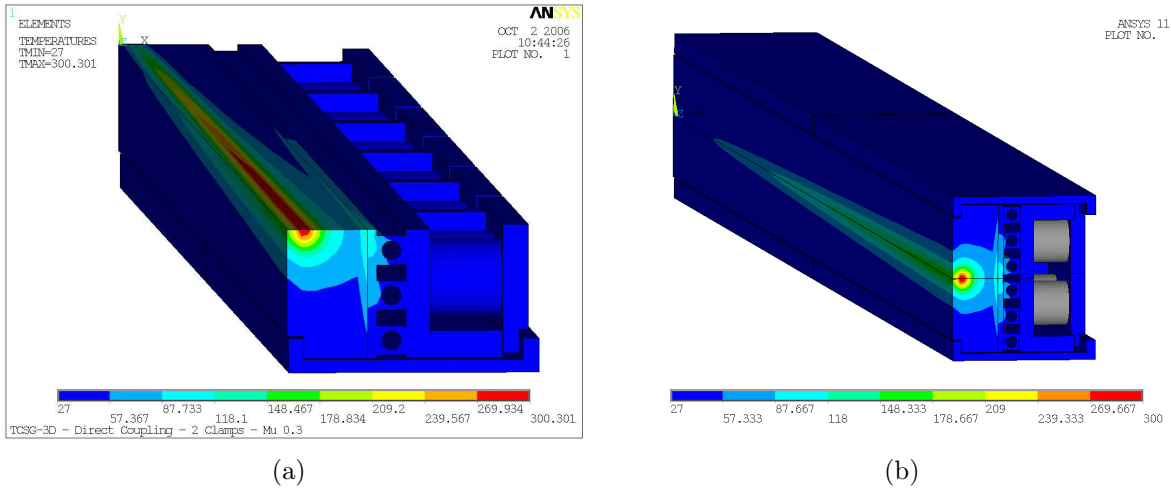


Figure 4.9: 3D temperature plots calculated at $7.2 \mu\text{s}$ of collimator movement ($32 \cdot 10^{12}$ protons, beam impact $+5 \text{ mm}$) for one collimator jaw (provided by [153]) by thermal analysis of the simulated energy deposition calculated with FLUKA. The values for the specific heat capacity for Glidcop® have been provided by the supplier and the values for the C-C composite have been measured. This model leaves out the first and last 10 cm of the collimator and therefore does not contain the tapered region of the collimator jaw. The mesh size in x and y was 1.5 to 2 mm , in z 5 to 10 mm .

2. A few of the surface velocity signals were overlaid with so-called "speckle dropouts".

The maximum LDV controller output is $\pm 10 \text{ V}$. The measurement range can be adjusted to four different maximum velocity ranges: 10 m/s , 1.25 m/s , 250 mm/s and 50 mm/s (which correspond to the four calibration factors of 1000 mm/s/V , 125 mm/s/V , 25 mm/s/V and 5 mm/s/V).

The calibration factor can be reobtained by comparing the recorded surface velocity values of an unknown calibration factor with those of a known calibration factor. These four different ranges can be combined in six possible ratios to help retrieve the unknown calibration factor (see tab. 4.6).

Table 4.6: Summary of possible ratios for the velocity ranges of the LDV and their corresponding calibration factors.

Ratio	Applicable calibration factors
$1 : 1$	$1000/1000, 125/125, 25/25, 5/5$
$1 : 5$	$125/25, 5/25$
$1 : 8$	$125/1000$
$1 : 25$	$5/125$
$1 : 40$	$25/1000$
$1 : 200$	$5/1000$

Summarizing [143] (chapter 6.9, p. 157 ff), "speckle dropouts" are spikes in the signal of the LDV that appear due to the vertical (in-plane) movement of the speckle pattern of

the coherent laser light being reflected from the retro-reflecting tape glued to the examined surface. In [144] it is stated that:

"A speckle dropout occurs when the intensity of the reflected laser light in the aperture of the LDV sensor head is too low. One reason for this effect is the long distance between the surface under investigation and the LDV sensor head. The distance between two bright speckle spots increases with the aforementioned distance and reaches a value where it is bigger than the aperture dimension of the LDV sensor head. This was the case in the mentioned setup with 18 m distance between the LDV sensor head and the collimator jaw surface. Therefore, the total speckle pattern was able to move with the surface of the collimator jaw in vertical direction. If the collimator jaw movement was more than 50 μm (average size of the glass balls in the retro-reflecting tape), then a speckle dropout occurred."

The change in intensity of the speckle pattern due to this vertical movement could then be misrepresented as movement in the direction of the probing laser beam.

Since "speckle dropouts" have a larger amplitude than the signal for out of plane oscillations, they can be identified by velocity values that are multiples of their neighboring velocity values. In this chapter, these velocity values were replaced by the average of the left and right neighbors. This simple averaging procedure is not capable of separating the surface velocity in beam direction from the overlapping speckle dropout.

When either a missing calibration factor or speckle dropouts had to be addressed during the analysis of the data, it is referred to within the appropriate section.

In parallel to the surface velocity-time signal, the recording of the FFT was requested by the collimator design team in order to use them for modal analysis. This demand limited the available recording times. However, it has to be stated that with hindsight, longer recording times would have been preferable for the work covered in this chapter.

4.1.3.2 Reproducibility Test

Measurements with the same intensity ($4.8 \cdot 10^{12}$ protons) and the same beam impact parameter on the collimator jaw (+4 mm) were used to confirm the reproducibility of the experimental conditions with the data recorded by the LDV in this section. For each of the four measurement points, four velocity-time-signals have been recorded. Measurements for each measurement point have been sampled with different sample frequencies. The presented sequence of the measurement points was chosen by complexity of the data handling, starting with the simplest (logged calibration factors and no speckle dropouts).

4.1.3.2.1 Measurement Point #3

At measurement point #3 the recording times cover values from 1.28 ms (Measurement #27) to 320 ms (Measurement #28) (see tab. 4.7 on p. 80). The calibration factors for all these four measurements have been logged.

In fig. 4.10 on p. 81 the similarity of the velocity signals for measurement #27, #29 and #30 can be seen qualitatively. However measurement #28 – which was recorded with a sample frequency lower than the other three measurements (see tab. 4.7 on 80) – clearly could not resolve the high frequency response of the vibrating collimator jaw.

Table 4.7: Entries of logbook for measurement point #3, a beam impact parameter on the collimator jaw of $+4\text{ mm}$ and an intensity of $4.8 \cdot 10^{12}$ protons (1 batch). Abbreviation: l = logged.

Extraction No.	Measurement No. CCC	Measurement No. LDV	Calibration factor [mm/s/V]	Sample frequency [MHz]	Recording time [ms]
17		27	125 (l)	25.6	1.28
18		28	1000 (l)	0.1024	320
19		29	125 (l)	2.56	12.8
20		30	125 (l)	5.12	6.4

Hence the surface velocity amplitudes do not reach the same peak velocities as the other measurements.

In fig. 4.11(a) on p. 81 one can see that the values of the numerically obtained surface displacement show a similar behaviour. In order to quantify the reproducibility of the experimental conditions, one can compare the calculated displacements for the first response (around $47\text{ }\mu\text{s}$) of the three measurements with the high sample frequencies (measurement #27, #29 and #30). Comparing these values to the measurement with the highest sample frequency (measurement #27) results in a difference of less than 4% (see tab. 4.8). Measurement #28 was left out since the first maximum (= first response) was shifted in time ($\approx 10\text{ }\mu\text{s}$) from the others due the coarse setting of the point of origin, related to its low sample frequency. An estimate of the reproducibility of the overall experimental setup as done later in section 4.1.3.2.2 starting on p. 82 cannot be made since the measurements for measurement point #3 were made with different sample frequencies.

Table 4.8: Calculated difference of measurements at measurement point #3, with beam impact parameter on collimator jaw of $+4\text{ mm}$ and beam intensity of $4.8 \cdot 10^{12}$ protons (1 batch) for first response of three measurements with high sample frequency.

Measurement No. LDV	Sample frequency [MHz]	Displacement first response [m]	At time [s]	Fraction of m. #27 [%]	Difference to m. #27 [%]
27	25.6	$3.20 \cdot 10^{-6}$	$4.74 \cdot 10^{-5}$	100.0	0.0
29	2.56	$3.08 \cdot 10^{-6}$	$4.73 \cdot 10^{-5}$	96.1	3.9
30	5.12	$3.13 \cdot 10^{-6}$	$4.77 \cdot 10^{-5}$	97.7	2.3

At 3.6 ms one can observe a difference in amplitude of about $3.5\text{ }\mu\text{m}$ (fig. 4.11(b)) on p. 81 which corresponds to a velocity of $9.7 \cdot 10^{-4}\text{ m/s}$ (which is less than 0.4% of the maximum recorded value – see fig. 4.10 on p. 81).

As seen in fig. 4.12 on p. 82, the displacement of the longest recording signal of all measurements for measurement #28 shows the maximum of $14\text{ }\mu\text{m}$ just towards the end of its recording time (at 278 ms). Between 20 and 150 ms the displacement oscillates around $2.5\text{ }\mu\text{m}$ with a time period of roughly 15 ms . An offset was expected from the previous simulations (see [139] and [135]). After 150 ms one can observe a transition from a clear

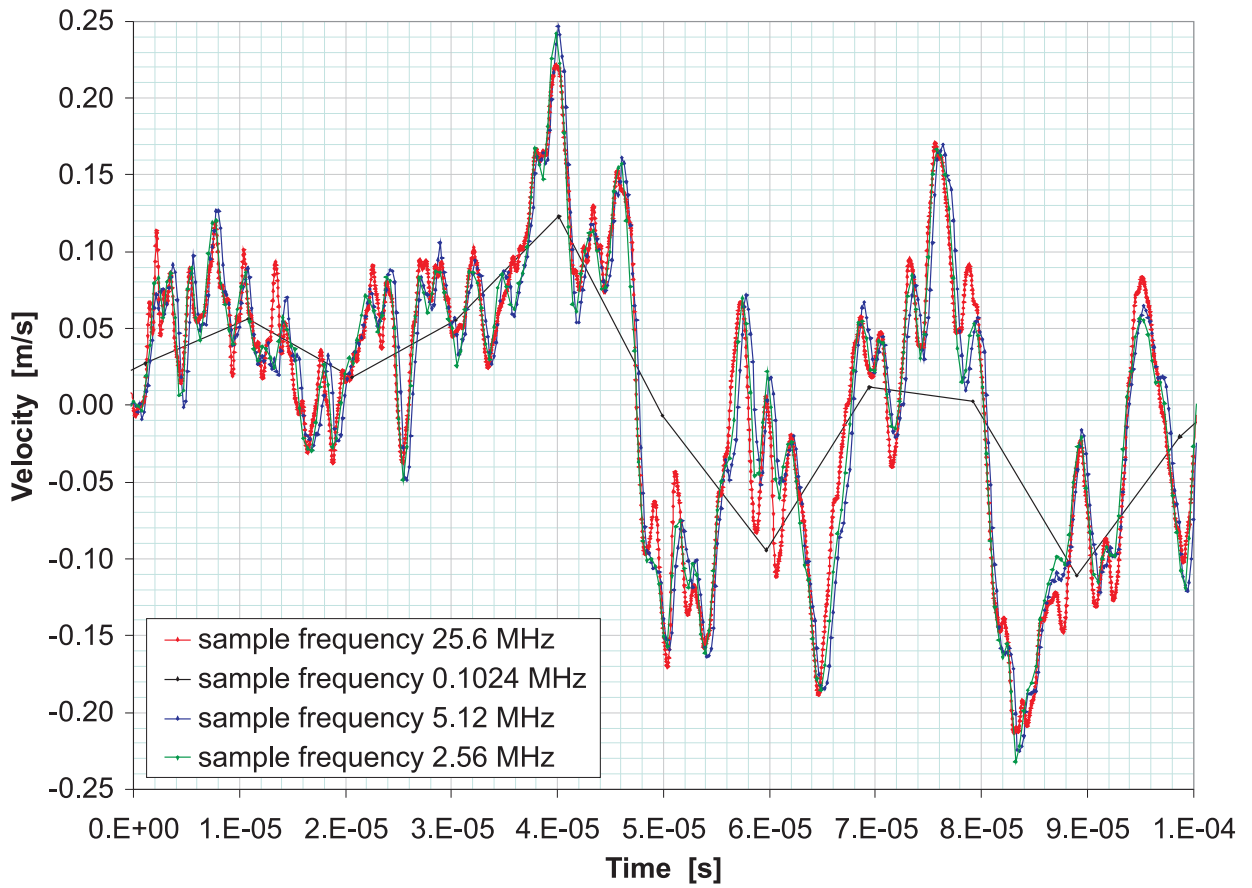
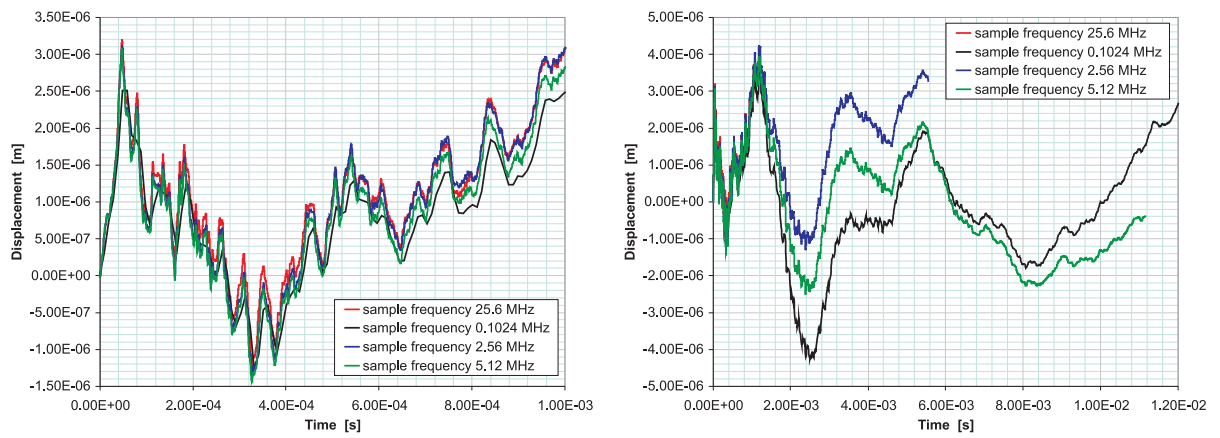


Figure 4.10: Plot of the measured surface velocity signals for measurements #27 (25.6 MHz sample frequency), #28 (0.1024 MHz), #29 (2.56 MHz), #30 (5.12 MHz) for reproducibility comparison within the first 100 μ s of collimator movement. Number of protons: $4.8 \cdot 10^{12}$ (1 batch), beam impact parameter: +4 mm, measurement point #3.



(a) The first ms of collimator movement.

(b) The first 12 ms of collimator movement.

Figure 4.11: Plots of the surface displacement for measurements #27 (25.6 MHz sample frequency), #28 (0.1024 MHz), #29 (2.56 MHz), #30 (5.12 MHz) for reproducibility comparison of collimator movement. Number of protons: $4.8 \cdot 10^{12}$ (1 batch), beam impact parameter: +4 mm, measurement point #3.

oscillation pattern to a less well defined displacement profile. The observed drift of the displacement beyond 150 ms corresponds to a velocity of around $73 \mu\text{m/s}$. Even though measurement #28 was recorded with the lowest sample frequency and cannot reach the same peak velocities as the measurements recorded with higher sample frequencies, it can be trusted to describe the long time oscillation pattern well.

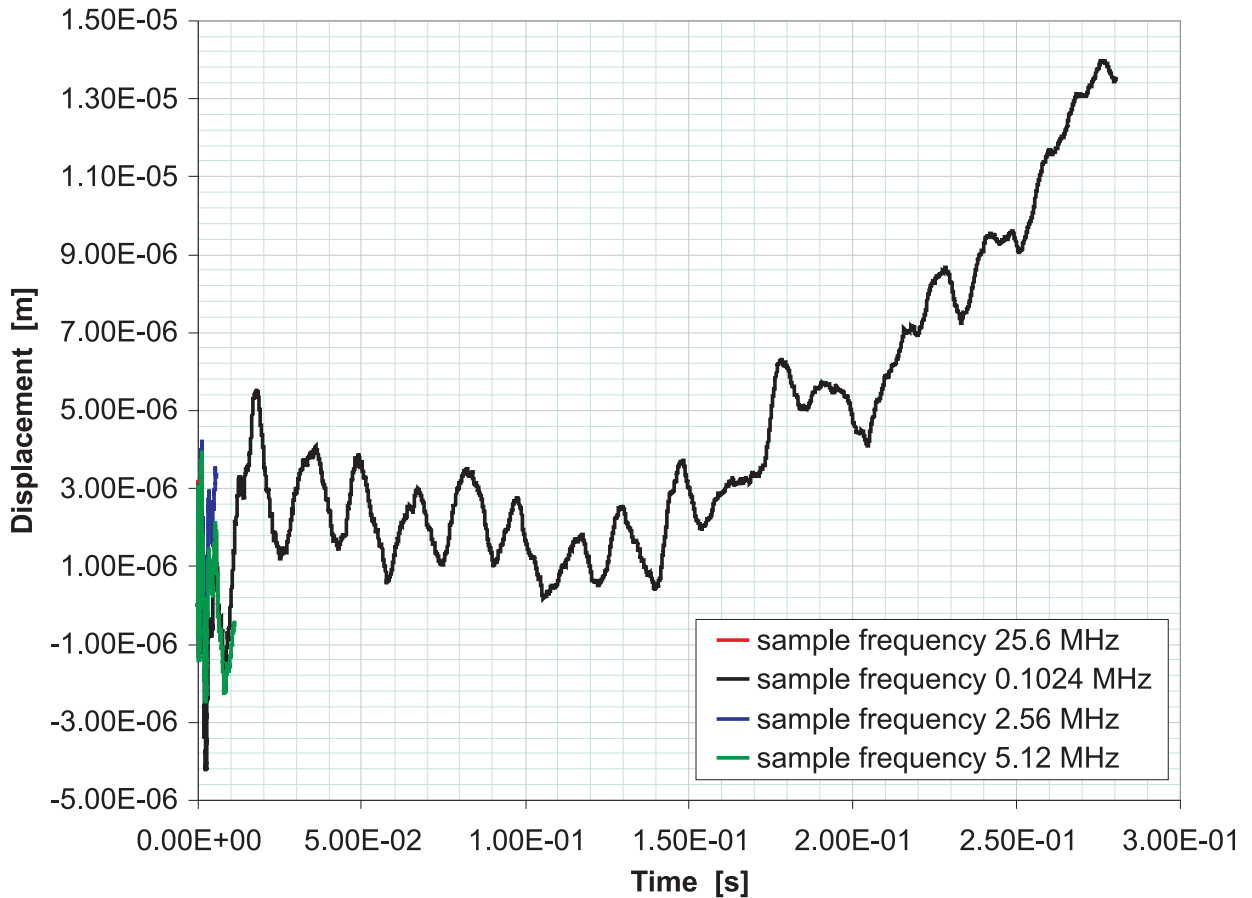


Figure 4.12: Plot of the surface displacement for measurements #27 (25.6 MHz sample frequency), #28 (0.1024 MHz), #29 (2.56 MHz), #30 (5.12 MHz) for reproducibility comparison of collimator movement for the first 300 ms. Number of protons: $4.8 \cdot 10^{12}$ (1 batch), beam impact parameter: +4 mm, measurement point #3.

4.1.3.2.2 Measurement Point #4

At measurement point #4 the recording times cover only two values 1.28 ms (Measurement #33 and #34) and 6.4 ms (Measurement #31 and #32) (see tab. 4.9 on p. 83). The calibration factors for measurements #31 and #32 have been logged, whereas the calibration factor for the measurements #33 and #34 could be reobtained via comparison of these known velocity amplitudes. In measurements #32 and #33 (low and high resolution) speckle dropouts were averaged out (see tab. 4.10 on p. 83).

In fig. 4.13 on p. 84 the similarity of the velocity signals for measurement #31, #32, #33 and #34 can be seen. The comparison of the surface velocities (and the numerically obtained displacement values) on the large time scale shows that the jaw response is the

Table 4.9: Entries of logbook for measurement point #4, a beam impact parameter on the collimator jaw of $+4\text{ mm}$ and an intensity of $4.8 \cdot 10^{12}$ protons (1 batch). Abbreviations: l = logged, r = reobtained.

Extraction No.	Measurement No. CCC	Calibration factor	Sample frequency	Recording time
	LDV	$[\text{mm}/\text{s}/\text{V}]$	$[\text{MHz}]$	$[\text{ms}]$
21	31	125 (l)	5.12	6.4
22	32	1000 (l)	5.12	6.4
23	33	1000 (r)	25.6	1.28
24	34	125 (r)	25.6	1.28

Table 4.10: List of removed speckle dropouts for measurement #32 and #33.

Measurement No.	LDV	Speckle dropout interval [s]
32		$0.3906 \cdot 10^{-6} - 1.7578 \cdot 10^{-6}$
32		$0.2046874 \cdot 10^{-3} - 0.2060546 \cdot 10^{-3}$
33		$0.7031 \cdot 10^{-6} - 2.0312 \cdot 10^{-6}$

same (see fig. 4.14 on p. 84); however there are small differences in the response pattern on the microsecond scale (see fig. 4.13) on p. 84). One should also note that the corrected velocity signal for measurement #33 might contain the tail of the removed speckle dropout around $2\text{ }\mu\text{s}$. These amplitudes – which are very likely to belong to this speckle dropout – were not removed as they were already in the range of the neighboring amplitudes. In fig. 4.14 on p. 84 one can observe that the displacement in measurement #32 after 0.2 ms is lower than the other three. In particular about $1.5\text{ }\mu\text{m}$ lower at 1 ms (see fig. 4.14(a) on p. 84) and about $3\text{ }\mu\text{m}$ lower at 2 ms (see fig. 4.14(b) on p. 84). One should keep in mind that a speckle dropout was averaged out at around 0.2 ms for measurement #32 (see tab. 4.10).

In order to quantify the reproducibility of the experimental conditions during the LDV measurement of the collimator response, one can calculate the difference of velocity ($v_1(t) - v_2(t)$) between the two sets of two measurements (v_1, v_2) that were recorded for the identical beam parameters and with the same time resolution (see tab. 4.11 on p. 85). One has to keep in mind that the velocity resolution was different for the two measurements in each set (see tab. 4.9). For this comparison a limited time interval (see tab. 4.11 on p. 85) was arbitrarily chosen with the following properties:

- Limiting time interval limited to times before complete damping of oscillation
- No speckle dropouts
- Interval as large as possible to allow good statistics

For this time interval, the difference between the first and second velocity was counted for 100 bins and led towards a distribution close to a Gaussian (see fig. 4.15 on p. 85). Hence the distribution was compared with a Gaussian approximation, μ chosen to be the

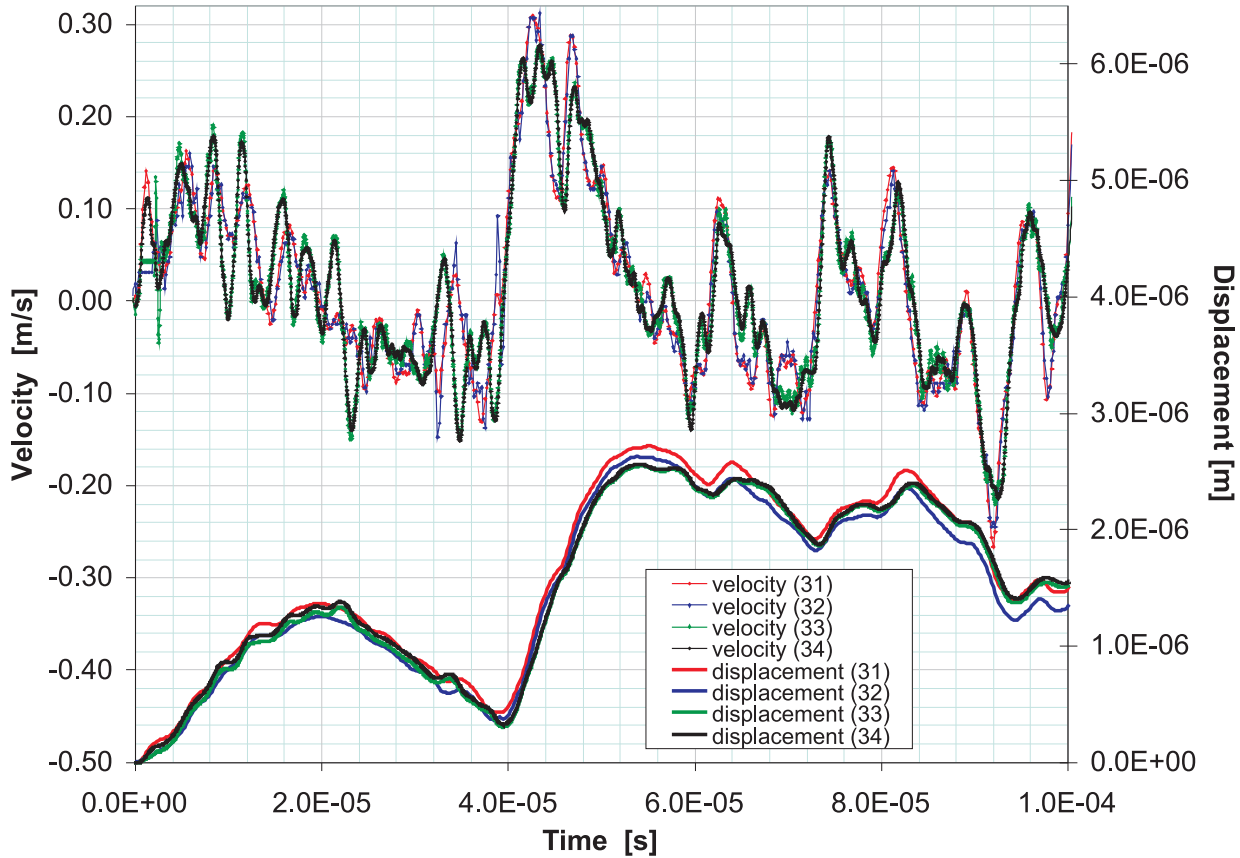


Figure 4.13: Plot of the corrected surface velocity signals (thin lines with marker – upper part of plot) and their corresponding numerically obtained surface displacement (thick lines without marker – lower part of plot) for measurements #31, #32, #33, #34 for reproducibility comparison within the first $100 \mu\text{s}$ of collimator movement. Number of protons: $4.8 \cdot 10^{12}$ (1 batch), beam impact parameter: +4 mm, measurement point #4.

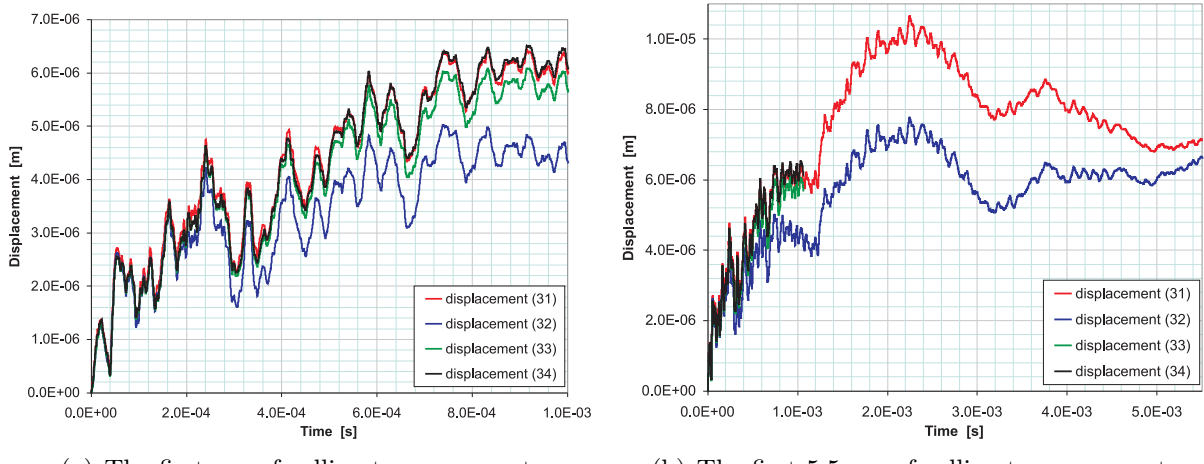
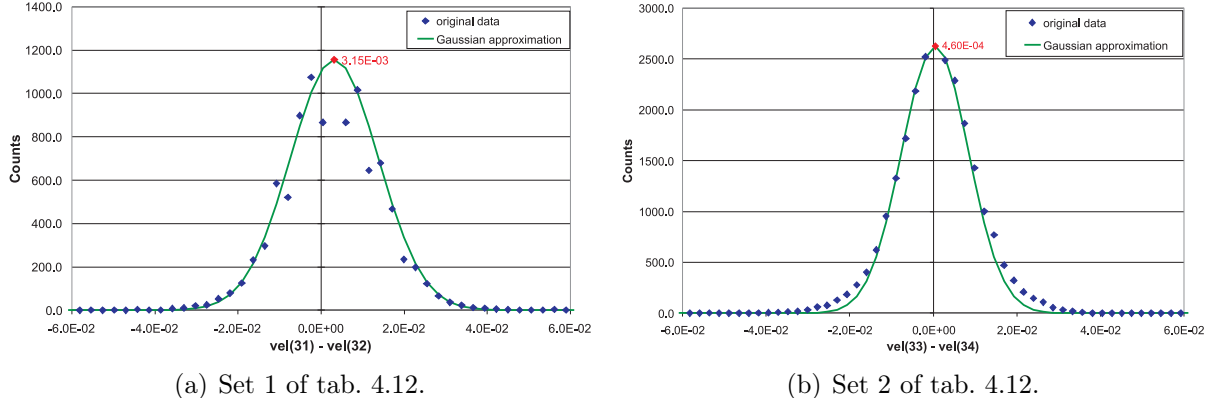


Figure 4.14: Plot of the numerically obtained surface displacement for measurements #31, #32, #33, #34 for reproducibility comparison of collimator movement. Number of protons: $4.8 \cdot 10^{12}$ (1 batch), beam impact parameter: +4 mm, measurement point #4.

Table 4.11: Sets for quantification of reproducibility during LDV measurements.

Set	Measurements	Examined time interval [s]	Maximum velocity of set [m/s]
1	#31, #32	$0.3906 \cdot 10^{-6} - 1.7578 \cdot 10^{-6}$	0.312
2	#33, #34	$0.2046874 \cdot 10^{-3} - 0.2060546 \cdot 10^{-3}$	0.277


 Figure 4.15: Histogram and Gaussian approximation of mean error between two measurements of sets according to values in tab. 4.12. Number of protons: $4.8 \cdot 10^{12}$ (1 batch), beam impact parameter: +4 mm, measurement point #4.

maximum of the distribution and σ approximated with the FWHM (see tab. 4.12). In order to estimate the upper limit of the error of reproducibility of the overall experimental conditions – using the LDV measurement as the sole measure – the following comparison has been used: the ratio between the maximum velocity in the chosen interval (see tab. 4.11) and the mean error μ plus the $x \cdot \sigma$ confidence interval was expressed in percent (see tab. 4.13 on p. 86). With these assumptions the error for the reproducibility can be stated with at most 18% for a 5σ confidence interval.

 Table 4.12: Parameters μ and σ for Gaussian approximation of calculated differences between measurements belonging to one set (details see text).

Set	Mean error μ [m/s]	σ of mean error [m/s]
1	$3.15 \cdot 10^{-3}$	$10.66 \cdot 10^{-3}$
2	$0.46 \cdot 10^{-3}$	$7.98 \cdot 10^{-3}$

4.1.3.2.3 Measurement Point #1

At measurement point #1 the recording times cover values from 1.28 ms (measurement #35) to 128 ms (measurement #38) (see tab. 4.14 on p. 86). The calibration factors for all measurements have not been logged. However it can be seen in fig. 4.16 on p. 87 that the calibration factor is the same for all measurements, hence the calibration factor was arbitrarily chosen 1000 mm/s/V for the shown plots.

Table 4.13: Relative error of reproducibility expressed in percent (see text on p. 85 for further explanation).

Relative error of reproducibility for confidence interval						
of $\sigma =$	0	1	2	3	4	5
in %	0	68.2	95.4	99.7	99.994	99.99994
Set 1	1.0	4.4	7.8	11.3	14.7	18.1
Set 2	0.2	3.0	5.9	8.8	11.7	14.6

 Table 4.14: Entries of logbook for measurement point #1, a beam impact parameter on the collimator jaw of $+4\text{ mm}$ and an intensity of $4.8 \cdot 10^{12}$ protons (1 batch). Abbreviation: a = arbitrarily chosen.

Extraction No.	Measurement No. CCC	Calibration factor [mm/s/V]	Sample frequency [MHz]	Recording time [ms]
25	35	1000 (a)	25.6	1.28
26	36	1000 (a)	5.12	6.4
27	37	1000 (a)	1.024	32
28	38	1000 (a)	0.256	128

Due to the unknown calibration factor no absolute values can be extracted from this set of measurements. However in fig. 4.16 on p. 87 the similarity of the velocity signals and the numerically obtained displacement signals for measurement #35, #36 and #37 can be seen. Measurement #38 – which was recorded with a lower sample frequency than the other three measurements (see tab. 4.14) – clearly could not reach the same peak velocities as the other measurements, but (as seen in section 4.1.3.2.1 starting on p. 79) the calculated displacements show close similarity (see fig. 4.17(a) on p. 88). In fig. 4.17(b) one can see an oscillation with an estimated time period of 18 ms for measurement signal #38. This is in agreement with the time period of measurement #15 of about 17 ms deduced in section 4.1.3.3.2 starting on p. 93.

4.1.3.2.4 Measurement Point #2

At measurement point #2 the recording times cover values from 1.28 ms (measurement #40) to 128 ms (measurement #39) (see tab. 4.15 on p. 87). The calibration factors for all measurements have not been logged.

At first glance the recorded velocity values can be roughly estimated to two ratios between the measurement ranges: range #39 : range #40 : range #41 : range #42 = $1 : 1 : 1 : 5$ or 8. The measurements that have been recorded with a higher time resolution showed – as expected – high frequency components (see fig. 4.19 on p. 90). In order to determine the precise numerical ratio, the original recorded velocity signals with a high time resolution (measurements #40, #41 and #42) were smoothed numerically (with [155]) in order to be compared with the low time resolution measurement #39 (see fig. 4.18 on

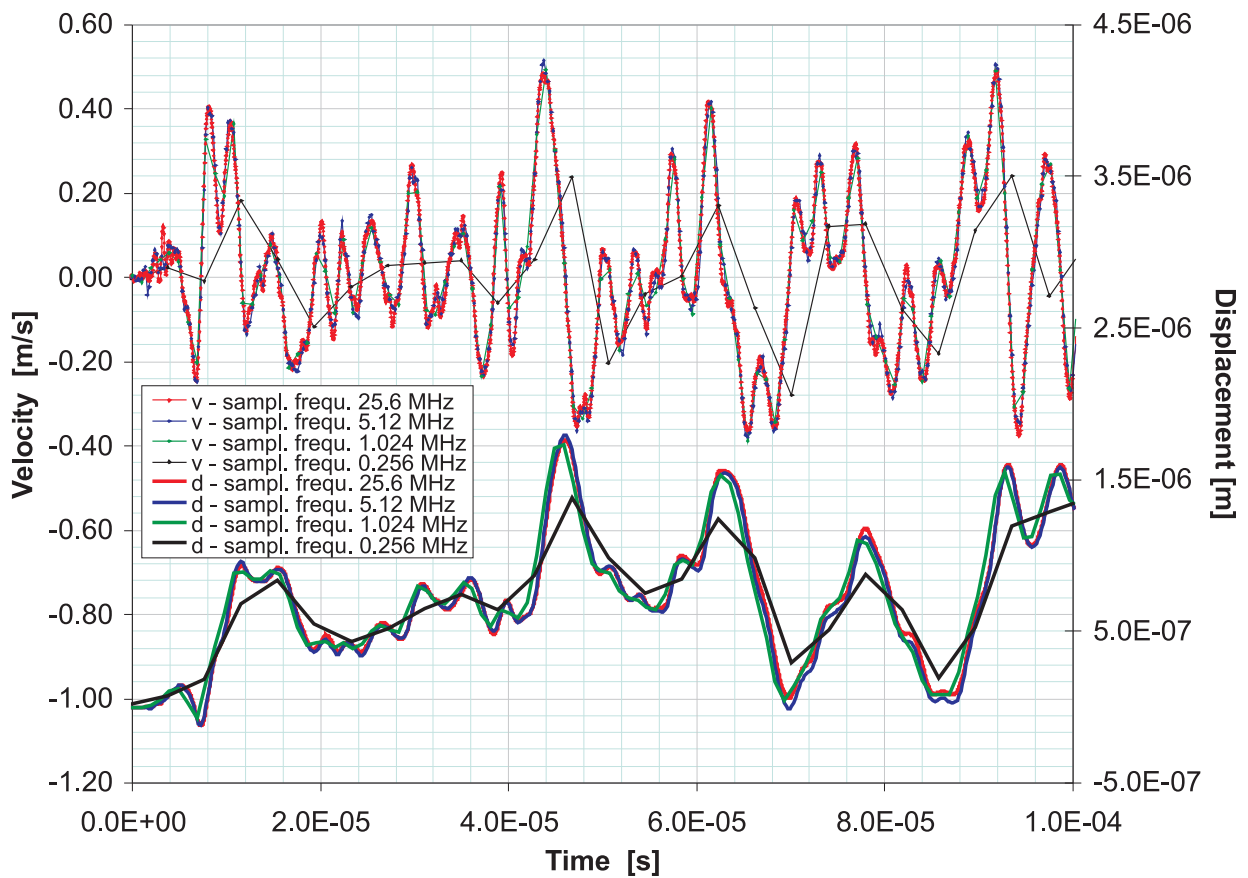


Figure 4.16: Plot of the recorded surface velocity signals (thin lines with marker – upper part of plot) and their corresponding numerically obtained surface displacement (thick lines without marker – lower part of plot) for measurements #35 (sample frequency 25.6 MHz), #36 (5.12 MHz), #37 (1.024 MHz), #38 (0.256 MHz) for reproducibility comparison within the first 100 μ s of collimator movement with an arbitrarily chosen calibration factor of 1000 $mm/s/V$ for the velocity range. Number of protons: $4.8 \cdot 10^{12}$ (1 batch), beam impact parameter: +4 mm, measurement point #1.

Table 4.15: Entries of logbook for measurement point #2, a beam impact parameter on the collimator jaw of +4 mm and an intensity of $4.8 \cdot 10^{12}$ protons (1 batch). Abbreviations: r = reobtained, a = arbitrarily chosen

Extraction No.	Measurement No.	Calibration factor [mm/s/V]	Sample frequency [MHz]	Recording time [ms]
CCC	LDV			
29	39	125 (r,a)	0.256	128
31	40	125 (r,a)	25.6	1.28
33	41	125 (r,a)	10.24	3.2
34	42	25 (r,a)	5.12	6.4

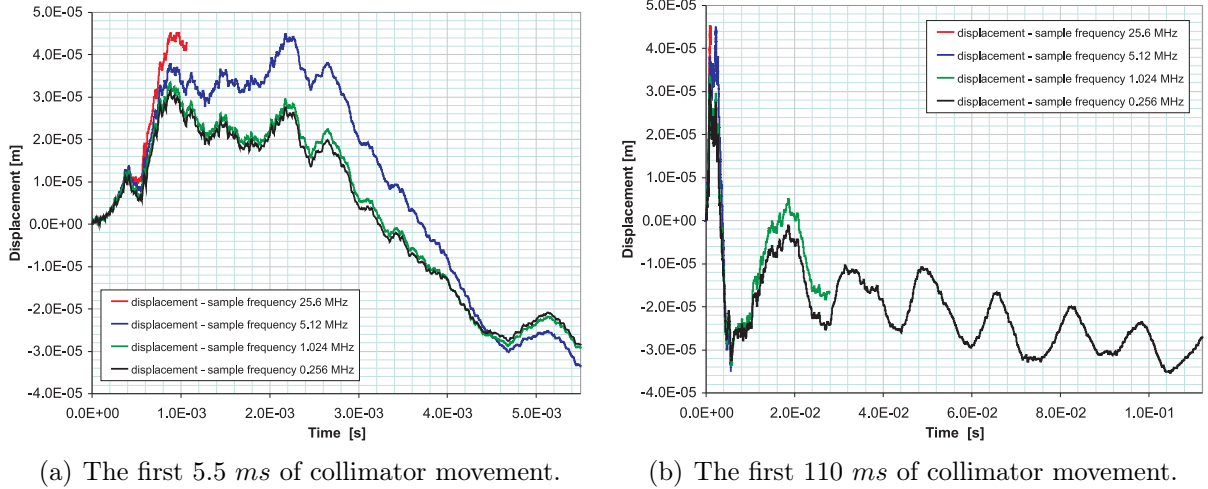


Figure 4.17: Plot of the surface displacement obtained by numerical integration of the surface velocities (with an arbitrarily chosen calibration factor of 1000 mm/s/V for the velocity range) for measurements #35 (sample frequency 25.6 MHz), #36 (5.12 MHz), #37 (1.024 MHz), #38 (0.256 MHz) for reproducibility comparison of collimator movement. Number of protons: $4.8 \cdot 10^{12}$ (1 batch), beam impact parameter: $+4 \text{ mm}$, measurement point #1.

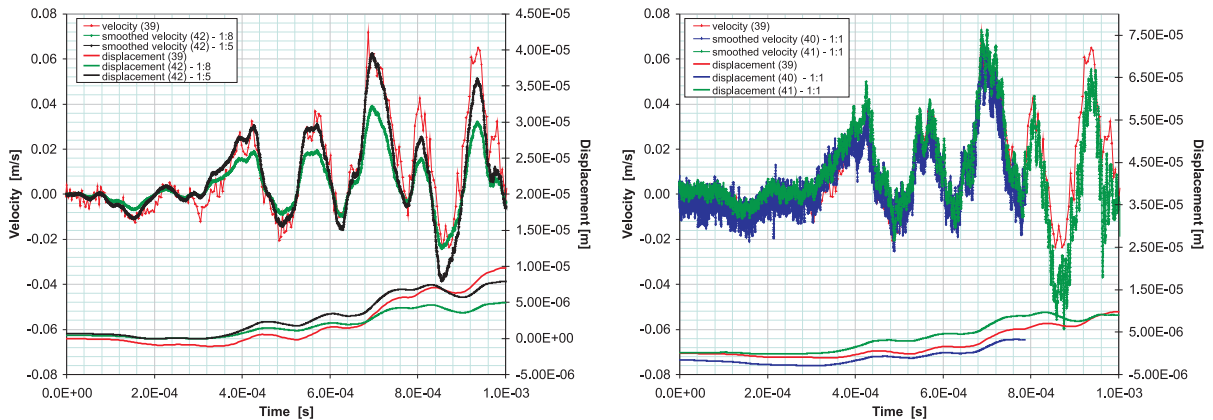
p. 89):

$$y_s(i) = \frac{1}{2N+1} (y(i+N) + y(i+N-1) + \dots + y(i-N)) \quad (4.2)$$

with $y_s(i)$ as the smoothed value for the i^{th} data point, N as the number of neighboring data points on either side of $y_s(i)$ and $2N+1$ as the smoothing span. The smoothing span for each measurement was chosen as the ratio between the recording time of measurement #39 and the recording time of the measurement itself (see tab. 4.16). For this comparison the calibration factor of measurement #40 and #41 was arbitrarily set to 1000 mm/s/V . For measurement #42, the smoothed velocity signals were resized by both possible ratios (1:5 and 1:8) and compared with measurement #39 (see fig. 4.18(a) on p. 89). The ratio of this matching procedure is 1 : 1 : 1 : 5 (see fig. 4.18(b) for the matching ratio of measurement #40 and #41) which is valid for two sets of calibration factors (see tab. 4.6 on p. 78): 125 : 125 : 125 : 25 and 25 : 25 : 25 : 5, respectively.

Table 4.16: Smoothing spans for measurements at point #2 (beam impact parameter $+4 \text{ mm}$, intensity $4.8 \cdot 10^{12}$ protons).

Measurement No.	LDV	Smoothing span
39		None
40		99
41		39
42		119

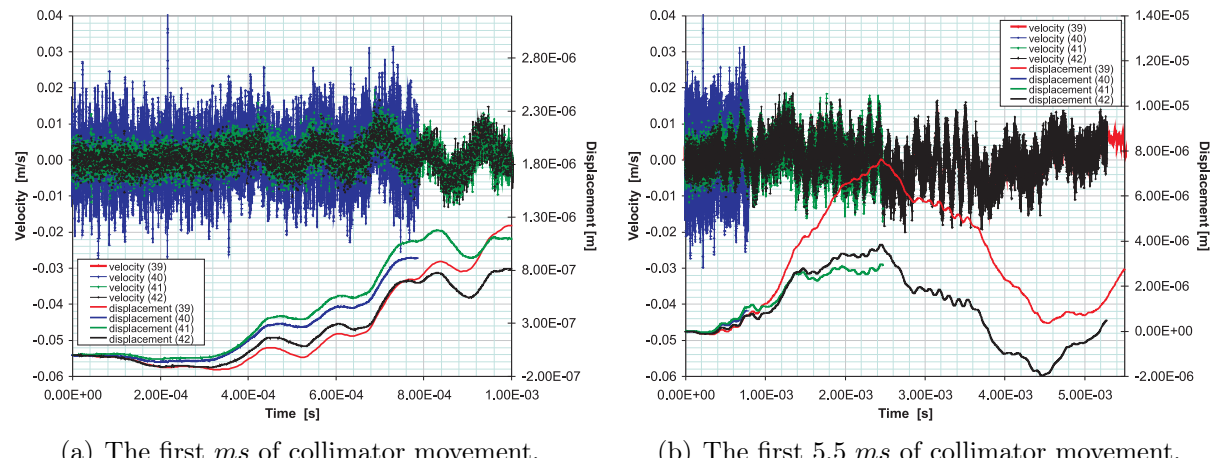


(a) Measurements #39 (original recorded velocity signal) and numerically smoothed velocity signal for measurement #42 with the two possible ratios 1:5 and 1:8.

(b) Measurement #39 with smoothed measurements #40 and #41 with the ratio 1:1.

Figure 4.18: Plot of the (partly) smoothed surface velocity signals (upper part of plot) and their corresponding numerically obtained surface displacement (lower part of plot) within the first ms of collimator movement for reproducibility comparison. Number of protons: $4.8 \cdot 10^{12}$ (1 batch), beam impact parameter: +4 mm, measurement point #2. The calibration factor was arbitrarily chosen to be 1000 mm/s/V.

For presentation and comparison, the first set of calibration factors (125 : 125 : 125 : 25) was chosen. If however the second set of calibration factors (25 : 25 : 25 : 5) was chosen, the scales of the plots have to be divided by 5. Hence the data can only be described qualitatively in this section. In both fig. 4.19 on p. 90 and fig. 4.20 p. 91, the similarity of the numerically obtained displacement signals for measurement #39, #40, #41 and #42 can easily be seen. However measurement #39 – which was recorded with a lower sample frequency than the other three measurements (see tab. 4.15 on p. 87) – clearly could not reach the same peak velocities as the other measurements. Fig. 4.20 on p. 91 shows the qualitative behavior of the displacement for the longest recording time at this measurement point.


 (a) The first *ms* of collimator movement.

 (b) The first 5.5 *ms* of collimator movement.

Figure 4.19: Plot of the recorded surface velocity signals (thin lines with marker – upper part of plot) and their corresponding numerically obtained surface displacement (thick lines without marker – lower part of plot) for measurements #39, #40, #41, #42 of collimator movement for reproducibility comparison. The calibration factor was arbitrarily chosen to be 125 mm/s/V. Number of protons: $4.8 \cdot 10^{12}$ (1 batch), beam impact parameter: +4 mm, measurement point #2.

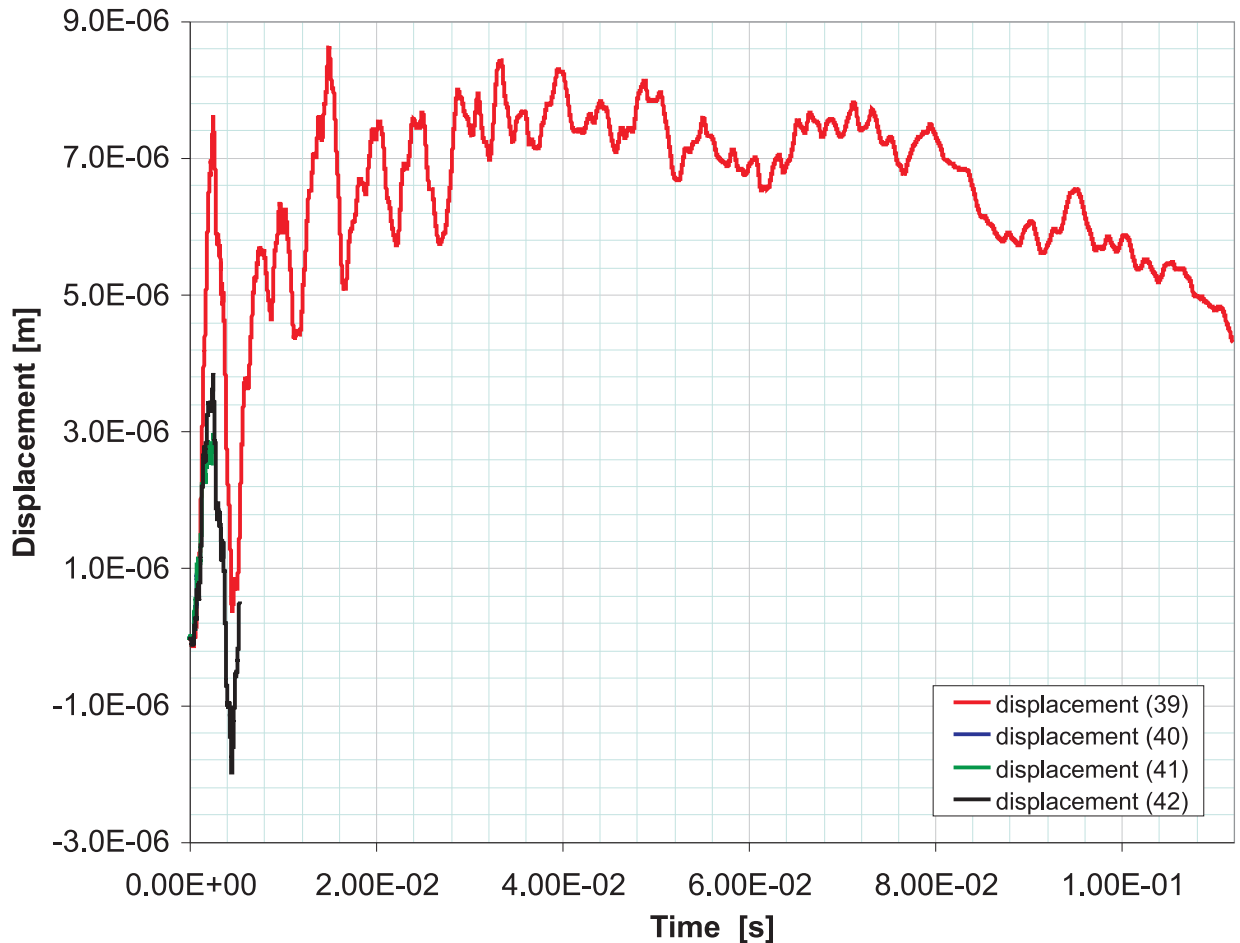


Figure 4.20: Plot of the surface displacement for measurements #39, #40, #41, #42 for reproducibility comparison within the first 112 ms of collimator movement. The calibration factor was arbitrarily chosen to be 125 mm/s/V. Number of protons: $4.8 \cdot 10^{12}$ (1 batch), beam impact parameter: +4 mm, measurement point #2.

4.1.3.3 Collimator Response

4.1.3.3.1 Dependence on Measurement Point

The measurements in this section have been obtained using an intensity of $4.8 \cdot 10^{12}$ protons and a beam impact parameter on the collimator jaw of $+4 \text{ mm}$. For this comparison the measurements were chosen according to the following criteria:

- No speckle dropouts
- Known calibration factor
- Same time resolution: set #1 (see tab. 4.17) with a recording time of 1.28 ms and set #2 (see tab. 4.18) with a recording time of 6.4 ms .
- Measurement position on the collimator jaw (measurement point #1, #3 and #4)

Due to the unknown calibration factor of the measurements #35 (matching parameters of set #1) and #36 (matching parameters of set #2) at measurement point #1, the data for this measurement point could not be included in the representation. The values for measurement point #3 and #4 are absolute values. One should also keep in mind that the measurement point #3 was at least 2 mm off-axis, whereas measurement point #4 was at least 10 mm off-axis (see tab. 4.2 on p. 69).

Table 4.17: Entries of logbook for measurements with a beam impact parameter on the collimator jaw of $+4 \text{ mm}$ and an intensity of $4.8 \cdot 10^{12}$ protons (1 batch) with a recording time of 1.28 ms (a sample frequency of 25.6 MHz), known calibration factor and no speckle dropouts (set #1). Abbreviations: l = logged, r = reobtained.

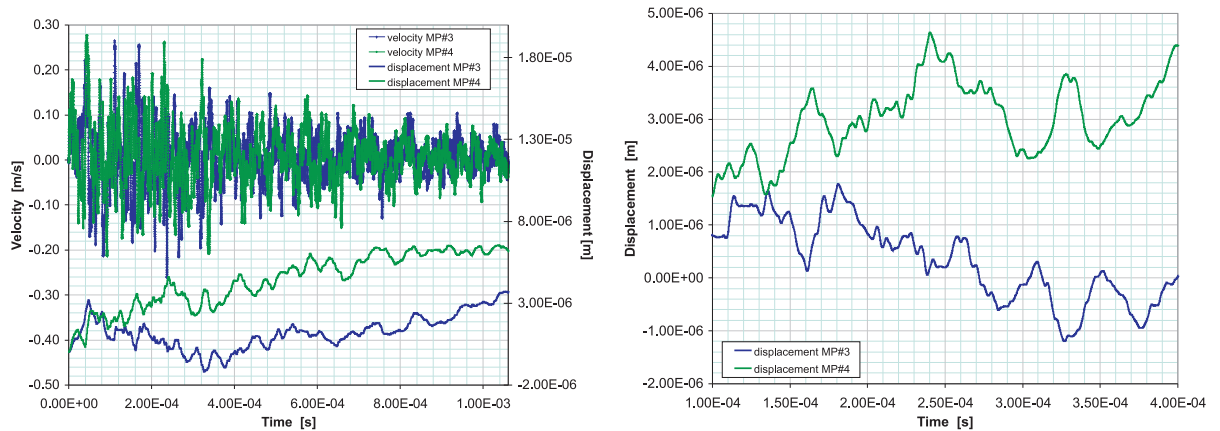
Extraction No.	Measurement No. CCC	Measurement point no.	Calibration factor
	LDV		[mm/s/V]
17	27	3	125 (l)
24	34	4	125 (r)

Table 4.18: Entries of logbook for measurements with a beam impact parameter on the collimator jaw of $+4 \text{ mm}$ and an intensity of $4.8 \cdot 10^{12}$ protons (1 batch) with a recording time of 6.4 ms (a sample frequency of 5.12 MHz), known calibration factor and no speckle dropouts (set #2). Abbreviations: l = logged.

Extraction No.	Measurement No. CCC	Measurement point no.	Calibration factor
	LDV		[mm/s/V]
20	30	3	125 (l)
21	31	4	125 (l)

In fig. 4.21 on p. 93 and fig. 4.22 on p. 94, it can be seen that the maximum velocity values for measurement point #3 (measurement #27) and measurement point #4

(measurement #34) are in the same order of magnitude. This is in agreement with the calculated energy deposition (see fig. 4.7 on p. 76). Comparing the response pattern for the two measurements, one can observe differences as expected for different locations along the collimator jaw axis. In the time interval from 0.13 ms to 0.35 ms the displacement of measurement #34 seems to mirror that of measurement #27 (see fig. 4.21(a)). This mirroring in displacement is also observable for measurement #30 and #31 for the time interval from 1.2 ms to 3.2 ms (see fig. 4.22 on p. 94).



(a) Surface velocity signals (thin lines with marker – upper part of plot) and their corresponding numerically obtained surface displacement (thick lines without marker – lower part of plot) for the first 1.06 ms of collimator movement.

(b) Numerically obtained surface displacement for time interval $100 - 400\text{ }\mu\text{s}$ of collimator movement.

Figure 4.21: Plot for different measurement points on the collimator jaw of collimator movement: measurements #27 (measurement point #3) and #34 (measurement point #4). Number of protons: $4.8 \cdot 10^{12}$ (1 batch), beam impact parameter: $+4\text{ mm}$.

4.1.3.3.2 Dependence on Beam Intensity

For this comparison the measurements with the proton beam impact parameter of $+5\text{ mm}$ at measurement point #3 were chosen (see tab. 4.19 on p. 94). Two measurements (#16 and #18) contain several speckle dropouts due to the high intensity, which were replaced with an average of the left and the right neighbor of each speckle dropout (see tab. 4.20 on p. 95).

For measurement #18 a large number of speckle dropouts were removed entirely by setting the velocity equal to zero for the period $1.593 \cdot 10^{-3} - 1.694 \cdot 10^{-3}\text{ s}$ (see tab. 4.20). This removal of speckle dropouts might lead to a high inaccuracy of the numerically obtained displacement. Therefore the displacement, especially after 1.593 ms , should only be seen in its qualitative behaviour.

Fig. 4.23 on p. 96 and fig. 4.24 on p. 97 show the comparison between the original recorded and the speckle dropout-corrected signal and their corresponding numerically obtained displacements. Fig. 4.23 on p. 96 shows a few speckle dropouts just after the beam impact, whereas fig. 4.24 on p. 97 illustrates the numerous speckle dropouts after about 1.6 ms of collimator movement.

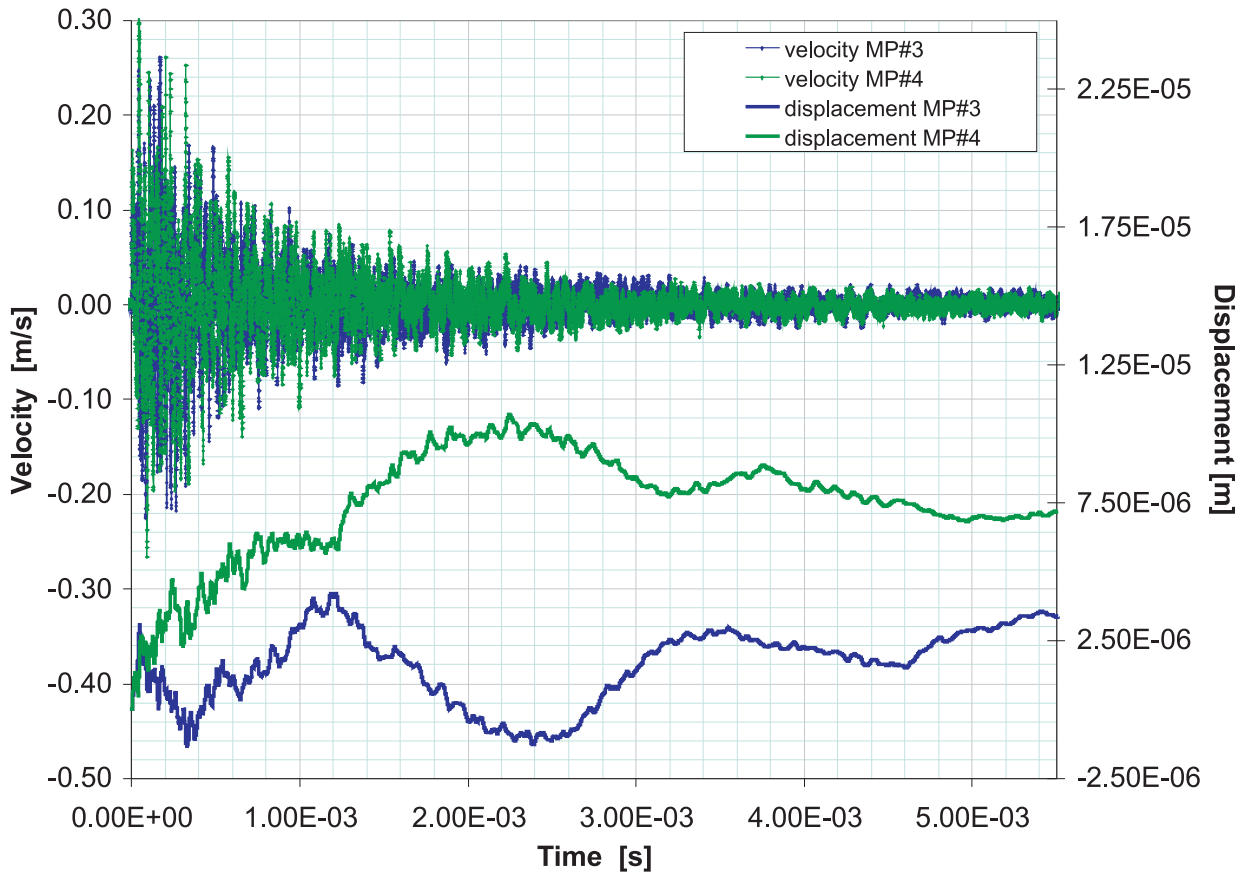


Figure 4.22: Plot of the surface velocity signals (thin lines with marker – upper part of plot) and their corresponding numerically obtained surface displacement (thick lines without marker – lower part of plot) for different measurement points on the collimator jaw within 5.5 ms of collimator movement: measurements #30 (measurement point #3) and #31 (measurement point #4). Number of protons: $4.8 \cdot 10^{12}$ (1 batch), beam impact parameter: +4 mm.

Table 4.19: Entries of logbook for measurements with a beam impact parameter on the collimator jaw of +5 mm at measurement point #3 with varying intensities. Abbreviation: l = logged.

Extraction No.	Measurement CCC	Measurement No. LDV	Number of protons [$\cdot 10^{12}$]	Number of batches	Calibration factor [mm/s/V]	Sample frequency [MHz]	Recording time [ms]
2		14	4.8	1	1000 (l)	1.024	32
4		15	9.6	2	1000 (l)	0.256	128
5		16	19.2	4	1000 (l)	5.12	6.4
7		18	28.8	6	1000 (l)	5.12	6.4

Table 4.20: List of removed speckle dropouts for measurement #16 and #18.
(*) set of 11 speckle dropouts – velocity set to 0.

Measurement No.	LDV	Speckle dropout interval [s]
16		$3.320 \cdot 10^{-6} - 5.273 \cdot 10^{-6}$
16		$9.492 \cdot 10^{-5} - 9.648 \cdot 10^{-5}$
16		$1.803 \cdot 10^{-4} - 1.826 \cdot 10^{-4}$
16		$2.402 \cdot 10^{-4} - 2.422 \cdot 10^{-4}$
16		$2.719 \cdot 10^{-4} - 2.738 \cdot 10^{-4}$
16		$3.555 \cdot 10^{-4} - 3.570 \cdot 10^{-4}$
16		$8.412 \cdot 10^{-4} - 8.430 \cdot 10^{-4}$
16		$8.820 \cdot 10^{-4} - 8.830 \cdot 10^{-4}$
16		$1.684 \cdot 10^{-3} - 1.685 \cdot 10^{-3}$
18		$5.664 \cdot 10^{-6} - 1.074 \cdot 10^{-5}$
18		$2.967 \cdot 10^{-4} - 2.988 \cdot 10^{-4}$
18		$3.287 \cdot 10^{-4} - 3.309 \cdot 10^{-4}$
18		$3.666 \cdot 10^{-4} - 3.687 \cdot 10^{-4}$
18		$4.420 \cdot 10^{-4} - 4.437 \cdot 10^{-4}$
18		$9.848 \cdot 10^{-4} - 9.863 \cdot 10^{-4}$
18		$1.093 \cdot 10^{-3} - 1.095 \cdot 10^{-3}$
18		$1.593 \cdot 10^{-3} - 1.694 \cdot 10^{-3}$ (*)
18		$1.801 \cdot 10^{-3} - 1.802 \cdot 10^{-3}$
18		$1.828 \cdot 10^{-3} - 1.829 \cdot 10^{-3}$
18		$3.038 \cdot 10^{-3} - 3.040 \cdot 10^{-3}$

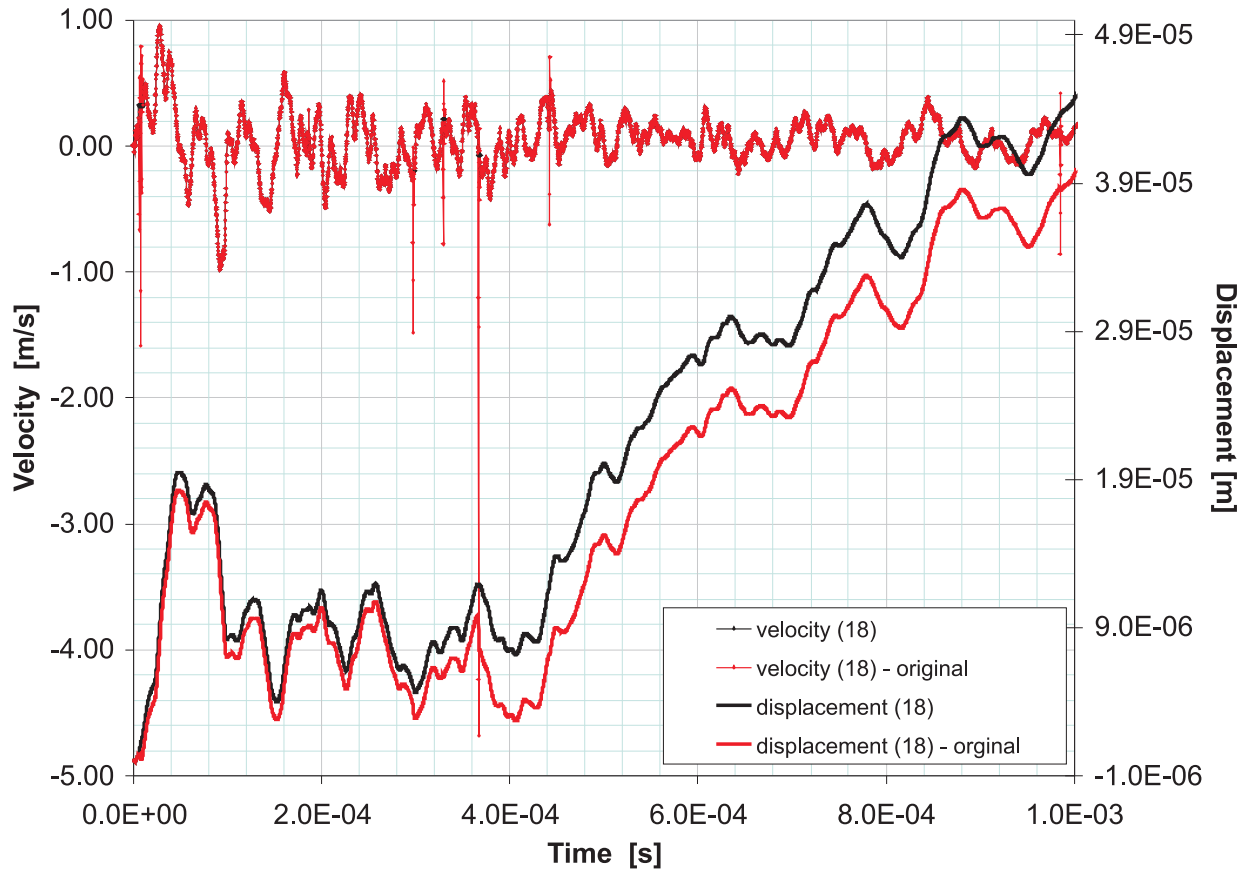


Figure 4.23: Plot of the surface velocity signals (thin lines with marker – upper part of plot) and their corresponding numerically obtained surface displacement (thick lines without marker – lower part of plot) for measurement #18 the first *ms* of collimator movement for comparison of originally recorded (uncorrected) and speckle dropouts corrected signal. The red curves represent the originally recorded signal, the black curves the speckle dropouts corrected signal. Number of protons: $28.8 \cdot 10^{12}$ (6 batches), beam impact parameter: +5 mm, measurement point #3.

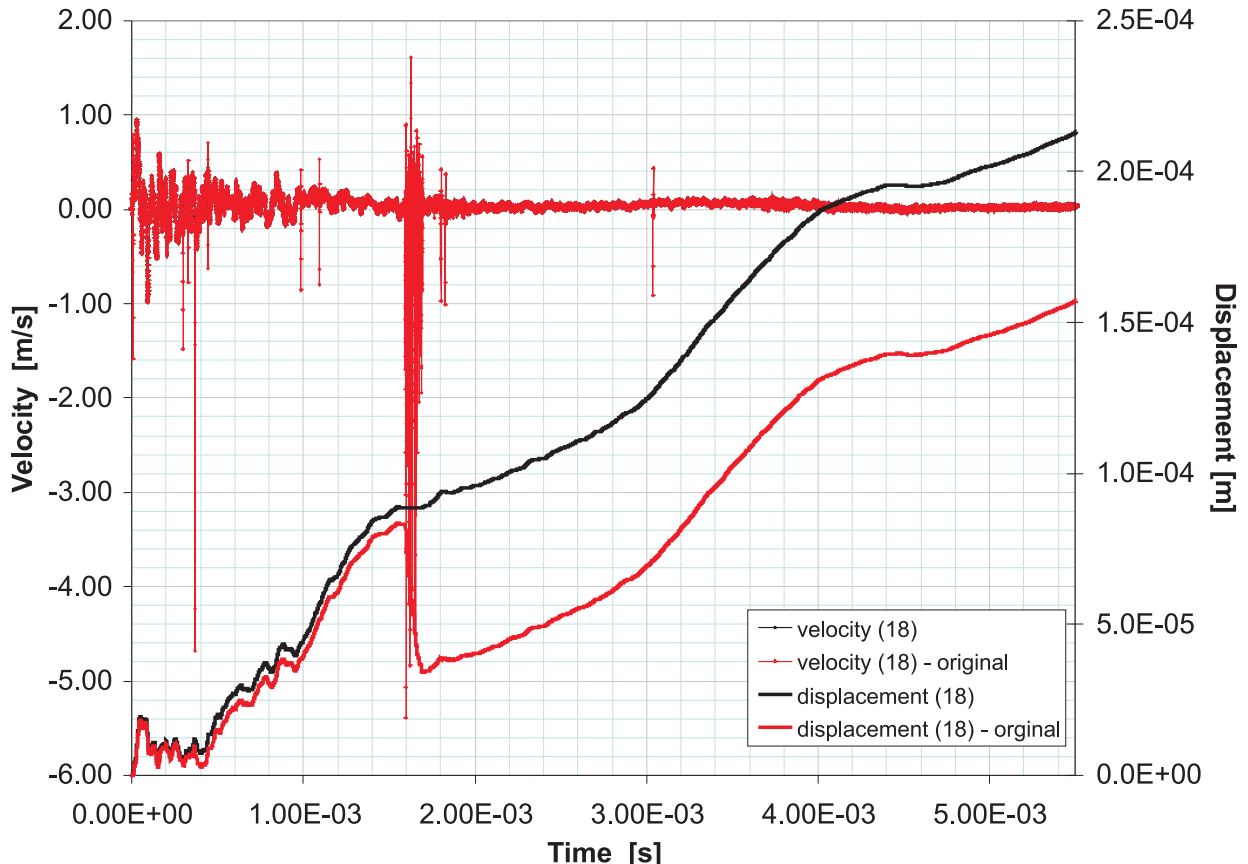
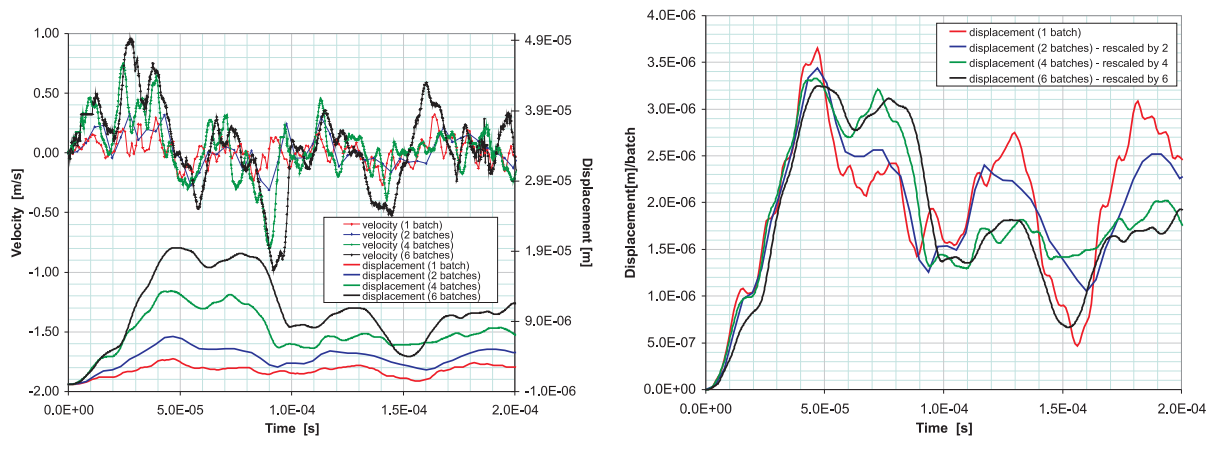


Figure 4.24: Plot of the surface velocity signals (thin lines with marker – upper part of plot) and their corresponding numerically obtained surface displacement (thick lines without marker) for measurement #18 within 6.2 ms of collimator movement for comparison of originally recorded (uncorrected) and speckle dropouts corrected signal. The red curve represents the originally recorded signal, the black curve the speckle dropouts corrected signal. Number of protons: $28.8 \cdot 10^{12}$ (6 batches), beam impact parameter: +5 mm, measurement point #3.

Looking at fig. 4.25(a) allows one to see the proportionality of both the surface velocity and displacement for the different proton beam intensities. One should keep in mind that before the first maximum of the displacement is reached, speckle dropouts had to be removed for the two high intensity beam impacts (measurement #16 and #18). In fig. 4.25(b) – where the velocity was normalized to the same beam intensity (1 batch) – it can be seen that the first maximum displacement (at around $50 \mu s$) roughly scales according to proton beam intensity. For the purpose of clarity a linear fit through the origin has been applied to the displacement of this first maximum vs. beam intensity in fig. 4.26 on p. 99. The linearity has also been demonstrated with the accelerometer measurements ([137] right figure on slide 19).



(a) Plot of the corrected surface velocity signals (thin lines with marker – upper part of plot) and their corresponding numerically obtained surface displacement (thick lines without marker – lower part of plot).

(b) Plot of the surface displacement rescaled to 1 batch.

Figure 4.25: Plots for different proton beam intensities the first $200 \mu s$ of collimator movement: measurements #14 ($4.8 \cdot 10^{12}$ protons = 1 batch), #15 ($9.6 \cdot 10^{12}$ protons = 2 batches), #16 ($19.2 \cdot 10^{12}$ protons = 4 batches) and #18 ($28.8 \cdot 10^{12}$ protons = 6 batches). Beam impact parameter: $+5 \text{ mm}$, measurement point #3.

In fig. 4.27(a) on p. 99, both high intensity beam impacts show a stronger change in the amplitude below 1 ms . In fig. 4.27(b) one can see an offset of the displacement for longer recording times (measurement #14 and #15) of about $40 \mu \text{m}$ for measurement #14 and about $90 \mu \text{m}$ for measurement #15.

For the long-term behavior of the jaw only one measurement (measurement #15) was recorded (see fig. 4.28 on p. 100), in which one can see that the displacement not only exhibits an oscillation with a time period of roughly 17 ms between 10 and 95 ms , but also around an offset. This offset seems to "drift" slowly (comparable with a velocity of around $2.6 \cdot 10^{-4} \text{ m/s}$). The displacement is obtained from the velocity signal by numerical integration. In order to avoid a drift in displacement due to a (small) constant shift in the velocity signal, the average velocity before the response of the collimator due to beam impact is subtracted from each recorded value ([154]). One should keep in mind that for measurement #18 there were only 18 measurement points (whose average could be used for

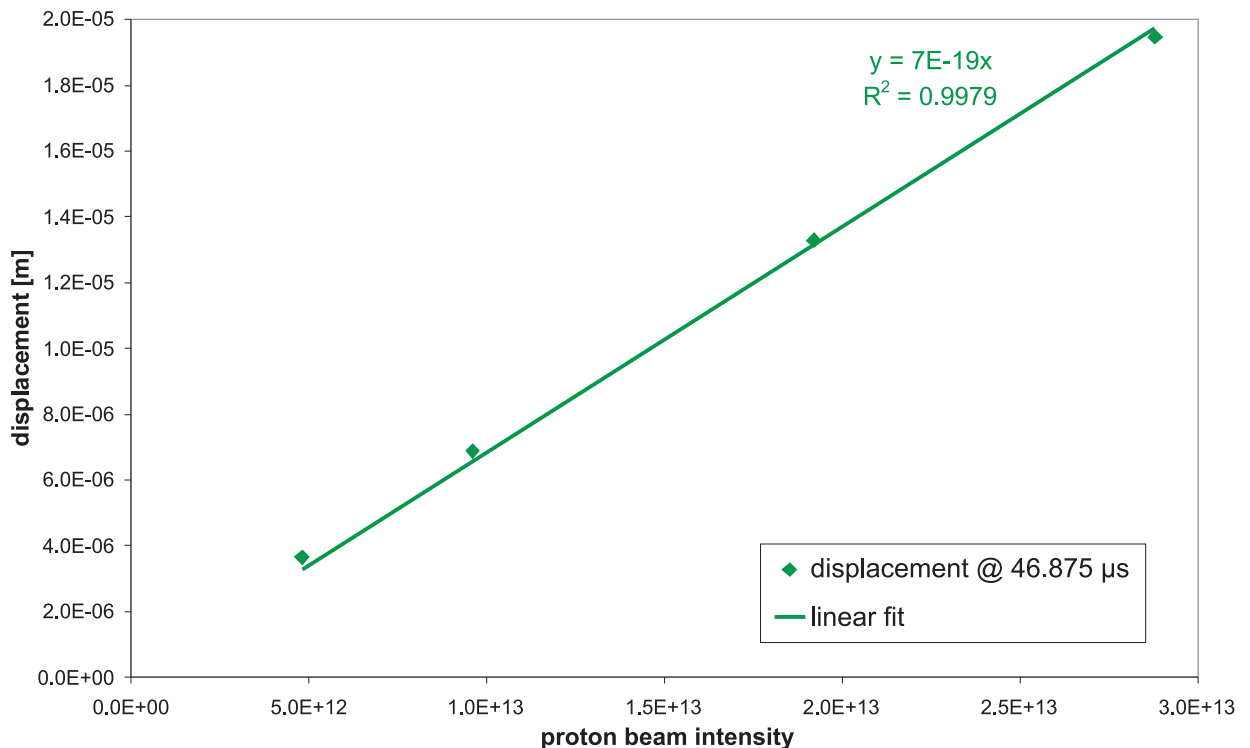


Figure 4.26: Plot of the surface displacement of first response at $46.875 \mu s$ vs. proton beam intensity for a beam impact parameter of $+5 \text{ mm}$ at measurement point #3 (measurements #14 ($4.8 \cdot 10^{12}$ protons = 1 batch), #15 ($9.6 \cdot 10^{12}$ protons = 2 batches), #16 ($19.2 \cdot 10^{12}$ protons = 4 batches) and #18 ($28.8 \cdot 10^{12}$ protons = 6 batches)) and the linear fit through the origin.

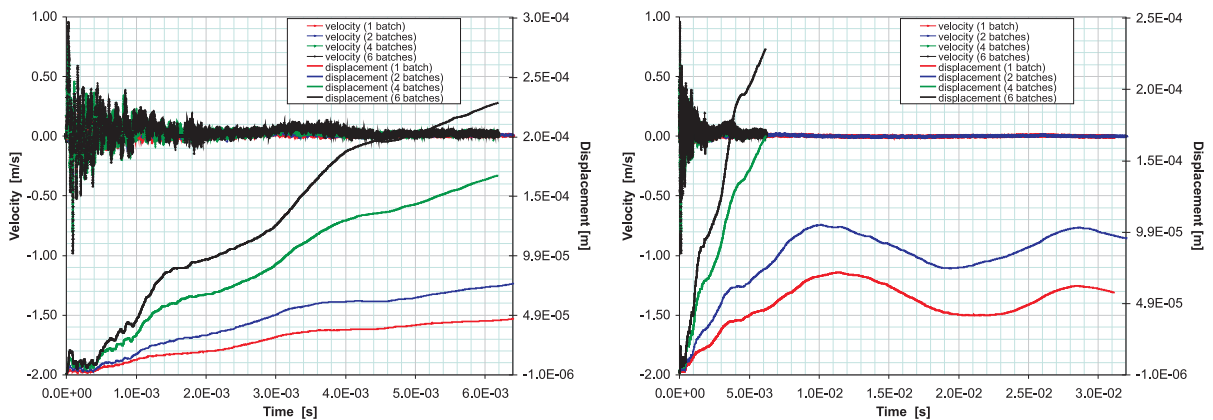


Figure 4.27: Plot of the corrected surface velocity signals (thin lines with marker – upper part of plot) and their corresponding numerically obtained surface displacement (thick lines without marker – lower part of plot) for different proton beam intensities: measurements #14 ($4.8 \cdot 10^{12}$ protons = 1 batch), #15 ($9.6 \cdot 10^{12}$ protons = 2 batches), #16 ($19.2 \cdot 10^{12}$ protons = 4 batches) and #18 ($28.8 \cdot 10^{12}$ protons = 6 batches) of collimator movement. Beam impact parameter: $+5 \text{ mm}$, measurement point #3.

subtraction) before the response of the collimator jaw was recorded. In general, a longer recording time for the high intensity impacts would have been an advantage.

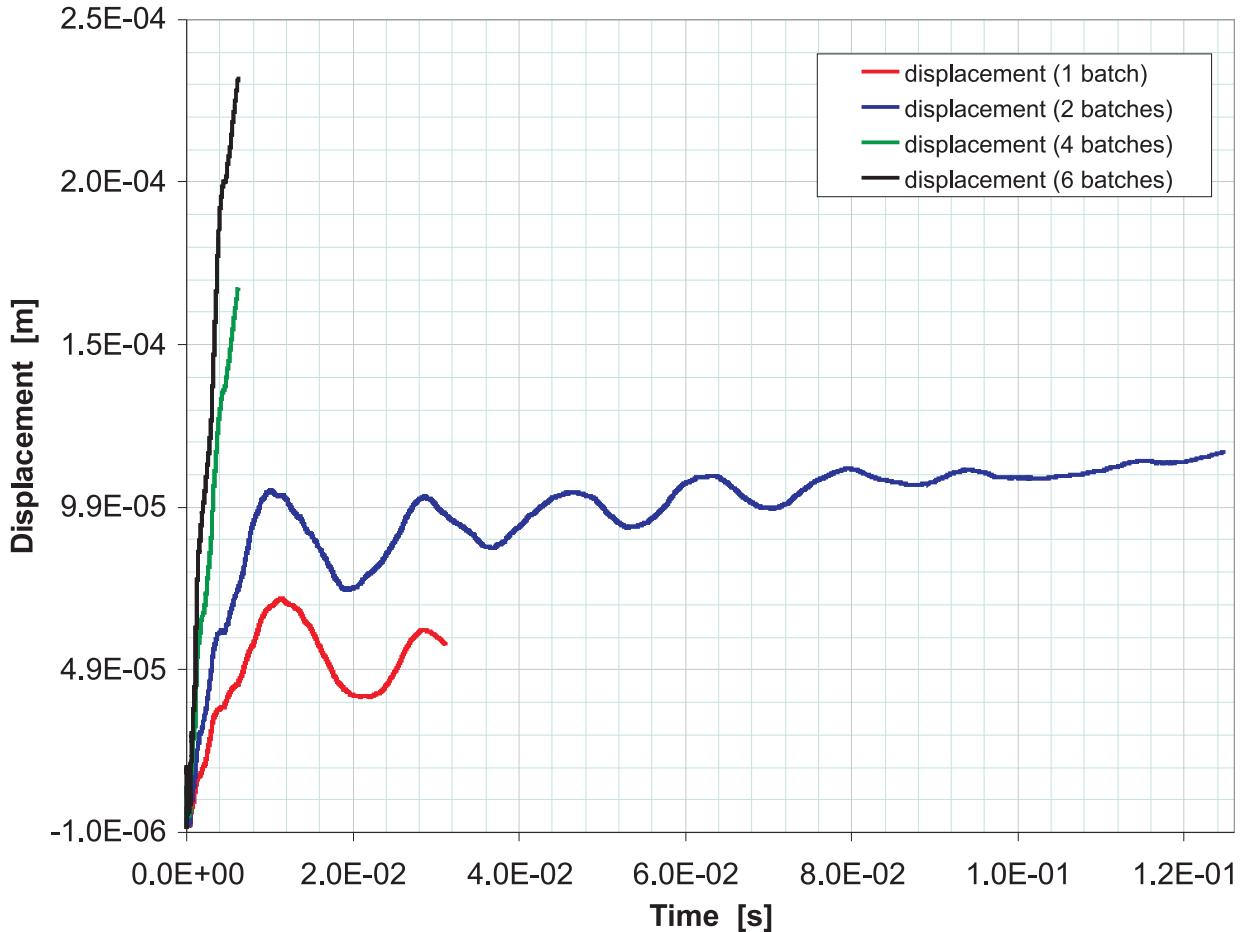


Figure 4.28: Plot of the surface displacement for different proton beam intensities in the first 124 ms of collimator movement: measurements #14 ($4.8 \cdot 10^{12}$ protons = 1 batch), #15 ($9.6 \cdot 10^{12}$ protons = 2 batches), #16 ($19.2 \cdot 10^{12}$ protons = 4 batches) and #18 ($28.8 \cdot 10^{12}$ protons = 6 batches). Beam impact parameter: +5 mm, measurement point #3.

4.1.3.3.3 Dependence on Beam Impact Parameter

For this comparison the measurements at highest proton beam intensity ($28.8 \cdot 10^{12}$) at measurement point #3 were chosen (see tab. 4.21 on p. 101). Most of the measurements (#18, #19, #20, #21, #22 and #23) contain speckle dropouts which were again replaced with an average of the left and right neighbor of each speckle dropout. Tab. 4.23 on p. 105 gives an overview of the amount of speckle dropouts that had to be removed and the ratio between the sum of speckle dropout time intervals and the recorded time of collimator movement. The calculated displacement of those measurements with a large amount of removed speckle dropouts can only be seen in their qualitative behaviour. The calibration factor for measurement #25 (proton impact parameter: -2 mm) was not logged and therefore this measurement was excluded from the comparison.

The measurements with the higher beam impact parameter show – as expected – a larger displacement (see fig. 4.29 on p. 102). In fig. 4.30 on p. 103 one can see that several

Table 4.21: Entries of logbook for measurements with an intensity of $28.8 \cdot 10^{12}$ protons (6 batches) at measurement point #3 for different beam impact parameters on the collimator jaw. Abbreviations: l = logged, a = arbitrarily chosen.

Extraction No.	Measurement No. CCC	Measurement No. LDV	Proton beam impact parameter [mm]	Calibration factor [mm/s/V]	Sample frequency [MHz]	Recording time [ms]
7		18	5	1000 (l)	5.12	6.4
8		19	4	1000 (l)	5.12	6.4
9		20	3	1000 (l)	51.2	0.64
10		21	2	1000 (l)	25.6	1.28
11		22	1	1000 (l)	25.6	1.28
12		23	0	1000 (l)	25.6	1.28
13		24	-1	1000 (l)	25.6	1.28

Table 4.22: Ratios of time interval for removed speckle dropouts versus recorded time after beam impact and number of removed speckle dropouts for measurements #18, #19, #20, #21, #22 and #23.

Measurement No. LDV	Ratio of speckle dropout time to recorded time after beam impact [%]	Number of removed speckle dropouts
18	1.83	≈ 20
19	6.62	69
20	4.48	14
21	12.95	35
22	2.72	14
23	0.79	4

speckle dropouts had to be removed for the measurements with beam impact parameters inside the collimator jaw. Therefore – when taking a closer look at the first response in fig. 4.31 on p. 104 – it seems that the displacement for the proton beam impact parameter of $+2\text{ mm}$ (measurement #21) is bigger than for $+3\text{ mm}$ (measurement #20).

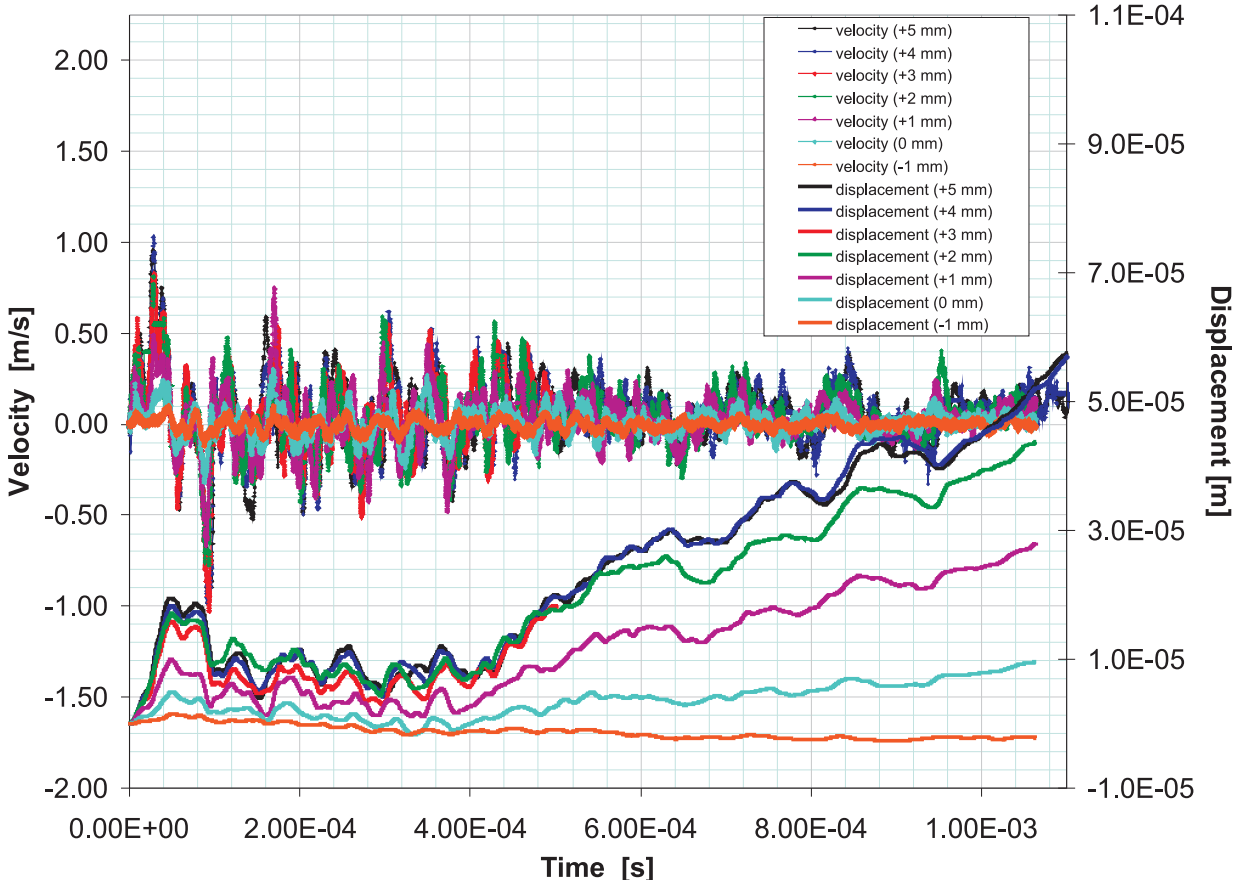


Figure 4.29: Plot of the corrected surface velocity signals (thin lines with marker – upper part of plot) and their corresponding numerically obtained surface displacement (thick lines without marker – lower part of plot) for different beam impact parameters in the first 1.1 ms of collimator movement: measurements #18 ($+5\text{ mm}$), #19 ($+4\text{ mm}$), #20 ($+3\text{ mm}$), #21 ($+2\text{ mm}$), #22 ($+1\text{ mm}$), #23 (0 mm) and #24 (-1 mm). Beam intensity: $28.8 \cdot 10^{12}$, measurement point #3.

If one plots the displacement vs. proton beam impact parameter for two different times (see fig. 4.32 on p. 105) one can see a kink at a proton impact parameter of $+2\text{ mm}$. This behaviour was also observed with the accelerometer measurements ([137] left figure on slide 19). The beam FWHM was measured to be 1 mm (see section 4.1.2.3 starting on p. 71). Assuming a Gaussian beam cross section one can calculate the σ -value [156] (section 31.4.3, p. 299):

$$HWHM = 1.177 \cdot \sigma \quad (4.3)$$

with $HWHM$ as the half-width at half maximum. Assuming different confidence intervals, this leads to the different beam widths as stated in tab. 4.23 on p. 105. With the assumption

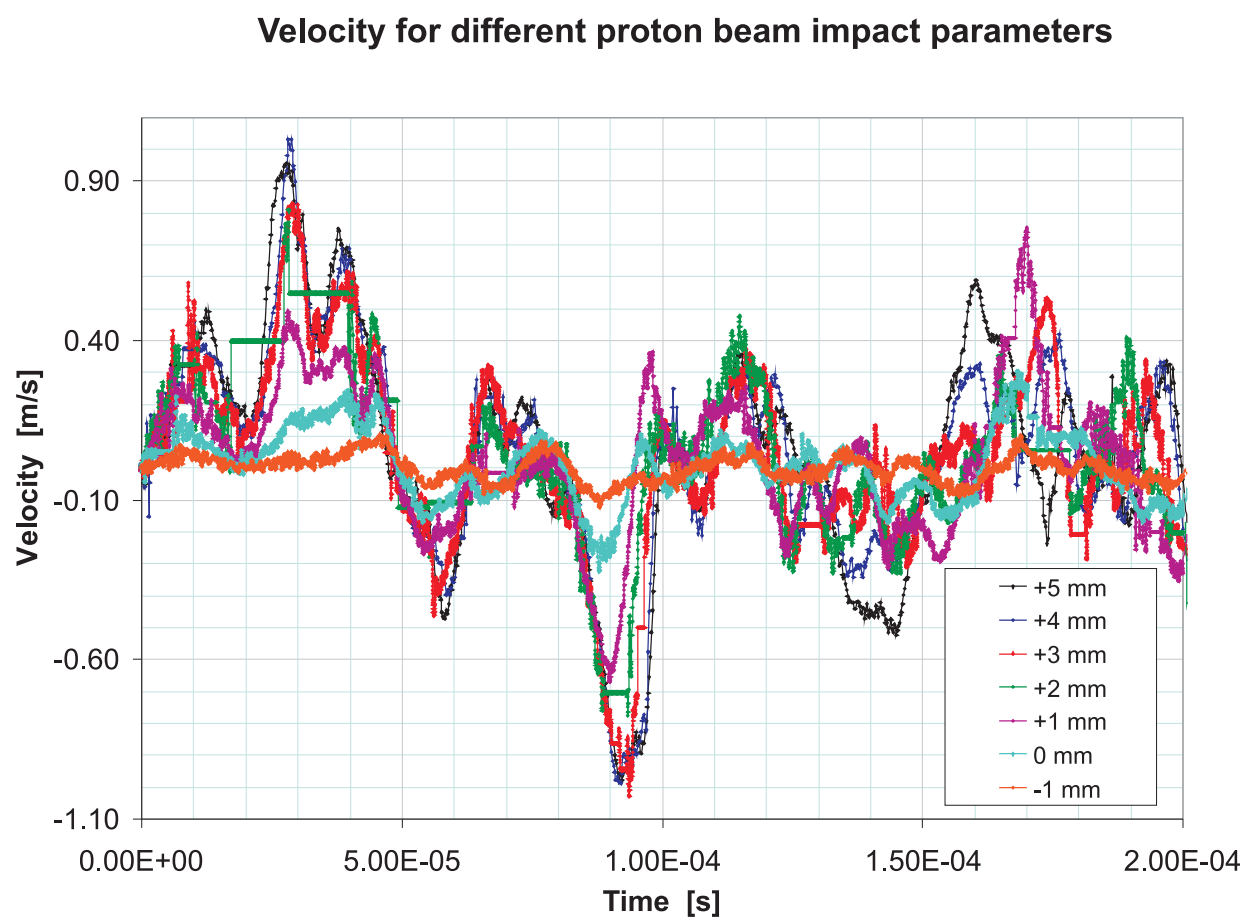


Figure 4.30: Plot of the corrected surface velocity signals for different beam impact parameters (from $+5\text{ mm}$ (measurement #18) to -1 mm (measurement #24) in steps of 1 mm) $200\text{ }\mu\text{s}$ of collimator movement. Beam intensity: $28.8 \cdot 10^{12}$, measurement point #3.

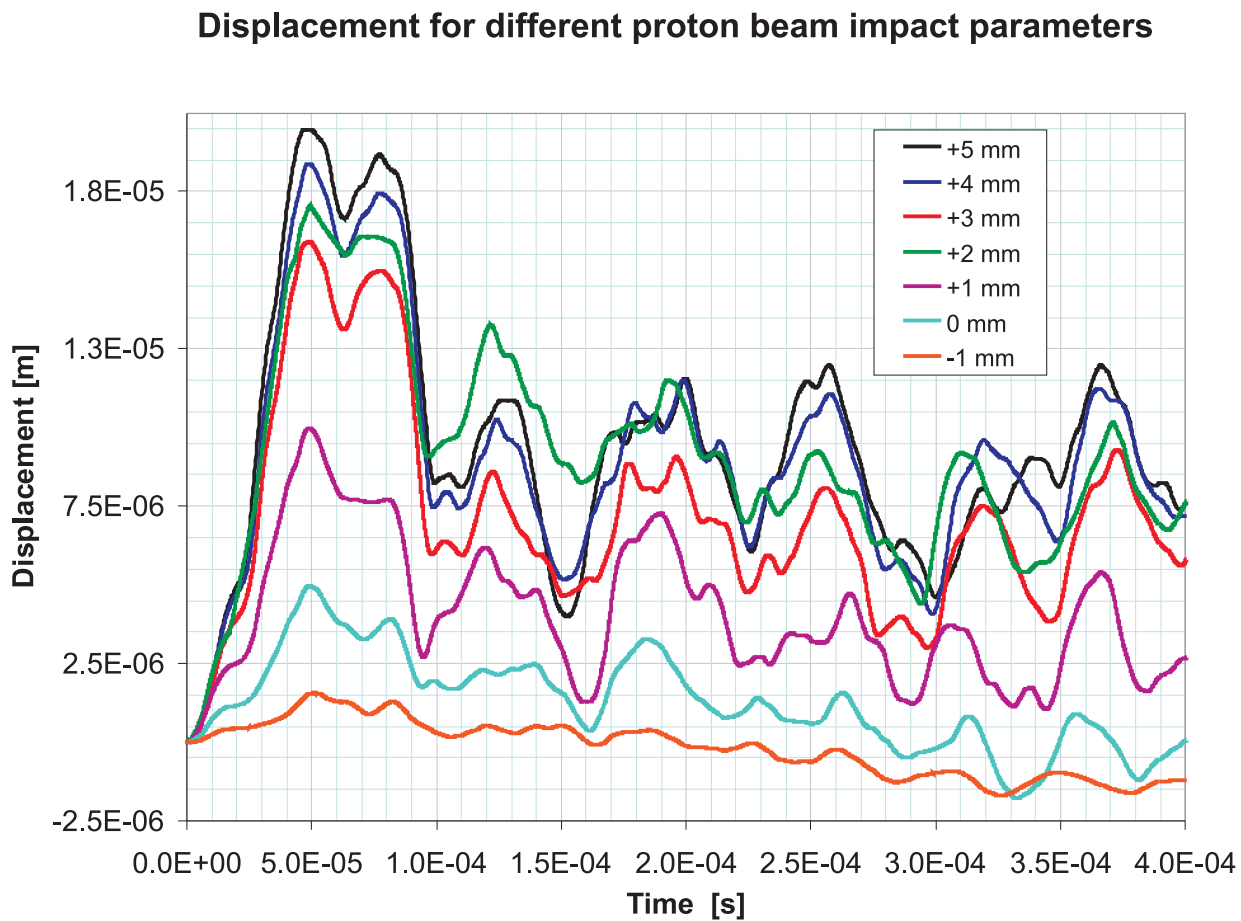


Figure 4.31: Plot of the numerically obtained surface displacement for different beam impact parameters (from $+5\text{ mm}$ (measurement #18) to -1 mm (measurement #24) in steps of 1 mm) for $400\text{ }\mu\text{s}$ of collimator movement. Beam intensity: $28.8 \cdot 10^{12}$, measurement point #3.

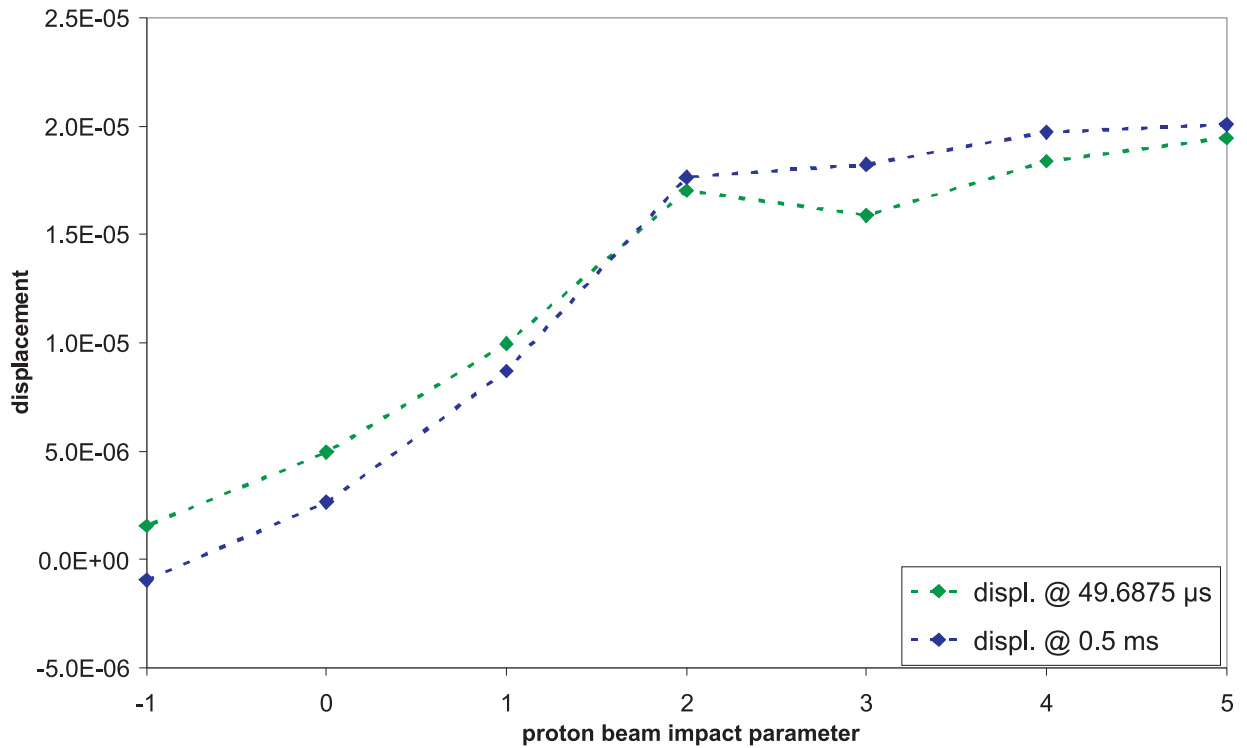


Figure 4.32: Plot of the surface displacement at two different times of collimator movement ($49.6875 \mu s$ and $0.5 ms$) vs. beam impact parameter for a beam intensity of $28.8 \cdot 10^{12}$ protons at measurement point #3. Beam impact parameter varying from $+5mm$ (measurement #18) to $-1 mm$ (measurement #24) in steps of $1 mm$.

of a 5σ beam width, the whole beam would be deposited for beam impact parameters larger than $2 mm$.

Table 4.23: Proton beam width with a FWHM of $1 mm$ assuming a Gaussian beam cross section with dependence on confidence interval (see text around equ. 4.3 on p. 102 for further explanation).

Confidence interval	beam width [mm]	1 σ	2 σ	3 σ	4 σ	5 σ
		68.2%	95.4%	99.7%	99.994%	99.99994%
	for half of beam	0.42	0.85	1.27	1.70	2.12
	for whole beam	0.85	1.70	2.55	3.40	4.25

4.1.4 Summary

The LDV team (Roman Wilfinger, Herta Richter and Jacques Lettry) recorded the velocity-time-signal (and its FFT) of the collimator jaw surface with a LDV device within the TT40 collimator test in November 2006. The data for the velocity-time-signal obtained with the LDV underwent comparisons of reproducibility, of dependence on measurement points, of beam intensity and beam impact parameter. These led to the following results (see also [157]):

- The maximum displacement reached within recording time of the LDV was about $235 \mu m$ at the end of the recording time ($6.34 ms$) at measurement point #3 for a beam intensity of $28.8 \cdot 10^{12}$ protons (= 6 batches) and a beam impact parameter of $+5 mm$ (see section 4.1.3.3.2 p. 93 ff, measurement #18).
- The data is stable versus the sample frequency and the measurements are reproducible (see section 4.1.3.2 p. 79 ff). For two sets of two measurements, the nominal experimental conditions and the settings of the LDV were the same (except for the velocity-resolution), which allowed an estimate of the limit of the error of reproducibility of the overall experimental setup of 18% assuming a 5σ confidence interval (see section 4.1.3.2.2 p. 82 ff).
- The data underlines the dependence on the probed measurement points (see section 4.1.3.3.1 p. 92 ff) and the proton beam parameters such as intensity (see section 4.1.3.3.2 p. 93 ff) and beam impact parameter (see section 4.1.3.3.3 p. 100 ff).
- The displacement at about $50 \mu s$ of collimator movement scales according to beam intensity (see section 4.1.3.3.2 p. 93 ff).

4.2 Irradiation of Metallic Targets with Uranium Ion Beam

The experiment S334 for the investigation of metallic (for CERN) and carbon (for GSI) targets was carried out in August 2007 at the HHT experimental area at GSI [158]. tab. 4.24). The target length for the samples was chosen so that the Bragg peak of each material would lie approximately in the middle of the target axis for the first beam impact (with the exception of the 2 mm targets).

Table 4.24: List of metal targets irradiated at GSI.

target material [–]	cylinder length [mm]	sample number [–]
Cu	2	23
		25
	7	26
		27
		28
Pb	7	20
		21
		22
Ta	5	14
		15
		16
W	5	17
		18
		19

In the preparatory stage of the experiment, a series of simulations had been performed by N. Tahir *et. al.* [159] for all target materials with a set of beam parameters that had been planned for the experiment. The simulations were obtained for a beam kinetic energy of 400 MeV/u and beam sizes ranging from 0.2 to 1 mm (FWHM) using SRIM [160] for the calculation of energy deposition. The simulated beam time structure consisted of either one, two or four bunches with a bunch length of 80 ns (FWHM) impacting within a total pulse duration of either 250, 500 or 1000 ns .

The experiment subsequently ran with different beam parameters (see the detailed summary of all beam parameters in tables B.2 and B.1: the impacting ^{238}U beam from the SIS18 accelerator with a kinetic energy of 350 MeV/u was focused to a beam width between 0.65 and 0.9 mm (FWHM). Beam intensities of between $8.87 \cdot 10^6$ and $2.42 \cdot 10^9$ ions were used to irradiate the metal targets. The beam time distribution for each beam impact on a sample was chosen to be either a single bunch with a width of 300 ns (FWHM) or a four-fold bunch structure consisting of four 80 ns (FWHM) evenly distributed bunches within about 1 μs (see fig. 4.33). Each of the samples received a minimum of two consecutive beam impacts, separated by between 2 and 26 minutes.

During the experiment the oscillations of the lateral area of the samples were recorded with a Laser Doppler Vibrometer (LDV) [158]. After the test, the irradiated specimens

were investigated at CERN [161]: the investigations revealed beam offsets with respect to the target cylinder axis well below 0.5 mm for most of the targets.

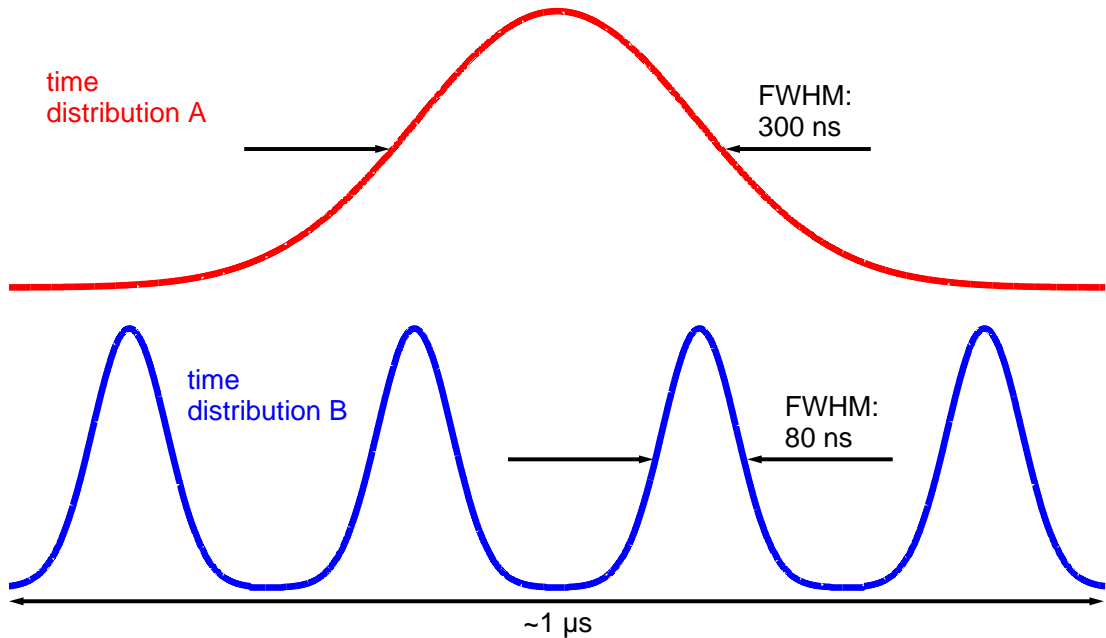


Figure 4.33: Schematic pulse time distribution of the experiment at GSI. Distribution A: single bunch with width of 300 ns (FWHM). Distribution B: four equally strong and evenly spaced bunches with a peak-to-peak-spacing of 260 ns and a bunch width of 80 ns (FWHM).

Chapter 5

Simulating Dynamic Target Response upon Impact of Uranium Ion Beams

Well focused high intensity particle beams deposit large amounts of energy within the material they irradiate. For beam intercepting devices (BID), where structural integrity and lifetime are important issues, it is of interest to understand the dynamic response of the target, especially for pulsed beam time distributions. In this chapter, the Monte Carlo code FLUKA([1],[2]) was used to calculate the energy deposited by the particle beam in a static target, and the explicit code ANSYS AUTODYN® [3] modeled the non-linear dynamic response of the target. With significant structural changes to the target, any given incident particle bunch will interact with a different target volume compared to its predecessor. This important effect can be taken into account by running a new FLUKA simulation on the altered geometry, whose energy deposition map can then be used as a new input for the modified ANSYS AUTODYN® model. ANSYS AUTODYN® is a conventional hydrocode which has a large database of generic material models. However, one is limited not only by the code and the solvers themselves, but also by the parameters given for the material. Data on dynamic phenomena due to large energy densities is scarce and some parameters poorly known. This chapter summarizes the attempt to simulate the dynamic response of targets subjected to a highly focused uranium ion beam with a commercially available hydrocode.

5.1 Energy Deposition Simulation

The incident uranium ion beam deposits its energy in the target material. In order to calculate the energy deposition profile the FLUKA code was used. The main development version FLUKA2009¹ was used to obtain the results presented here.² The input files used for running the FLUKA simulations for this whole chapter were modified versions of a template provided by [162]. One should be aware that the newly released FLUKA2011 version contains an improved calculation of the stopping power for high Z projectiles [163].

¹ FLUKA2009 Version 0.0 Nov-24 by A. Ferrari, using DPMJET event generator version 3.0 and particle production model RQMD version 2.4.

² The specific FLUKA cards and their settings can be found in tab. A.1 on p. 139 in Appendix A.

5.1.1 Energy Deposition Simulation for Copper

The resultant peak energy density for the two copper samples 26 and 28 can be seen in tab. 5.1. There, the results for the second shot on sample 28 are only quoted for the preferred case of a simplified ejection geometry (see section 5.3.1 starting on p. 117 for details). The maximum peak energy density reached for each of the two samples was $2.32 \cdot 10^3$ and $2.34 \cdot 10^3$ [J/g], respectively. 97 % of the incident energy was deposited within the target, with the exception of 92 % for shot 2 on sample 28 where a simplified target geometry after material ejection – again only considering the preferred case – was assumed (see fig. 5.15(a) – 5.15(c) on p. 127). Fig. 5.1 on p. 111 displays the energy deposition for the beam parameters given for sample 26 – assuming an unchanged target for each of the eight consecutive beam impacts. Fig. 5.2(b) on p. 111 shows the energy profile – with a larger beam width ($FWHM = 0.9$) – around the Bragg peak only for the first shot on sample 28. For the two considered cases of the second shot – see explanations of section 5.3.1.2 on p. 126 – the energy deposition is displayed in figures 5.3(a) on p. 112 for the first case (fig. 5.15(a) – 5.15(c) on p. 127) and 5.4(a) on p. 112 for the second case (fig. 5.16(a) – 5.16(c) on p. 128).

Table 5.1: Uranium ion beam parameters for two 7 mm long copper samples irradiated with time distribution A and a kinetic energy of 350 MeV/u resulting in a total available beam energy per incident ion of 83.3 GeV. Calculations of total deposited energy and peak energy density were performed with FLUKA. The peak energy density is the energy density in the Bragg peak, assuming an intact target for each shot (exception: shot 2 on sample 28 was obtained for preferred simplified target geometry after material ejection – see fig. 5.15(a) – 5.15(c) on p. 127). The density of copper was taken to be 8.9 g/cm³.

shot on sample	beam intensity [–]	beam size (FWHM) [mm]	total deposited energy [J]	peak energy density [J/g]
<i>sample 26</i>				
1	$1.48 \cdot 10^8$	0.85	1.92	$1.62 \cdot 10^2$
2	$1.52 \cdot 10^8$	0.85	1.97	$1.67 \cdot 10^2$
3	$3.19 \cdot 10^8$	0.85	4.13	$3.49 \cdot 10^2$
4	$5.11 \cdot 10^8$	0.85	6.62	$5.60 \cdot 10^2$
5	$5.87 \cdot 10^8$	0.85	7.60	$6.43 \cdot 10^2$
6	$8.89 \cdot 10^8$	0.85	11.51	$9.74 \cdot 10^2$
7	$8.59 \cdot 10^8$	0.85	11.12	$9.41 \cdot 10^2$
8	$2.12 \cdot 10^9$	0.85	27.44	$2.32 \cdot 10^3$
Total	$5.59 \cdot 10^9$	-	72.30	$6.12 \cdot 10^4$
<i>sample 28</i>				
1	$2.22 \cdot 10^9$	0.9	28.76	$2.20 \cdot 10^3$
2	$2.36 \cdot 10^9$	0.9	29.03	$2.34 \cdot 10^3$
Total	$4.58 \cdot 10^9$	-	57.79	$4.54 \cdot 10^3$

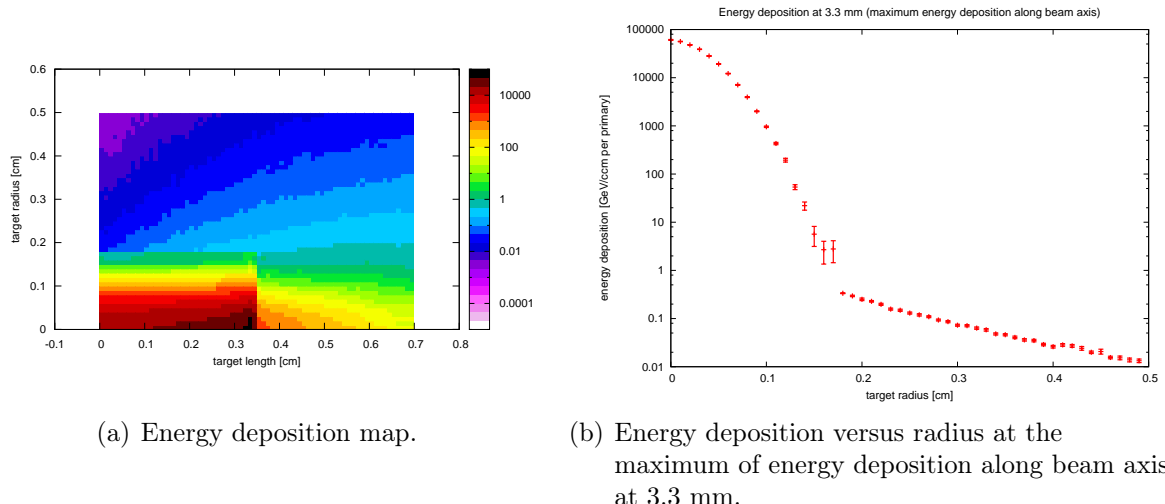


Figure 5.1: FLUKA simulation results for uranium ion beam with kinetic energy of $350 \text{ MeV}/u$ with Gaussian distribution (FWHM of 0.85 mm) impacting from left. Energy deposition is integrated over the whole polar angle given in GeV/cm^3 per incident primary in steps of 0.1 mm along beam axis and radius.

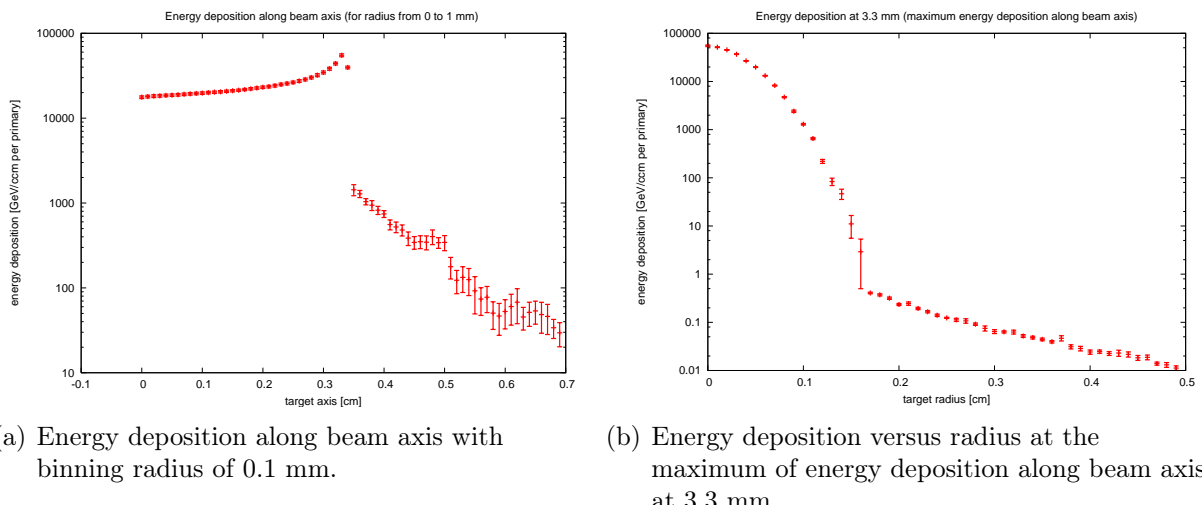


Figure 5.2: FLUKA simulation results for uranium ion beam with kinetic energy of $350 \text{ MeV}/u$ with Gaussian distribution (FWHM of 0.90 mm) impacting from left. Energy deposition is integrated over the whole polar angle given in GeV/cm^3 per incident primary in steps of 0.1 mm along beam axis and radius.

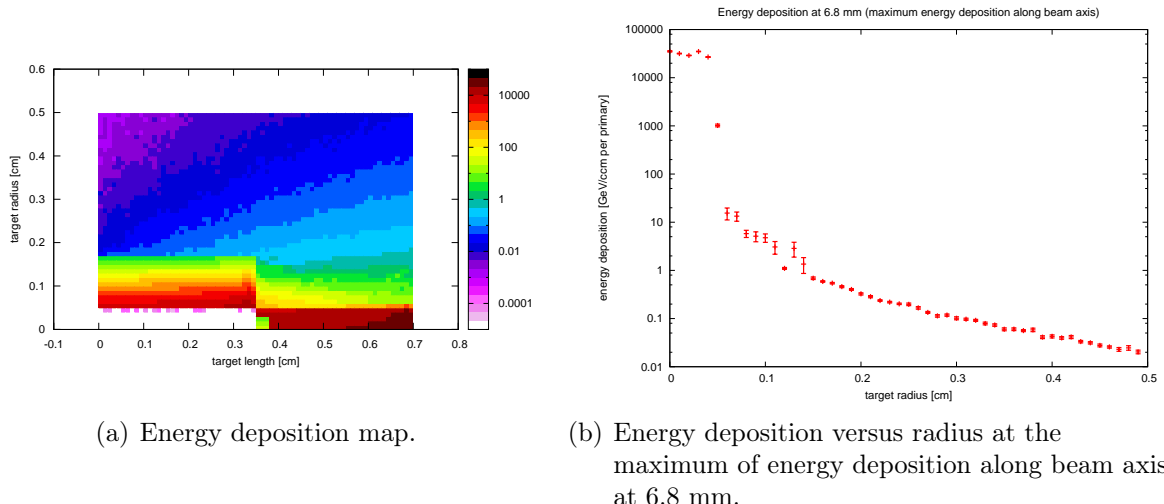


Figure 5.3: FLUKA simulation results for uranium ion beam with kinetic energy of 350 MeV/u with Gaussian distribution (FWHM of 0.9 mm) impacting from left. Energy deposition is integrated over the whole polar angle given in GeV/cm^3 per incident primary in steps of 0.1 mm along beam axis and radius.

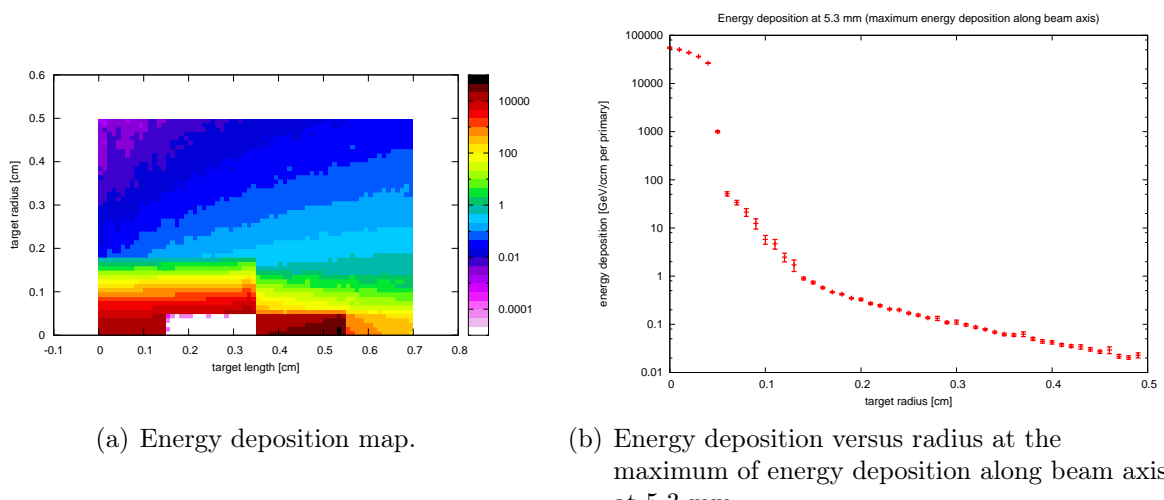


Figure 5.4: FLUKA simulation results for uranium ion beam with kinetic energy of 350 MeV/u with Gaussian distribution (FWHM of 0.9 mm) impacting from left. Energy deposition is integrated over the whole polar angle given in GeV/cm^3 per incident primary in steps of 0.1 mm along beam axis and radius.

5.2 Simulating Dynamic Response

5.2.1 Material Description

ANSYS AUTODYN® simulates the target response by solving the conservation laws of mass, momentum and energy in combination with the given material model, initial and boundary conditions. The material model comprises the equation of state (EOS), the strength model and the failure model. The EOS governs the hydrostatic component of the stress tensor. The deviatoric components are determined through the constitutive relations of the strength model. The failure model accounts for the fact that materials cannot sustain infinite tensile stresses. There are different solvers available within ANSYS AUTODYN® to allow the simulation of dynamic material response. Apart from Eulerian and Lagrangian solvers, there is also an Smooth Particle Hydrodynamics (SPH) solver [164] which was used for this work.³ One needs to note that heat conduction within ANSYS AUTODYN® is not implemented for the SPH solver.

All simulations presented here have been obtained with 2D models⁴ with axial symmetry – justified due to the small beam offset (see the paragraph on the first metallurgical examinations in sect. 4.2 on page 108) – and a SPH particle size of 0.1 mm (the same energy binning as for the FLUKA models). One should keep in mind that the size of the SPH particle has a direct impact on the maximum possible time for each calculation step [3]: the numerical stability of the solution can be achieved by observing the maximum time-step length given by the Courant-Friedrichs-Lowy (CFL) condition – sometimes shortened to "Courant condition":

$$\Delta t \leq \frac{d}{c + \frac{|u|}{k_n}} \quad (5.1)$$

where Δt is the maximum possible time step for a given local configuration, d is the local dimension of the SPH particle, c is the local speed of sound, u is the local SPH particle velocity due to material flow, and k_n is a velocity safety factor which can be chosen from $0.0 < k_n \leq 1.0$; in all performed simulations the recommended default value of $k_n = 1.0$ was used. An extra hard-coded safety factor of $\frac{2}{3}$ is implemented in ANSYS AUTODYN® reducing the time step even more than the CFL condition in equ. (5.1). For a speed of sound of 5000 m/s (rough range for metals), the given SPH particle size of 0.1 mm and assuming no material flow, equ. (5.1) results in a maximum time-step of 20 ns (without taking into account the hard-coded safety factor of $\frac{2}{3}$).

Another criterion for the time-step needs to be entered into the simulations, to take into account that the full energy deposition needs to happen during the length of the bunch. If the time-step was very large but the bunch length very short, the energy deposition would not be fully loaded into the dynamic model leading to gross underestimates. For all shown simulations this time-step was kept at 16 ns. This would allow for a minimum of 18 instances of the fractionized energy depositions for a bunch length of 300 ns.

As the common failure model, the hydrodynamic tensile limit (HTL or P_{MIN}) model was chosen: when the hydrostatic component of the stress tensor reaches a value below

³ See section 5.2.2 starting on p. 115 for the rationale.

⁴ Initially, simulations were performed with 3D models with varying beam offset as the results of the metallurgical examinations were not available.

a certain pressure (P_{MIN}), it results in bulk failure [3]. The reheat option was disabled, resulting in a hydrostatic component of the stress tensor equal to zero after failure. In the experiment, the targets were mounted in a groove so that the movement of the sample perpendicular to the incident ion beam was suppressed (see [158] for the technical drawing of the sample holder). A screw slightly pressing the sample into the groove prevented the sample from shifting in the direction of the ion beam axis. It can be expected that both ways of fixation damped the oscillation of the samples. In the simulation, however, any asymmetry of the mounting was not accounted for by applying boundary conditions for free surfaces.

5.2.1.1 Copper

At first, two 7 mm long copper samples were considered. Out of the available models in ANSYS AUTODYN® (see tab. 5.2), the following subset was chosen: the EOS was chosen to be the Tillotson EOS [111]. The Johnson-Cook strength model was derived for oxygen free high conductivity (OFHC) copper [99].

Table 5.2: Available material models for copper in ANSYS AUTODYN®.

Material	EOS	Strength	Failure	Reference
Cu	Shock	-	-	[165]
Cu	Tillotson	-	-	[111]
OFHC-Cu	Shock	Steinberg-Guinan	-	[166]
OFHC-Cu	Linear	Zerilli-Armstrong	-	EOS: [167] Yield: [168]
OFHC-Cu	Linear	Johnson-Cook	-	[167]
Cu	Shock	Piecewise Johnson-Cook	-	[169]
OFHC-Cu	Linear	Johnson-Cook	Johnson-Cook	[167]

The choice of the EOS, the strength and failure models and the solver implicates the following limitations which have to be taken into account when interpreting the outcome of the simulations: the Tillotson EOS [111] is given in analytical form and was obtained for hypervelocity impacts covering a pressure range from 0 up to about 100 TPa. This was achieved by combining Thomas-Fermi statistical theory for the high pressure region (1 – 100 TPa) and data from shock experiments for the low pressure region (up to 1 TPa). In addition, the Tillotson EOS does not describe materials under tension specifically.

The Johnson-Cook strength model [99] includes strain hardening, the effect of strain rate and thermal softening. The constants describing these effects were obtained through fitting data from torsion tests with strain rates up to about 400 s^{-1} and dynamic Hopkinson bar tensile tests. Simulations with the Johnson-Cook strength model were then compared with the outcome of cylindrical impact tests. The agreement of numerical simulations and experimental results for the OFHC copper were not as good as for the other target materials (Armco iron and 4340 steel) but still considered acceptable by the authors of [99]. In the Johnson-Cook strength model, the yield stress Y is defined – in the notation of ANSYS AUTODYN® (compare to its notation in equ. (3.36) on p. 48) – as:

$$Y = [A + B\epsilon_p^n] [1 + C \ln \epsilon_p^*] [1 - T_H^m] \quad (5.2)$$

with ϵ_p as the effective plastic strain, ϵ_p^* as the normalized effect plastic strain rate ($\epsilon_p^* = \dot{\epsilon}_p / \dot{\epsilon}_{p,0}$ with the reference strain rate $\dot{\epsilon}_{p,0} = 1.0 \text{ s}^{-1}$), T_H as the homologous temperature (see footnote 96 on p. 49) and the specific material constants A , B , n , C and m (see tab. 5.3).

Table 5.3: Material constants from [99] for equ. (5.2) for OFHC copper.

material constant	name	value	units
A	yield stress at $\epsilon_p^* = 1 \text{ s}^{-1}$ and $T_H = 0$	$9.0 \cdot 10^4$	kPa
B	strain hardening constant	$2.92 \cdot 10^5$	kPa
n	strain hardening exponent	$3.1 \cdot 10^{-1}$	–
C	strain rate constant	$2.5 \cdot 10^{-2}$	–
m	thermal softening exponent	1.09	–
T_m	melting temperature	1356	K

The P_{MIN} failure model represents the most simplified model of material failure as the threshold does not depend on any other quantity [3]. However, from spall experiments it is known that the spall strength of a material depends on different parameters⁵, such as the shock amplitude (see e.g. [170], [171] and [172]), stress rate (see e.g. [173]), cleanliness, grain size and porosity of the material (see e.g. [174], [175] and [176]) predeformation (see e.g. [177]) and temperature (see e.g. [178]). As previously mentioned, when choosing the SPH solver one also needs to be aware that thermal heat dissipation by conduction or radiation is not included.

Notably, the EOS, the strength and failure models have not been developed together. In addition, the most important limitations of the parts comprising the present model are summarized as follows:

- Inclusion of phase changes reached by shock processes but no specific formulation for material under tension
- Strength model developed for OFHC copper though likely that the OFHC copper was not used in the experiment
- Target failure upon reaching constant threshold
- No conventional heat transfer mechanisms (conduction, radiation, convection)

5.2.2 Interfacing ANSYS AUTODYN[®] with FLUKA

The static energy deposition map was read via a user subroutine into the hydrocode ANSYS AUTODYN[®] as an additional load with the following time characteristic: each bunch was approximated with a simple rectangular function with the deposition time equal to the FWHM of the measured bunch width (see fig. 5.5 on p. 116 for an example of the single bunch beam time distribution). Even though the pressure front is influenced by the steepness of the shoulder of the energy deposition, this simplification was accepted in order to keep the interface between FLUKA and ANSYS AUTODYN[®] simple for

⁵ An incomplete list follows with publications describing different dependencies investigated in spall experiments.

the first stage of simulations. Both subroutines for 3D (by the author of [179]) and 2D simulations were written for this purpose [180]. In the future it was planned to link FLUKA and ANSYS AUTODYN® completely: for a subsequent beam hit, the deformed SPH target structure obtained by ANSYS AUTODYN® would be read into FLUKA as a voxel geometry⁶. In FLUKA a new energy density map would be calculated and would serve as a new and updated input to the model in ANSYS AUTODYN®. The SPH solver in ANSYS AUTODYN® and the voxel geometry in FLUKA would allow a more compatible interchange of simulations results after implementation of the relevant subroutines.

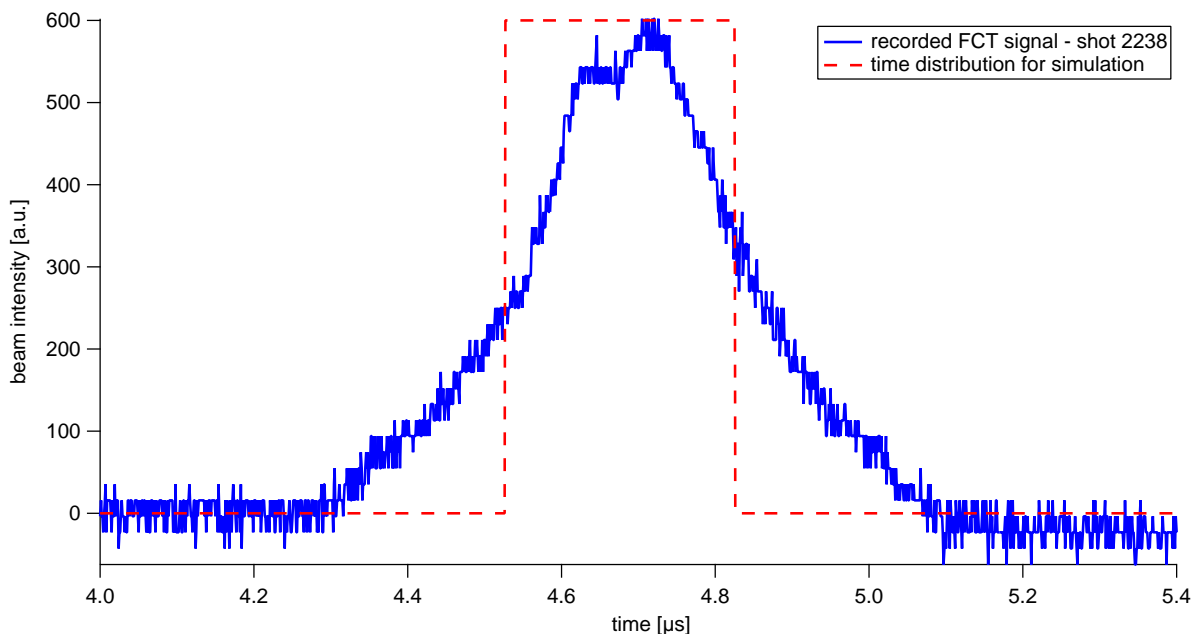


Figure 5.5: Comparison between typical signal (here: shot 2238) of single bunch beam time distribution (distribution A) recorded with fast current transformer (FCT) with simplified beam time distribution used for simulations with ANSYS AUTODYN®. Data of FCT: courtesy plasma physics group at GSI.

5.3 Results

The results of the metallurgical analysis of the irradiated samples have been presented recently [161] and will be published in more detail at a later stage. However, at the time of working on the simulations, few metallurgical results were available [181]. In order to compare metallurgical findings and simulations, an approximative and simple approach has been chosen: failed nodes are used to describe the status of the irradiated targets.⁷

⁶ A voxel is the three-dimensional equivalent of a pixel and is the volume element of which structures, e.g. human organs – or other more complicated ("fringed") structures – can be comprised in FLUKA

⁷ The approach described below is slightly more complex than in the first published results in [182]. In [182] plots of material status have been used which show the status of the material with respect to the previous cycle. For the display of failed notes, there is no difference between these two methods [183]. As the ejection criteria was only based on failed nodes, no modifications of the method used for [182] had to be taken into account.

Fragment plots – as they are called in the terminology of ANSYS AUTODYN® – omit these failed nodes from the presentation and leave elastically and plastically deformed nodes. When the minimum and maximum values for a plot of effective plastic strain are set very low⁸ and a contour plot with only two colors is chosen, one can easily distinguish between nodes that deformed elastically throughout the whole simulation and those that did so plastically [184].

On a plot of yield stress nodes, the nodes of yield stress 0 kPa can either be obtained through reaching the failure condition or through thermal softening if this is implemented in the strength model. By choosing a fragment plot while displaying the yield stress, one is left with only nodes that have been thermally softened. The combination of these plots allows for a first understanding of the status of the irradiated target. For this work, only failed nodes are assumed to not be part of the lattice while softened nodes were still assumed to be part of the simulated target samples.

5.3.1 Copper

The first two samples of copper which have been simulated within this work are sample nr. 26 and 28 which were irradiated with the time distribution A of fig. 4.33 on p. 108. The ion beam parameters for the two samples are summarized in tab. 5.1 on p. 110. The simulated time covered 5 ms after beam impact.

In all performed simulations, the influence of the strength model on the yield stress is dominated by effective (plastic) strain with some contribution due to temperature increase while the effect of the effective plastic strain rate is low. This is not surprising, as the strain rate constant (see tab. 5.3 on p. 115) in equ. (5.2) on p. 114 is smaller than the constants governing strain hardening and thermal softening.

5.3.1.1 Simulation of Sample 26

5.3.1.1.1 Simulation Results

Three out of eight shots (namely 5, 7 and 8) were simulated to obtain a first indication of material degradation. For this purpose, each of the simulations was carried out on an intact target. For each of these three intensities three different values for the hydrodynamic tensile limit were assumed (-216 MPa, -1.08 GPa and -5.4 GPa), which lie within the range of measured spall strengths (see [170]–[178]).

The simulation for the lowest P_{MIN} value (-216 MPa) already showed target bulk failure for the shot with the lowest simulated intensity (see fig. 5.6 on p. 119). Only the highest beam intensity for a P_{MIN} value equal to -5.4 GPa resulted in bulk failure in a confined area around the Bragg peak (see figures 5.7(g) – 5.7(i) on p. 120). Very similar behavior was observed when a P_{MIN} of -3.24 GPa was assumed for an ion beam intensity of $2.12 \cdot 10^9$ (see fig. 5.8 on p. 121). However, for the model with a P_{MIN} of -1.08 GPa the following observations were made (see fig. 5.9 on p. 122): it was found that for intensities below $5.87 \cdot 10^8$ uranium ions the simulation shows no destruction (see figures 5.9(a) – 5.9(c)). For the intensity of $8.59 \cdot 10^8$ bulk failure was observed in the confined area around the Bragg peak, but no material was ejected from the target (see figures 5.9(d) – 5.9(f)). For the highest intensity ($2.12 \cdot 10^9$) only, bulk failure occurred from the entry point of the

⁸ Suggested to be set as low as $1 \cdot 10^{-5}$ and $2 \cdot 10^{-5}$, respectively. [184].

uranium ion beam up to the Bragg peak, which led to material ejection (see figures 5.9(g) – 5.9(i)). The progression of bulk failure in this simulation had already come to rest at around 2 ms (see fig. 5.10 on p. 123).

5.3.1.1.2 Comparison with Metallurgical Examination and BIG-2 Code

The metallurgical examination of sample 26 in fig. 5.11(a) on p. 123 shows that – despite taking eight shots of increasing intensities – the target was only partially shot through. The estimated depth of the ejection zone of about 3.8 mm coincided closely with the expected position of the Bragg peak in an intact target at 3.3 mm (see fig. 5.1 on p. 111). Therefore it was deduced that only the highest intensity shot caused the observed destruction of the target.

The simulation for the lowest P_{MIN} value (-216 MPa) already showed target bulk failure for the shot with the lowest simulated intensity (see fig. 5.6(a) – 5.6(c) on p. 119) and hence could be ruled out due to experimental observation [161]. Both models with a P_{MIN} of -5.4 and -3.24 GPa (figures 5.7 on p. 120 and 5.8 on p. 121) were ruled out, as neither exhibits an ejection cone for the impact with the highest beam intensity.

As can be seen in fig. 5.11(b) on p. 123, the depth of the ejected region of sample 26 from the simulation with P_{MIN} equal to -1.08 GPa about the same as the one observed experimentally. Therefore it was deduced that out of the limited amount of trials the P_{MIN} value of -1.08 GPa was a reasonable choice for the next simulation steps. It is however noteworthy that the simulation model did not reproduce the details inside the ejection region. This can be better seen in the more detailed micrography in fig. 5.12 on p. 124 where a plug whose crystal structure looks different from its surrounding blocks for around the first third of the beam penetration depth.

In fig. 5.13 on p. 125, one can see for the model with a P_{MIN} of -1.08 GPa that the maxima of both the pressure in the Bragg peak and the equivalent to the velocity history obtained with the LDV scale approximately linearly with uranium ion beam intensity for the latter model.

Unfortunately, it is difficult to compare the results of the simulation between the two codes ANSYS AUTODYN® and BIG-2 – as part of the preparatory study [159] – since the beam parameters of the simulations are already different (see tab. 5.4 on p. 124). Tab. 5.4 also shows that even for a similar employed maximum specific energy deposition, one does not obtain the same value for the first maximum of the surface velocity of 4.65 m/s (fig. 5.13) and ~2.2 m/s (see fig. 2.e of [159]), respectively, nor for the first maximum of the surface pressure of 3.44 MPa (see fig. 5.13) and ~7.3 MPa (see fig. 2.d of [159]). Although the peak energy density was similar for both simulations, the total beam intensity underlying the ANSYS AUTODYN® results was a factor of four higher than for the BIG-2 simulation.

It is difficult to pinpoint the cause of this difference to just one simple factor as there are a variety of differences between the two codes:

- While FLUKA-ANSYS AUTODYN® version uses a static energy deposition map, BIG-2 adjust its energy deposition to the dilution of the material density upon heating.
- BIG-2 progressed through many years of theoretical, experimental and computation work with the sole purpose of being a versatile tool used for highly dynamic and high

CHAPTER 5. SIMULATING DYNAMIC TARGET RESPONSE

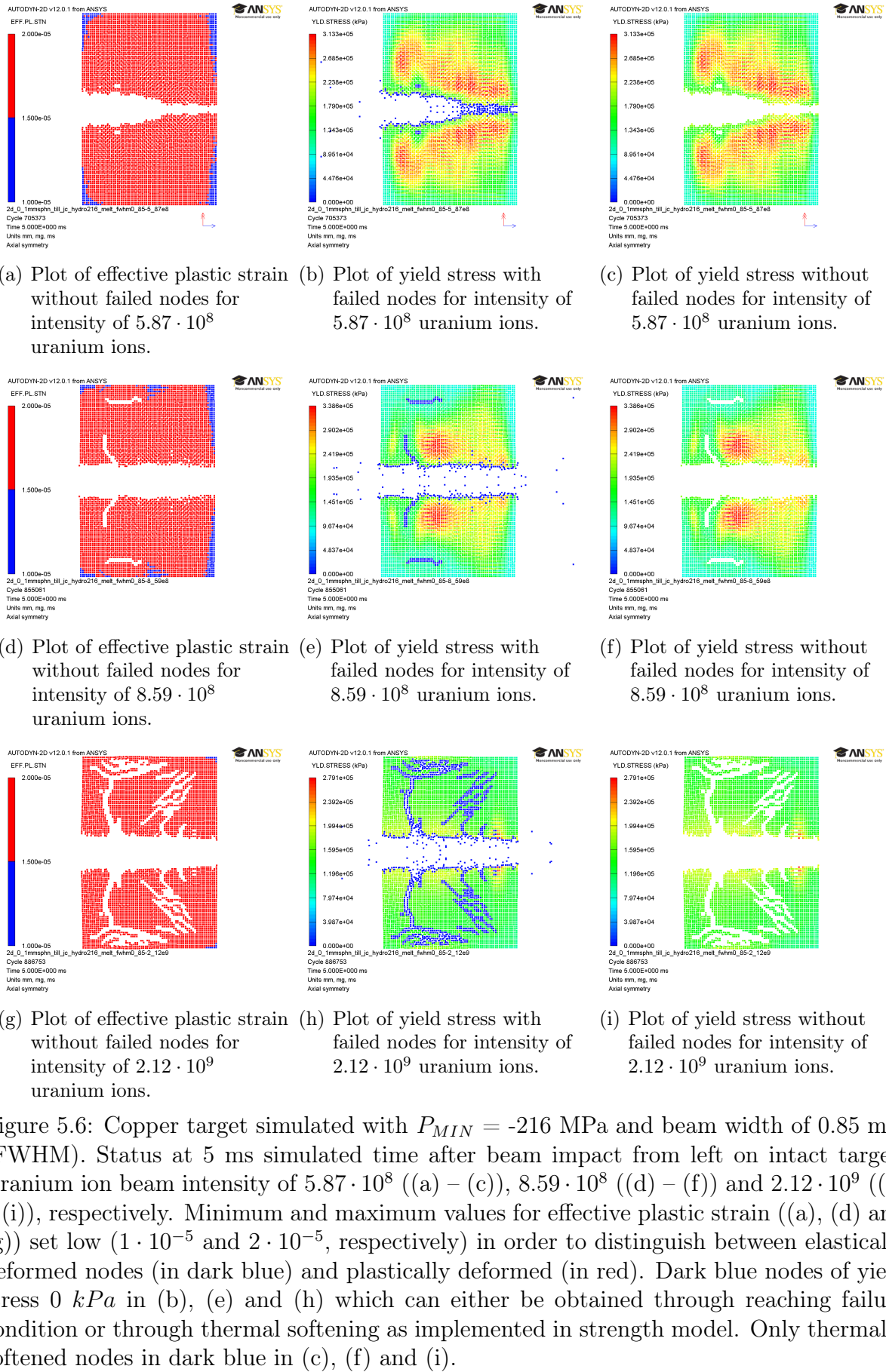


Figure 5.6: Copper target simulated with $P_{MIN} = -216$ MPa and beam width of 0.85 mm (FWHM). Status at 5 ms simulated time after beam impact from left on intact target. Uranium ion beam intensity of $5.87 \cdot 10^8$ ((a) – (c)), $8.59 \cdot 10^8$ ((d) – (f)) and $2.12 \cdot 10^9$ ((g) – (i)), respectively. Minimum and maximum values for effective plastic strain ((a), (d) and (g)) set low ($1 \cdot 10^{-5}$ and $2 \cdot 10^{-5}$, respectively) in order to distinguish between elastically deformed nodes (in dark blue) and plastically deformed (in red). Dark blue nodes of yield stress 0 kPa in (b), (e) and (h) which can either be obtained through reaching failure condition or through thermal softening as implemented in strength model. Only thermally softened nodes in dark blue in (c), (f) and (i).

CHAPTER 5. SIMULATING DYNAMIC TARGET RESPONSE

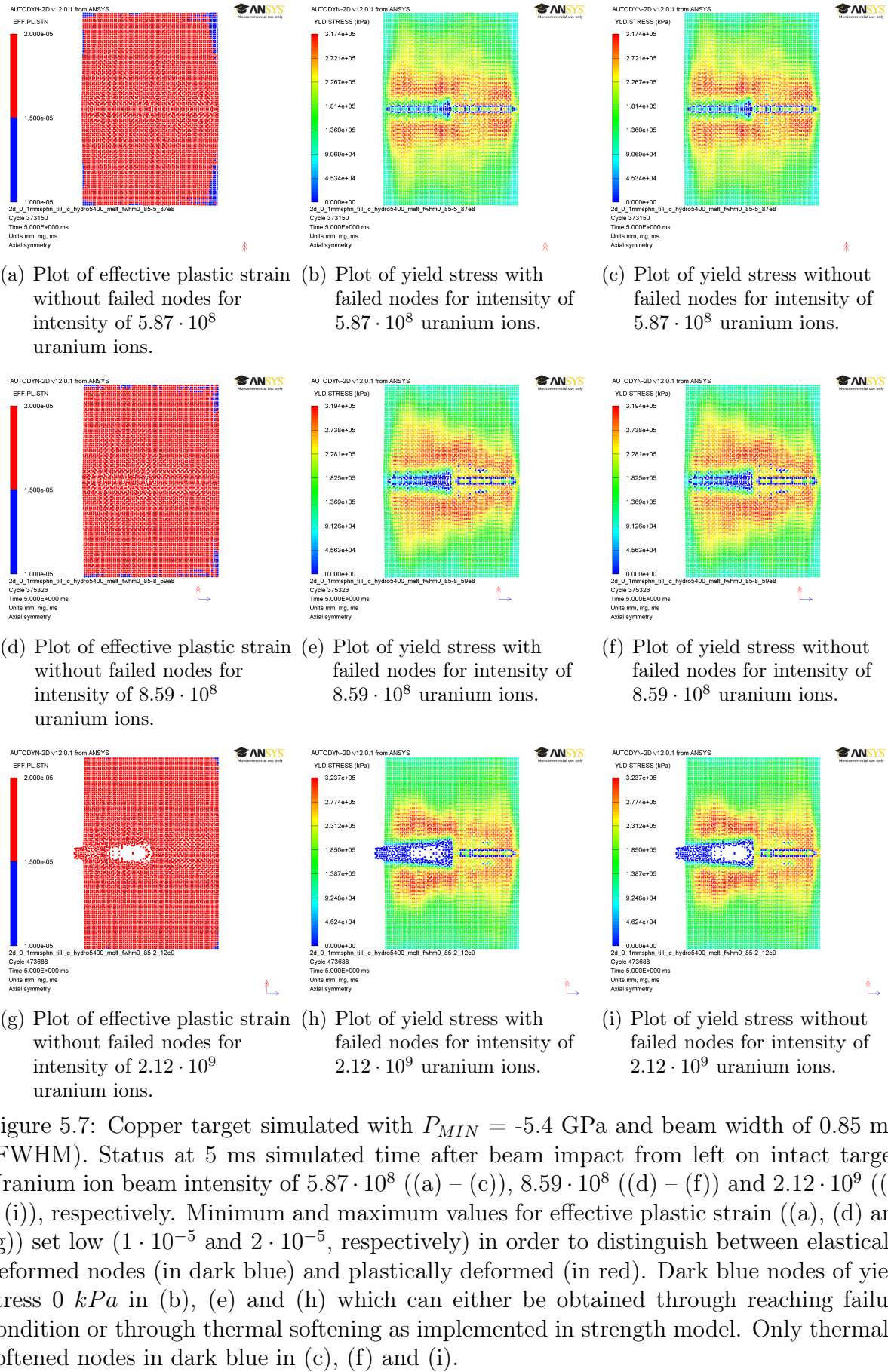
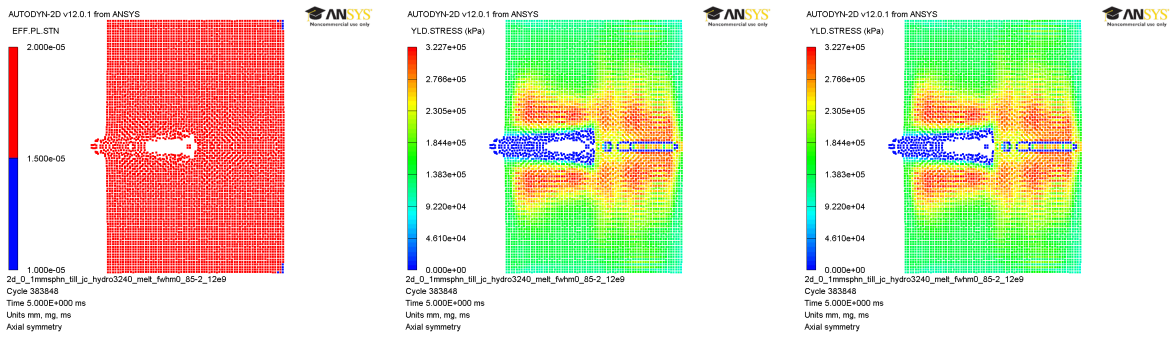


Figure 5.7: Copper target simulated with $P_{MIN} = -5.4$ GPa and beam width of 0.85 mm (FWHM). Status at 5 ms simulated time after beam impact from left on intact target. Uranium ion beam intensity of $5.87 \cdot 10^8$ ((a) – (c)), $8.59 \cdot 10^8$ ((d) – (f)) and $2.12 \cdot 10^9$ ((g) – (i)), respectively. Minimum and maximum values for effective plastic strain ((a), (d) and (g)) set low ($1 \cdot 10^{-5}$ and $2 \cdot 10^{-5}$, respectively) in order to distinguish between elastically deformed nodes (in dark blue) and plastically deformed (in red). Dark blue nodes of yield stress 0 kPa in (b), (e) and (h) which can either be obtained through reaching failure condition or through thermal softening as implemented in strength model. Only thermally softened nodes in dark blue in (c), (f) and (i).



(a) Plot of effective plastic strain without failed nodes. (b) Plot of yield stress with failed nodes. (c) Plot of yield stress without failed nodes.

Figure 5.8: Copper target simulated with $P_{MIN} = -3.24$ GPa, intensity of $2.12 \cdot 10^9$ uranium ions and beam width of 0.85 mm (FWHM). Status at 5 ms simulated time after beam impact from left on intact target. Minimum and maximum values for effective plastic strain (a) set low ($1 \cdot 10^{-5}$ and $2 \cdot 10^{-5}$, respectively) in order to distinguish between elastically deformed nodes (in dark blue) and plastically deformed (in red). Dark blue nodes of yield stress 0 kPa in (b) which can either be obtained through reaching failure condition or through thermal softening as implemented in strength model. Only thermally softened nodes in dark blue in (c).

energy density physics while the combination of FLUKA and ANSYS AUTODYN[®] has only been developed in [180] on a comparably crude basis.

- The different models for the EOS, the strength and failure criteria used for simulating the results in this FLUKA-ANSYS AUTODYN[®] have not been developed together while BIG-2 is developed with these different aspects in mind, leading to a multi-parameter description connecting different physics-regimes.
- The results of the FLUKA-ANSYS AUTODYN[®] modeling attempts closest to the observed experimental reality has been achieved by varying only one parameter, the hydrodynamic tensile limit P_{MIN} . The assumption of a constant value which is related to the spall fracture is already a strongly simplified working premise.
- Years of theoretical and experimental work for BIG-2 with specific dedication to the described field of physics stand on a more sound basis, both theoretically and experimentally, than the current "composite" of FLUKA – used for matter not undergoing phase changes upon beam interaction – and ANSYS AUTODYN[®] – applied mainly in highly dynamic events such as solid-on-solid or explosive-on-solid interaction, often in different energy (density) regimes, which are based on different physical models.

As a first hint of the surface velocities measured in reality is the first, but still preliminary assessment of the LDV measurements [161] for sample 26 on slide 10: all presented velocities are below 4 m/s. However, it is true for both simulation codes in tab. 5.4 on p. 124 that their results are based on an entirely intact, unirradiated and unrestrained target and no offset of the impinging beam. The oscillation patterns of both simulation codes (see fig. 5.14 on p. 125 and fig. 2.e in [159]) are different from one another and neither reproduces the sequence as it was recorded in the experiment (see figure from [161] on

CHAPTER 5. SIMULATING DYNAMIC TARGET RESPONSE

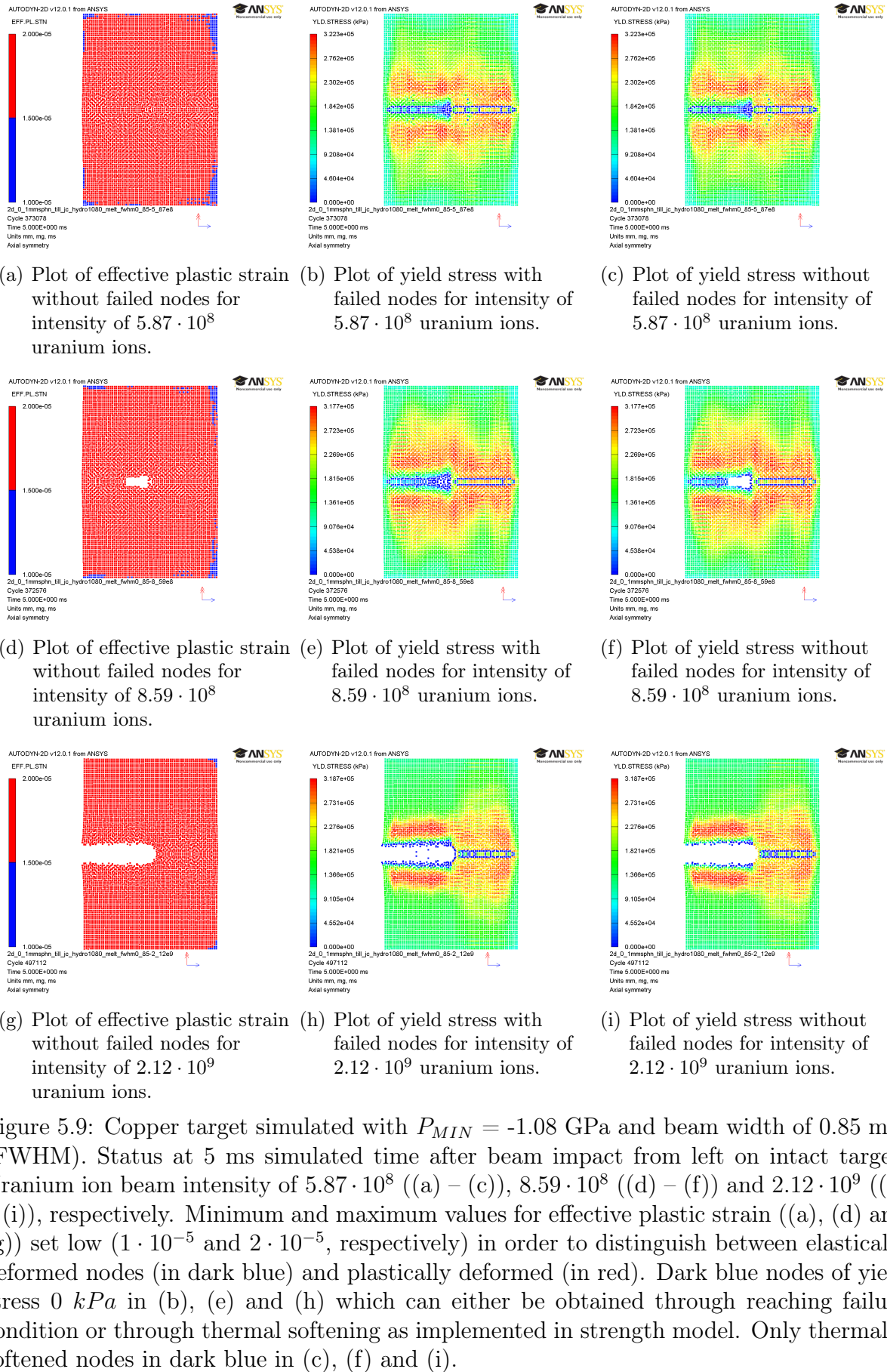
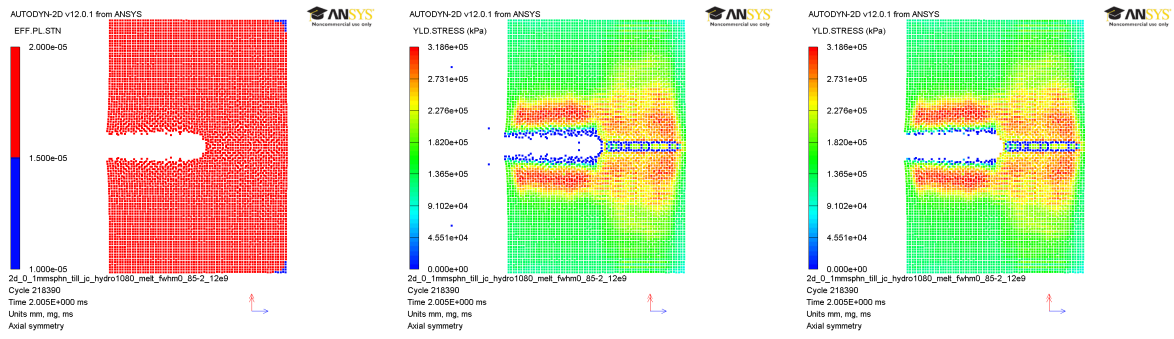
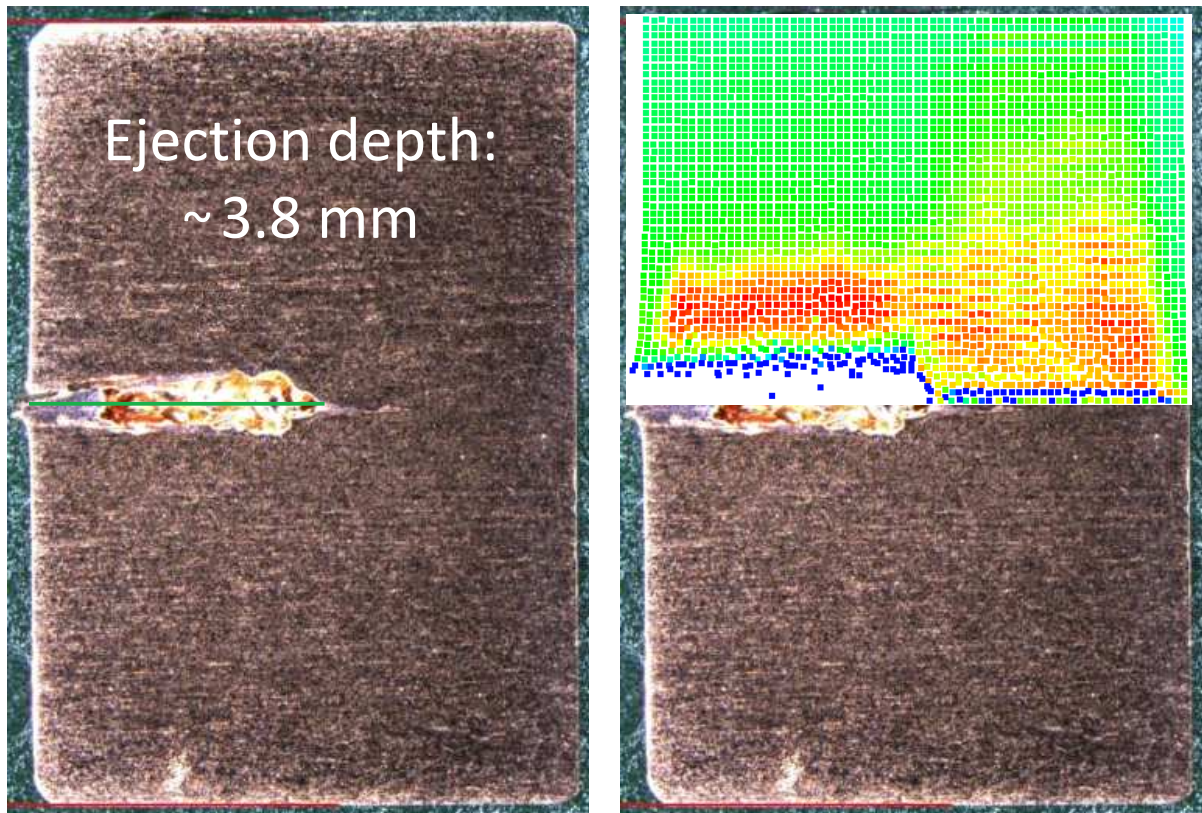


Figure 5.9: Copper target simulated with $P_{MIN} = -1.08$ GPa and beam width of 0.85 mm (FWHM). Status at 5 ms simulated time after beam impact from left on intact target. Uranium ion beam intensity of $5.87 \cdot 10^8$ ((a) – (c)), $8.59 \cdot 10^8$ ((d) – (f)) and $2.12 \cdot 10^9$ ((g) – (i)), respectively. Minimum and maximum values for effective plastic strain ((a), (d) and (g)) set low ($1 \cdot 10^{-5}$ and $2 \cdot 10^{-5}$, respectively) in order to distinguish between elastically deformed nodes (in dark blue) and plastically deformed (in red). Dark blue nodes of yield stress 0 kPa in (b), (e) and (h) which can either be obtained through reaching failure condition or through thermal softening as implemented in strength model. Only thermally softened nodes in dark blue in (c), (f) and (i).



(a) Plot of effective plastic strain (b) Plot of yield stress with (c) Plot of yield stress without
without failed nodes. failed nodes. failed nodes.

Figure 5.10: Copper target simulated with $P_{MIN} = -1.08$ GPa, intensity of $2.12 \cdot 10^9$ uranium ions and beam width of 0.85 mm (FWHM). Status at 2 ms simulated time after beam impact from left on intact target. Minimum and maximum values for effective plastic strain (a) set low ($1 \cdot 10^{-5}$ and $2 \cdot 10^{-5}$, respectively) in order to distinguish between elastically deformed nodes (in dark blue) and plastically deformed (in red). Dark blue nodes of yield stress 0 kPa in (b) which can either be obtained through reaching failure condition or through thermal softening as implemented in strength model. Only thermally softened nodes in dark blue in (c).



(a) Estimated penetration depth about 3.8 mm. (b) Overlay with fig. 5.9(h) from p. 122 – plot of yield stress with failed nodes.

Figure 5.11: Photograph from the metallurgical examination of sample 26. (Micrography courtesy Jacques Lettry et al. [161])

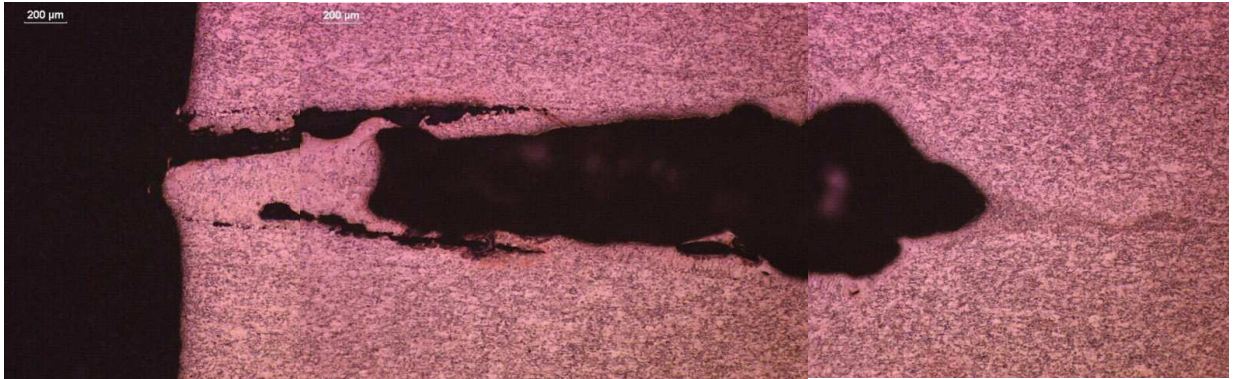


Figure 5.12: Photograph of details of the beam entrance zone from the metallurgical examination of sample 26. (Micrography courtesy Jacques Lettry et al. [161])

slide 10). Despite these limitations one will be able to get more insight from the simulation point of view when measurement results are thoroughly analyzed (e.g. to cross-check possible issues related to calibration factors).

Table 5.4: Beam parameters for simulations obtained with ANSYS AUTODYN[®] (abbreviated AA) and the BIG-2 (abbreviated B2 in the table below) code for comparable maximum energy deposition. Values for BIG-2 are from [159]. Simulation AA was calculated for a single 300 ns bunch (beam time distribution A) while simulation BIG-2 was calculated for two bunches with a FWHM bunch width of 80 ns and a total pulse duration of 500 ns (approximation of beam time distribution B). For the calculation of the peak energy density for AA the density of copper was taken to be 8.9 g/cm³. The initial density for copper for the model run with the BIG-2 code was taken to be 8.93 g/cm³[185].

	beam kinetic energy [MeV/u]	beam size (FWHM) [mm]	total beam intensity [-]	peak energy density [kJ/g]	first maximum surface velocity [m/s]	first maximum surface pressure [MPa]
AA	350	0.85	$5.87 \cdot 10^8$	0.643	4.65	3.44
B2	400	0.5	$1.5 \cdot 10^8$	0.7	~ 2.2	~ 7.3

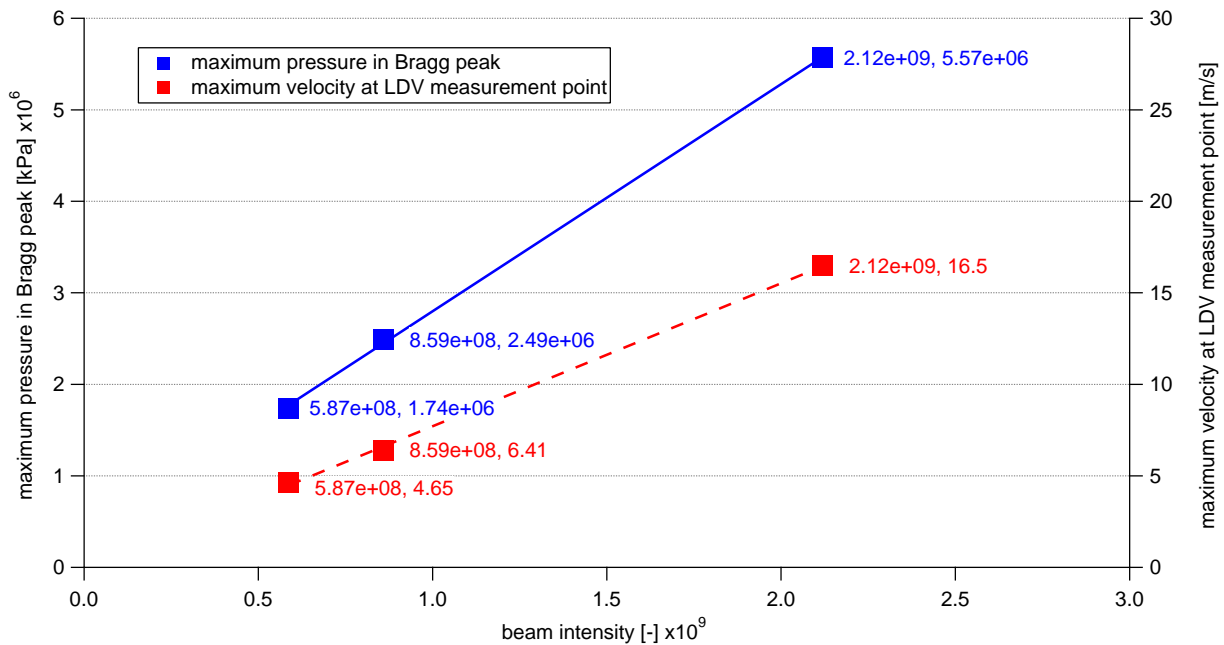


Figure 5.13: First maxima of SPH node histories for shots 5, 7 and 8 for $P_{MIN} = -1.08$ GPa. The pressure values have been obtained for the node receiving the maximum energy deposition. The velocity values are displayed for the center node on the lateral surface of the cylinder where the measurement point of the Laser Doppler vibrometer was situated. The uranium ion beam intensity followed by the plot value are shown for each point.

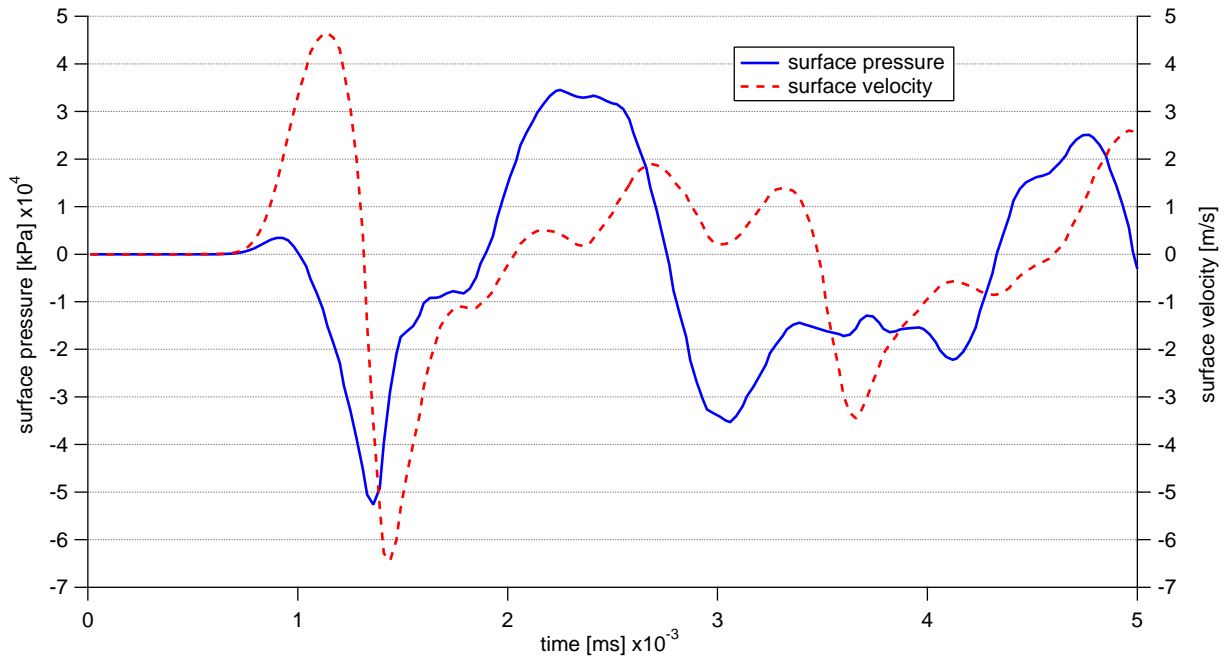


Figure 5.14: First 5 μ s of SPH node histories for surface pressure and surface velocity for $5.87 \cdot 10^8$ ions and $P_{MIN} = -1.08$ GPa.

5.3.1.2 Simulation of Sample 28

5.3.1.2.1 Simulation results

Because of the results in section 5.3.1.1 (p. 117 ff), the first set of simulations of sample 28 were performed with a P_{MIN} value equal to -1.08 GPa. With this setting, the simulation of the first beam impact on target 28 caused – as expected from the simulations for sample 26 due to similar beam parameters – material ejection (see fig. 5.15(a) – 5.15(c) on p. 127). For the next step, a simplified geometry for the ejection cone was assumed in order to allow a qualitative prediction of the second beam impact on the same target (see gray overlay in fig. 5.15(a) – 5.15(c)).

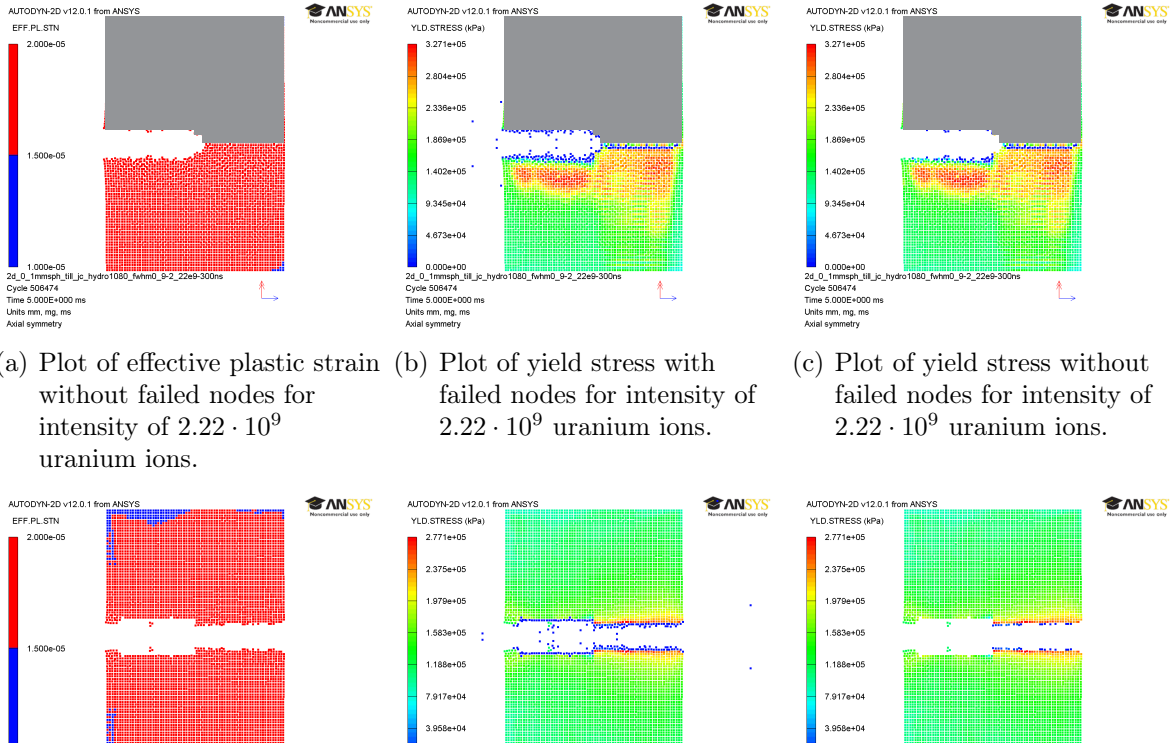
A second set of simulations was performed to gauge the two shot scenario with a slightly higher hydrodynamic tensile limit. The comparison of the result achieved as seen in fig. 5.8 on p. 121 with the metallurgical investigation on sample 26 suggested that a P_{MIN} value of -3.24 GPa was too high. Despite this finding, the same value was used for a similar two-shot scenario: as the beam parameters used to achieve fig. 5.16(a) – 5.16(c) on p. 128 are similar to those of the first shot on sample 28 (see fig. 5.8). The outcome of both simulations are comparable, as it was the case for the simulations performed with a P_{MIN} value of -1.08 GPa. This degenerated target was again approximated by leaving out a cylinder inside the bulk target with dimensions slightly larger than the volume containing the failed nodes.

5.3.1.2.2 Comparison with metallurgical examination

From the first examination of the targets after irradiation – which did not include any microographies as only beam offsets were determined – it was already known that sample 28 was shot through [181]. The cut as seen in fig. 5.17(a) on p. 129 was only available at a later stage. Without this information the following conclusions could already be drawn: on one hand, the simulation of the second beam impact for the model with P_{MIN} equal to -1.08 GPa results in a full penetration of the target (see fig. 5.15(d) – 5.15(f) on p. 127). On the other hand, the dynamic simulation of the second shot interacting with this simplified geometry – as seen in fig. 5.16(d) – 5.16(f) on p. 128 – only results in one void, on the side of the target facing the beam. Therefore, the P_{MIN} value equal to -3.24 GPa can be seen as an exclusive upper boundary of a possible range of suitable values for the hydrodynamic limit with respect to the current parameters used for these sets of simulations. But it is evident from the experience with sample 26 that the details of beam entrance channel also could not be simulated with the same structures seen in fig. 5.18 on p. 129.

5.3.1.3 Comparison Results of Metallurgical Examination of Samples 26 and 28

Despite the fact that sample 26 received a slightly higher number of ^{238}U ions ($5.59 \cdot 10^9$) the post-irradiation analysis reveals less damage when compared to sample 28 ($4.58 \cdot 10^9$). This can be understood looking at tab. 5.1 on p. 110: only the last shot on sample 26 (27.44 J – when assuming an intact target) reached a value for the total energy deposition that is comparable to the first impact on sample 28 (28.76 J).



(a) Plot of effective plastic strain without failed nodes for intensity of $2.22 \cdot 10^9$ uranium ions.

(b) Plot of yield stress with failed nodes for intensity of $2.22 \cdot 10^9$ uranium ions.

(c) Plot of yield stress without failed nodes for intensity of $2.22 \cdot 10^9$ uranium ions.

(d) Plot of effective plastic strain without failed nodes for intensity of $2.36 \cdot 10^9$ uranium ions.

(e) Plot of yield stress with failed nodes for intensity of $2.36 \cdot 10^9$ uranium ions.

(f) Plot of yield stress without failed nodes for intensity of $2.36 \cdot 10^9$ uranium ions.

Figure 5.15: Copper target simulated with $P_{MIN} = -1.08$ GPa and beam width of 0.9 mm (FWHM). Status at 5 ms simulated time after beam impact from left. Uranium ion beam intensity of $2.22 \cdot 10^9$ ((a) – (c)) on intact target and $2.36 \cdot 10^9$ ((d) – (f)) for second shot on simplified target (grey overlay over upper half of simulation results (a) – (c)), respectively. Simplified geometry after first beam impact approximated by leaving two cylinders ($r_1 = 0.5$ mm, $l_1 = 3.5$ mm and $r_2 = 0.3$ mm, $l_2 = 0.3$ mm) empty to account for failed nodes. Minimum and maximum values for effective plastic strain ((a) and (d)) set low ($1 \cdot 10^{-5}$ and $2 \cdot 10^{-5}$, respectively) in order to distinguish between elastically deformed nodes (in dark blue) and plastically deformed (in red). Dark blue nodes of yield stress 0 kPa in (b) and (e) which can either be obtained through reaching failure condition or through thermal softening as implemented in strength model. Only thermally softened nodes in dark blue in (c) and (f).

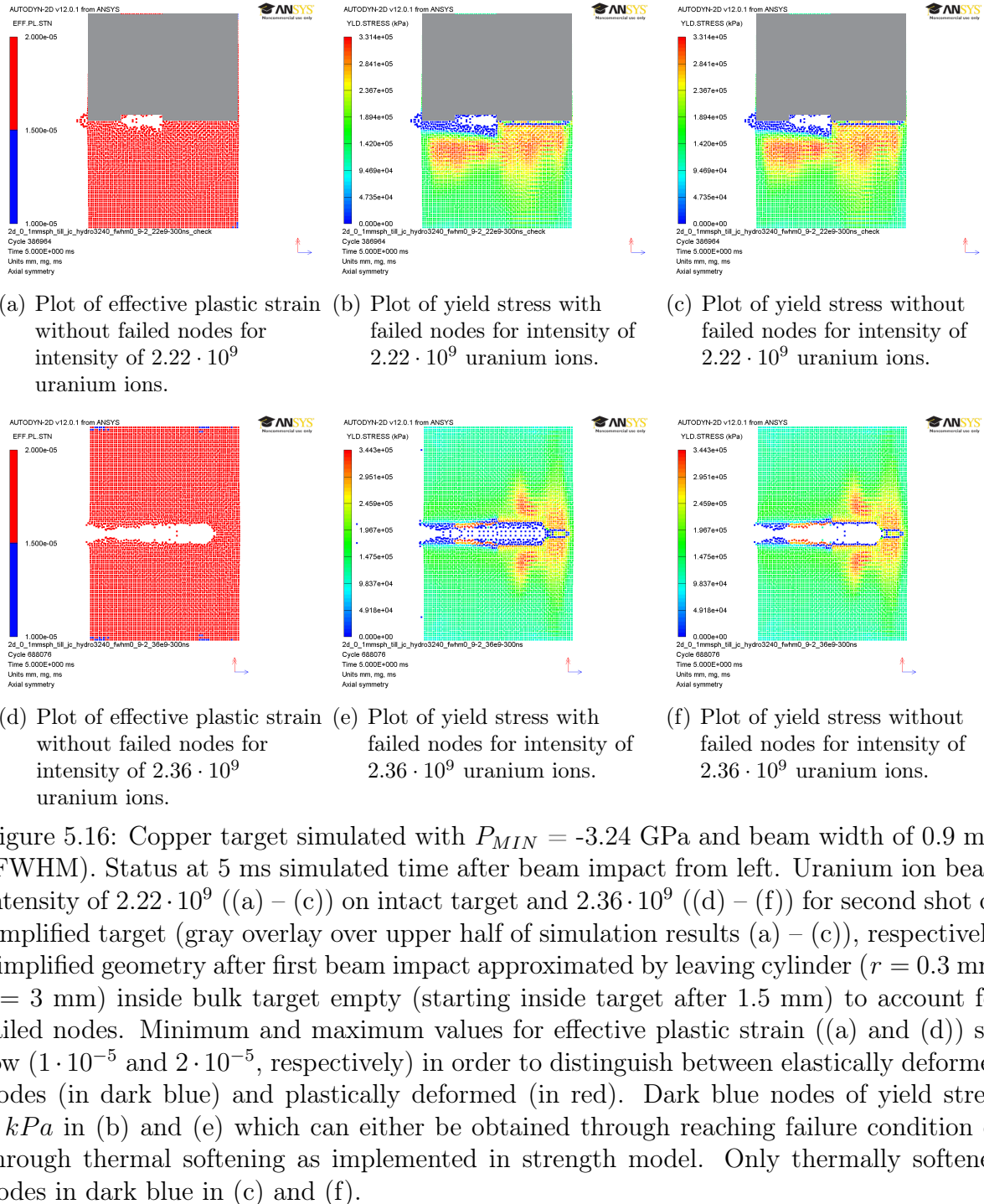
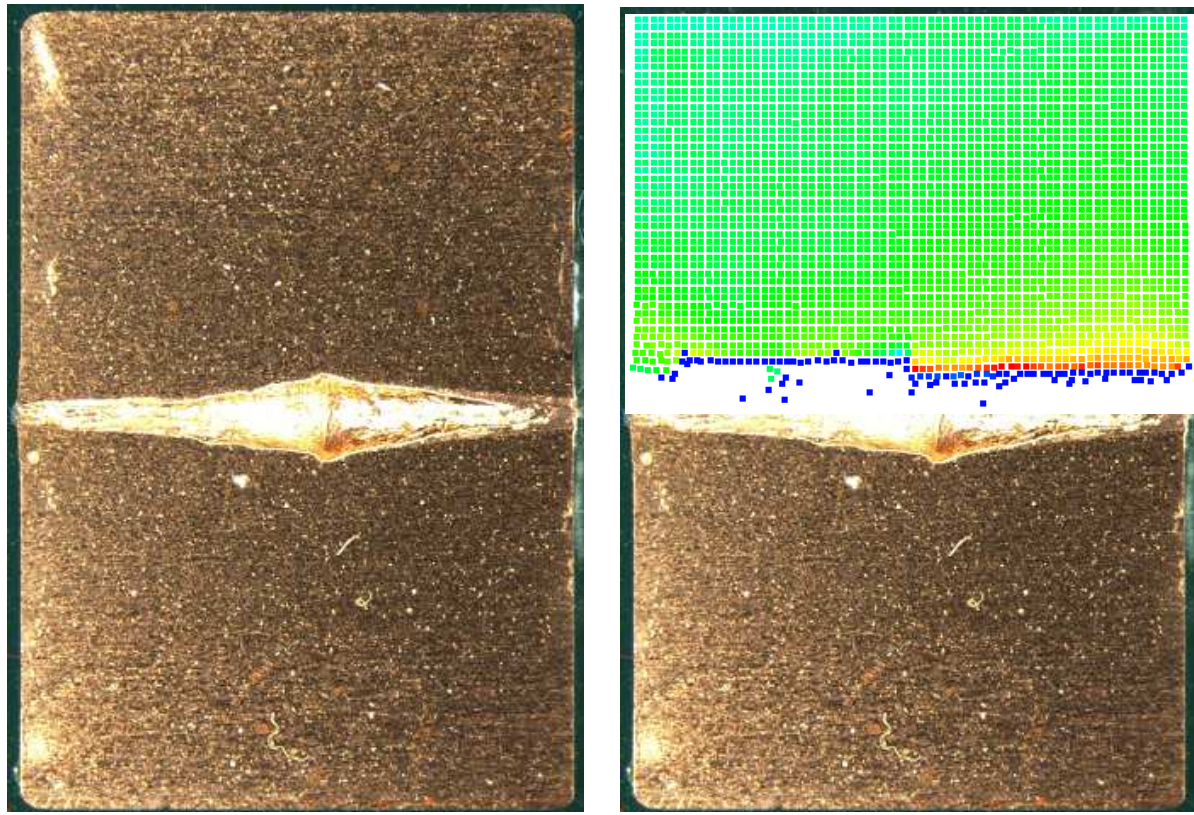


Figure 5.16: Copper target simulated with $P_{MIN} = -3.24$ GPa and beam width of 0.9 mm (FWHM). Status at 5 ms simulated time after beam impact from left. Uranium ion beam intensity of $2.22 \cdot 10^9$ ((a) – (c)) on intact target and $2.36 \cdot 10^9$ ((d) – (f)) for second shot on simplified target (gray overlay over upper half of simulation results (a) – (c)), respectively. Simplified geometry after first beam impact approximated by leaving cylinder ($r = 0.3$ mm, $l = 3$ mm) inside bulk target empty (starting inside target after 1.5 mm) to account for failed nodes. Minimum and maximum values for effective plastic strain ((a) and (d)) set low ($1 \cdot 10^{-5}$ and $2 \cdot 10^{-5}$, respectively) in order to distinguish between elastically deformed nodes (in dark blue) and plastically deformed (in red). Dark blue nodes of yield stress 0 kPa in (b) and (e) which can either be obtained through reaching failure condition or through thermal softening as implemented in strength model. Only thermally softened nodes in dark blue in (c) and (f).



(a) Estimated penetration depth about 3.8 mm.

(b) Overlay with fig. 5.15(e) from p. 127 – plot of yield stress with failed nodes.

Figure 5.17: Photograph from the metallurgical examination of sample 28. (Micrography courtesy Jacques Lettry et al. [161])

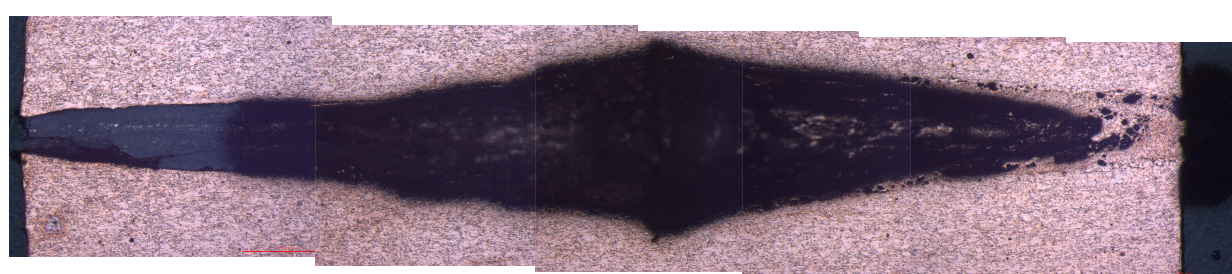


Figure 5.18: Collage of photographs of details of the beam entrance zone from the metallurgical examination of sample 28. (Micrographies courtesy Jacques Lettry et al. [161])

5.3.2 Simulation of Other Metallic Targets

The available material models in ANSYS AUTODYN[®] are stated in tab. 5.5. Since no samples had undergone a metallurgical analysis at the starting point of the simulations, the emphasis was put on those targets that had received few high energy shots.

Table 5.5: Available material models for lead, tantalum and tungsten in ANSYS AUTODYN[®].

Material	EOS	Strength	Failure	Reference
Lead	Shock	-	-	[165]
Lead	Shock	Steinberg-Guinan	-	[166]
Lead	Shock	von Mises	-	[169]
Tantalum	Shock	-	-	[165]
Tantalum	Shock	Steinberg-Guinan	-	[166]
Tantalum	Shock	von Mises	-	[169]
Tungsten	Tillotson	-	-	[111]
Tungsten	Shock	-	-	[165]
Tungsten	Shock	Steinberg-Guinan	-	[166]
Tungsten	Shock	von Mises	-	[169]

5.3.2.1 Lead

The lead target which had received few high energy shots, target Pb-22, was chosen, which had been irradiated twice – first with $2.16 \cdot 10^9$ and then with $2.06 \cdot 10^9$ (see tab. B.2 on p. 142). The material model for the EOS and the strength model was the shock EOS and the Steinberg-Guinan strength model as derived in [166]. The Steinberg-Guinan strength model includes the formalism for these concepts: firstly, it is assumed that at strain rates higher than $\cdot 10^5/s$ there is a maximum yield stress independent of strain rate. Secondly, in order to accommodate the increase of the shear modulus with increasing pressure as well as the decrease of the same with temperature, the dependency on both pressure and temperature was included as well. Therefore, both the shear modulus and yield stress are set to zero when the melting temperature is reached.

In literature ([186], [187]), spall strengths for lead were measured to be in the range of 0.22 – 0.5 GPa. Therefore, simulations with $P_{MIN} = 0.2$ GPa and 0.5 GPa were performed. As can be seen in fig. 5.19 on p. 131, the lead targets exhibit gross destruction after the first shot for both P_{MIN} values. However, destroyed targets as seen in fig. 5.19 had not been reported after the irradiation. There was only micrography of a lead target at the time of the simulation available ([181]): Target 20, which had also received two high intensity shots of slightly lower intensity ($1.85 \cdot 10^9$ and $1.84 \cdot 10^9$ – see tab. B.2). This target did not show any large voids other than at the beam heating zone seen in the simulation, nor did it show large bulking at the surface. Hence, further simulations of lead targets have been stalled.

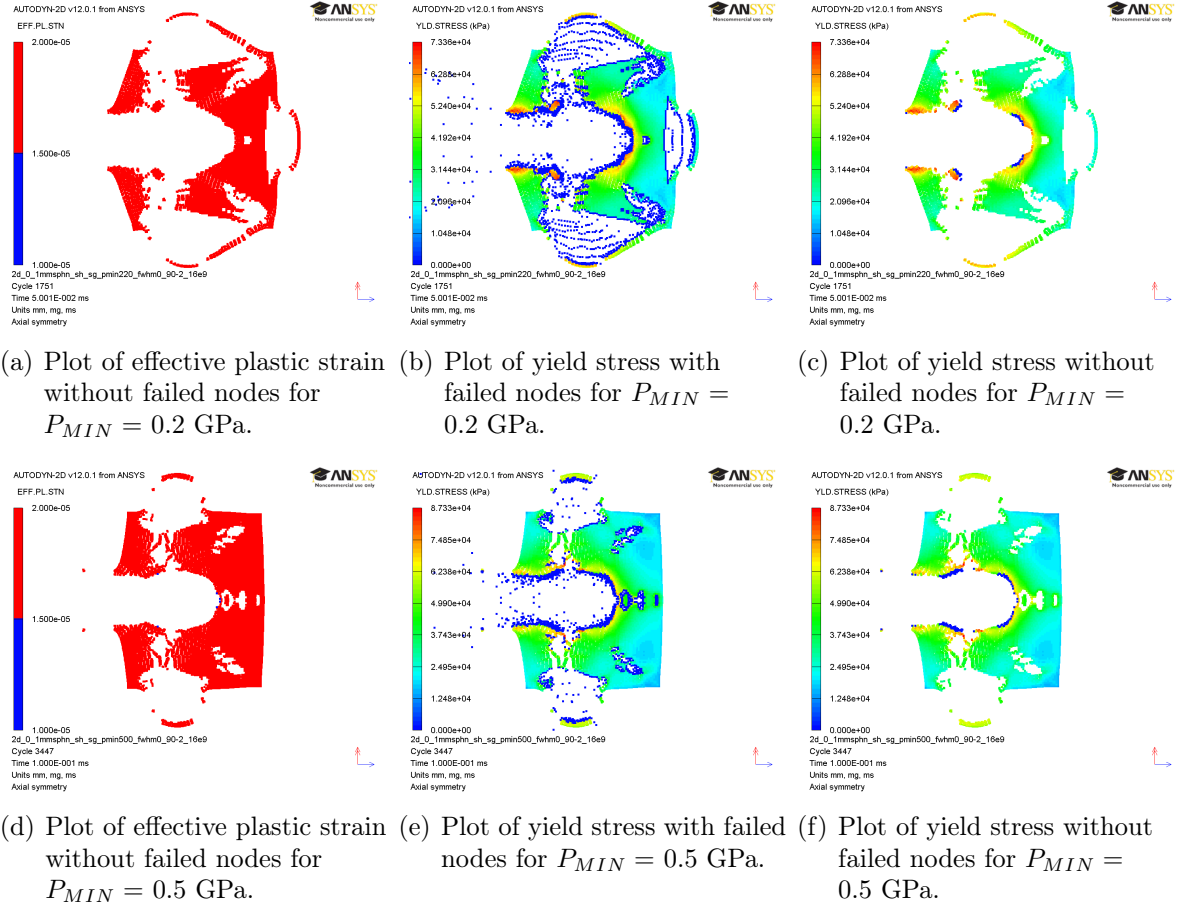


Figure 5.19: Lead target simulated with Uranium ion beam intensity of $2.16 \cdot 10^9$ and beam width of 0.90 mm (FWHM) impacting from left on intact target. The maximum energy deposition occurred at 3.6 mm inside the 7 mm long target. Status at 0.05 ms simulated time after beam impact for fig. 5.19(a) – fig. 5.19(c) and at 0.1 ms simulated time after beam impact for fig. 5.19(d) – fig. 5.19(f) . $P_{MIN} = 0.2$ GPa for ((a) – (c)) and $P_{MIN} = 0.5$ GPa for ((d) – (f)), respectively. Minimum and maximum values for effective plastic strain (a) and (d)) set low ($1 \cdot 10^{-5}$ and $2 \cdot 10^{-5}$, respectively) in order to distinguish between elastically deformed nodes (in dark blue) and plastically deformed (in red). Dark blue nodes of yield stress 0 kPa in (b) and (e) which can either be obtained through reaching failure condition or through thermal softening as implemented in strength model. Only thermally softened nodes in dark blue in (c) and (f).

5.3.2.2 Tantalum

For tantalum, the target having received just two high energy shots was target Ta-14. It was irradiated first with $2.39 \cdot 10^9$ followed by an impact of $2.42 \cdot 10^9$ uranium ions (see tab. B.1 on p. 141). As for the lead model, the material model for EOS and strength model was the shock EOS and the Steinberg-Guinan strength model as developed in [166].

Spall strengths in the range of 4.6 – 8.1 GPa were quoted ([68], [188], [189], [190], [191]). Within this parameter range, three values for P_{MIN} were chosen for simulations – 4.4, 5.25 and 8.1 GPa – and the obtained results are presented in fig. 5.20 on p. 133. No micrography of a tantalum target had been produced after these simulations were performed. Due to the lack of proper experimental comparison, no further simulations were initiated. In hindsight however, it seems that out of the three simulation results the ones with $P_{MIN} = 4.4$ and 5.25 GPa resemble the observed beam ejection zone the most closely – albeit not ideally.

5.3.2.3 Tungsten

Target 18 received the two highest intensity beam impact for tungsten: $2.24 \cdot 10^9$ and $2.16 \cdot 10^9$. With the same strategy as for both lead and tantalum, the tungsten model used the EOS and strength model [166].

Values of spall strength for tungsten cover a range from 0.4 to 3.1 GPa ([68], [192], [193]). In order to investigate this large range, three simulations with P_{MIN} of 0.4, 0.8 and 2.9 GPa were performed. The results are displayed in fig. 5.21 on p. 134. At the time when the simulation results were available, the micrography of W-18 was also available for comparison ([181]). Comparing the outcome of this first simulation study revealed that the P_{MIN} value yielding the results closest to what has been observed from the investigated specimen was 2.9 GPa. Yet, the cracks as observed in a detailed micrography could not be reproduced and this was the reason why no further simulations were performed for tungsten.

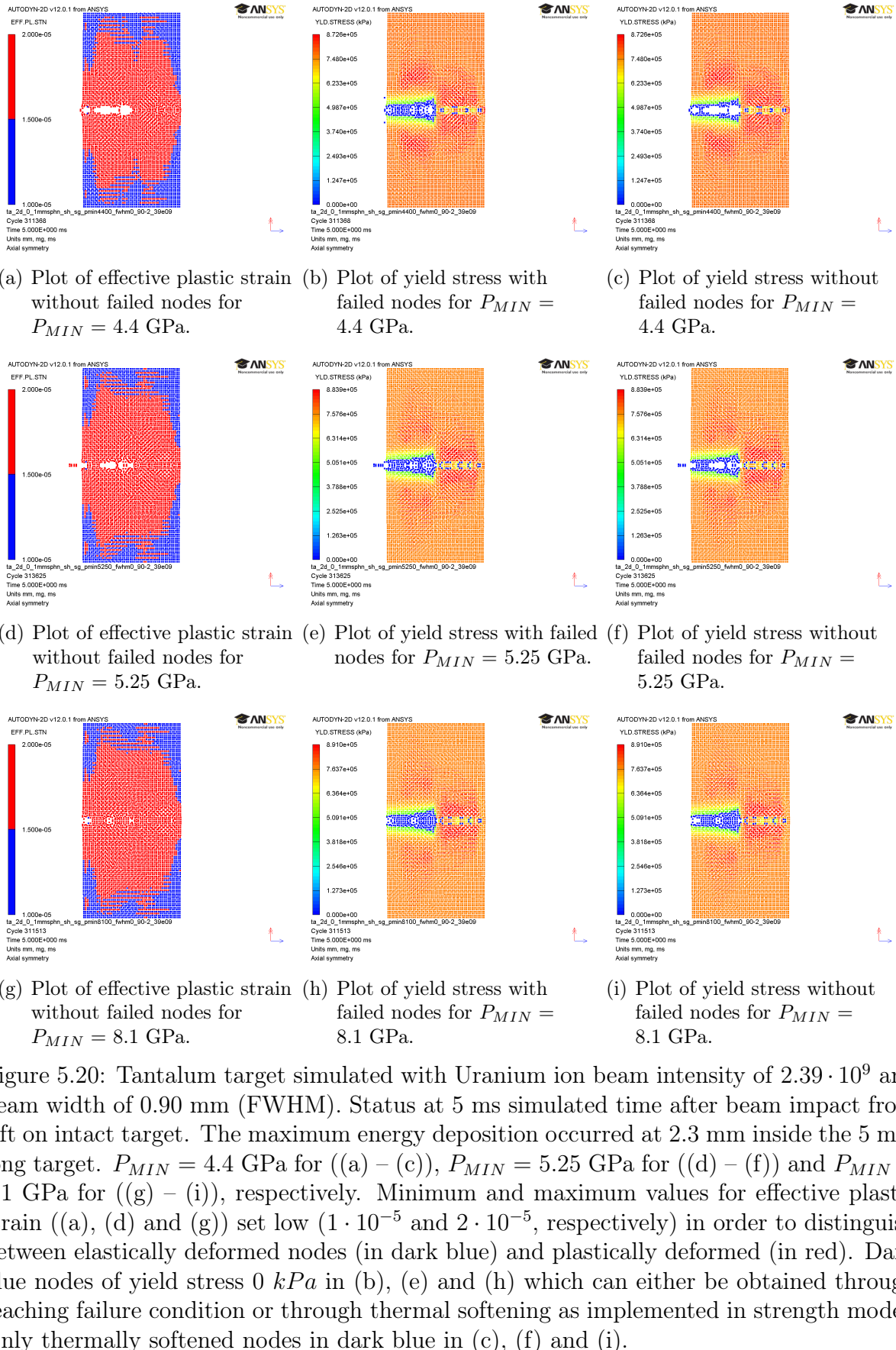


Figure 5.20: Tantalum target simulated with Uranium ion beam intensity of $2.39 \cdot 10^9$ and beam width of 0.90 mm (FWHM). Status at 5 ms simulated time after beam impact from left on intact target. The maximum energy deposition occurred at 2.3 mm inside the 5 mm long target. $P_{MIN} = 4.4$ GPa for ((a) – (c)), $P_{MIN} = 5.25$ GPa for ((d) – (f)) and $P_{MIN} = 8.1$ GPa for ((g) – (i)), respectively. Minimum and maximum values for effective plastic strain ((a), (d) and (g)) set low ($1 \cdot 10^{-5}$ and $2 \cdot 10^{-5}$, respectively) in order to distinguish between elastically deformed nodes (in dark blue) and plastically deformed (in red). Dark blue nodes of yield stress 0 kPa in (b), (e) and (h) which can either be obtained through reaching failure condition or through thermal softening as implemented in strength model. Only thermally softened nodes in dark blue in (c), (f) and (i).

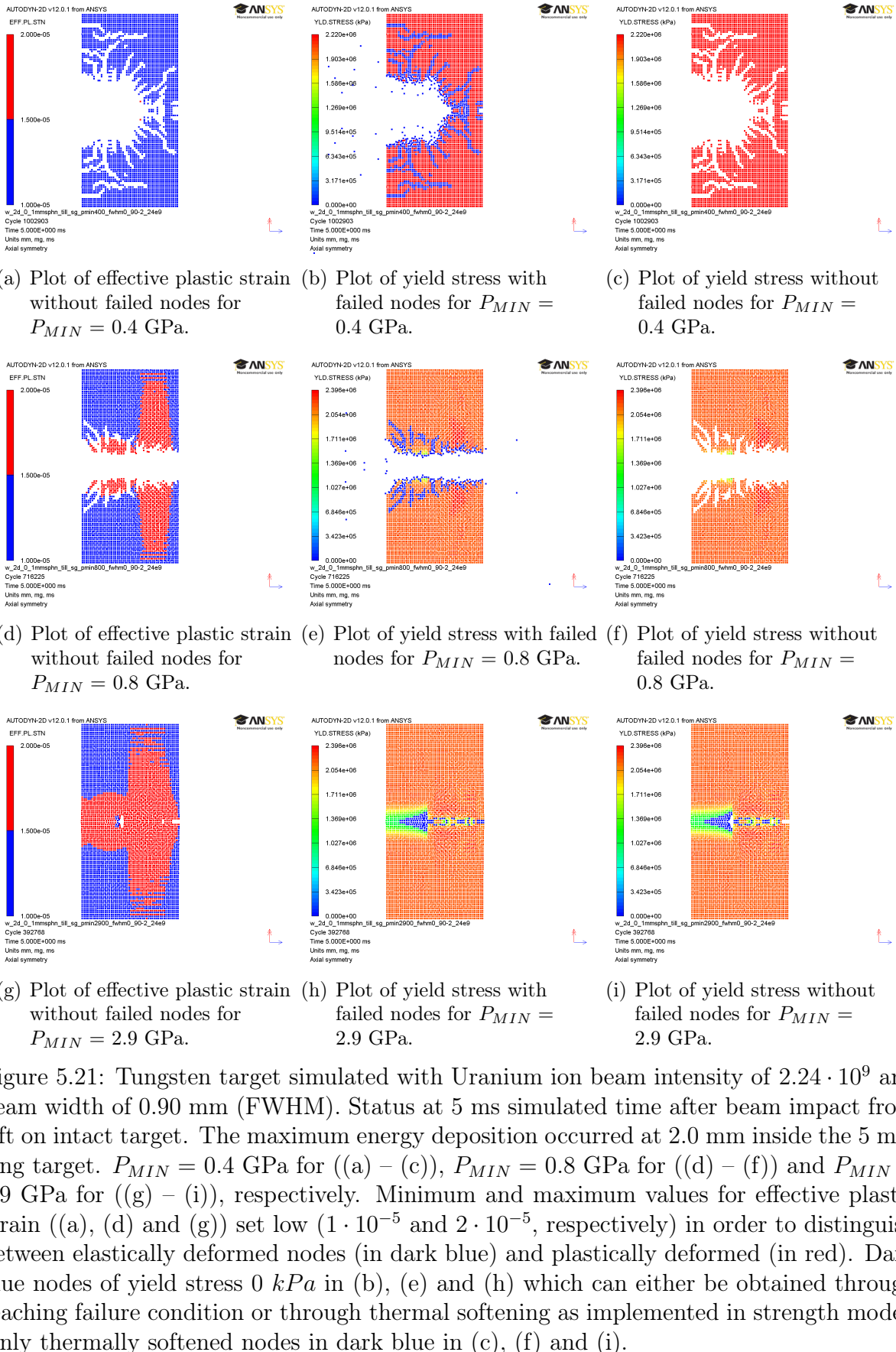


Figure 5.21: Tungsten target simulated with Uranium ion beam intensity of $2.24 \cdot 10^9$ and beam width of 0.90 mm (FWHM). Status at 5 ms simulated time after beam impact from left on intact target. The maximum energy deposition occurred at 2.0 mm inside the 5 mm long target. $P_{MIN} = 0.4$ GPa for ((a) – (c)), $P_{MIN} = 0.8$ GPa for ((d) – (f)) and $P_{MIN} = 2.9$ GPa for ((g) – (i)), respectively. Minimum and maximum values for effective plastic strain ((a), (d) and (g)) set low ($1 \cdot 10^{-5}$ and $2 \cdot 10^{-5}$, respectively) in order to distinguish between elastically deformed nodes (in dark blue) and plastically deformed (in red). Dark blue nodes of yield stress 0 kPa in (b), (e) and (h) which can either be obtained through reaching failure condition or through thermal softening as implemented in strength model. Only thermally softened nodes in dark blue in (c), (f) and (i).

Chapter 6

Summary and Outlook

The main focus for this thesis is the combined description of all collected Laser Doppler Vibrometer (LDV) surface velocity measurements of the collimator impact test in section 4.1 and the simulations of highly focused and energetic uranium ion beams impacting on metal targets.

The LDV measurement results were compared to check for reproducibility and for the dependence on measurement points, of beam intensity and beam impact parameter. The maximum displacement reached within recording time of the LDV was about $235 \mu\text{m}$ at the end of the recording time (6.34 ms) for a beam intensity of $28.8 \cdot 10^{12}$ protons (= 6 batches) and a beam impact parameter of $+5 \text{ mm}$. The taken data is stable versus the sample frequency, the measurements are reproducible and it could be shown that the surface displacement of collimator jaw at the first maximum (about $50 \mu\text{s}$) scales according to beam intensity.

The simulations of uranium ion beams impacting metallic targets concentrated on the simulation of two copper targets whose metallurgical results were available the earliest after the irradiation at GSI in Darmstadt, Germany. By simulating a model with the Tillotson EOS for copper, the Johnson-Cook strength model for OFHC copper for three different intensities, and by varying the hydrodynamic tensile limit P_{MIN} to predict the damage of an irradiated copper target, results closely related to the observed experimental outcome could be obtained for sample 26. Moreover, using the value for the hydrodynamic tensile limit, two consecutive shots on the same sample could be simulated in first approximation. This two-staged approach was in qualitative agreement with post-irradiation investigations of sample 28.

However, there are several points one should consider when deciding upon the suitability of the FLUKA-ANSYS AUTODYN[®] combination for use in the design of beam intercepting devices for energetic beams interacting with matter:

- FLUKA provides only a static energy deposition map which is transferred to the dynamic – and therefore changing – model in ANSYS AUTODYN[®] at a constant rate (flat top) for the FWHM time of the bunch. Immediate density dilution due to heat load is therefore not considered for the energy deposition map. In extreme cases, the larger penetration depth of the impinging beam due to this reduced density is not taken into account.
- Both FLUKA and ANSYS AUTODYN[®] are both well-developed high-end tools

albeit for different and not necessarily matching fields: FLUKA is used for matter not undergoing phase changes upon beam interaction, while ANSYS AUTODYN® is applied mainly in highly dynamic events such as solid-on-solid or explosive-on-solid interaction which are based on different physical models.

- The marrying of FLUKA and ANSYS AUTODYN® (as done in [180]) is based on a more simplistic approach regarding the computational work in comparison to a dedicated one-program frame-work – such as BIG-2 – and would demand more programming. As of the different nature of both software packages, more development would have to be invested to create a strongly interlinked FLUKA-ANSYS AUTODYN® version.
- The models used in ANSYS AUTODYN® to describe the EOS and the strength and failure model in this work usually have a specific range for which they worked efficiently and they were not conceived together or developed for each other. The limitation of each of these sub-models and the assumptions on which they are based will therefore also have a larger impact, but for this work it had to be assumed that the given sub-models are not only compatible but also valid in neighboring regions of their parameter space.
- As ANSYS AUTODYN® is a commercially available code, the purchasers would most probably like to have a product which allows them to obtain results in a fairly straightforward way for their specific field of application. Putting it simplistically, this requirement might lead to a provision of a "black box" to the majority of customers for whom the code has been designed. Catering to a certain target group will therefore reduce the needed flexibility for applications which are not part of the original portfolio. Even though ANSYS AUTODYN® provides customer support and offers several possibilities to interact with the code, some features needed for a fringe customer such as high power targetry are less developed or missing.
- The results of the FLUKA-ANSYS AUTODYN® modeling attempts closest to the observed experimental reality have been achieved by varying only one parameter, the hydrodynamic tensile limit P_{MIN} . The assumption of a constant value which is related to the spall fracture is already a strongly simplified working premise. Spall fracture is a phenomena observed and measured for solids and strongly depends on material properties – such as grain size – and the dynamic load – e.g. reached pressure. In an ideal physics model the hydrodynamic tensile limit would have to be dependent on and/or parametrized with all these dependencies.
- The target mounting has not been included in the simulations for reasons of complexity and symmetry.
- The comparison of the simulation results with the metallurgical results is in principal problematic: the simulations of each shot have been performed for an intact target, but started with a simplified ejection geometry for the last shot. The previous lower intensity shots influences not only the material properties but also the precise shape of the ejection geometry.

- ANSYS AUTODYN® model does not contain heat transfer mechanisms other than direct application of heat in the form of the energy deposition map. Because of this and the explicit nature of the code, long term simulations are not the strongest suit for the ideal comparison with targets that have been cooled and recrystallized.
- Despite best efforts from all involved parties some timing issues unfortunately could not be avoided:
 - After the preparatory studies with the BIG-2 code ([159]) were finalized, the beam parameters had to be adjusted to technical circumstances and were no longer in agreement with [159].
 - The time lines of the efforts of the simulation work for this thesis and the still outstanding complete experimental summary – both the metallurgical summary as well as the in-depth analysis of the recorded LDV data – could not be matched efficiently.

From the side of the experiment, it is clear now that for a more quantitative comparison of the simulations with the LDV data and the metallurgical results single shots on targets would have been a better choice. To quote [161] (from slide 32) for the learned lesson of the metallurgical examination for the next phase of the experiment:

The GSI samples were all multi shot irradiated, the understanding of the metallurgical observations becomes very complex and single shot probes would have been necessary.

In addition, more measurement devices such as pressure gauges would have enriched the insight into the simulation capabilities of the current FLUKA-ANSYS AUTODYN® version.

The ideal simulation to be compared with the metallurgical examinations and the LDV data would have to overcome all the above disadvantages. However it is clear that as a first attempt on the road to a more precise description the current simulation work was a step well worth taking with regards to the lessons learned.

A lot of different aspects will play into the decision of whether the interlinking of FLUKA and ANSYS AUTODYN® will continue, some of which are going to be technical questions or questions related to physics models. Others will involve management decisions such as possible tighter collaboration with either research groups with different more developed codes, or industry. The original idea to simulate the target response due to consecutive bunches with FLUKA and ANSYS AUTODYN® would need an interface between those codes, capable of handling the two different geometry concepts applied. The needed development would be an interface allowing the combination of the capabilities of both simulation tools: significant changes to the geometry due to the dynamic impact of a bunch as simulated by ANSYS AUTODYN® could be taken into account in subsequent energy deposition simulations with FLUKA.

Appendix A

FLUKA Parameters

Table A.1: FLUKA cards for energy deposition calculations for copper target.
 As there are no entries for WHAT(5) and WHAT(6) they are omitted from this listing.
 METARGET is the region containing the target.

Card	WHAT(1)	WHAT(2)	WHAT(3)	WHAT(4)	SDUM
<i>General</i>					
DEFAULTS					
<i>Physics</i>					
EVENTYPE					DPMJET
PHYSICS	3.0				EVAPORAT
PHYSICS	1.0				COALESCE
DELTARAY	5D-04			COPPER	NOPRINT
PAIRBREM	3.0		5D-05	COPPER	
<i>Transport</i>					
DISCARD	NEUTRIE	ANEUTRIE	NEUTRIM	ANEUTRIM	
PART-THR	-0.02	NEUTRON			
LOW-NEUT	260.0		0.02		
EMFCUT	-5D-05	5D-06		METARGET	
<i>Biasing</i>					
EMF-BIAS	1022.0	1.0	1.0	METARGET	LPBEMF

Appendix B

Beam Parameters

Table B.1: List of beam parameters of targets made of tantalum and tungsten irradiated at GSI.

target material [-]	cylinder length [mm]	beam time distribution [-]	sample number [-]	shots on sample [-]	beam size (FWMH) [mm]	beam intensity [-]
Ta	5	A	15	6	0.65	$4.47 \cdot 10^8$ $4.23 \cdot 10^8$ $6.33 \cdot 10^8$ $5.43 \cdot 10^8$ $9.47 \cdot 10^8$ $8.90 \cdot 10^8$
			14	2	0.9	$2.39 \cdot 10^9$ $2.42 \cdot 10^9$
		B	16	3	0.9	$1.98 \cdot 10^9$ $1.97 \cdot 10^9$ $2.00 \cdot 10^9$
		A	17	5	0.65	$4.83 \cdot 10^8$ $6.93 \cdot 10^8$ $7.43 \cdot 10^8$ $9.16 \cdot 10^8$ $9.37 \cdot 10^8$
			18	2	0.9	$2.24 \cdot 10^9$ $2.16 \cdot 10^9$
		B	19	3	0.9	$1.97 \cdot 10^9$ $1.99 \cdot 10^9$ $1.91 \cdot 10^9$

Table B.2: List of beam parameters of targets made of copper and lead irradiated at GSI.

target material [-]	cylinder length [mm]	beam time distribution [-]	sample number [-]	shots on sample [-]	beam size (FWMH) [mm]	beam intensity [-]
Cu	2	A	23	2	0.9	$2.21 \cdot 10^9$ $2.23 \cdot 10^9$
			25	2	0.9	$1.91 \cdot 10^9$ $1.89 \cdot 10^9$
		A	26	8	0.85	$1.48 \cdot 10^8$ $1.52 \cdot 10^8$ $3.19 \cdot 10^8$
						$5.11 \cdot 10^8$ $5.87 \cdot 10^8$ $8.89 \cdot 10^8$
						$8.59 \cdot 10^8$ $2.12 \cdot 10^9$
	7	A	28	2	0.9	$2.22 \cdot 10^9$ $2.36 \cdot 10^9$
			27	4	0.9	$1.87 \cdot 10^9$ $8.87 \cdot 10^6$ $1.90 \cdot 10^9$ $1.90 \cdot 10^9$
Pb	7	A	21	7	0.65	$2.86 \cdot 10^7$ $7.73 \cdot 10^7$ $6.82 \cdot 10^7$
			22	2	0.9	$1.23 \cdot 10^8$ $1.93 \cdot 10^8$ $3.02 \cdot 10^8$ $4.38 \cdot 10^8$
		B	20	2	0.9	$2.16 \cdot 10^9$ $2.06 \cdot 10^9$
		B	20	2	0.9	$1.85 \cdot 10^9$
						$1.84 \cdot 10^9$

List of Figures

3.1 Schematic stress-strain curves for ductile and brittle materials. The elastic region for the brittle curve is marked with the elastic limit EL after which plastic deformation occurs. The slope of the stress-strain curve in the elastic regions is equal to the elastic modulus E (here marked only for the brittle material). The transition from elastic to plastic behavior for ductile materials is gradual. The proportional limit P is reached before the ductile material shows a fully plastic response. Due to the difficulties of setting a specific value for this transition, the yield strength σ_Y is defined by the following convention: the stress value at the intersection of the engineering stress-strain curve with a parallel line to the proportional elastic part of its stress-strain curve. Generally, the parallel line is offset by 0.2% along the strain axis. M marks the maximum load reached during a tensile test, indicating the necking of the material. The hereby reached stress is called tensile strength σ_{TS} . While the engineering stress decreases, the true stress increases. In the true stress-strain curve, M' marks the onset of necking. The corrected true stress-strain curve accounts for the non-uniaxial stress state in the necked region. Ductile fracture occurs at strains far greater than that of brittle fracture. The true fracture stress is noted as σ_f for ductile failure. By definition, brittle materials fracture after little plastic deformation, without necking.

21

3.2 Ranges in dynamic mechanical testing: The characteristic time scale is given as the time required to produce 1% strain at the corresponding strain rate. The creep behavior is usually investigated at high temperature for metals. Although the quasistatic stress-strain curve is often treated as an inherent property of a material, it is a valid description of the material only at the strain rate at which the test was conducted. Constant strain-rate tests can be performed with specialized testing apparatus to a certain strain rate limit. At the high rates and the associated very short time scale involved in shock waves, thermodynamic considerations become important. At these high rates, the nominal transition between isothermal and adiabatic conditions happens. The internal heat generated during the inelastic deformation process does not have time to dissipate, and therefore the mean temperature of the specimen is increased. Fig. 1 (p. 201) from [66], modified original figure caption of fig. 1 (p. 280) in [67] and with text mostly taken from section 8.1.1 of [67] and chapter 4 in [66]. Used with kind permission of Wiley & Sons.

27

3.13 Propagation of shock waves in materials undergoing phase transformations of the type $\Delta V < 0$, $\Delta S < 0$, $\frac{dP}{dT} > 0$. (a) Stable two-shock wave structure. (b) Hugoniot curve with discontinuity in slope with their Rayleigh slopes for each phase: a shock with a peak pressure P_2 is an example of a stable two-shock wave structure, while the peak pressure P_3 serves as a limit case between two-wave and single-wave structure and a shock with peak pressure P_4 is another example showing a stable single-shock wave structure above the phase transition. Shock waves with peak pressures below P_1 will result in no phase transformation, hence the shock wave will also display a single shock. Fig. 8.6 (p. 210) from [65], modified original figure caption with text adapted from section 8.3 (p. 206 ff) of [65]. Used with kind permission of Wiley & Sons.

45

3.14 Pressure-volume-temperature surface for a material with solid to liquid transition of the type $\Delta V > 0$, $\Delta S > 0$, $\frac{dP}{dT} > 0$. The melting pressure increases with temperature. The mixed phase region is shown by the dotted strip within the area $NMRP$. The dashed line QW is the projection of the mixed phase region on the pressure-temperature plane. FGH is an isotherm originating in the liquid. Fig. 14, p. 534 from [78], modified original figure caption of fig. 8.11 (p. 218) from [65] with text adapted from section 8.3 (p. 206 ff) in [65] and section VI, p. 557 in [78]. Used with kind permission of American Physical Society and Wiley & Sons.

46

3.15 Schematic pressure-volume-temperature plots summarize possible equilibrium phases and phase changes. Non-equilibrium states take place in the remainder of the pressure-volume-temperature space. The slope $\frac{\partial p}{\partial T}$ of all phase-equilibrium lines obey the equation (3.34) on p. 40. A line separating a single-phase region from a two-phase region summarizes the saturation states. (a) Phase diagram for a pure substance that contracts upon melting and (b) for a substance that expands upon melting (also shown are the projections in pressure-temperature and pressure-volume space). s . . . solid phase, l . . . liquid phase, and g . . . gaseous phase. Fig. 1.4 (p. 27) from [109], modified original figure caption and with text mostly taken from section 1.5.1 in [109]. Used with kind permission of Springer Science+Business Media.

51

LIST OF FIGURES

3.16 Schematic phase diagram of matter in pressure-volume space. The diagram shows the relative position of the Hugoniot, isotherm, isentrope, and melting curve. The **Hugoniot** is the summary of all possible states that can be reached through shock wave transitions. In this case the Hugoniot is for a material at zero stress and it is assumed that the hydrodynamic elastic limit (HEL) is insignificantly small. The **isentrope** is the loci of all possible states with constant entropy, which includes reversible processes where there is no exchange of heat with the surrounding and no dissipation. For weak shocks, loading paths of Hugoniots can be approximated by isentropes. For high stress shock compression this is not possible, due an increase in entropy and irreversible heating of the shocked material. There are two isentropes: S_0 corresponds to the initial (or reference) state, while S_1 represents a possible unloading path of the material if it was shocked to the state G . It should be noted that the material may melt or even reach the mixed liquid-vapor state upon unloading. If the material was shock loaded to a higher stress state, the isentrope could lie above the critical point leading to evaporation of the material during unloading. The **isotherm** is the series of states connected to each other through processes during which the temperature does not change. Quasi-static loading conditions follow isotherms. In this figure the isotherm is drawn for the initial (or reference) state. Fig. 2.6 (p. 45) from [68], modified original figure caption and with text mostly taken from section 2.3.1 in [68]. Used with kind permission of Springer Science+Business Media.

3.17 Condon-Morse curve. (a) Energy E vs. atomic distance x . (b) Force $F = -\frac{dE}{dx}$ vs. atomic distance x . (c) Pressure P vs. volume V . The shape of this isothermal 0 Kelvin compressibility curve is the reason for the steepening of the shock wave front. Fig. 5.3 (p. 127) from [65], modified original figure caption. Used with kind permission of Wiley & Sons.

3.18 Shock Hugoniot and release isentrope leading to calculation of temperatures T_1 and T_2 : in solid materials the shock Hugoniot and release isentrope are fairly close. The point P_1, V_1 is on the shock Hugoniot. When the pressure is released, unloading follows the release isentrope to point 2. It can be seen that V_2 is different from V_0 , because T_2 is higher than T_0 . This irreversibility of the process produces lost energy (shown by the hatched area). Indicated are the three temperatures T_0 , T_1 and T_2 . Fig. 5.10 (p. 147) from [65], modified original figure caption with text taken from section 5.5 of [65]. Used with kind permission of Wiley & Sons.

3.19 Unloading isentropes on a P-V-diagram: the unloading isentropes (S_1 to S_4) will pass through a base boundary according to the strength of the shock wave - from low pressures (e.g. isentrope S_1 at p_1) to high pressures (e.g. isentrope S_4 at p_4). p_c represents the cold curve (elastic pressure curve) – even extending into the negative pressures – while p_H stands for the Hugoniot. The curve OKA separates single- and two-phase regions where the point K represents the critical point. The first branch OK is the boiling curve (beginning of vaporization) and the second branch KA is the saturated vaporization curve (beginning of condensation). Fig. 11.58 (p. 765) from [88], modified original figure caption with text taken from section §21 of [88]. Used with kind permission of Elsevier. 60

3.20 Dominating effects of states of matter: the numerical values are only approximate and correspond to a material with normal density $\rho_0 = 1 \text{ g/cm}^3$. Modifications according to the atomic number Z will have to be considered as various effects scale differently with Z . $1 \text{ eV} = 1/k_B \text{ Kelvin}$, where k_B is the Boltzmann constant. $1 \text{ eV} \approx 11604.5 \text{ Kelvin}$. Region 1 corresponds to material around room temperature in which the chemical properties (determined by the structure of the outer electron shells of the atom) are important. The inset on the right shows details of this region (solid (S), liquid (L) and gaseous (G) phase, melting (M), critical point (C) and triple point (T). Fig. 1 (p. 5) from [107], modified original figure caption with text taken from section 1(a) in [107]. Used with kind permission of Elsevier. 61

3.21 Three-dimensional pressure-volume-temperature surface for copper: M ... melting region; R ... evaporating region with the critical point(CP); physical states: *solid*, *liquid*, *gas*, *liquid + gas*, and *plasma* (arrows indicate the decrease in plasma nonideality parameter); H_1 , H_p ... principal and porous Hugoniots; S ... release isentropes of shock-compressed metal; IEX ... isobaric expansion ("exploding wires") data; DAC ... static compression in diamond anvil cells; LM ... density of liquid metal at room pressure; states generated in copper by the LHC beam covering strongly coupled plasma region: LHC . Fig. 12 from [127], with slightly modified original figure caption. Used with kind permission of N. Tahir and American Physical Society. 65

4.1 Vertical cut in proton beam direction through the collimator tank used for the tests in TT40 in November 2006. The proton beam from the SPS arrives from the right. Windows are numbered downstream from the upstream face. starting at 147 mm (counted from the upstream face of the collimator jaw itself). The collimator tank installed for the TT40 test was turned upside down (figure from [140]). 69

4.2	Vertical cut orthogonal to proton beam direction through the collimator tank used for the tests in TT40 in November 2006 (modified figure from [141]). The retro-reflective tapes (in this figure called "reflective tape") were placed behind the quartz windows on the jaw surface either 2 or 10 mm (in this figure 10 mm) above the central axis of the collimator jaw. The collimator tank installed for the TT40 test was turned upside down. The positioning of the C-C collimator jaw is controlled by stepper motors. For this picture the beam axis center is assumed to lie outside the collimator jaw (corresponding to a negative beam impact parameter).	70
4.3	Installed collimator tank for the TT40 test in November 2007 with marked measurement point positions. The proton beam comes from the right. (Pictures courtesy Roman Wilfinger [142])	71
4.4	Layout of the experimental setup for the experiment in November 2006: The LDV sensor head is positioned in a shielding hut 18 m upstream of the collimator while the laser beam itself is steered towards the jaw surface via a rotating mirror (number 0) – in front of the shielding hut – towards the fixed mounted mirrors (one for every measurement point: number 1 – 4) in front of the collimator (modified figure from [145]).	72
4.5	Picture of the fixed mirrors in front of the collimator (on the right side). In the back the paper wall for aiming the laser beam with the help of webcams onto the correct measurement point can be seen. One can see that the mirror for the measurement point #2 was not in line with those for measurements #1, #3 and #4. Wilfinger (Picture courtesy Roman Wilfinger [142]) . . .	72
4.6	Calculated energy deposition of collimator jaw in $\frac{GeV}{cm^3}$ per incident primary proton for proton beam impact parameter +5 mm. Incident proton beam axis is z-direction. Provided by [151]). The mesh size was 1 mm for both x- and y-direction and 10 mm for z. Cross section in the x-y-plane at 85 cm with averaged values between 80 and 90 cm downstream from frontal face. Center of the collimator geometry: $x = -2000$ cm, $y = 0$ cm.	75
4.7	Calculated energy deposition of collimator jaw in $\frac{GeV}{cm^3}$ per incident primary proton for proton beam impact parameter +5 mm. Incident proton beam axis is z-direction. Provided by [151]). The mesh size was 1 mm for both x- and y-direction and 10 mm for z. Along z-axis (collimator front face starts at 4000 cm) representing the maximum energy deposition values within the jaw ($x = 5$ mm and $y = 0$ mm). The drop in energy deposition at 4110 cm at the end of the collimator is due to its tapering.	76
4.8	Calculated energy deposition of collimator jaw in $\frac{GeV}{cm^3}$ per incident primary proton for proton beam impact parameter +5 mm. Incident proton beam axis is z-direction. Two intersecting planes along z-axis ($z = 0$ mm) for $x = 0$ mm and $y = 0$ mm. The intersecting plane in x-y-plane at $z = 85$ cm is the same as in fig. 4.6 on p. 75 (provided by [151], using "SimpleGeo" [152]). The plot is rotated around the z-axis by 90° in order to show the region of maximum energy deposition in the x-z-plane undistorted. The mesh size was 1 mm for both x- and y-direction and 10 mm for z.	77

4.9	3D temperature plots calculated at $7.2 \mu s$ of collimator movement ($32 \cdot 10^{12}$ protons, beam impact $+5 mm$) for one collimator jaw (provided by [153]) by thermal analysis of the simulated energy deposition calculated with FLUKA. The values for the specific heat capacity for Glidcop [®] have been provided by the supplier and the values for the C-C composite have been measured. This model leaves out the first and last $10 cm$ of the collimator and therefore does not contain the tapered region of the collimator jaw. The mesh size in x and y was 1.5 to $2 mm$, in z 5 to $10 mm$	78
4.10	Plot of the measured surface velocity signals for measurements #27 (25.6 MHz sample frequency), #28 (0.1024 MHz), #29 (2.56 MHz), #30 (5.12 MHz) for reproducibility comparison within the first $100 \mu s$ of collimator movement. Number of protons: $4.8 \cdot 10^{12}$ (1 batch), beam impact parameter: $+4 mm$, measurement point #3.	81
4.11	Plots of the surface displacement for measurements #27 (25.6MHz sample frequency), #28 (0.1024 MHz), #29 (2.56 MHz), #30 (5.12 MHz) for reproducibility comparison of collimator movement. Number of protons: $4.8 \cdot 10^{12}$ (1 batch), beam impact parameter: $+4 mm$, measurement point #3. . . .	81
4.12	Plot of the surface displacement for measurements #27 (25.6 MHz sample frequency), #28 (0.1024 MHz), #29 (2.56 MHz), #30 (5.12 MHz) for reproducibility comparison of collimator movement for the first 300 ms. Number of protons: $4.8 \cdot 10^{12}$ (1 batch), beam impact parameter: $+4 mm$, measurement point #3.	82
4.13	Plot of the corrected surface velocity signals (thin lines with marker – upper part of plot) and their corresponding numerically obtained surface displacement (thick lines without marker – lower part of plot) for measurements #31, #32, #33, #34 for reproducibility comparison within the first $100 \mu s$ of collimator movement. Number of protons: $4.8 \cdot 10^{12}$ (1 batch), beam impact parameter: $+4 mm$, measurement point #4.	84
4.14	Plot of the numerically obtained surface displacement for measurements #31, #32, #33, #34 for reproducibility comparison of collimator movement. Number of protons: $4.8 \cdot 10^{12}$ (1 batch), beam impact parameter: $+4 mm$, measurement point #4.	84
4.15	Histogram and Gaussian approximation of mean error between two measurements of sets according to values in tab. 4.12. Number of protons: $4.8 \cdot 10^{12}$ (1 batch), beam impact parameter: $+4 mm$, measurement point #4. . . .	85
4.16	Plot of the recorded surface velocity signals (thin lines with marker – upper part of plot) and their corresponding numerically obtained surface displacement (thick lines without marker – lower part of plot) for measurements #35 (sample frequency 25.6 MHz), #36 (5.12 MHz), #37 (1.024 MHz), #38 (0.256 MHz) for reproducibility comparison within the first $100 \mu s$ of collimator movement with an arbitrarily chosen calibration factor of $1000 mm/s/V$ for the velocity range. Number of protons: $4.8 \cdot 10^{12}$ (1 batch), beam impact parameter: $+4 mm$, measurement point #1.	87

4.17 Plot of the surface displacement obtained by numerical integration of the surface velocities (with an arbitrarily chosen calibration factor of 1000 mm/s/V for the velocity range) for measurements #35 (sample frequency 25.6 MHz), #36 (5.12 MHz), #37 (1.024 MHz), #38 (0.256 MHz) for reproducibility comparison of collimator movement. Number of protons: $4.8 \cdot 10^{12}$ (1 batch), beam impact parameter: $+4 \text{ mm}$, measurement point #1.	88
4.18 Plot of the (partly) smoothed surface velocity signals (upper part of plot) and their corresponding numerically obtained surface displacement (lower part of plot) within the first ms of collimator movement for reproducibility comparison. Number of protons: $4.8 \cdot 10^{12}$ (1 batch), beam impact parameter: $+4 \text{ mm}$, measurement point #2. The calibration factor was arbitrarily chosen to be 1000 mm/s/V	89
4.19 Plot of the recorded surface velocity signals (thin lines with marker – upper part of plot) and their corresponding numerically obtained surface displacement (thick lines without marker – lower part of plot) for measurements #39, #40, #41, #42 of collimator movement for reproducibility comparison. The calibration factor was arbitrarily chosen to be 125 mm/s/V . Number of protons: $4.8 \cdot 10^{12}$ (1 batch), beam impact parameter: $+4 \text{ mm}$, measurement point #2.	90
4.20 Plot of the surface displacement for measurements #39, #40, #41, #42 for reproducibility comparison within the first 112 ms of collimator movement. The calibration factor was arbitrarily chosen to be 125 mm/s/V . Number of protons: $4.8 \cdot 10^{12}$ (1 batch), beam impact parameter: $+4 \text{ mm}$, measurement point #2.	91
4.21 Plot for different measurement points on the collimator jaw of collimator movement: measurements #27 (measurement point #3) and #34 (measurement point #4). Number of protons: $4.8 \cdot 10^{12}$ (1 batch), beam impact parameter: $+4 \text{ mm}$	93
4.22 Plot of the surface velocity signals (thin lines with marker – upper part of plot) and their corresponding numerically obtained surface displacement (thick lines without marker – lower part of plot) for different measurement points on the collimator jaw within 5.5 ms of collimator movement: measurements #30 (measurement point #3) and #31 (measurement point #4). Number of protons: $4.8 \cdot 10^{12}$ (1 batch), beam impact parameter: $+4 \text{ mm}$	94
4.23 Plot of the surface velocity signals (thin lines with marker – upper part of plot) and their corresponding numerically obtained surface displacement (thick lines without marker – lower part of plot) for measurement #18 the first ms of collimator movement for comparison of originally recorded (uncorrected) and speckle dropouts corrected signal. The red curves represent the originally recorded signal, the black curves the speckle dropouts corrected signal. Number of protons: $28.8 \cdot 10^{12}$ (6 batches), beam impact parameter: $+5 \text{ mm}$, measurement point #3.	96

4.24 Plot of the surface velocity signals (thin lines with marker – upper part of plot) and their corresponding numerically obtained surface displacement (thick lines without marker) for measurement #18 within 6.2 ms of collimator movement for comparison of originally recorded (uncorrected) and speckle dropouts corrected signal. The red curve represents the originally recorded signal, the black curve the speckle dropouts corrected signal. Number of protons: $28.8 \cdot 10^{12}$ (6 batches), beam impact parameter: +5 mm, measurement point #3.	97
4.25 Plots for different proton beam intensities the first 200 μs of collimator movement: measurements #14 ($4.8 \cdot 10^{12}$ protons = 1 batch), #15 ($9.6 \cdot 10^{12}$ protons = 2 batches), #16 ($19.2 \cdot 10^{12}$ protons = 4 batches) and #18 ($28.8 \cdot 10^{12}$ protons = 6 batches). Beam impact parameter: +5 mm, measurement point #3.	98
4.26 Plot of the surface displacement of first response at 46.875 μs vs. proton beam intensity for a beam impact parameter of +5 mm at measurement point #3 (measurements #14 ($4.8 \cdot 10^{12}$ protons = 1 batch), #15 ($9.6 \cdot 10^{12}$ protons = 2 batches), #16 ($19.2 \cdot 10^{12}$ protons = 4 batches) and #18 ($28.8 \cdot 10^{12}$ protons = 6 batches)) and the linear fit through the origin.	99
4.27 Plot of the corrected surface velocity signals (thin lines with marker – upper part of plot) and their corresponding numerically obtained surface displacement (thick lines without marker – lower part of plot) for different proton beam intensities: measurements #14 ($4.8 \cdot 10^{12}$ protons = 1 batch), #15 ($9.6 \cdot 10^{12}$ protons = 2 batches), #16 ($19.2 \cdot 10^{12}$ protons = 4 batches) and #18 ($28.8 \cdot 10^{12}$ protons = 6 batches) of collimator movement. Beam impact parameter: +5 mm, measurement point #3.	99
4.28 Plot of the surface displacement for different proton beam intensities in the first 124 ms of collimator movement: measurements #14 ($4.8 \cdot 10^{12}$ protons = 1 batch), #15 ($9.6 \cdot 10^{12}$ protons = 2 batches), #16 ($19.2 \cdot 10^{12}$ protons = 4 batches) and #18 ($28.8 \cdot 10^{12}$ protons = 6 batches). Beam impact parameter: +5 mm, measurement point #3.	100
4.29 Plot of the corrected surface velocity signals (thin lines with marker – upper part of plot) and their corresponding numerically obtained surface displacement (thick lines without marker – lower part of plot) for different beam impact parameters in the first 1.1 ms of collimator movement: measurements #18 (+5 mm), #19 (+4 mm), #20 (+3 mm), #21 (+2 mm), #22 (+1 mm), #23 (0 mm) and #24 (-1 mm). Beam intensity: $28.8 \cdot 10^{12}$, measurement point #3.	102
4.30 Plot of the corrected surface velocity signals for different beam impact parameters (from +5 mm (measurement #18) to -1 mm (measurement #24) in steps of 1 mm) 200 μs of collimator movement. Beam intensity: $28.8 \cdot 10^{12}$, measurement point #3.	103
4.31 Plot of the numerically obtained surface displacement for different beam impact parameters (from +5 mm (measurement #18) to -1 mm (measurement #24) in steps of 1 mm) for 400 μs of collimator movement. Beam intensity: $28.8 \cdot 10^{12}$, measurement point #3.	104

4.32 Plot of the surface displacement at two different times of collimator movement ($49.6875 \mu s$ and $0.5 ms$) vs. beam impact parameter for a beam intensity of $28.8 \cdot 10^{12}$ protons at measurement point #3. Beam impact parameter varying from $+5 mm$ (measurement #18) to $-1 mm$ (measurement #24) in steps of $1 mm$	105
4.33 Schematic pulse time distribution of the experiment at GSI. Distribution A: single bunch with width of $300 ns$ (FWHM). Distribution B: four equally strong and evenly spaced bunches with a peak-to-peak-spacing of $260 ns$ and a bunch width of $80 ns$ (FWHM).	108
5.1 FLUKA simulation results for uranium ion beam with kinetic energy of $350 MeV/u$ with Gaussian distribution (FWHM of $0.85 mm$) impacting from left. Energy deposition is integrated over the whole polar angle given in GeV/cm^3 per incident primary in steps of $0.1 mm$ along beam axis and radius.	111
5.2 FLUKA simulation results for uranium ion beam with kinetic energy of $350 MeV/u$ with Gaussian distribution (FWHM of $0.90 mm$) impacting from left. Energy deposition is integrated over the whole polar angle given in GeV/cm^3 per incident primary in steps of $0.1 mm$ along beam axis and radius.	111
5.3 FLUKA simulation results for uranium ion beam with kinetic energy of $350 MeV/u$ with Gaussian distribution (FWHM of $0.9 mm$) impacting from left. Energy deposition is integrated over the whole polar angle given in GeV/cm^3 per incident primary in steps of $0.1 mm$ along beam axis and radius.	112
5.4 FLUKA simulation results for uranium ion beam with kinetic energy of $350 MeV/u$ with Gaussian distribution (FWHM of $0.9 mm$) impacting from left. Energy deposition is integrated over the whole polar angle given in GeV/cm^3 per incident primary in steps of $0.1 mm$ along beam axis and radius.	112
5.5 Comparison between typical signal (here: shot 2238) of single bunch beam time distribution (distribution A) recorded with fast current transformer (FCT) with simplified beam time distribution used for simulations with ANSYS AUTODYN [®] . Data of FCT: courtesy plasma physics group at GSI.	116
5.6 Copper target simulated with $P_{MIN} = -216 MPa$ and beam width of $0.85 mm$ (FWHM). Status at $5 ms$ simulated time after beam impact from left on intact target. Uranium ion beam intensity of $5.87 \cdot 10^8$ ((a) – (c)), $8.59 \cdot 10^8$ ((d) – (f)) and $2.12 \cdot 10^9$ ((g) – (i)), respectively. Minimum and maximum values for effective plastic strain ((a), (d) and (g)) set low ($1 \cdot 10^{-5}$ and $2 \cdot 10^{-5}$, respectively) in order to distinguish between elastically deformed nodes (in dark blue) and plastically deformed (in red). Dark blue nodes of yield stress $0 kPa$ in (b), (e) and (h) which can either be obtained through reaching failure condition or through thermal softening as implemented in strength model. Only thermally softened nodes in dark blue in (c), (f) and (i).	119

5.7 Copper target simulated with $P_{MIN} = -5.4$ GPa and beam width of 0.85 mm (FWHM). Status at 5 ms simulated time after beam impact from left on intact target. Uranium ion beam intensity of $5.87 \cdot 10^8$ ((a) – (c)), $8.59 \cdot 10^8$ ((d) – (f)) and $2.12 \cdot 10^9$ ((g) – (i)), respectively. Minimum and maximum values for effective plastic strain ((a), (d) and (g)) set low ($1 \cdot 10^{-5}$ and $2 \cdot 10^{-5}$, respectively) in order to distinguish between elastically deformed nodes (in dark blue) and plastically deformed (in red). Dark blue nodes of yield stress 0 kPa in (b), (e) and (h) which can either be obtained through reaching failure condition or through thermal softening as implemented in strength model. Only thermally softened nodes in dark blue in (c), (f) and (i).	120
5.8 Copper target simulated with $P_{MIN} = -3.24$ GPa, intensity of $2.12 \cdot 10^9$ uranium ions and beam width of 0.85 mm (FWHM). Status at 5 ms simulated time after beam impact from left on intact target. Minimum and maximum values for effective plastic strain (a) set low ($1 \cdot 10^{-5}$ and $2 \cdot 10^{-5}$, respectively) in order to distinguish between elastically deformed nodes (in dark blue) and plastically deformed (in red). Dark blue nodes of yield stress 0 kPa in (b) which can either be obtained through reaching failure condition or through thermal softening as implemented in strength model. Only thermally softened nodes in dark blue in (c).	121
5.9 Copper target simulated with $P_{MIN} = -1.08$ GPa and beam width of 0.85 mm (FWHM). Status at 5 ms simulated time after beam impact from left on intact target. Uranium ion beam intensity of $5.87 \cdot 10^8$ ((a) – (c)), $8.59 \cdot 10^8$ ((d) – (f)) and $2.12 \cdot 10^9$ ((g) – (i)), respectively. Minimum and maximum values for effective plastic strain ((a), (d) and (g)) set low ($1 \cdot 10^{-5}$ and $2 \cdot 10^{-5}$, respectively) in order to distinguish between elastically deformed nodes (in dark blue) and plastically deformed (in red). Dark blue nodes of yield stress 0 kPa in (b), (e) and (h) which can either be obtained through reaching failure condition or through thermal softening as implemented in strength model. Only thermally softened nodes in dark blue in (c), (f) and (i).	122
5.10 Copper target simulated with $P_{MIN} = -1.08$ GPa, intensity of $2.12 \cdot 10^9$ uranium ions and beam width of 0.85 mm (FWHM). Status at 2 ms simulated time after beam impact from left on intact target. Minimum and maximum values for effective plastic strain (a) set low ($1 \cdot 10^{-5}$ and $2 \cdot 10^{-5}$, respectively) in order to distinguish between elastically deformed nodes (in dark blue) and plastically deformed (in red). Dark blue nodes of yield stress 0 kPa in (b) which can either be obtained through reaching failure condition or through thermal softening as implemented in strength model. Only thermally softened nodes in dark blue in (c).	123
5.11 Photograph from the metallurgical examination of sample 26. (Micrography courtesy Jacques Lettry et al. [161])	123
5.12 Photograph of details of the beam entrance zone from the metallurgical examination of sample 26. (Micrography courtesy Jacques Lettry et al. [161])	124

5.13 First maxima of SPH node histories for shots 5, 7 and 8 for $P_{MIN} = -1.08 \text{ GPa}$. The pressure values have been obtained for the node receiving the maximum energy deposition. The velocity values are displayed for the center node on the lateral surface of the cylinder where the measurement point of the Laser Doppler vibrometer was situated. The uranium ion beam intensity followed by the plot value are shown for each point.	125
5.14 First $5 \mu\text{s}$ of SPH node histories for surface pressure and surface velocity for $5.87 \cdot 10^8$ ions and $P_{MIN} = -1.08 \text{ GPa}$	125
5.15 Copper target simulated with $P_{MIN} = -1.08 \text{ GPa}$ and beam width of 0.9 mm (FWHM). Status at 5 ms simulated time after beam impact from left. Uranium ion beam intensity of $2.22 \cdot 10^9$ ((a) – (c)) on intact target and $2.36 \cdot 10^9$ ((d) – (f)) for second shot on simplified target (grey overlay over upper half of simulation results (a) – (c)), respectively. Simplified geometry after first beam impact approximated by leaving two cylinders ($r_1 = 0.5 \text{ mm}$, $l_1 = 3.5 \text{ mm}$ and $r_2 = 0.3 \text{ mm}$, $l_2 = 0.3 \text{ mm}$) empty to account for failed nodes. Minimum and maximum values for effective plastic strain ((a) and (d)) set low ($1 \cdot 10^{-5}$ and $2 \cdot 10^{-5}$, respectively) in order to distinguish between elastically deformed nodes (in dark blue) and plastically deformed (in red). Dark blue nodes of yield stress 0 kPa in (b) and (e) which can either be obtained through reaching failure condition or through thermal softening as implemented in strength model. Only thermally softened nodes in dark blue in (c) and (f).	127
5.16 Copper target simulated with $P_{MIN} = -3.24 \text{ GPa}$ and beam width of 0.9 mm (FWHM). Status at 5 ms simulated time after beam impact from left. Uranium ion beam intensity of $2.22 \cdot 10^9$ ((a) – (c)) on intact target and $2.36 \cdot 10^9$ ((d) – (f)) for second shot on simplified target (gray overlay over upper half of simulation results (a) – (c)), respectively. Simplified geometry after first beam impact approximated by leaving cylinder ($r = 0.3 \text{ mm}$, $l = 3 \text{ mm}$) inside bulk target empty (starting inside target after 1.5 mm) to account for failed nodes. Minimum and maximum values for effective plastic strain ((a) and (d)) set low ($1 \cdot 10^{-5}$ and $2 \cdot 10^{-5}$, respectively) in order to distinguish between elastically deformed nodes (in dark blue) and plastically deformed (in red). Dark blue nodes of yield stress 0 kPa in (b) and (e) which can either be obtained through reaching failure condition or through thermal softening as implemented in strength model. Only thermally softened nodes in dark blue in (c) and (f).	128
5.17 Photograph from the metallurgical examination of sample 28. (Micrography courtesy Jacques Lettry et al. [161])	129
5.18 Collage of photographs of details of the beam entrance zone from the metallurgical examination of sample 28. (Microographies courtesy Jacques Lettry et al. [161])	129

5.19 Lead target simulated with Uranium ion beam intensity of $2.16 \cdot 10^9$ and beam width of 0.90 mm (FWHM) impacting from left on intact target. The maximum energy deposition occurred at 3.6 mm inside the 7 mm long target. Status at 0.05 ms simulated time after beam impact for fig. 5.19(a) – fig. 5.19(c) and at 0.1 ms simulated time after beam impact for fig. 5.19(d) – fig. 5.19(f) . $P_{MIN} = 0.2$ GPa for ((a) – (c)) and $P_{MIN} = 0.5$ GPa for ((d) – (f)), respectively. Minimum and maximum values for effective plastic strain (a) and (d)) set low ($1 \cdot 10^{-5}$ and $2 \cdot 10^{-5}$, respectively) in order to distinguish between elastically deformed nodes (in dark blue) and plastically deformed (in red). Dark blue nodes of yield stress 0 kPa in (b) and (e) which can either be obtained through reaching failure condition or through thermal softening as implemented in strength model. Only thermally softened nodes in dark blue in (c) and (f). 131

5.20 Tantalum target simulated with Uranium ion beam intensity of $2.39 \cdot 10^9$ and beam width of 0.90 mm (FWHM). Status at 5 ms simulated time after beam impact from left on intact target. The maximum energy deposition occurred at 2.3 mm inside the 5 mm long target. $P_{MIN} = 4.4$ GPa for ((a) – (c)), $P_{MIN} = 5.25$ GPa for ((d) – (f)) and $P_{MIN} = 8.1$ GPa for ((g) – (i)), respectively. Minimum and maximum values for effective plastic strain ((a), (d) and (g)) set low ($1 \cdot 10^{-5}$ and $2 \cdot 10^{-5}$, respectively) in order to distinguish between elastically deformed nodes (in dark blue) and plastically deformed (in red). Dark blue nodes of yield stress 0 kPa in (b), (e) and (h) which can either be obtained through reaching failure condition or through thermal softening as implemented in strength model. Only thermally softened nodes in dark blue in (c), (f) and (i). 133

5.21 Tungsten target simulated with Uranium ion beam intensity of $2.24 \cdot 10^9$ and beam width of 0.90 mm (FWHM). Status at 5 ms simulated time after beam impact from left on intact target. The maximum energy deposition occurred at 2.0 mm inside the 5 mm long target. $P_{MIN} = 0.4$ GPa for ((a) – (c)), $P_{MIN} = 0.8$ GPa for ((d) – (f)) and $P_{MIN} = 2.9$ GPa for ((g) – (i)), respectively. Minimum and maximum values for effective plastic strain ((a), (d) and (g)) set low ($1 \cdot 10^{-5}$ and $2 \cdot 10^{-5}$, respectively) in order to distinguish between elastically deformed nodes (in dark blue) and plastically deformed (in red). Dark blue nodes of yield stress 0 kPa in (b), (e) and (h) which can either be obtained through reaching failure condition or through thermal softening as implemented in strength model. Only thermally softened nodes in dark blue in (c), (f) and (i). 134

List of Tables

2.1	Names, acronyms and abbreviations in chapter 2 (including those used in tab. 2.2 starting on p. 4)	3
2.2	Example of target facilities around the world (inspired by slide 3 of [4]). Abbreviations and Symbols: stat. (status); mat. (material), t_{pulse} (beam pulse duration), f_{pulse} (pulse repetition rate), E_{kin} (kinetic beam energy), $\langle P_{beam} \rangle$ (time averaged beam power), \dagger (per nucleon); bl (blanket), $(Xx)^{cl}$ (cladding/tubes with material Xx), C-C (carbon-carbon composite), δ (with regards to direct target), Xx^f (foil of material Xx), $^{\lambda}$ (liquid), η (with regards to neutron-converter), ZA (Zirkaloy); driver beam types: $^{(p)}$ (proton), $^{(3)He}$ (3 He), $^{(d)}$ (deuterium), $^{(Ar)}$ (argon), $^{(U)}$ (uranium); for beta-beam: $^{(6)He}$ for production of 6 He and ^{18}Ne for production of ^{18}Ne ; abbreviations for status of facilities: E (existing), DF (design study finalized), UC (under construction), US (under study)	4
2.3	Physics driven requirements (+ ... required, ++ ... emphasized) for high power targets (based on [39], [40], [42], [44], [45], [48], [51], [52] and [46])	9
3.1	General trends of ductile-brittle relationship (compiled from [62] p. 25 ff. and [61] tab. 10.1) (*) The ductile-to-brittle transition temperature is observed for low-strength steels that have a body centered cubic crystal structure. No transition temperature is found for ductile low-strength face centered cubic and most hexagonal close packed metals, or for brittle high-strength metals. (**) The lack of notches or stress concentrations allows shear deformation to occur so that high stresses can spread within the specimen, which is needed for ductile behavior of the material. (***) The larger (or thicker) the specimen, the more likely the occurrence of discontinuities (serving as stress concentrations) and triaxial tensile stresses, which both serve as a basis for brittle fracture. (****) A more pronounced effect for metals with high strength levels. (*****) Brittle materials fracture in a ductile manner when exposed to high hydrodynamic pressures.	24
4.1	Acronyms and abbreviations of section 4.1	68
4.2	Positions of the retro-reflecting tape on the collimator jaw for every window in the collimator tank. The distances are counted from the side facing upstream to the beam. Priority was given to the measurement points behind window 1 and 3.	69

4.3	Positions of measurement points on the collimator as assigned during the TT40 test.	69
4.4	Extract of the two logbooks by the collimator team [146] and the LDV team. The LDV was recording the surface velocities with different sample frequencies. The total number of samples was limited to 32 768 ($= 2^{15}$), hence an increase of the LDV sample frequency results in a shorter LDV recording time. Abbreviations (see section 4.1.3.1 starting on p. 73 for more details): (a) = arbitrarily chosen (could not be reobtained), (l) = logged, (r) = reobtained, (r,a) = only partly reobtained (see section 4.1.3.2.4 starting on p. 86).	74
4.5	Maximum values of simulated energy deposition for the collimator jaw C-C composite and copper (Glidcop [®]) support plate by FLUKA (provided by [151]). The coordinates of the maxima given are the same as in figures 4.6, 4.7 on p. 76 and 4.8 on p. 77. The mesh size was 1 mm for both x - and y -direction and 10 mm for z	75
4.6	Summary of possible ratios for the velocity ranges of the LDV and their corresponding calibration factors.	78
4.7	Entries of logbook for measurement point #3, a beam impact parameter on the collimator jaw of +4 mm and an intensity of $4.8 \cdot 10^{12}$ protons (1 batch). Abbreviation: l = logged.	80
4.8	Calculated difference of measurements at measurement point #3, with beam impact parameter on collimator jaw of +4 mm and beam intensity of $4.8 \cdot 10^{12}$ protons (1 batch) for first response of three measurements with high sample frequency.	80
4.9	Entries of logbook for measurement point #4, a beam impact parameter on the collimator jaw of +4 mm and an intensity of $4.8 \cdot 10^{12}$ protons (1 batch). Abbreviations: l = logged, r = reobtained.	83
4.10	List of removed speckle dropouts for measurement #32 and #33.	83
4.11	Sets for quantification of reproducibility during LDV measurements.	85
4.12	Parameters μ and σ for Gaussian approximation of calculated differences between measurements belonging to one set (details see text).	85
4.13	Relative error of reproducibility expressed in percent (see text on p. 85 for further explanation).	86
4.14	Entries of logbook for measurement point #1, a beam impact parameter on the collimator jaw of +4 mm and an intensity of $4.8 \cdot 10^{12}$ protons (1 batch). Abbreviation: a = arbitrarily chosen.	86
4.15	Entries of logbook for measurement point #2, a beam impact parameter on the collimator jaw of +4 mm and an intensity of $4.8 \cdot 10^{12}$ protons (1 batch). Abbreviations: r = reobtained, a = arbitrarily chosen	87
4.16	Smoothing spans for measurements at point #2 (beam impact parameter +4 mm, intensity $4.8 \cdot 10^{12}$ protons).	88
4.17	Entries of logbook for measurements with a beam impact parameter on the collimator jaw of +4 mm and an intensity of $4.8 \cdot 10^{12}$ protons (1 batch) with a recording time of 1.28 ms (a sample frequency of 25.6 MHz), known calibration factor and no speckle dropouts (set #1). Abbreviations: l = logged, r = reobtained.	92

LIST OF TABLES

4.18	Entries of logbook for measurements with a beam impact parameter on the collimator jaw of $+4\text{ mm}$ and an intensity of $4.8 \cdot 10^{12}$ protons (1 batch) with a recording time of 6.4 ms (a sample frequency of 5.12 MHz), known calibration factor and no speckle dropouts (set #2). Abbreviations: l = logged.	92
4.19	Entries of logbook for measurements with a beam impact parameter on the collimator jaw of $+5\text{ mm}$ at measurement point #3 with varying intensities. Abbreviation: l = logged.	94
4.20	List of removed speckle dropouts for measurement #16 and #18. (*) set of 11 speckle dropouts – velocity set to 0.	95
4.21	Entries of logbook for measurements with an intensity of $28.8 \cdot 10^{12}$ protons (6 batches) at measurement point #3 for different beam impact parameters on the collimator jaw. Abbreviations: l = logged, a = arbitrarily chosen.	101
4.22	Ratios of time interval for removed speckle dropouts versus recorded time after beam impact and number of removed speckle dropouts for measurements #18, #19, #20, #21, #22 and #23.	101
4.23	Proton beam width with a FWHM of 1 mm assuming a Gaussian beam cross section with dependence on confidence interval (see text around equ. 4.3 on p. 102 for further explanation).	105
4.24	List of metal targets irradiated at GSI.	107
5.1	Uranium ion beam parameters for two 7 mm long copper samples irradiated with time distribution A and a kinetic energy of 350 MeV/u resulting in a total available beam energy per incident ion of 83.3 GeV . Calculations of total deposited energy and peak energy density were performed with FLUKA. The peak energy density is the energy density in the Bragg peak, assuming an intact target for each shot (exception: shot 2 on sample 28 was obtained for preferred simplified target geometry after material ejection – see fig. 5.15(a) – 5.15(c) on p. 127). The density of copper was taken to be 8.9 g/cm^3	110
5.2	Available material models for copper in ANSYS AUTODYN [®]	114
5.3	Material constants from [99] for equ. (5.2) for OFHC copper.	115
5.4	Beam parameters for simulations obtained with ANSYS AUTODYN [®] (abbreviated AA) and the BIG-2 (abbreviated B2 in the table below) code for comparable maximum energy deposition. Values for BIG-2 are from [159]. Simulation AA was calculated for a single 300 ns bunch (beam time distribution A) while simulation BIG-2 was calculated for two bunches with a FWHM bunch width of 80 ns and a total pulse duration of 500 ns (approximation of beam time distribution B). For the calculation of the peak energy density for AA the density of copper was taken to be 8.9 g/cm^3 . The initial density for copper for the model run with the BIG-2 code was taken to be 8.93 g/cm^3 [185].	124
5.5	Available material models for lead, tantalum and tungsten in ANSYS AUTODYN [®]	130

A.1	FLUKA cards for energy deposition calculations for copper target. As there are no entries for WHAT(5) and WHAT(6) they are omitted from this listing. METARGET is the region containing the target.	139
B.1	List of beam parameters of targets made of tantalum and tungsten irradiated at GSI.	141
B.2	List of beam parameters of targets made of copper and lead irradiated at GSI.142	

References

- [1] A. Ferrari, P. R. Sala, A. Fassò, and J. Ranft. FLUKA: A multi-particle transport code (Program version 2005). Technical Report CERN-2005010 and INFNTC 05/11 and SLAC-R773, CERN, INFN Milan, SLAC, Oct 2005.
- [2] A. Fassò, A. Ferrari, S. Roesler, P. R. Sala, F. Ballarini, A. Ottolenghi, G. Battistoni, F. Cerutti, E. Gadioli, M. V. Garzelli, A. Empl, and J. Ranft. The physics models of FLUKA: status and recent development. Technical report, SLAC.
- [3] Century Dynamics. AUTODYN Theory Manual. Technical Report Revision 4.3, Century Dynamics, 2005.
- [4] P. Hurh. LBNE Target – R&D/Conceptual Design Activities and Opportunities. Talk given at the Workshop of Applications of High Intensity Proton Accelerators (FNAL, Oct 19-21, 2009), Oct 2009.
- [5] J. Alessi, D. Barton, D. Beavis, S. Bellavia, I. Ben-Zvi, J. Brennan, M. Diwan, P. K. Feng, J. Gallardo, D. Gassner, R. Hahn, D. Hseuh, S. Kahn, H. Kirk, Y. Y. Lee, E. Lessard, D. Lowenstein, H. Ludewig, K. Mirabella, W. Marciano, I. Marneris, T. Nehring, C. Pearson, A. Pendzick, P. Pile, D. Raparia, T. Roser, A. Ruggiero, N. P. Samios, N. Simos, J. Sandberg, N. Tsoupas, J. Tuozzolo, B. Viren, J. Beebe-Wang, J. Wei, W. T. Weng, N. Williams, P. Yamin, K. C. Wu, A. Zaltsman, S. Y. Zhang, W. Zhang, W. T. Weng, M. Diwan, and D. Raparia. The AGS-Based Super Neutrino Beam Facility Conceptual Design Report. Technical Report BNL-73210-2004-IR, Brookhaven National Laboratory (BNL), 2004.
- [6] A. Longhin. A new design for the CERN-Fréjus neutrino Super Beam. *EPJ*, arXiv:1106.1096 [physics.acc-ph], 2011.
- [7] Institute of High Energy Physics CAS Beijing (China). Physics Design and Technology Development of CSNS Accelerator – Second CSNS International Accelerator Technology Advisory Committee Review Meeting. <http://csns.ihep.ac.cn/english/image/CSNS%20Accelerator.pdf>, Jan 2010.
- [8] Institute of High Energy Physics CAS Beijing (China). Physics Design and Technology Development of CSNS Target Station and Instruments – Second CSNS International Neutron Technology Advisory Committee Review Meeting. <http://csns.ihep.ac.cn/english/Target/image/physical%20design%20and%20technology%20development%20of%20CSNS%20TS&NI%20for%20NTAC.pdf>, Apr 2010.

- [9] M. Lindroos, T. Satogata, R. Calaga, H. Danared, G. Devanz, R. Duperrier, J. Eguia, M. Eshraqi, S. Gammino, H. Hahn, A. Jansson1, C. Oyon, S. Pape-Møller, S. Peggs, A. Ponton, K. Rathsman, R. Ruber, T. Satogata, and G. Trahern. The European Spallation Source. In *Proceedings of the 2010 ECAART (European Conference on Accelerators in Applied Research and Technology) Conference, Athens, Greece (Sep 2010)*, 2010.
- [10] E. Noah. Private communication – documents in preparation within ESS project, August 2011.
- [11] Final Report of the EURISOL Design Study (2005-2009) – EURISOL A Design Study for European Isotope-Separation-On-Line Radioactive Ion Beam Facility. Technical report, GANIL, Caen (France), Nov 2009.
- [12] M. Thoennessen. Plans for the Facility for Rare Isotope Beams. *Nuclear Physics A*, 834(1-4):688c – 693c, 2010. The 10th International Conference on Nucleus-Nucleus Collisions (NN2009).
- [13] D. J. Morrissey. Status of the FRIB project with a new fragment separator. *Journal of Physics: Conference Series*, 267(1):012001, 2011.
- [14] F. Pellemoine, W. Mittig, M. Avilov, D. Ippel, J. Lenz, J. Oliva, I. Silverman, D. Youchison, and T. Xu. Thermo-mechanical behaviour of a single slice test device for the FRIB high power target. *Nuclear Instruments and Methods in Physics Research Section A: Accelerators, Spectrometers, Detectors and Associated Equipment*, In Press, Corrected Proof, 2011.
- [15] M. Dombsky, P. Bricault, P. Schmor, and M. Lane. ISAC target operation with high proton currents. *Nuclear Instruments and Methods in Physics Research Section B: Beam Interactions with Materials and Atoms*, 204:191 – 196, 2003. 14th International Conference on Electromagnetic Isotope Separators and Techniques Related to their Applications.
- [16] P. Bricault. Status report of the radioactive ion beam production at TRIUMF (invited). *Review of Scientific Instruments*, 77(3):03A710, 2006.
- [17] P. Bricault. Progress towards new RIB and higher intensities at TRIUMF. Talk given at 19th International Conference on Cyclotrons and their Applications, Lanzhou, P. R. China http://cyclotrons10.impcas.ac.cn/JACoWPub/talks/thm1cio04_talk.pdf, Sep 2010.
- [18] D. J. S. Findlay. ISIS - pulsed neutron and muon source. In *Particle Accelerator Conference, 2007. PAC. IEEE*, pages 695 – 699, june 2007.
- [19] Second Target Station – Specifications – Technical description of the Second Target Station. <http://www.isis.stfc.ac.uk/about-isis/target-station-2/science/technical-description-of-the-second-target-station8195.pdf>, Jul 2011.

- [20] E. Kugler. The ISOLDE facility. *Hyperfine Interactions*, 129:23 – 42, 2000. 10.1023/A:1012603025802.
- [21] U Köster. ISOLDE target and ion source chemistry. *Radiochim. Acta*, 89(CERN-OPEN-2001-075. 11-12):749 – 756, Jan 2001.
- [22] The ISOLDE facility. <http://isolde.web.cern.ch/isolde/facility/facility.php>, Jul 2011.
- [23] Y. Ikeda. Current status of 1 MW pulse spallation neutron source (JSNS) of J-PARC. *Journal of Nuclear Materials*, 343(1-3):7 – 13, 2005. Proceedings of the 6th International Workshop on Spallation Materials Technology.
- [24] J-PARC Annual Report 2009. Technical report, J-PARC, Oct 2010.
- [25] L. Rybarczyk. Possible Upgrade Paths for the LANSCE H- Injector. In *Proceedings of LINAC 2006, Knoxville, Tennessee USA*, pages 330 – 332, 2006.
- [26] R. W. Garnett, L. J. Rybarczyk, D. E. Rees, T. Tajima, and E. J. Pitcher. High-Power Options for LANSCE. Talk given at the 2011 Particle Accelerator Conference, USA, http://www.c-ad.bnl.gov/pac2011/proceedings/talks/thocn4_talk.pdf, Mar 2011.
- [27] The Los Alamos Neutron Science Center (LANSCE). lansce.lanl.gov/, Jul 2011.
- [28] S. Choubey, R. Gandhi, S. Goswami, J. S. Berg, R. Fernow, J. C. Gallardo, R. Gupta, H. Kirk, N. Simos, N. Souchlas, M. Ellis, P. Kyberd, E. Benedetto, E. Fernandez-Martinez, I. Efthymiopoulos, R. Garoby, S. Gilardoni, M. Martini, G. Prior, P. Ballett, S. Pascoli, A. Bross, S. Geer, C. Johnstone, J. Kopp, N. Mokhov, J. Morfin, D. Neuffer, S. Parke, M. Popovic, J. Strait, S. Striganov, A. Blondel, F. Dufour, A. Laing, F. J. P. Soler, M. Lindner, T. Schwetz, A. Alekou, M. Apollonio, M. Aslaninejad, C. Bontoiu, P. Dornan, R. Eccleston, A. Kurup, K. Long, J. Pasternak, J. Pozimski, A. Bogacz, V. Morozov, Y. Roblin, S. Bhattacharya, D. Majumdar, Y. Mori, T. Planche, M. Zisman, D. Cline, D. Stratakis, X. Ding, P. Coloma, A. Donini, B. Gavela, J. Lopez Pavon, M. Maltoni, C. Bromberg, M. Bonesini, T. Hart, Y. Kudenko, N. Mondal, S. Antusch, M. Blennow, T. Ota, R. J. Abrams, C. M. Ankenbrandt, K. B. Beard, M. A. C. Cummings, G. Flanagan, R. P. Johnson, T. J. Roberts, C. Y. Yoshikawa, P. Migliozzi, V. Palladino, A. de Gouvea, V. B. Graves, Y. Kuno, J. Peltoniemi, V. Blackmore, J. Cobb, H. Witte, M. Mezzetto, S. Rigolin, K. T. McDonald, L. Coney, G. Hanson, P. Snopok, L. Tortora, C. Andreopoulos, J. R. J. Bennett, S. Brooks, O. Caretta, T. Davenne, C. Densham, R. Edgecock, D. Kelliher, P. Loveridge, A. McFarland, S. Machida, C. Prior, G. Rees, C. Rogers, J. W. G. Thomason, C. Booth, G. Skoro, Y. Karadzhov, R. Matev, R. Tsenov, R. Samulyak, S. R. Mishra, R. Petti, M. Dracos, O. Yasuda, S. K. Agarwalla, A. Cervera-Villanueva, J. J. Gomez-Cadenas, P. Hernandez, T. Li, J. Martin-Albo, P. Huber, J. Back, G. Barker, P. Harrison, D. Meloni, J. Tang, and W. Winter. International Design Study for the Neutrino Factory – Interim Design Report. Technical Report IDS-NF-20, 2011.

- [29] SNS Parameter list, SNS 100000000-PL0001-R13. http://neutrons.ornl.gov/pubs/sns_parameters_list_june05.pdf, Jun 2005.
- [30] W. Wagner, Y. Dai, H. Glasbrenner, M. Grosse, and E. Lehmann. Status of SINQ, the only MW spallation neutron source—highlighting target development and industrial applications. *Nuclear Instruments and Methods in Physics Research Section A: Accelerators, Spectrometers, Detectors and Associated Equipment*, 562(2):541 – 547, 2006. Proceedings of the 7th International Conference on Accelerator Applications - AccApp05.
- [31] The Neutron Source Developement Group (NSDG). SINQ Target Development. graph: Operational History of the SINQ Facility since its start up in 1997 – on http://nsdg.web.psi.ch/4_develop.htm, 2011.
- [32] W. Wagner and M. Wohlmuther. Illustrated history of the SINQ target development. <http://nsdg.web.psi.ch/SINQ%20new%20target.pdf>, 2011.
- [33] SPES – Selective Production of Exotic Species – Technical Design Report. Technical report, Laboratori Nazionali di Legnaro, Apr 2008.
- [34] J. C. Putaux, P. Bertrand, M. Ducourtieux, A. Ferro, P. Foury, O. Kaitasov, L. Kotfila, N. Lecesne, R. Leroy, C. F. Liang, M. Loiselet, J. Mandin, L. Maunoury, A. C. Mueller, J. Obert, J. Y. Pacquet, N. Pauwels, J. C. Potier, J. Proust, E. Robert, M. O. Ruault, G. Ryckewaert, P. Sortais, M. Toulemonde, and A. C. C. Villari. Graphite target for the SPIRAL project. *Nuclear Instruments and Methods in Physics Research Section B: Beam Interactions with Materials and Atoms*, 126(1-4):113 – 116, 1997. International Conference on Electromagnetic Isotope Separators and Techniques Related to Their Applications.
- [35] R. Leroy, C. Barue, C. Canet, M. Dubois, M. Dupuis, F. Durantel, W. Farabolini, J-L. Flambard, G. Gaubert, S. Gibouin, C. Huet-Equilibec, Y. Huguet, P. Jardin, N. Lecesne, P. Leherissier, F. Lemagnen, J. Y. Pacquet, F. Pellemoine, M. G. Saint Laurent, O. Tuske, and A. C. C. Villari. Radioactive Ion beam production at GANIL : status and prospectives. In *Electron cyclotron resonance ion sources: 16th International Workshop on ECR Ion Sources, ECRIS '04, Berkeley, California, 26-30 September 2004*, pages 137 – 142, 2005.
- [36] S. Gales, G. Gaubert, F. Chautard, D. Beaumel, W. Catford, A. Görzen, O. Lopez, F. de Oliveira Santos, B. Blank, and J.-C. Thomas. GANIL / SPIRAL – 2001–2007 – Achievements, Highlights and Perspectives. Technical Report GANIL R 08 01, in2p3-00336915, GANIL, Nov 2008.
- [37] Project Team of the SPIRAL 2 APD phase. The SPIRAL 2 Project – APD Report – Chapter III Driver Accelerator. Technical report, GANIL, CNRS/IN2P3, CEA/DSM, 2005.
- [38] Project Team of the SPIRAL 2 APD phase. The SPIRAL 2 Project – APD Report – Chapter IV Converter, Target and Ion Source. Technical report, GANIL, CNRS/IN2P3, CEA/DSM, 2005.

- [39] F. Mezei. Accelerator requirements for next generation neutron sources. *Nuclear Instruments and Methods in Physics Research Section A: Accelerators, Spectrometers, Detectors and Associated Equipment*, 562(2):553 – 556, 2006. Proceedings of the 7th International Conference on Accelerator Applications - AccApp05.
- [40] G. S. Bauer. Physics and technology of spallation neutron sources. *Nuclear Instruments and Methods in Physics Research Section A: Accelerators, Spectrometers, Detectors and Associated Equipment*, 463(3):505 – 543, 2001. Accelerator driven systems.
- [41] G. S. Bauer. Overview on spallation target design concepts and related materials issues. *Journal of Nuclear Materials*, 398(1-3):19 – 27, 2010. Proceedings of the Ninth International Workshop on Spallation Materials Technology.
- [42] N. Watanabe. Neutronics of pulsed spallation neutron sources. *Reports on Progress in Physics*, 66(3):339, 2003.
- [43] IFMIF – International Fusion Materials Irradiation Facility. <http://www.frascati.enea.it/ifmif/>, Jul 2011.
- [44] E. Noah, R. Catherall, Y. Kadi, C. Kharoua, J. Lettry, and T. Stora. Driver Beam-Led EURISOL Target Design Constraints. (EURISOL-03-21-2008-0018), Nov 2008.
- [45] H. L. Ravn. Advanced target concepts for production of radioactive ions and neutrino beams. *Nuclear Instruments and Methods in Physics Research Section B: Beam Interactions with Materials and Atoms*, 204:197 – 204, 2003. 14th International Conference on Electromagnetic Isotope Separators and Techniques Related to their Applications.
- [46] P. Sievers. A stationary target for the CERN-neutrino-factory. *Nuclear Instruments and Methods in Physics Research Section A: Accelerators, Spectrometers, Detectors and Associated Equipment*, 503(1-2):344 – 347, 2003. Proceedings of the 3rd International Workshop on Neutrino Factories based on Muon Storage Rings.
- [47] P. Sievers and P. Pugnat. Response of Solid and Liquid Targets to High Power Proton Beams for Neutrino Factories. Technical report, CERN.
- [48] The ISS Accelerator Working Group, M. Apollonio, J. S. Berg, A. Blondel, A. Bogacz, S. Brooks, J-E. Campagne, D. Caspar, C. Cavata, P. Chimenti, J. Cobb, M. Dracos, R. Edgecock, I. Efthymiopoulos, A. Fabich, R. Fernow, F. Filthaut, J. Gallardo, R. Garoby, S. Geer, F. Gerigk, G. Hanson, R. Johnson, C. Johnstone, D. Kaplan, E. Keil, H Kirk, A. Klier, A. Kurup, J. Lettry, K. Long, S. Machida, K. McDonald, F. Méot, Y. Mori, D. Neuffer, V. Palladino, R. Palmer, K. Paul, A. Poklonskiy, M. Popovic, C. Prior, G. Rees, C. Rossi, T. Rovelli, R. Sandström, R. Seviour, P. Sievers, N. Simos, Y. Torun, M. Vretenar, K. Yoshimura, and M. S. Zisman. Accelerator design concept for future neutrino facilities. *Journal of Instrumentation*, 4(07):P07001, 2009.

[49] A. Bandyopadhyay, S. Choubey, R. Gandhi, S. Goswami, B. L. Roberts, J. Bouchez, I. Antoniadis, J. Ellis, G. F. Giudice, T. Schwetz, S. Umasankar, G. Karagiorgi, A. Aguilar-Arevalo, J. M. Conrad, M. H. Shaevitz, S. Pascoli, S. Geer, J. E. Campagne, M. Rolinec, A. Blondel, M. Campanelli, J. Kopp, M. Lindner, J. Peltoniemi, P. J. Dornan, K. Long, T. Matsushita, C. Rogers, Y. Uchida, M. Dracos, K. Whisnant, D. Casper, M.-C. Chen, B. Popov, J. Äystö, D. Marfatia, Y. Okada, H. Sugiyama, K. Jungmann, J. Lesgourgues, M. Zisman, M. A. Tórtola, A. Friedland, S. Davidson, S. Antusch, C. Biggio, A. Donini, E. Fernandez-Martinez, B. Gavela, M. Maltoni, J. Lopez-Pavon, S. Rigolin, N. Mondal, V. Palladino, F. Filthaut, C. Albright, A. de Gouvea, Y. Kuno, Y. Nagashima, M. Mezzetto, S. Lola, P. Langacker, A. Baldini, H. Nunokawa, D. Meloni, M. Diaz, S. F. King, K. Zuber, A. G. Akeroyd, Y. Grossman, Y. Farzan, K. Tobe, M. Aoki, H. Murayama, N. Kitazawa, O. Yasuda, S. Petcov, A. Romanino, P. Chimenti, A. Vacchi, A. Yu. Smirnov, E. Couce, J. J. Gomez-Cadenas, P. Hernandez, M. Sorel, J. W. F. Valle, P. F. Harrison, C. Lunardini, J. K. Nelson, V. Barger, L. Everett, P. Huber, W. Winter, W. Fetscher, and A. van der Schaaf. Physics at a future Neutrino Factory and super-beam facility. *Reports on Progress in Physics*, 72(10):106201, 2009.

[50] T. Stora. EUROnu-WP4-011: Baseline ion production dedicated to beta-beams. Technical report, EUROnu, 2010.

[51] G. S. Bauer. Development of high power targets. In *Proceedings of EPAC 2004*, pages 276 – 280, 2004.

[52] A. Fabich. Target R&D for high power proton beam applications. *AIP Conference Proceedings*, 981(1):127 – 131, 2008.

[53] P. Drumm, C. Densham, and R. Bennett. Target studies for the neutrino factory at the Rutherford Appleton Laboratory. *Nuclear Instruments and Methods in Physics Research Section A: Accelerators, Spectrometers, Detectors and Associated Equipment*, 472(3):627 – 631, 2001.

[54] C. Grupen and B. Shwartz. *Particle Detectors*. Cambridge Univ. Press.

[55] K. Nakamura and Particle Data Group. Review of particle physics. *Journal of Physics G: Nuclear and Particle Physics*, 37(7A):075021, 2010.

[56] P. Sigmund. *Stopping of heavy ions: a theoretical approach*. Springer.

[57] A. Ferrari and P. R. Sala. Physics of showers induced by accelerator beams. In *Proceedings of the 1995 Frédéric Joliot Summer School in Reactor Physics, Cadarache, France, August 22-30, 1995*. CEA, 1996.

[58] S. G. Brush. *Theories of the equation of state of matter at high pressures and temperatures*, volume 1 of *Progress in High Temperature Physics and Chemistry*, pages 1 – 137. Pergamon Press, Oxford, 1st edition, 1967.

[59] W. D. Callister Jr and D. G. Rethwisch. *Materials Science and Engineering: An Introduction*. John Wiley & Sons, 2006.

- [60] Y. Ch. Fung and P. Tong. *Classical and Computational Solid Mechanics*. World Scientific.
- [61] R. W. Hertzberg. *Deformation and fracture mechanics of engineering materials*. John Wiley & Sons, 3rd edition.
- [62] D. J. Wulpi. *Understanding how components fail*. American Society of Metals.
- [63] D. Gross and Th. Seelig. *Fracture mechanics: with an introduction to micromechanics*. Springer.
- [64] ASTM E399 - 08 Standard Test Method for Linear-Elastic Plane-Strain Fracture Toughness K_{Ic} of Metallic Materials. Technical report, American Society for Testing and Materials.
- [65] M. A. Meyers. *Dynamic behaviour of materials*. Wiley & Sons.
- [66] U. S. Lindholm. *Part 1 – Chapter 4 – High Strain Rate Tests*, volume 5 of *Techniques in Metals Research*, pages 199 – 271. Wiley Interscience, 1971.
- [67] J. A. Zukas, T. Nicholas, H. F. Swift, L. B. Greshchuk, and D.P. Curran. *Impact Dynamics*. Wiley.
- [68] T. Antoun, L. Seaman, D. R. Curran, G. I. Kanel, S. V. Razorenov, and A. V. Utkin. *Spall fracture*. Springer.
- [69] R. J. Clifton. *Mechanics Today*, volume 1, chapter 3, pages 102 – 167. Pergamon Press, 1972.
- [70] Th. V. Karman and P. Duwez. The Propagation of Plastic Deformation in Solids. *Journal of Applied Physics*, 21(10):987 – 994, 1950.
- [71] G. E. Duvall. The Physics Connection. In L. E. Murr, K. P. Staudhammer, and M. A. Meyers, editors, *Metallurgical Applications of Shock-Wave and High-Strain-Rate Phenomena*, pages 1 – 25. Marcell Dekker, 1986.
- [72] W. Band and G. E. Duvall. Physical Nature of Shock Propagation. *American Journal of Physics*, 29(11):780 – 785, 1961.
- [73] I. C. Skidmore. An introduction to shock waves in solids. *Applied Material Research*, (4):131 – 147, 1965.
- [74] Rinehart, J. S. Compilation of Dynamic Equation of State Data for Solids and Liquids. Technical report, U.S. Naval Ordnance Test Station.
- [75] Kohn, B. J. Compilation of Hugoniot equations of state. Technical report, Air Force Weapons Laboratory, Kirtland Air Force Base.
- [76] Marsh (editor), S. P. LASL Shock Hugoniot Data. Technical report, Los Alamos Scientific Laboratory.

- [77] P. R. Levashov, K. V. Khishchenko, I. V. Lomonosov, and V. E. Fortov. Database on Shock-Wave Experiments and Equations of State Available via Internet. In *Shock Compression of Condensed Matter - 2003: Proceedings of the Conference of the American Physical Society Topical Group on Shock Compression of Condensed Matter*, volume 706, pages 87 – 90. AIP, 2004.
- [78] G. E. Duvall and R. A. Graham. Phase transitions under shock-wave loading. *Rev. Mod. Phys.*, 49(3):523 – 579, Jul 1977.
- [79] R. A. Graham and J. R. Asay. Measurement of wave profiles in shock-loaded solids. *High Temp. High Press.*, 10:355 – 390, 1978.
- [80] L. C. Chhabildas and R. A. Graham. Developments in measurement techniques for shock-loaded solids. In *Techniques and Theory of Stress Measurements for Shock Wave Applications*, volume 83, pages 1 – 18. American Society of Mechanical Engineers, Applied Mechanics Division, AMD, 1987.
- [81] D. E. Grady. The Shock Wave Profile. *AIP Conference Proceedings*, 955(1):3 – 11, 2007.
- [82] G. I. Kanel, S. V. Razorenov, and V. E. Fortov. *Shock-wave phenomena and the properties of condensed matter*. Springer.
- [83] J. W. Swegle and D. E. Grady. Shock viscosity and the prediction of shock wave rise times. *Journal of Applied Physics*, 58(2):692 – 701, 1985.
- [84] D. E. Grady. Structured shock waves and the fourth-power law. *Journal of Applied Physics*, 107(1):013506, 2010.
- [85] Grady, D. E. Dynamic material properties of armor ceramics. Technical Report SAND 91-0147.4C-704, Sandia National Laboratory, 1991.
- [86] J. W. Swegle and D. E. Grady. Shock viscosity and the calculation of steady shock wave profiles. In Y. M. Gupta, editor, *Proceedings of the Fourth American Physical Society Topical Conference on Shock Waves in Condensed Matter*, pages 353 – 357, 1985.
- [87] S. Eliezer, A. Ghatak, and H. Hora. *Fundamentals of equations of state*. World Scientific.
- [88] Ya. B. Zel'dovich and Yu. P. Raizer. *Physics of Shock Waves and High-Temperature Hydrodynamic Phenomena*, volume II. 1967.
- [89] B. K. Godwal, S. K. Sikka, and R. Chidambaram. Equation of state theories of condensed matter up to about 10 TPa. *Physics Reports*, 102(3):121 – 197, 1983.
- [90] V. E. Fortov. Intense shock waves and extreme states of plasmas. In M. H. Manghnani, W. J. Nellis, and M. F. Nicol, editors, *Proceedings of the International Conference on High Pressure Sciene and Technology (AIRAPT-17)*, volume 1, pages 3 – 10. Universities Press, Hyderabad, India, 2000.

- [91] V. E. Fortov and I. V. Lomonosov. Shock waves and equations of state of matter. *Shock Waves*, 20(1):53 – 71, 2010.
- [92] F. C. Perry. Thermoelastic Response of Polycrystalline Metals to Relativistic Electron Beam Absorption. *Journal of Applied Physics*, 41(12):5017 – 5022, 1970.
- [93] W. B. Gauster. Effect of heating rate in thermoelastic stress production. *Journal of the Mechanics and Physics of Solids*, 19(3):137 – 145, 1971.
- [94] F. C. Perry and M. M. Widner. In-depth heating by an intense relativistic electron beam. *Applied Physics Letters*, 29(5):282 – 284, 1976.
- [95] J. W. Nunziato and E. K. Walsh. Instantaneous and equilibrium Grüneisen parameters for a nonlinear viscoelastic polymer. *Journal of Applied Physics*, 44(3):1207 – 1211, 1973.
- [96] C. E. Ragan III, M. G. Silbert, and B. C. Diven. Shock compression of molybdenum to 2.0 TPa by means of a nuclear explosion. *Journal of Applied Physics*, 48(7):2860 – 2870, 1977.
- [97] K. Baumung, H. J. Bluhm, B. Goel, P. Hoppé, H. U. Karow, D. Rusch, V. E. Fortov, G. I. Kanel, S. V. Razorenov, A. V. Utkin, and O. Yu. Vorobjev. Shock-wave physics experiments with high-power proton beams. *Laser and Particle Beams*, 14(02):181 – 209, 1996.
- [98] D. H. H. Hoffmann, A. Blazevic, P. Ni, O. Rosmej, M. Roth, N. A. Tahir, A. Tauschwitz, S. Udrea, D. Varentsov, K. Weyrich, and Y. Maron. Present and future perspectives for high energy density physics with intense heavy ion and laser beams. *Laser and Particle Beams*, 23(01):47 – 53, 2005.
- [99] G. R. Johnson and W. H. Cook. A constitutive model and data for metals subjected to large strains, high strain rates and high temperatures. In *Proceedings of the 7th International Symposium on Ballistics*, pages 541 – 547. American Defense Preparedness Association, 1983.
- [100] J. A. Zukas, editor. *High Velocity Impact Dynamics*. John Wiley & Sons, October 1990.
- [101] F. J. Zerilli and R. W. Armstrong. Dislocation-mechanics-based constitutive relations for material dynamics calculations. *Journal of Applied Physics*, 61(5):1816 – 1825, 1987.
- [102] F. J. Zerilli and R. W. Armstrong. Description of tantalum deformation behavior by dislocation mechanics based constitutive relations. *Journal of Applied Physics*, 68(4):1580 – 1591, 1990.
- [103] F. J. Zerilli and R. W. Armstrong. Dislocation mechanics based constitutive relations for dynamic straining to tensile instability. In S. C. Schmidt, J. N. Johnson, and L. W. Davison, editors, *Shock Compression of Condensed Matter – 1989*, pages 357 – 360. Elsevier, 1990.

[104] M. A. Meyers and C. T. Aimone. Dynamic fracture (spalling) of metals. *Progress in Materials Science*, 28(1):1 – 96, 1983.

[105] M. A. Meyers. Dynamic failure: mechanical and microstructural aspects. *J. Phys. IV France*, 04:C8–597 – C8–621, Sep 1994.

[106] D. E. Grady. The spall strength of condensed matter. *Journal of the Mechanics and Physics of Solids*, 36(3):353 – 384, 1988.

[107] S. G. Brush. *Theory of the equation of state of matter at high pressures and temperatures*, volume 1 of *Progress in High Temperature Physics and Chemistry*, chapter 1, pages 1 – 137. Pergamon, 1966.

[108] D. A. Young. *Phase Diagrams of the Elements*. The University of California Press, May 1991.

[109] M. Kaviany. *Principles of convective heat transfer*. Springer.

[110] A. I. Burshtein. *Introduction to thermodynamics and kinetic theory of matter*. Wiley, 2nd edition.

[111] J. H. Tillotson. Metallic Equations of State for Hypervelocity Impact. Technical Report GA-3216, John Jay Hopkins Laboratory for Pure and Applied Science, 1962.

[112] A. V. Bushman, G. I. Kanel, A. L. Ni, V. E. Fortov, and J. W. Shaner. *Intense dynamic loading of condensed matter*. CRC Press.

[113] B. I. Bennett, J. D. Johnson, G. I. Kerley, and G. T. Rood. Recent Developments in the Sesame Equation-of-State Library. Technical Report LA-7130, Los Alamos National Laboratory, 1978.

[114] N. G. Cooper. An Invitation to Participate in the LASL Equation of State Library. Technical Report LASL-79-62, Los Alamos National Laboratory, 1980.

[115] T-4 Handbook of Material Properties Data Bases – Vol. 1c: Equations of State. Technical Report LA-10160-MS, Los Alamos National Laboratory, 1984.

[116] SESAME: The Los Alamos National Laboratory Equation Of State Database. Technical Report LA-UR-92-3407, Los Alamos National Laboratory, 1992.

[117] C. E. Morris. Shock-wave equation-of-state studies at Los Alamos. *Shock Waves*, 1(3):213 – 222, Sep 1991.

[118] A. V. Bushman and V. E. Fortov. Model equations of state. *Soviet Physics Uspekhi*, 26(6):465 – 496, 1983.

[119] I. V. Lomonosov, A. V. Bushman, and V. E. Fortov. Equations of state for metals at high energy densities. In S. C. Schmidt, J. W. Shaner, G. A. Samara, and M. Ross, editors, *High-pressure science and technology 1993*, volume 309, pages 117 – 120. AIP, 1994.

- [120] I. V. Lomonosov, A. V. Bushman, and V. E. Fortov. Wide-range multi-phase equation of state of metals. In S. C. Schmidt, J. W. Shaner, G. A. Samara, and M. Ross, editors, *High-pressure science and technology 1993*, volume 309, pages 121 – 124. AIP, 1994.
- [121] I. V. Lomonosov, V. E. Fortov, and K. V. Khishchenko. Wide Range Equation of State for Large Computer Codes: User Guide. Technical report, Defense Technical Information Center OAI-PMH Repository [<http://stinet.dtic.mil/oai/oai>] (United States), 1998.
- [122] I. V. Lomonosov, V. E. Fortov, K. V. Khishchenko, and P. R. Levashov. Phase Diagrams and Thermodynamic Properties of Metals at High Pressures, High Temperatures. In *Shock Compression of Condensed Matter - 2001: 12th APS Topical Conference*, volume 620, pages 111 – 114. AIP, 2002.
- [123] V. E. Fortov, V. V. Kim, I. V. Lomonosov, A. V. Matveichev, and A. V. Ostrik. Numerical modeling of hypervelocity impacts. *International Journal of Impact Engineering*, 33(1-12):244 – 253, 2006. Hypervelocity Impact Proceedings of the 2005 Symposium.
- [124] I. V. Lomonosov. Multi-Phase Equation of State for Aluminum. *AIP Conference Proceedings*, 955(1):63 – 66, 2007.
- [125] V.E. Fortov, B. Goel, C.-D. Munz, A.L. Ni, A. Shutov, and O.Yu Vorobiev. Numerical simulations of non-stationary fronts and interfaces by the Godunov method in moving grids. *Nucl. Sci. Eng.*, 123:169 – 189, 1996.
- [126] N. A. Tahir, R. Schmidt, M. Brugger, I. V. Lomonosov, A. Shutov, A. R. Piriz, S. Udrea, D. H. H. Hoffmann, and C. Deutsch. Prospects of high energy density physics research using the CERN super proton synchrotron (SPS). *Laser and Particle Beams*, 25(04):639 – 647, 2007.
- [127] N. A. Tahir, R. Schmidt, A. Shutov, I. V. Lomonosov, A. R. Piriz, D. H. H. Hoffmann, C. Deutsch, and V. E. Fortov. Large Hadron Collider at CERN: Beams generating high-energy-density matter. *Phys. Rev. E*, 79(4):046410–1 – 046410–8, Apr 2009.
- [128] N. A. Tahir, R. Schmidt, M. Brugger, A. Shutov, I. V. Lomonosov, A. R. Piriz, and D. H. H. Hoffmann. Simulations of full impact of the Large Hadron Collider beam with a solid graphite target. *Laser and Particle Beams*, 27(03):475 – 483, Jun 2009.
- [129] Richter, H. Laser Doppler Vibrometer Measurements During TT40 High Intensity Collimator Test 2006. Technical Note EDMS document 916430, CERN, May 2008. Draft in discussion.
- [130] V. Kain, R. W. Assmann, and H. Vincke. Memorandum (version 3). https://proj-lti.web.cern.ch/proj-lti/LTIcoordination/RelatedMeetings/TT40col/material/Memorandum_TT40Hi_v2.pdf, Nov 2006.

- [131] AB-OP Department SPS Section. Instructions and general information for the LHC 12 or 72 bunches beam. http://pcr-consigns.web.cern.ch/PCR-Consigns/beam-settings/LHC/2007_LHC25NS_72BUNCH/LHC_references_frames.htm, Aug 2007.
- [132] A. Bertarelli, O. Aberle, R. W. Assmann, S. Calatroni, A. Dallocchio, T. Kurtyka, M. Mayer, R. Perret, S. Redaelli, and G. Robert-Demolaize. Mechanical Design for Robustness of the LHC Collimators. In *Proceedings of the Particle Accelerator Conference 2005 (PAC 2005)*, pages 913 – 915, may 2005.
- [133] A. Bertarelli, O. Aberle, R. Assmann, A. Dallocchio, T. Kurtyka, M. Magistris, M. Mayer, and M. Santana-Leitner. Permanent Deformation of the LHC Collimator Jaws Induced by Shock Beam Impact: an Analytical and Numerical Interpretation. In *Proceedings of EPAC 2006*, pages 1801 – 1803, 2006.
- [134] C. Bracco, R. Assmann, and S. Redaelli. Scope of the TT40 Collimator Tests and of the LSS5 Tests. <http://proj-lti.web.cern.ch/proj-lti/LTIconditioning/RelatedMeetings/TT40col/talks/APC-ChiaraBracco-13-10-2006.pdf>, Oct 2006.
- [135] A. Dallocchio and A. Bertarelli. FE Simulation of 450 GeV Injection Error Test on Collimator. Talk given at the Workshop on Materials for Collimators and Beam Absorbers, Sep 2007.
- [136] A. Dallocchio, G. Belingardi, T. Kurtyka, and A. Bertarelli. *Study of Thermo-Mechanical Effects Induced in Solids by High Energy Particle Beams: Analytical and Numerical Methods.* oai:cds.cern.ch:1314219. PhD thesis, Turin, Politecnico di Torino.
- [137] S. Redaelli, R. Assmann, and G. Spiezzi. Accelerometer and microphone measurements of the LHC collimator during impacts of proton beams. Talk given at the Workshop on Materials for Collimators and Beam Absorbers, Sep 2007.
- [138] A. Bertarelli. Private communication, Aug 2007.
- [139] A. Bertarelli. Private communication, Sep 2006.
- [140] S. Girod. Modified LHC TCS collimator for vibration test in TT40 (sketch SPSTC-STV0006), Jun 2006.
- [141] M. Lazzaroni. Private communication, Sep 2006.
- [142] R. Wilfinger. Private picture repository, Nov 2008.
- [143] R. Wilfinger. *Proton Induced Thermal Stress-Wave Measurements for ISOLDE and CNGS.* PhD thesis, University of Technology Vienna (Austria), Dec 2005.
- [144] R. Wilfinger. Private communication, Jun 2008.

[145] M. Lazzaroni. <https://proj-lti.web.cern.ch/proj-lti/LTIcoordination/RelatedMeetings/TT40col/material/integration%20laser%20dans%20TT40-SPSTCSTV0010.pdf>, Jan 2007.

[146] C. Bracco. Private communication, Aug 2007.

[147] V. Kain. Private communication, Aug 2007.

[148] LHC Design Report Volume III – The LHC Injector Chain – Part 2: The SPS as LHC Injector – Chapter 12: Beam Parameters and Requirements. <http://ab-div.web.cern.ch/ab-div/Publications/LHC-DesignReport.html>, Aug 2007.

[149] V. Kain. Private communication, Jan 2007.

[150] MatWeb Material Property Data. <http://www.matweb.com/search/SpecificMaterial.asp?bassnum=BGRAP1>.

[151] M. Brugger. Private communication, Sep 2007.

[152] C. Theis, K. H. Buchegger, M. Brugger, D. Forkel-Wirth, S. Roesler, and H. Vincke. Interactive three-dimensional visualization and creation of geometries for Monte Carlo calculations. *Nuclear Instruments and Methods in Physics Research Section A: Accelerators, Spectrometers, Detectors and Associated Equipment*, 562(2):827 – 829, 2006. Proceedings of the 7th International Conference on Accelerator Applications - AccApp05.

[153] A. Dallocchio. Private communication, Sep 2007.

[154] R. Wilfinger. Private communication, Aug 2006.

[155] MATLAB Version 7.3.0.267 (R2006b). Curve Fitting Tool, Aug 2006.

[156] Yao W.-M. et al. Review of Particle Physics. *Journal of Physics G: Nuclear and Particle Physics*, 33(1):1, 2006.

[157] H. Richter, R. Wilfinger, and J. Lettry. LHC Collimator Jaw Vibration Measurement using a Laser Doppler Vibrometer. Talk given at the Workshop on Materials for Collimators and Beam Absorbers, CERN (Geneva, Switzerland), Sep 2007.

[158] R. Wilfinger, A. Kelić, B. Achenbach, K. H. Behr, A. Bruenle, F. Cerutti, R. Catherall, H. Geissel, D. H. H. Hoffmann, A. Hug, Ch. Karagiannis, B. Kindler, K. Knie, M. Krause, M. Kulish, J. Lettry, B. Lommel, J. Menzel, N. Müller, H. Richter, K. Suemmerer, N. Tahir, M. Tomut, Ch. Trautmann, S. Udrea, D. Varentsov, H. Weick, M. Winkler, and Y. Zhao. Study of Thermal Stress Waves Induced by Relativistic Heavy-Ion Beams. Technical report, GSI, 2008.

[159] N. A. Tahir, V. Kim, A. Matvechev, A. Ostrik, I. V. Lomonosov, A. R. Piriz, J. J. Lopez Cela, and D. H. H. Hoffmann. Numerical modeling of heavy ion induced stress waves in solid targets. *Laser and Particle Beams*, 25(04):523 – 540, 2007.

[160] J. F. Ziegler. SRIM - The Stopping and Range of Ions in Matter. <http://www.srim.org/>, 2007.

[161] J. Lettry, F. Cerutti, A. Gerardin, S. Sgobba, and R. Wilfinger. GSI S-334 experiment. Talk given at the 4th High Power Targetry Workshop (Malmö, Sweden), organized by the European Spallation Source (ESS), May 2011.

[162] F. Cerutti. Private communication, Jul 2008.

[163] F. Cerutti. Private communication, Apr 2011.

[164] Century Dynamics. SPH User Manual & Tutorial. Technical Report Revision 4.3, Century Dynamics, 2005.

[165] R. G. McQueen. Selected Hugoniots. Technical Report LA-4167-MS, Los Alamos Scientific Laboratory, May 1969.

[166] D. J. Steinberg. Equation of state and strength properties of selected materials. Technical Report UCRL-MA-106439, Lawrence Livermore National Laboratories, 1991.

[167] G. R. Johnson and W. H. Cook. Fracture characteristics of three metals subjected to various strains, strain rates, temperatures and pressures. *Engineering Fracture Mechanics*, 21(1):31 – 48, 1985.

[168] G. R. Johnson and T. J. Holmquist. Evaluation of cylinder-impact test data for constitutive model constants. *Journal of Applied Physics*, 64(8):3901 – 3910, 1988.

[169] D. A. Matuska. HULL Users Manual. Technical Report AFATL-TR-84-59, Orlando Technology Inc Shalimar Fl, 1984.

[170] V. A. Ogorodnikov, A. G. Ivanov, E. S. Tyun'kin, V. A. Grigor'ev, and A. A. Khokhlov. Dependence of spall strength of metals on the amplitude of a shock-wave load. *Combustion, Explosion, and Shock Waves*, 28:88 – 92, 1992. 10.1007/BF00754975.

[171] R. S. Hixson, G. T. Gray, P. A. Rigg, L. B. Addessio, and C. A. Yablinsky. Dynamic Damage Investigations Using Triangular Waves. In *American Institute of Physics Conference Series*, volume 706 of *American Institute of Physics Conference Series*, pages 469 – 472, July 2004.

[172] D. B. Holtkamp, D. A. Clark, E. N. Ferm, R. A. Gallegos, D. Hammon, W. F. Hemsing, G. E. Hogan, V. H. Holmes, N. S. P. King, R. Liljestrand, R. P. Lopez, F. E. Merrill, C. L. Morris, K. B. Morley, M. M. Murray, P. D. Pazuchanics, K. P. Prestridge, J. P. Quintana, A. Saunders, T. Schafer, M. A. Shinas, and H. L. Stacy. A Survey of High Explosive-Induced Damage and Spall in Selected Metals Using Proton Radiography. In *American Institute of Physics Conference Series*, volume 706 of *American Institute of Physics Conference Series*, pages 477 – 482, July 2004.

[173] J. N. Johnson, G. T. Gray III, and N. K. Bourne. Effect of pulse duration and strain rate on incipient spall fracture in copper. *Journal of Applied Physics*, 86(9):4892 – 4901, 1999.

[174] Zurek, A. K., Johnson, J. N., and Frantz, C. E. Characterization of Dynamic Fracture in Copper under Uniaxial Stress and Uniaxial Strain. *J. Phys. Colloques*, 49:C3–269 – C3–276, 1988.

[175] W. R. Thissell, A. K. Zurek, D. A. S. MacDougall, D. Miller, R. Everett, A. Geltmacher, R. Brooks, and D. Tonks. The Effect of Material Cleanliness on Dynamic Damage Evolution in 10100 Cu. In Furnish, M. D. and Horie, Y. and Thadhani, N. N., editor, *Shock Compression of Condensed Matter*, volume 620 of *American Institute of Physics Conference Series*, pages 475 – 478, July 2002.

[176] S. V. Razorenov, G. I. Kanel, B. Herrmann, E. B. Zaretsky, and G. E. Ivanchihina. Influence of Nano-Size Inclusions on Spall Fracture of Copper Single Crystals. In Elert, M. and Furnish, M. D. and Chau, R. and Holmes, N. and Nguyen, J., editor, *Shock Compression of Condensed Matter*, volume 955 of *American Institute of Physics Conference Series*, pages 581 – 584, December 2007.

[177] S. Christy, H.-R. Pak, and M. A. Meyers. Effect of Metallurgical Parameters on Dynamic Fracture by Spalling of Copper. In L. E. Murr, K. P. Staudhammer, and M. A. Meyers, editors, *Metallurgical Applications of Shock-Wave and High-Strain-Rate Phenomena*, pages 835 – 863. Marcell Dekker, 1986.

[178] S. V. Razorenov, G. I. Kanel, K. Baumung, and H. J. Bluhm. Hugoniot Elastic Limit and Spall Strength of Aluminum and Copper Single Crystals over a Wide Range of Strain Rates and Temperatures. In Furnish, M. D. and Horie, Y. and Thadhani, N. N., editor, *Shock Compression of Condensed Matter*, volume 620 of *American Institute of Physics Conference Series*, pages 503 – 506, July 2002.

[179] L. Bruno. Numerical tools for the design of beam intercepting devices. Talk given at the Workshop on Materials for Collimators and Beam Absorbers, CERN (Geneva, Switzerland), Sep 2007.

[180] Bruno, L. and Richter, H. FLUKA to AUTODYN interface - 2D & 3D - v.2. <https://edms.cern.ch/document/976965/2>.

[181] J. Lettry, R. Wilfinger, A. Gerardin, and S. Sgobba. Private communication - material to be published, 2008.

[182] Richter, H., Noah, E., Aigner, H., and Poljanc, K. Simulation of target response due to uranium ion beam impact. *Eur. Phys. J. A*, 42(3):301 – 306, 2009.

[183] S. Thippadu. Private communication - ANSYS AUTODYN® support, February 2009.

[184] N. Mladenov. Private communication - ANSYS AUTODYN® support, November 2010.

[185] N. A. Tahir. Private communication, Apr 2009.

- [186] G. I. Kanel, S. V. Razorenov, A. V. Utkin, and D. E. Grady. The spall strength of metals at elevated temperatures. *AIP Conference Proceedings*, 370(1):503 – 506, 1996.
- [187] A. A. Bogach. Analysis of temperature influence on the dynamic fracture of metals. *AIP Conference Proceedings*, 429(1):223 – 226, 1998.
- [188] Thissell, W. R., Zurek, A. K., Macdougall, D. A.S., and Tonks, D. Damage evolution and damage model validation in spalled tantalum. *J. Phys. IV France*, 10:Pr9–769 – Pr9–774, 2000.
- [189] Ch. Czarnota, S. Mercier, and A. Molinari. Modelling of nucleation and void growth in dynamic pressure loading, application to spall test on tantalum. *International Journal of Fracture*, 141:177 – 194, 2006. 10.1007/s10704-006-0070-y.
- [190] Chhabildas, L.C. and Asay, J.R. Dynamic yield strength and spall strength measurements under quasi-isentropic loading. Technical Report SAND-90-0883C and CONF-9008125-3, Sandia National Laboratory, 1990.
- [191] M. D. Furnish, W. D. Reinhart, W. M. Trott, L. C. Chhabildas, and T. J. Vogler. Variability in Dynamic Properties of Tantalum: Spall, Hugoniot Elastic Limit and Attenuation. *AIP Conference Proceedings*, 845(1):615 – 618, 2006.
- [192] Zurek, A. K. and Gray, G. T. Dynamic Strength and Strain Rate Effects on Fracture Behavior of Tungsten and Tungsten Alloys. *J. Phys. IV France*, 01:C3–631 – C3–637, 1991.
- [193] L. Hu, P. Miller, and J. Wang. High strain-rate spallation and fracture of tungsten by laser-induced stress waves. *Materials Science and Engineering: A*, 504(1-2):73 – 80, 2009.

CURRICULUM VITAE

PERSONAL INFORMATION

Name

Address

Telephone

E-Mail

Nationality

Date of birth

HERTA RICHTER

Hormayrgasse 23

1170 Wien

AUSTRIA

+43 664 46 20 445

hertha.richter@cern.ch

Austrian

20th of October 1981

EDUCATION

▷ Period

- Acquired qualifications
- Institute
- PhD Thesis

April 2006 – October 2011

PhD (Dr. techn.)

CERN, Switzerland and Vienna University of Technology, Austria
Simulating Transient Effects of Pulsed Beams on Beam Intercepting Devices

▷ Period

- Acquired qualifications
- Institute
- Master Thesis

October 2000 – March 2006

MSc in Technical Physics (Dipl. Ing.)

Vienna University of Technology, Austria

Control of the Measuring Process for Acquisition of In-Plane and Out-of-Plane Oscillations of Surfaces

▷ Period

- Institute
- Aim

February – June 2004

West University of Timișoara, Romania

Erasmus semester at Physics department

PUBLICATION

- Paper

H. Richter et al.: *Simulation of target response due to uranium ion beam impact* The European Physical Journal A - Hadrons and Nuclei. Springer, 2009

WORK EXPERIENCE

▷ Period

- Current employer
- Employment
- Main responsibilities

Sep 2009 – Dec 2011

CERN – European Organization for Nuclear Research,
Geneva/Switzerland

Fellow

Radiation protection simulations for the CERN injector chain with FLUKA (interface LINAC 2 – LINAC 4, LBS dump)

▷ Period

- Employer
- Employment
- Main responsibilities

August 2006 – July 2009

CERN – European Organization for Nuclear Research,
Geneva/Switzerland

PhD Student

Simulation of interaction of uranium ion beam with metal targets, Laser Doppler Vibrometer measurements

▷ Period	December 2004 – May 2005
◦ Employer	Institute of General Physics, Vienna University of Technology – Group "Sensors and Ultrasonics" , Vienna/Austria
◦ Employment	Employee with a limited contract of employment
◦ Main responsibilities	Enhancement of software in order to measure in- and out-of-plane oscillations of surfaces within project "QxSens" (Multi-channel measurement and control system based on resonant piezoelectric crystal sensors)
▷ Period	October 2004 – June 2006
◦ Employer	Press Department of HTU (= HochschülerInnenschaft der TU Wien [Student Association of the Vienna University of Technology]) , Vienna/Austria
◦ Main responsibilities	Editorial and layout
▷ Period	October 2004 – January 2005
◦ Employer	Institute of General Physics, Vienna University of Technology , Vienna/Austria
◦ Main responsibilities	Tutor for problem-solving classes (First semester of Technical Physics)
▷ Period	July – mid-September 2004
◦ Employer	CERN – European Organization for Nuclear Research , Geneva/Switzerland
◦ Employment	Summer student
◦ Main responsibilities	Project "A Method for Sequential Particle Identification" within HARP work group (supervisor: Anselmo Cervera Villanueva), attending summer student lectures
▷ Period	October 2003 – January 2004
◦ Employer	Lernen 8 – private tutoring center for school children , Vienna/Austria
◦ Main responsibilities	Private tutor of mathematics for school children (from 12 – 18 years)
▷ Period	October – December 2003
◦ Employer	Institute of General Physics, Vienna University of Technology , Vienna/Austria
◦ Main responsibilities	Undergraduate laboratory demonstrator for students of Technical Physics in third semester
▷ Period	Winter term 2004, 2003, 2002
◦ Employer	Verein Sprungbrett (information center for girls and young women) , Vienna/Austria
◦ Main responsibilities	Informing young women at the end of their school career about studies at the Vienna University of Technology (school visits and support of social worker in workshops based at the university)

▷ Period	September 2003
◦ Employer	Atomic Institute of the Austrian Universities , Vienna/Austria
◦ Main responsibilities	Writing and editing of lecture handouts for the course "Teilchenbeschleuniger" (= Particle Accelerators)
▷ Period	Nov. 2001 – September 2005
◦ Employer	Women's Department of HTU (= HochschülerInnen-schaft der TU Wien [Student Association of the Vienna University of Technology]), Vienna/Austria
◦ Position	Assistant (Nov 2001 – Sep 2002), consultant (Oct 2002 – Sep 2003), freelancer (Oct 2003 – Sep 2005)
◦ Main projects	Organization of series of panel discussions called "Technikerin – ein Berufsbild" (= female technician – a job description), organization of fourth and fifth presentation of "Lise Meitner Literaturpreis" (2003, 2005) – literary award in German speaking countries for women dedicated to writing about women in science and technology
LANGUAGES	
NATIVE TONGUE	German
OTHER LANGUAGES	English (fluent), French (good), Romanian (basic), Spanish (basic), Hebrew (beginner)
SKILLS & QUALIFICATIONS	
◦ Radiation protection	Swiss radiation protection expert type B/C
◦ Operating systems	Microsoft (98, Me, 2000, XP, 7), Linux, Mac OS, DOS
◦ Office programs	Microsoft: Word, Excel, PowerPoint, OneNote, Outlook; Browser: Firefox, Internet Explorer
◦ Layout and graphics programs	LaTeX (TeXnic Center, LyX), QuarkXpress, Photoshop, SmartDraw, CorelDraw X3, GIMP, Adobe Acrobat, Adobe Lightroom
◦ Other programs	ANSYS AUTODYN, FLUKA, SimpleGeo, Igor Pro, MATLAB, Mathematica, Notepad++, PuTTY, WinSCP, HTML web-design
◦ Programming languages	FORTRAN, C++, LabView
◦ Driving licenses	Austrian driving-license for motorcycles (A) and cars (B)
INTERESTS	Photography, hiking, traveling, astronomy

Vienna, 12 October 2011

Herta Richter